

Bernhard STANJE, BSc MSc

**LITHIUM DIFFUSIVITY IN RESTRICTED DIMENSIONS: DIFFUSION ALONG  
THE INNER SURFACES AND IN DISORDERED, NANOSTRUCTURED IONIC  
CONDUCTORS**

DISSERTATION

zur Erlangung des akademischen Grades  
*Doktor der technischen Wissenschaften (Dr. techn.)*  
eingereicht an der  
Technischen Universität Graz

Betreuer:  
*Univ.-Prof. Dr. rer. nat. Martin Wilkening*  
Institut für Chemische Technologie von Materialien

Graz, Februar 2016



## Affidavit

I declare that I have authored this thesis independently, that I have not used other than the declared sources/resources, and that I have explicitly indicated all material which has been quoted either literally or by content from the sources used. The text document uploaded to TUGRAZonline is identical to the present doctoral dissertation.

## Eidesstattliche Erklärung

Ich erkläre an Eides statt, dass ich die vorliegende Arbeit selbstständig verfasst, andere als die angegebenen Quellen/Hilfsmittel nicht benutzt, und die den benutzten Quellen wörtlich und inhaltlich entnommenen Stellen als solche kenntlich gemacht habe. Das in TUGRAZonline hochgeladene Textdokument ist mit der vorliegenden Dissertation identisch.

Graz, 12.01.2017  
Date

  
Signature



“ *A learning experience is one of those things that says, 'You know that thing you just did? Don't do that.'* ”

---

Douglas Adams, *The Salmon of Doubt*, 2005



# Acknowledgement

Mein größter Dank gilt in erster Linie Herrn Prof. Martin Wilkening, der mir nicht nur die Möglichkeit gab, meine Dissertation in seiner Arbeitsgruppe durchzuführen, sondern mich auch hervorragend betreut und sich vor allem immer für mich Zeit genommen hat. Ich kann mich wirklich an keine Situation erinnern, in der ich keine Rückmeldung innerhalb von Minuten erhalten hätte, ganz unabhängig von der Tageszeit oder der Wichtigkeit meiner Frage. Ich danke dir für deine Ideen, deinen Rat und dein Vertrauen in mich. Weiters möchte ich mich herzlich für die zahlreichen Gelegenheiten danken, meine wissenschaftliche Arbeit auf Konferenzen im Ausland zu präsentieren, als auch für die Möglichkeit eines Forschungsaufenthalts bei Prof. Saiful Islam in Bath (UK).

Großer Dank gilt meinen Arbeitskollegen der Arbeitsgruppe Wilkening, auch bekannt als AGW, sowie allen anderen Kollegen am Institut. Im Laufe meiner Zeit hier am ICTM habe ich viele Menschen kennengelernt und darf inzwischen einige davon zu meinen Freunden zählen. Besonders bedanken möchte ich mich bei Viktor und Patrick, die mich vor allem zu Beginn meiner Dissertation tatkräftig unterstützt haben: ohne euch wäre ich heute nicht dazu in der Lage ein NMR Spektrometer zu bedienen, noch könnte ich die Daten in Igor entsprechend verarbeiten. Weiters würde ich mich gerne bei Liane für die Hilfe bei sämtlichen organisatorischen Aufgaben bedanken. An den Rest der AGW : *Dōmo arigatō!* Für alles – die Atmosphäre, die Unterstützung und die zahlreichen lustigen Momente. Ihr seid spitze!

Danke Mama! Danke Papa! Danke Michael! Ohne euch wäre ich jetzt nicht da wo ich bin. Ich weiß zu schätzen, dass ihr immer für mich da seid und mich in jeder Hinsicht unterstützt!

Last but no least: Danke Mel! Wenn ich nun anfangen würde alles aufzulisten wofür ich dir in diesem Moment dankbar bin, dann würde dies den Rahmen der Arbeit sprengen. Ich bin glücklich, dass ich dich meine bessere Hälfte nennen darf, denn ohne dich wäre alles nur halb so schön.



# Abstract

Electrochemical energy storage plays an important role in today's society. The constant demand for improvements in the worldwide living standards made the development of new electrochemical energy storage systems one of the biggest and most profitable challenges of our modern society. With the rise of steadily advancing electronics such as notebooks, smartphones, electric vehicles *etc.*, conventional batteries are seeking continuous improvement in order to imbue their performance demand. Alternative materials have to meet many requirements to be even considered as a replacement candidate of conventional used materials in energy storage systems. Potential candidates will have to fulfill extravagant requirements such as high conductivities, high capacities, exceptional charging and discharging rates, low costs, environmentally friendliness among others. In order to access these parameters a proper characterization of alternative energy storage materials is inevitable. The performance of lithium ion batteries is strongly linked to the mobility of their charge carriers, therefore a detailed characterization of ion dynamics is necessary. A wide repertoire of methods can be used to gather information on ionic diffusion in solids from a macroscopic and microscopic point of view.

The following thesis shows how nuclear magnetic resonance (NMR) and impedance spectroscopy (IS) can be used to study fast and slow Li ion diffusivity in various lithium ion conductor materials. These methods provide access to various diffusion properties such as diffusion coefficients ( $D$ ), jump rates ( $\tau$ ) and activation energies ( $E_a$ ) for long- as well as for short-range Li ion diffusion.

The investigated materials can be divided into four different categories: (i) lithium ion diffusion in low-dimensional materials (one-dimensional  $\text{Li}_3\text{BiS}_5$  and two-dimensional  $2\text{H-Li}_x\text{NbS}_2$ ), (ii) lithium ion diffusion in three-dimensional Li oxides (single crystalline garnet-type  $\text{Li}_6\text{La}_3\text{ZrTaO}_{12}$  (LLZTO) and bismuth doped LLZO  $\text{Li}_{7-x}\text{La}_3\text{Zr}_{2-x}\text{Bi}_x\text{O}_{12}$ ), (iii) the influence of mechanical treatment on lithium diffusivity in the aluminosilicate mineral petalite ( $\text{LiAlSi}_4\text{O}_{10}$ ) and (iv) a novel electrolyte concept "ionic liquids-in-salt" for high-temperature lithium batteries.

(i) The one-dimensional conductor  $\text{Li}_3\text{BiS}_5$  was successfully synthesized as a phase-pure material. Activation energies as high as 0.66(8) eV were extracted from spin-lock NMR measurements. This is in line with results from NMR motional line narrowing hinting at a lithium jump-rate in the order of *ca.*  $2 \cdot 10^4 \text{ s}^{-1}$  at 500 K identifying  $\text{Li}_3\text{BiS}_5$  as a moderate conductor. Variable-temperature  $^7\text{Li}$  NMR spectroscopy was used to study translational Li ion diffusion in the model system hexagonal (2H-)  $\text{Li}_x\text{NbS}_2$  (with  $x = 0.3, 0.7$  and 1). Information on the dimensionality of the diffusion process was experimentally obtained by frequency dependent  $R_\rho$  measurements carried out at  $T = 444$  K approving the two-dimensional Li diffusion process. Increasing lithium content  $x$  revealed a decrease in Li diffusivity.

(ii)  $^7\text{Li}$  NMR relaxometry measurements using both laboratory and spin-lock techniques were used to probe Li jump rates in single crystalline LLZTO with the nominal composition  $\text{Li}_6\text{La}_3\text{ZrTaO}_{12}$ . The data perfectly mirror a modified Bloembergen-Purcell-Pound-type (BPP) relaxation response being

based on a Lorentzian-shaped relaxation function. Besides the extremely fast Li ion conductor LLZTO another Li oxide with garnet-type structure namely  $\text{Li}_{7-x}\text{La}_3\text{Zr}_{2-x}\text{Bi}_x\text{O}_{12}$  was investigated. Here the effect of Bismuth doping ( $x = 0.10, 0.20, \dots, 1.00$ ) was investigated by solid state  $^7\text{Li}$  NMR showing that fast Li ion diffusivity for LLZBO is only achieved for high Bi contents.

(iii) The influence of mechanical treatment, and thus nanostructuring and the introduction of defects, on Li ion dynamics in both crystalline petalite  $\text{LiAlSi}_4\text{O}_{10}$  and its glassy form was comprehensively investigated by solid-state NMR and impedance spectroscopy. The various nanostructured samples were prepared by high-energy ball milling. Ball-milling of the crystalline petalite results in an enhancement of long-range ion transport by several orders of magnitude. The opposite trend, however, is found when  $\text{LiAlSi}_4\text{O}_{10}$  glass is treated for several hours in a planetary mill. The Li ion conductivities of the two samples, *viz* the crystalline and glassy forms, head towards each other with increasing milling time.

(iv) The mixture of an ionic liquid with a lithium salt represents a conceptually new class of electrolyte materials for high-temperature lithium batteries, termed “ionic liquid-in-salt”.  $^7\text{Li}$  NMR was used to study both local electronic structures and  $\text{Li}^+$  self-diffusion in the mixture of LiTFSI and  $\text{Li}_x\text{EMIN}_{1-x}\text{TFSI}$  with  $x = 0.9$ . NMR experiments recorded up to delay times of 1000s directly reveal the pronounced bi-exponential  $^7\text{Li}$  SLR NMR transients, showing a subset of highly mobile Li ions, partly identified as  $[\text{Li}(\text{TFSI})_2]^-$ , which can be well discriminated from the response of pure LiTFSI. This sub-ensemble is regarded to be responsible for the enhancement in ion conductivity towards higher temperature.

keywords: *Li-ion dynamics, solid-state NMR spectroscopy, impedance spectroscopy*

# Kurzfassung

Elektrochemische Energiespeichersysteme spielen eine wichtige Rolle in der heutigen modernen Gesellschaft. Das Streben unserer Gesellschaft nach Fortschritt und der damit verbundenen Steigerung des Lebensstandards macht die Entwicklung von neuartigen Energiespeichersystemen zu einer profitablen Herausforderung für die Forschung. Im Zeitalter von stetiger Weiterentwicklung, betroffen sind vor allem Elektrogeräte (Notebooks, Smartphones, Elektroauto *usw.*), stoßen konventionelle Batteriesysteme an die Grenzen des Möglichen. Neu entwickelte Materialien müssen eine Unmenge an teils utopischen Eigenschaften mitsichbringen, um als Alternative in Frage zu kommen. Um einige dieser Eigenschaften zu nennen, müssten neue Materialien besonders gute Leitfähigkeiten, hohe Kapazitäten sowie aussergewöhnliche Lade- und Entladeeigenschaften aufweisen. Die Suche nach einer *eierlegenden Wollmilchsau* hat begonnen. Zugang zu diesen Eigenschaften erhält man durch eine ausreichende Charakterisierung der Materialien und ist für die Entwicklung neuartiger Materialien unumgänglich. Die Leistung einer Lithium-Ionenbatterie ist eng mit der Mobilität der Ladungsträger des Materials verknüpft, wodurch eine detaillierte Untersuchung der Ionendynamik umso wichtiger erscheint. Es können zahlreiche unterschiedliche Methoden genutzt werden, um Auskunft über Materialeigenschaften von einem makro- sowie mikroskopischen Blickpunkt aus zu erhalten.

In dieser Arbeit werden magnetische Kernresonanz (NMR) und Impedanzspektroskopie (IS) verwendet, um schnelle, sowie langsame Lithium-Ionenbewegung in verschiedensten Materialklassen, die für den Einsatz in zukünftigen Lithium-Ionenbatterien in Frage kommen, zu untersuchen. Mit diesen Methoden schafft man sich Zugang zu verschiedensten Materialparametern wie Diffusionskoeffizienten ( $D$ ), Sprungraten ( $\tau$ ) und lang- sowie kurzreichweitigen Aktivierungsenergien ( $E_a$ ).

Die untersuchten Materialien können in vier Kategorien unterteilt werden (*i*) Lithium-Ionendiffusion in nieder-dimensionalen Materialien ((ein-dimensionales 2H- $\text{Li}_x\text{NbS}_2$  und zwei-dimensionales  $\text{Li}_3\text{BiS}_5$ ), (*ii*) Lithium-Ionendiffusion in drei-dimensionalen Lithiumoxiden (Einkristall mit Granat-Struktur  $\text{Li}_6\text{La}_3\text{ZrTaO}_{12}$  (LLZTO) und mit Bismuth gedoptes LLZO  $\text{Li}_{7-x}\text{La}_3\text{Zr}_{2-x}\text{Bi}_x\text{O}_{12}$ ), (*iii*) der Einfluss von Mechanochemie auf die Leitfähigkeit von dem Schichtsilikat-Mineral Petalit ( $\text{LiAlSi}_4\text{O}_{10}$ ) und (*iv*) das neuartige Konzept "Ionische Flüssigkeit-in-Salz" für die Herstellung von Elektrolyten für Hochtemperaturbatterien.

(*i*) Der eindimensionale Ionenleiter  $\text{Li}_3\text{BiS}_5$  konnte erfolgreich als phasenreines Material hergestellt werden. Eine Aktivierungsenergie von 0.66(8) eV konnte durch die Charakterisierung mit der *s.g.* "spin-lock" NMR-Methode berechnet werden. Dieser Wert stimmt mit den Beobachtungen erhalten von der Linienverschmälerung der NMR-Spektren überein. Die Beobachtungen deuten auf eine Sprungrate von *ca.*  $2 \cdot 10^4 \text{ s}^{-1}$  bei 500 K hin, dies bedeutet, dass  $\text{Li}_3\text{BiS}_5$  als ein moderater Leiter eingestuft werden kann.  $^7\text{Li}$ -NMR-Spektroskopie wurde eingesetzt, um die translatorische Li-Ionenbewegung in dem zwei-dimensionalen und hexagonalem Modellsystem (2H-)  $\text{Li}_x\text{NbS}_2$  (mit  $x = 0.3, 0.7$  und 1) zu untersuchen. Durch die Verwendung von frequenzabhängigen  $R_\rho$ -Messungen bei einer Temperatur

von  $T = 444$  K konnten Information hinsichtlich der Dimensionalität des Lithium-Diffusionsprozesses experimentell ermittelt werden und die Zwei-Dimensionalität des Diffusionsprozesses konnte belegt werden. Mit steigendem Lithiumgehalt  $x$  verringert sich auch die Diffusivität in dem Festkörper.

(ii)  $^7\text{Li}$ -NMR-Relaxationsmessungen im Laborkoordinatensystem sowie im rotierenden Koordinatensystem wurden verwendet um Li-Sprungraten eines LLZTO-Einkristalls mit der nominalen Zusammensetzung  $\text{Li}_6\text{La}_3\text{ZrTaO}_{12}$  zu messen. Die erhaltenen Daten spiegeln das Verhalten eines modifizierten Bloembergen-Purcell-Pound-type (BPP) Modells, das auf einer lorentz-förmigen Spektraldichtefunktion basiert, perfekt wider. Zusätzlich zu diesem sehr schnellen Ionenleiter wurde ein weiteres Material zugehörig zur Gruppe der Lithiumoxide  $\text{Li}_{7-x}\text{La}_3\text{Zr}_{2-x}\text{Bi}_x\text{O}_{12}$ , ein Granat, untersucht. Bei diesem Material wurde der Einfluss von Fremdatomen, unterschiedlicher Bismuth-Gehälter  $x$  (mit  $x = 0.10, 0.20, \dots, 1.00$ ) mittels  $^7\text{Li}$ -Spin-Gitter-Relaxation-NMR (SLR) untersucht. Die Ergebnisse deuten darauf hin, dass schnelle Lithiumdiffusion nur bei höheren Bismuth-Gehältern im Material beobachtet werden kann.

(iii) Der Einfluss von struktureller Unordnung, *d.h.* die Nanostrukturierung des Materials inkl. dem Erzeugen von Fehlstellen und Defekten, auf die Lithiumdiffusivität im kristallinen Schichtsilikat Petalit  $\text{LiAlSi}_4\text{O}_{10}$  und in einem Petalit-Glas (Glas mit Petalit-Zusammensetzung) wurde mittels Festkörper-NMR und Impedanzspektroskopie (IS) untersucht. Die Nanostrukturierung erfolgte durch Hochenergie-Kugelmahlen des Materials in einer Planetenmühle. Das Mahlen der kristallinen Petalit-Probe führt zu einer Verbesserung/Steigerung der Leitfähigkeit über mehrere Größenordnungen. Das exakte Gegenteil wird beobachtet wenn das  $\text{LiAlSi}_4\text{O}_{10}$  Glas gemahlen wird. Die Lithium-Ionen Leitfähigkeiten beider Proben, kristallin sowie glasig, konvergieren mit steigender Mahlzeit, *d.h.* bei ausreichend langer Mahlzeit verhalten sich beide Materialien nahezu ident.

(iv) Die Mischung einer ionischen Flüssigkeit mit einem Lithium-Salz stellt eine neue Konzept-Klasse von Elektrolyten für Hochtemperatur-Lithium-Ionenbatterien dar. Dieses Konzept wurde "ionische Flüssigkeit-in-Salz" getauft.  $^7\text{Li}$  NMR wurde verwendet, um lokale elektronische Strukturen sowie die  $\text{Li}^+$ -Selbstdiffusion in LiTFSI gemischt mit  $\text{Li}_x\text{EMIM}_{1-x}\text{TFSI}$  mit  $x = 0.9$  zu untersuchen. Durch die Aufnahme von NMR-Experimenten mit Wartezeiten von bis zu 1000s kann man die gut ausgeprägten zweifach-exponentiellen  $^7\text{Li}$ -SLR-NMR-Transienten so auswerten, dass man die "schnellen" Li Ionen der Mischung von den "langsameren" Li Ionen des reinen LiTFSI trennen kann. Diese hochmobilen Ionen konnten teilweise als  $[\text{Li}(\text{TFSI})_2]^-$  identifiziert werden und diese Spezies ist vermutlich auch dafür verantwortlich, dass es zu einer enormen Verbesserung der Leitfähigkeiten bei hohen Temperaturen kommt.

Stichworte: *Li-Ionen Dynamik, Festkörper NMR Spektroskopie, Impedanzspektroskopie*

# Table of contents

<b>Acknowledgement</b> .....	<b>vii</b>
<b>Abstract</b> .....	<b>ix</b>
<b>Kurzfassung</b> .....	<b>xi</b>
<b>1 Introduction</b> .....	<b>1</b>
<b>2 Principles of diffusion in solids</b> .....	<b>3</b>
2.1 Fundamentals of diffusion .....	3
2.2 Diffusion in solids .....	4
2.2.1 Defects in crystal structures .....	5
2.2.2 Mechanisms of diffusion .....	7
2.3 Determination of diffusion parameter .....	9
2.4 Solid-state nuclear magnetic resonance .....	10
2.4.1 Basics of NMR .....	10
2.4.2 NMR relaxation and diffusion .....	18
2.4.3 Spin-alignment echo NMR .....	24
2.4.4 Magic-angle spinning NMR .....	25
2.5 Impedance spectroscopy .....	26
2.5.1 Basics of impedance spectroscopy .....	26
2.5.2 Conductivity spectra and diffusion .....	28
<b>3 Results</b> .....	<b>31</b>
3.1 Lithium ion diffusion in low-dimensional materials .....	33
3.1.1 One-dimensional Li diffusion in $\text{LiBi}_3\text{S}_5$ .....	33
3.1.2 Two-dimensional Li diffusion of $2\text{H-Li}_x\text{NbS}_2$ .....	43
3.2 Lithium ion diffusion in three-dimensional Li oxides .....	57
3.2.1 Extremely fast charge carriers in garnet-type $\text{Li}_6\text{La}_3\text{ZrTaO}_{12}$ .....	57
3.2.2 Li ion dynamics in Bi-doped garnet-type $\text{Li}_{7-x}\text{La}_3\text{Zr}_{2-x}\text{Bi}_x\text{O}_{12}$ .....	63
3.3 The influence of mechanical treatment on lithium diffusivity .....	77
3.3.1 Li ion diffusion and ionic conduction in aluminosilicate $\text{LiAlSi}_4\text{O}_{10}$ .....	77
3.4 A novel electrolyte concept for high-temperature Li ion batteries .....	83
3.4.1 "Ionic liquids-in-salt"-concept .....	83
<b>4 Conclusion and Outlook</b> .....	<b>97</b>

<b>A Supplemental material</b> .....	<b>101</b>
<b>B Experimental</b> .....	<b>111</b>
B.1 Apparatus .....	111
B.1.1 Solid-state NMR setup .....	111
B.1.2 Impedance spectroscopy setup .....	112
B.2 NMR pulse sequences .....	112
<b>C Publications</b> .....	<b>115</b>
C.1 Journal articles .....	115
C.2 Oral presentations .....	116
C.3 Poster presentations .....	116
<b>Bibliography</b> .....	<b>117</b>

# 1

## Introduction

In today's society, energy storage plays an indispensable role. The demand for improvements in the worldwide living standards of humankind is beyond dispute; the direct consequence of this irresistible trend is worldwide increasing energy consumption.[1] This desire created an intensive (over-)usage of fossil fuels causing an human-induced climate change. For the benefit of humankind, today's society is pursuing a more sustainable way by reducing air pollution, minimizing waste and reducing greenhouse gas emissions.[2] The exorbitant use of fossil resources has led to increased CO<sub>2</sub> production, which is responsible for global warming.[3] Renewable energy resources will play a crucial role in the world's future since renewable, green resources will have to step in to stop this irreversible impact of humankind on the environment. However, renewable energy sources, *e.g.* solar energy, wind energy, are non-continuous energy sources, since these sources are typically periodic or intermittent, they cannot supply the demand of energy at all times. Besides, most renewable energy sources (except biomass energy and hydro energy) can neither be transported nor stored without converting them to electricity. The storage of energy generated by renewable sources would allow the creation of a steady and reliable energy supply.[4]

Secondary Li-ion batteries are currently offering the highest energy density among the rechargeable battery technologies. Long-time application of Li-ion batteries will require a continual improvement of two major aspects – performance and safety. The volatile and flammable liquid electrolyte represents a serious safety issue in conventional batteries. Although the electrolyte aids the Li-ion transport in a battery, there is always a chance of leakage. In addition, the formation of dendrites of Li in a liquid electrolyte battery can lead to explosion. All-solid-state batteries can help to overcome the electrolyte safety issue, since the liquid electrolyte is replaced with a fast conducting solid.[5] The advantage of all-solid-state batteries besides increased safety is the potential reduction of volume and net weight of the battery itself as well as greater energy output. The introduction of alternative forms of transportation such as hybrid vehicles and plug-in electric cars have created a higher demand for

efficient energy storage systems. The key to the success of enhancing the performance of batteries are the materials.[6, 7] The development of new electrode and electrolyte materials is, besides the improvement of known materials, inevitable. Improving known materials can be as effective as the synthesis of completely new materials. Since the ionic transport in solids is strongly governed by structural disorder, defects and particle size, the introduction of such *via* high-energy ball milling can result in an enhancement of the Li diffusivity.[8–11]

A key criteria in the field of materials research is the understanding of the origins of fast ion transport, hence the detailed characterization of ion dynamics in the material is crucial.[12, 13] An appropriate tool to study ion dynamics is solid-state nuclear magnetic resonance (NMR) spectroscopy, allowing the characterization of diffusion parameters on a quite large time and length scale. A great variety of techniques can be employed to cover short- and long-range jumps from sub-Hz to GHz. Spin-lattice relaxation (SLR) measurements as a function of temperature can be employed to record so-called relaxation rates  $R$ . The rate peak maximum can provide information on Li diffusion parameters such as the activation energy  $E_a$ , the Li jump rate  $\tau$  and the self-diffusion coefficient  $D$ . The influence of correlation effects and dimensionality of the diffusion process can be accessed by frequency-dependent spin-lattice NMR measurements. Furthermore, spin-alignment echo (SAE) NMR measurements can directly access the jump rate of a single spin.

This work focuses on the characterization of diffusion processes in solids by using a large portfolio of various NMR techniques. Impedance spectroscopy (IS) is used as a complementary technique to determine the conductivity of a material by applying a frequency dependent electric field.

This thesis will start with a short introduction into the fundamentals of diffusion (section 2). It is followed by a section providing information on the principles of the two major methods used, namely solid-state NMR (section 2.4) and impedance spectroscopy (section 2.5). In Chapter 3, results are presented in a cumulative form of published (and peer-reviewed) articles. The thesis will conclude with a short summary and an outlook regarding future work (section 4). In the appendices supplemental material (A) of the papers and experimental information on setup (B) and pulse sequences (B.2) will be found.

# 2

## Principles of diffusion in solids

### 2.1 Fundamentals of diffusion

"*diffundere*" – a Latin word with the meaning "to spread out". Diffusion is the movement of matter against a concentration gradient driven by their thermal motion. Diffusion can be found in liquids, gases and solids.[14] The motion of particles in the liquid or gas phase is a completely random process and particles are usually moving from an area of high concentration to an area of lower concentration until they reach a thermodynamic equilibrium. The relationship between the flux of particles and the concentration can be described by *Fick's laws*. *Fick's first law* describes the particle flux (diffusion of particles) along an arbitrary direction  $x$  in an isotropic medium.

$$j_x = -D \frac{\partial c}{\partial x} \quad (2.1)$$

The variable  $j_x$  is the particle flux and  $\partial c / \partial x$  the concentration gradient across the  $x$ -direction;  $D$  denotes the *diffusion coefficient* or *diffusivity*. The diffusion flux is inversely proportional to the concentration gradient as indicated by the minus sign. As the diffusion process is not limited to a single dimension, equation 2.1 can be generalized to three dimensions by a shift to vector quantities according to

$$j = -D \nabla c. \quad (2.2)$$

Here, the vector of the particle flux in all three dimensions ( $x$ ,  $y$  and  $z$ ) is represented by  $j$  in the direction of the concentration gradient vector  $\nabla C$ . The symbol *nabla*  $\nabla$  stands for the vector differential operator in all three dimensions  $\nabla \equiv (\partial / \partial x, \partial / \partial y, \partial / \partial z)$ . Here,  $D$  is dependent on the direction of the concentration gradient and is represented by a tensor  $\hat{D}$ . For polycrystalline solids, where no macroscopic crystalline orientation can be found, an average diffusion coefficient is used to describe diffusion  $D \equiv \langle D \rangle$ . Since the particle flux in solids is almost impossible to determine,

equation 2.2 is combined with the *equation of continuity*:

$$\frac{\partial c}{\partial t} = -\nabla j, \quad (2.3)$$

to give *Fick's second law* (also known as *diffusion equation*):

$$\frac{\partial c}{\partial t} = \nabla(D\nabla C). \quad (2.4)$$

Equation 2.4 is only valid under the assumption that the number of moving particles is constant. *Fick's second law of diffusion* from equation 2.4 is a partial differential equation with non-linear solution in case of  $D$  being dependent on the concentration. In case of concentration independent diffusion, equation 2.4 can be simplified to:

$$\frac{\partial c}{\partial t} = D\nabla^2 c \equiv D\Delta c, \quad (2.5)$$

where for given initial and boundary conditions,  $\Delta$  denotes to the Laplace operator  $\Delta \equiv \nabla^2 \equiv \partial^2/\partial x^2 + \partial^2/\partial y^2 + \partial^2/\partial z^2$ . This form of *Fick's second law* is also known as the *linear diffusion equation*. For further information, the reader is referred to the works of Murch and Mehrer.[15, 16] In many cases, the temperature dependence of the diffusion coefficient follows an Arrhenius law:

$$D = D_0 \exp\left(\frac{\Delta H}{-k_B T}\right), \quad (2.6)$$

where  $D_0$  denotes the pre-exponential factor,  $\Delta H$  the activation enthalpy,  $T$  the temperature and  $k_B$  the Boltzmann constant. In case of constant pressure, the activation enthalpy is given by

$$\Delta H = \Delta E + p\Delta V. \quad (2.7)$$

As we are dealing with diffusion in solids the volume term can be neglected and  $\Delta H$  complies the activation energy  $\Delta E$ <sup>1</sup>:

$$D = D_0 \exp\left(\frac{E_a}{-k_B T}\right). \quad (2.8)$$

## 2.2 Diffusion in solids

Matter exists in four different fundamental states – solid, liquid, gas and plasma. A solid is characterized by structural rigidity and possesses a well-defined shape and volume. In solids, particles (atoms, molecules or ions) are generally held together by intramolecular (ionic-, metallic- and covalent bonding) and/or intramolecular (van der Waals forces and hydrogen bonds) chemical bonds. There are two major categories of solids – crystalline solids and amorphous solids (see figure 2.1). The chemical properties of a solid strongly depend on the modification (crystalline, amorphous and nanocrystalline) of the particles present.

---

<sup>1</sup> $\Delta E$  is referred to as  $E_a$

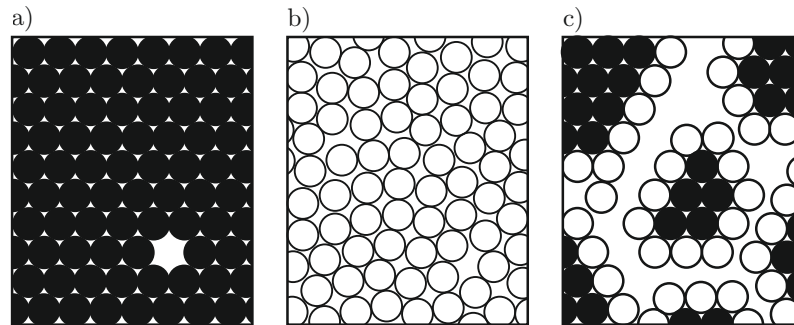


**Figure 2.1** – Simplified sketches of various modifications of solids. a) shows long-range order as seen in crystalline materials (here with an additional single vacancy), b) shows regions of short-range order as seen in amorphous solids (here with several defects) and c) shows regions of crystalline areas imbedded in an amorphous matrix as seen in nanocrystalline materials.

Crystalline solids are substances with a well-defined and distinct arrangement of particles also known as long-range order. The crystalline arrangement of particles can be described by Bravais-lattices.[17] Each atom or ion has a distinct position in the crystal lattice and can only move between these given positions. Crystals exhibit a defined and regular geometric pattern and feature long-range as well as short-range order (periodic repetition of arrangements over the entire crystal). A crystalline solid is an anisotropic material meaning that physical properties are dependent on the direction of the crystallites. A single crystal is a material with a perfect crystal lattice; no defects and grain boundaries often provide the single crystal with exceptional electric, mechanical and/or optical properties.

Nanocrystalline solids describe a subcategory of solids. A nanocrystalline material is by definition a polycrystalline material with a particle size of less than 100 nm in at least one dimension. Generally, nanocrystalline solids feature a large surface area due to a crystallite size of less than 20 nm. As seen in the illustration in figure 2.1c, a nanocrystalline solid can be composed of two different phases: (i) arbitrary arranged polycrystallites with a size of 5 - 50 nm and (ii) areas of grain boundaries or interfacial regions. Although nanocrystalline materials are usually synthesized starting from corresponding atomic or molecular building blocks, physical and chemical properties often vary significantly between the materials.

Amorphous solids or non-crystalline solids are substances without any long-range order in the positions of particles present. However, particles can arrange regularly in a small region creating a short-range order. In contrast to the crystalline counterpart, amorphous solids exhibit isotropic behavior meaning that their properties are identical in all directions. Usually amorphous materials and glasses are synthesized by rapid melt quenching. Crystalline materials are heated above their melting temperature to destroy their well-defined structure and are then rapidly cooled down to avoid recrystallization of the material. The term glass is used to describe amorphous solids if the process is occurring below the glass transition temperature  $T_g$ . [18] An ideal glass would be the exact opposite of an ideal crystal, there would be no structural order present in all respects.

### 2.2.1 Defects in crystal structures

The perfect lattice structure of crystals is a theoretical conception, since nature chooses imperfect lattices. In fact, imperfections (defects) are essential to the transport of atoms in a material, since

without defects migration of atoms can not be observed. Therefore, no diffusion would be found in an ideal crystal without any atomic imperfections. Even crystals of high purity under stable conditions contain point defects in their thermal equilibrium. Diffusion transport mechanisms require a vacant site or a displacement of atoms from their standard lattice sites into interstitial positions or onto different lattice site – defects play a key role in ion diffusion processes. These vacancies or defects in crystalline solids can be derived from construction faults of the real lattice. Traditionally, lattice defects are classified according to their dimensionality:

### Zero-dimensional defects

We are speaking of zero-dimensional effects or *point defects* when an isolated site of the crystal lattice is affected. Point defects can be further subdivided into *intrinsic* and *extrinsic* defects. Intrinsic defects occur in pure materials whereas extrinsic defects are caused by impurity atoms.

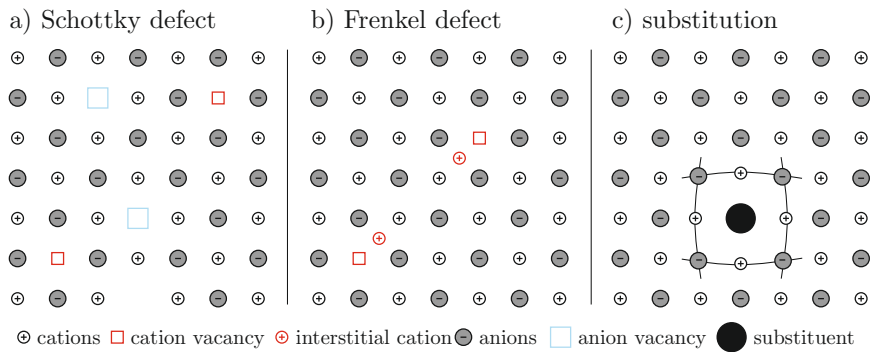


**Figure 2.2** – Sketches of various point defects in solids.

A *Schottky defect* is a neutral defect involving a vacancy on both the cation and the anion sublattice. The pair displacement of atoms from their regular lattice position creating a vacancy in the standard lattice onto an interstitial position creating an interstitial is called *Frenkel defect*. Since the vacancy is compensated by the interstitial, the Frenkel defect is a neutral defect. In materials with weak ionized atoms, it is energetically possible for cations and anions to switch sites, so if a cation substitutes an anion and/or *vice versa*, we are speaking of so-called *anti-site* defects. Extrinsic point defects involve foreign atoms; these can be added intentionally or exist as impurities if they are not. In general, small atoms are found in interstitial sites whereas larger atoms occupy lattice sites. The intentional insertion of foreign atoms is called *doping* and can be homo- or heterovalent depending on the atom used. Heterovalent doping will result in an excess charge, which will be compensated by the creation of additional vacancies of the opposite valency or interstitials to preserve charge neutrality. Homovalent doping usually occurs on a lattice site and results in a distortion in the crystal lattice. Depending on the size of the dopant, the incorporation of the dopant leads to an expansion or contraction of the crystal lattice. These point defects are especially important for conducting materials since they can affect the properties of the material and, as a direct consequence, properly introduced defects can be used to control electrical properties.

### One-dimensional defects

One-dimensional defects are *dislocations* and *line defects* resulting from the mislocation of the lattice planes in a crystal. Two different cases of dislocations can be distinguished: *edge dislocations* and *screw dislocations*; these defects often occur together as *mixed dislocations*. [19] A schematic drawing of these one-dimensional defects can be found in figure 2.3. Dislocations move easily on their glide planes and their motion produce plastic deformation of the crystal lattice.

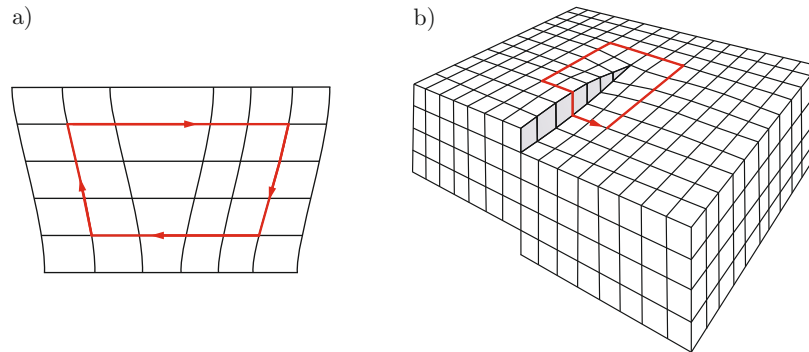


**Figure 2.3** – Illustration of one-dimensional defects in crystals. a) sketch of an edge dislocation and b) sketch of a screw dislocation.

### Two-dimensional defects

Two-dimensional defects are *planar defects* and include *stacking faults* and *grain boundaries*. These defects have two important features. First, due to the fact that they are surfaces in the crystal they show a particular atomic structure that is dependent on the orientation. Second, all these defects have a positive energy. Grain boundaries are interfaces that separate crystallites (*grains*). Such separation can occur between crystallites in the same phase if differently orientated or between crystallites of separate phases. A stacking fault is an error in the ordering of crystallographic planes (sequences). [16, 19–22]

### Three-dimensional defects

Three-dimensional defects alter the crystal pattern over a finite volume, hence they are called *bulk* (or *volume*) *defects*. This class of defects include *precipitates*, *voids* or *inclusions* of second-phase particles. Precipitates are small clusters of impurities, usually of a different phase, within a crystal structure. Voids are empty areas created by a large number of vacancies. [23]

## 2.2.2 Mechanisms of diffusion

As above-mentioned, defects are essential to the migration of atoms in a material. The migration of atoms in solids can be described by various diffusion mechanisms. A brief overview on the most common diffusion mechanisms is illustrated in figure 2.4. For more detailed information see, *e.g.*, Refs. [16] and [24].

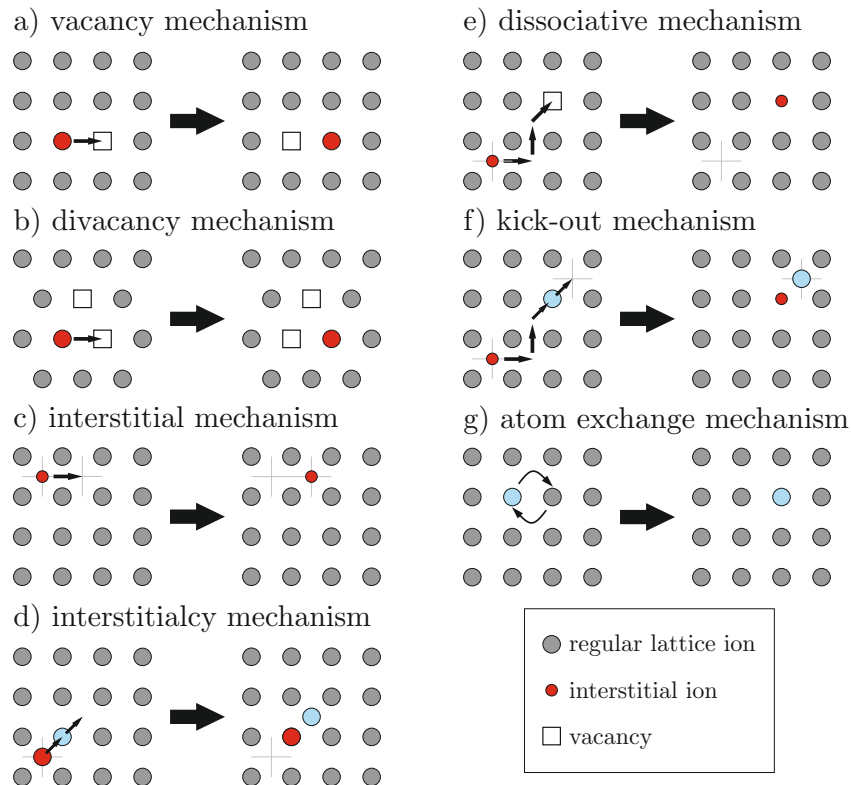


**Figure 2.4** – Schematic representation of various diffusion mechanisms in solids. [15, 16, 25]

### Vacancy mechanism

The *vacancy mechanism* is considered to be the most important diffusion mechanism in solids (illustrated in figure 2.4a). Atoms are simply exchanging positions with adjacent vacancies. In general, the diffusivity is determined by the availability and the mobility of the vacancies. The mechanism plays a crucial role in metals and alloys, since it is the preferred mechanism for both host and solute atoms.

### Divacancy mechanism

The *divacancy mechanism* is quite similar to the vacancy mechanism. In case of an existing binding energy with the tendency to create agglomerates of vacancies (divacancies, trivacancies *etc.*), diffusion can occur *via* these agglomerates of vacancies. An illustration of a divacancy mechanism can be found in figure 2.4b. The formation of agglomerates is favored at higher temperatures and often show increased diffusivities compared to monovacancies, *e.g.*, in fcc metals. The self-diffusion in fcc metals is caused by monovacancy- as well as by the divacancy mechanism.

### Interstitial mechanism

The (*direct*) *interstitial mechanism* does not require any defects in the crystal lattice. The interstitial atom can jump from one interstitial site to another without directly involving other atoms of the

lattice as shown in figure 2.4c. The mechanism is direct - the interstitial atom can migrate without slowdown. Therefore, the diffusion coefficient is usually higher compared to other mechanisms.

### Interstitialcy mechanism

In case of nearly equally sized interstitial- and lattice atoms, diffusion can occur by (*indirect*) *interstitialcy mechanism*. The mechanism is illustrated in figure 2.4d - two atoms, an interstitial atom and a lattice atom, move together simultaneously as a collective. The interstitial atom jumps to a regular lattice site, whereas the lattice atom moves to an interstitial position.

### Interstitial-substitutional mechanisms

Solute atoms can be dissolved on both interstitial and substitutional sites respectively. Diffusion can occur either by the way of a *dissociative mechanism* and/or by the *kick-out mechanism*. In both, instances an interstitial solute first diffuses *via* the interstitial mechanism. The initial interstitial mechanism in combination with a vacancy to form a substitutional solute is known as the *dissociative mechanism*. In the *kick-out mechanism*, the interstitial solute interacts with a regular lattice atom *via* the interstitialcy mechanism.

## 2.3 Determination of diffusion parameter

There are various methods available for the determination of diffusion parameters. These methods can be grouped into two major method categories, *microscopic* and *macroscopic methods*. Besides these two classes, we can subdivide methods further into *nuclear* and *non-nuclear methods*. Nuclear methods incorporate the usage of stable (NMR spectroscopy) or radioactive ( $\beta$ -NMR) nuclei to measure diffusivity. Figure 2.5 illustrates an overview on some well-established methods including an estimation for the order of magnitude of diffusivity  $D^T$ . A complete description of all these methods would be beyond the scope of this thesis. Therefore, only the two most relevant methods for this thesis - NMR spectroscopy and impedance spectroscopy - will be discussed in more detail in the following sections 2.4 and 2.5 respectively.

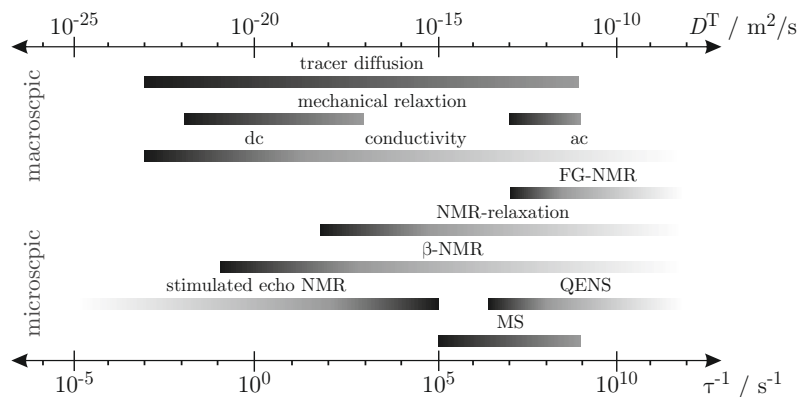


**Figure 2.5** – Overview on macro- and microscopic methods for the determination of diffusion parameters in solids (adapted from [26]). The scales indicate the order of magnitude of the diffusivity  $D^T$  and the correlation time  $\tau_c$  recorded with these methods.

All *macroscopic methods*, with the exception of field gradient (FG) NMR, are *direct methods* depending directly on Fick's laws. These direct methods involve the recording of concentration profiles and are sensitive to long-range diffusion. In contrast, *microscopic methods* or *indirect methods* are not based on Fick's laws. Indirect methods study phenomena influenced by diffusion processes and need a microscopic model of the atomic jump process in order to deduce diffusion coefficients. Indirect methods can be further subdivided into *relaxation methods* and *nuclear methods*. These diffusion coefficients are compulsory approximations to those measured by direct means. Nuclear methods study diffusion processes on a microscopic level. These include Mössbauer spectroscopy (MS), quasielastic neutron scattering (QENS) and nuclear magnetic relaxation (NMR), whereby the latter covers the widest range of diffusivities among nuclear methods (overview on various NMR experiments used in this work can be found in figure 2.6).

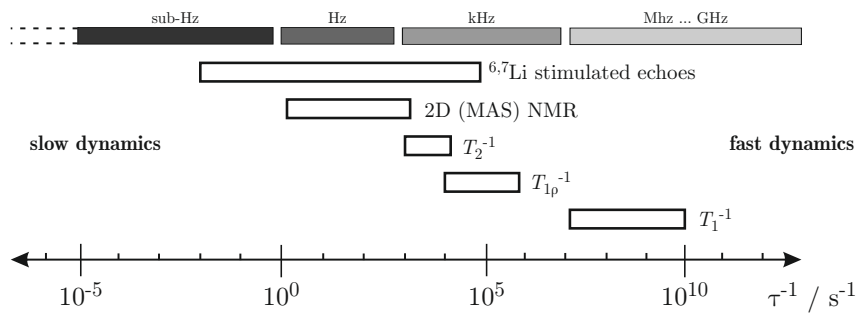


**Figure 2.6** – A more detailed overview on NMR techniques used in this work. The scales indicate the order of magnitude of the diffusivity  $D^T$  and the correlation time  $\tau_c$  recorded with these methods.

## 2.4 Solid-state nuclear magnetic resonance

The days when nuclear magnetic resonance (NMR) was a technique employable solely on solution-state samples have long since gone. Roots of NMR spectroscopy go back to mid 1940s when Purcell and Bloch experimentally demonstrated independently from each other that a magnetic nuclei can absorb radio frequency (RF) energy if placed in a magnetic field. Both, Purcell and Bloch were awarded the Nobel Prize in Physics in 1952 "for their development of new methods for nuclear magnetic precision measurements and discoveries in connection therewith".[27] In the last decades, solid-state NMR spectroscopy has become a truly useful method, employable to a very wide range of samples. Especially in the field of battery research, NMR spectroscopy plays a crucial role to access features of molecular structure and molecular dynamics. The following section will provide a short introduction to the theoretical basics of nuclear magnetic resonance and will explain some NMR techniques, such as *relaxometry* and *spin-echo alignment*, in more detail.[28–34]

### 2.4.1 Basics of NMR

#### Vector model of pulsed NMR

Nuclear magnetic resonance is the phenomenon observed from the interaction of a nucleus with a nuclear spin angular momentum  $\mathbf{I}^2$  (also known as *nuclear spin*) with a magnetic field. In case of

<sup>2</sup>bold letters outline a vector

$I \neq 0$ , nuclei possess a dipolar magnetic moment  $\boldsymbol{\mu}$ . In the semi-classical model of NMR only the net magnetization  $\boldsymbol{M}$  of a material and its behaviour in a magnetic field is considered, whereas the former is the vectorial sum of all the individual magnetic moments according to:

$$\boldsymbol{M} = \sum_i \boldsymbol{\mu}_i, \quad (2.9)$$

where  $\boldsymbol{\mu}_i$  is the magnetic moment associated with the  $i$ th nucleus. The magnetic moment  $\boldsymbol{\mu}$  is connected to the nuclear spin momentum  $\boldsymbol{I}$  by:

$$\boldsymbol{\mu} = \gamma \boldsymbol{I}. \quad (2.10)$$

where  $\gamma$  denotes the *magnetogyric ratio* (also known as *gyromagnetic ratio*), which is a nucleus-dependent constant. The spin angular momentum  $\boldsymbol{I}$  is defined by the *spin quantum number*  $I$  according to:

$$|\boldsymbol{I}| = \sqrt{I(I+1)}\hbar, \quad (2.11)$$

with  $I = 0, 1/2, 1, 3/2, \dots$  and  $\hbar$  denotes the Planck constant  $\hbar = \frac{h}{2\pi}$ . NMR measurements are possible for nuclei with a spin  $I$  of  $I \geq 1/2$ . The net magnetization can be written according to:

$$\boldsymbol{M} = \gamma \boldsymbol{J}, \quad (2.12)$$

where  $\boldsymbol{J}$  denotes the net nuclear spin angular momentum giving rise to the magnetization  $\boldsymbol{M}$ . When the nuclei are exposed to an external magnetic field  $\boldsymbol{B}_0$ , as it is the case in an NMR experiment, the magnet moment  $\boldsymbol{\mu}$  experiences by a torque  $\boldsymbol{T}$  resulting in a time-dependent precession of the spins:

$$\boldsymbol{T} = \frac{d\boldsymbol{J}}{dt}. \quad (2.13)$$

In analogy, the torque is given by

$$\boldsymbol{T} = \boldsymbol{M} \times \boldsymbol{B}. \quad (2.14)$$

By combining equations 2.10 and 2.13, the time-dependent motion of the magnetization vector  $\boldsymbol{M}$  in the field  $\boldsymbol{B}$  can be described

$$\frac{d\boldsymbol{M}}{dt} = \gamma \boldsymbol{M} \times \boldsymbol{B}. \quad (2.15)$$

The direction of magnetic field is usually taken along  $z$  by convention and is labelled  $\boldsymbol{B}_0$ , *i.e.*  $\boldsymbol{B} = (0, 0, B_0)$  in above equations. Equation 2.15 predicts that  $\boldsymbol{M}$  precesses about with a constant rate  $\omega = \gamma B$ . The frequency of the spin precession in  $\boldsymbol{B}_0$  is defined as  $\omega_0$ , the *Larmor frequency* (an illustration of the precession in static field is provided in figure 2.7 on page 13):

$$\omega_0 = -\gamma B_0. \quad (2.16)$$

### **Zeeman splitting**

The hamiltonian  $\hat{H}$  (also called *Zeeman hamiltonian*) is used to describe interaction of the magnetic moment  $\boldsymbol{\mu}$  with a static magnetic field  $\boldsymbol{B}_0$  and is given by

$$\hat{H} = -\hat{\boldsymbol{\mu}} \cdot \boldsymbol{B}_0, \quad (2.17)$$

where  $\hat{\mu}$  is the nuclear magnetic moment operator. This operator can be written in terms of the nuclear spin operator  $\hat{\mathbf{I}}$  as

$$\hat{\mu} = \gamma \hbar \hat{\mathbf{I}}. \quad (2.18)$$

Taking the applied field  $\mathbf{B}_0$  along  $z$ -direction, by combining 2.17 and 2.18, the Zeeman hamiltonian is

$$\hat{H} = -\gamma \hat{\mathbf{I}} \mathbf{e}_z \mathbf{B}_0 = -\gamma \hbar \hat{I}_z B_0, \quad (2.19)$$

with  $\mathbf{e}_z$  being the unit vector co-directional with the  $z$  axis. The eigenfunctions of  $\hat{H}$  are wavefunctions used to describe the possible states of a spin system in the magnetic field  $\mathbf{B}_0$ . As  $\hat{H}$  is proportional to the operator  $\hat{I}_z$ , the eigenfunctions of  $\hat{I}_z$  are the eigenfunctions of  $\hat{H}$ . Eigenfunctions can be written as  $|I, m\rangle$  in *bra-ket* notation or as  $\Psi_{I,m}$  with  $I$ , where  $I$  denotes the nuclear spin quantum number. As mentioned above, the spin quantum number  $I$  can take half or integer values (or zero), while the quantum number  $m$  can take  $2I + 1$  values,  $m = I, I - 1, I - 2, \dots, -I$ . The eigenvalues of  $\hat{H}$  are then the energy levels  $E_{I,m}$  the given spin system can take. The eigenvalues are obtained from operating with  $\hat{H}$  on the spin wavefunction:

$$\hat{H}|I, m\rangle = E_{I,m}|I, m\rangle, \quad (2.20)$$

with  $E_{I,m}$  corresponding to the energy of  $|I, m\rangle$ . Substituting equation 2.19 for  $\hat{H}$  give:

$$\hat{H}|I, m\rangle = -(\gamma \hbar B_0) \hat{I}_z |I, m\rangle = -(\gamma \hbar B_0) m |I, m\rangle, \quad (2.21)$$

The energies of the eigenstates can be calculated by comparing equations 2.20 and 2.21:

$$E_{I,m} = -\gamma \hbar m B_0. \quad (2.22)$$

The energy levels (also known as *Zeeman levels*) are equidistant to each other, hence the difference between the levels can be used to calculate the transition energy  $\Delta E$  of adjacent levels according to:

$$\hbar \omega_0 = \Delta E = -\gamma \hbar B_0 \quad \text{with} \quad (2.23)$$

$$\omega_0 = -\gamma B_0, \quad (2.24)$$

where  $\omega_0$  donates the resonance frequency. At equilibrium, assuming non-interacting spins, the distribution of the eigenstates  $\Psi$  follows a Boltzmann distribution. This phenomena is also known as *Zeeman splitting*. Nuclei with  $I \geq 1/2$  can exist in one of  $2I + 1$  eigenstates  $\Psi_{I,m}$  with a corresponding energy  $E_\Psi$ , the population  $p_\Psi$  of each eigenstate  $\Psi$  is given by

$$p_\Psi = \frac{\exp(-E_\Psi/kT)}{\sum_{\Psi'} \exp(-E_{\Psi'}/kT)}, \quad (2.25)$$

where  $E_\Psi$  is the corresponding energy of the eigenstate  $\Psi$ . For a spin- $1/2$  nucleus  $\sum_{m=\pm 1/2} \exp(-E_m/kT) \approx 2$ . In figure 2.7 the Zeeman splitting potential energy  $E_\Psi$  into  $2I + 1$  equidistant energy levels is illustrated for a  ${}^7\text{Li}$  nuclei with  $I = 3/2$ .

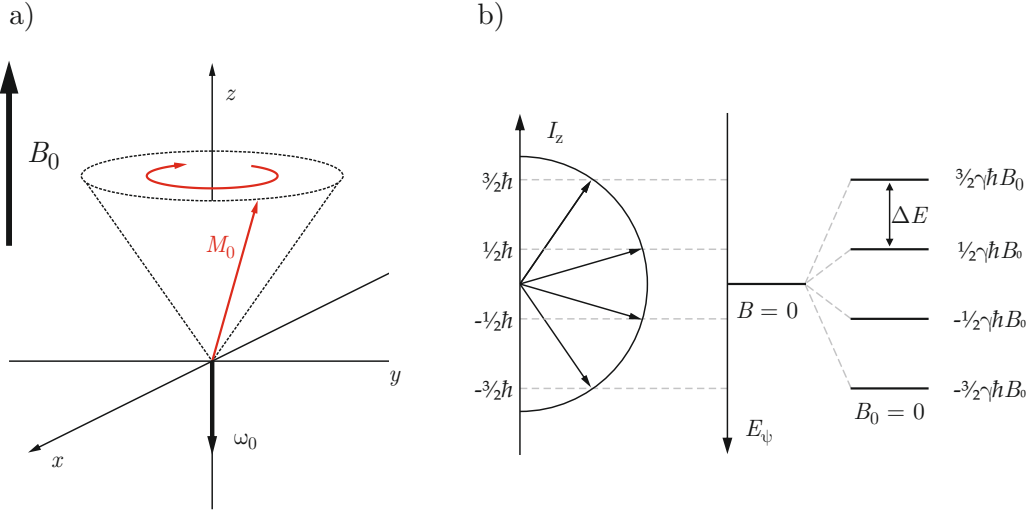


**Figure 2.7** – a) Precession of the magnetization vector  $\mathbf{M}_0$  in a static field  $\mathbf{B}_0$ . b) Zeeman splitting of the nuclear energy level produced from the interaction of the nuclear spins with a static field  $B_0$ . Here, the splitting of the potential energy  $E_\psi$  into  $2I + 1$  equidistant energy levels for a  ${}^7\text{Li}$  nuclei with a spin  $I = 3/2$  in an applied field  $\mathbf{B}_0$  with a positive  $\gamma$  is shown.

The transition of a spin system between energy levels is given by the condition  $\Delta m = \pm 1$  (a transition is only possible if the quantum number  $m$  is changed by 1). Hence, following this transition rule, the relative population of two eigenstates ( $p_m, p_{m-1}$ ) is temperature-dependent and follows a Boltzmann distribution according to:

$$\frac{p_{m-1}}{p_m} = \exp\left[\frac{-(E_{m-1} - E_m)}{k_B T}\right] = \exp\left[\frac{-\gamma\hbar B_0}{k_B T}\right]. \quad (2.26)$$

### The effect of radio-frequency pulses

As mentioned in the beginning of this section, NMR experiments measure the net magnetization  $\mathbf{M}$  of  $N$  nuclear spins in the field  $\mathbf{B}_0$ , which is given by the vectorial sum of all the individual magnetic moments according to:

$$\mathbf{M} = \sum_i^N \boldsymbol{\mu}_i. \quad (2.9)$$

At thermal equilibrium  $\mathbf{M} = \mathbf{M}_0$ , the magnetic moment precesses in the field  $\mathbf{B}_0$  along the  $z$ -axis so that  $M_z = M_0$  and  $M_x = M_y = 0$ . During an NMR experiment, an RF pulse will introduce an additional oscillating magnetic field,  $\mathbf{B}_1$ , with an angular frequency  $\omega_{\text{RF}}$  into the spin system. If the additional field is taken to oscillate along  $x$ , the total field felt by the nucleus is given by:

$$\mathbf{B}_{\text{total}} = \mathbf{B}_0 + \mathbf{B}_1 = \mathbf{e}_x 2B_1 \cos(\omega_{\text{RF}} t) + \mathbf{e}_z B_0, \quad (2.27)$$

where  $\mathbf{e}_x$  and  $\mathbf{e}_z$  are unit vectors along  $x$  and  $z$  respectively. The hamiltonian,  $\hat{H}$ , can be written in analogy to equation 2.17 and 2.19:

$$\hat{H} = -\hat{\boldsymbol{\mu}} \cdot \mathbf{B}_{\text{total}} = -\gamma(\hat{I}_z B_0 + \hat{I}_x B_1 \cos(\omega_{\text{RF}} t)). \quad (2.28)$$

The linear oscillating field can be described via a superposition of two counter rotating circular polarized fields with one rotating with  $\omega_{\text{RF}}$  about the  $z$ -axis and one rotating anti-clockwise with  $-\omega_{\text{RF}}$ . By using the resonance condition from equation 2.23 and  $\omega_1 = -\gamma B_1$ , the hamiltonian can be written as:

$$\hat{H} = \omega_0 \hat{I}_z + \omega_1 [(\hat{I}_x \cos(\omega_{\text{RF}} t) + \hat{I}_y \sin(\omega_{\text{RF}} t)) + (\hat{I}_x \cos(\omega_{\text{RF}} t) - \hat{I}_y \sin(\omega_{\text{RF}} t))]. \quad (2.29)$$

Since, only one of the components has any net-effect on the spin system, the second term addressing the rotation with  $-\omega_{\text{RF}}$  can be neglected. The hamiltonian can be rewritten by using the identity  $\hat{I}_x \cos(\omega_{\text{RF}} t) + \hat{I}_y \sin(\omega_{\text{RF}} t) = e^{-\frac{i}{\hbar} \omega_{\text{RF}} t \hat{I}_z} \hat{I}_x e^{\frac{i}{\hbar} \omega_{\text{RF}} t \hat{I}_z}$  (taken from textbook [34]) as:

$$\hat{H} = \omega_0 \hat{I}_z + \omega_1 e^{-\frac{i}{\hbar} \omega_{\text{RF}} t \hat{I}_z} \hat{I}_x e^{\frac{i}{\hbar} \omega_{\text{RF}} t \hat{I}_z} \quad (2.30)$$

In order to find the wave-functions  $\Psi$ , corresponding to  $\hat{H}$ , we have to solve the *time-dependent Schrödinger equation*:

$$i\hbar \frac{\sigma}{\sigma t} \Psi = \hat{H} \Psi, \quad (2.31)$$

with  $\Psi$  being the corresponding time-dependent wavefunction. By switching into the rotating frame of reference and introducing the rotation operator  $\hat{R}_z(\omega_{\text{RF}} t) = e^{-\frac{i}{\hbar} \omega_{\text{RF}} t \hat{I}_z}$ , we can remove the time-dependence of the hamiltonian (equation 2.28) and the hamiltonian and the wavefunction in the new frame can be written as:

$$\Psi' = \hat{R}_z^{-1}(\omega_{\text{RF}} t) \Psi = e^{i\omega_{\text{RF}} t \hat{I}_z} \Psi, \quad (2.32)$$

$$\hat{H}' = \hat{R}_z^{-1}(\omega_{\text{RF}} t) \hat{H} \hat{R}_z(\omega_{\text{RF}} t) - \omega_{\text{RF}} \hat{I}_z = (\omega_0 - \omega_{\text{RF}}) \hat{I}_z + \omega_1 \hat{I}_x, \quad (2.33)$$

where the hamiltonian and the wavefunctions in the new rotating frame of reference are marked by an apostrophe. In case of a resonant field with  $\omega_{\text{RF}} = \omega_0$ , the Schrödinger equation can be simplified according to:

$$i\hbar \frac{\sigma}{\sigma t} \Psi' = \hat{H}' \Psi' = \omega_1 \hat{I}_x \Psi'. \quad (2.34)$$

In the presence of  $B_1$  the population of the Zeeman levels oscillate with the frequency  $\omega_1/2\pi$  along the  $x$ -axis. Since the net magnetization depends on the population of the Zeeman levels, the magnetization can be rotated about the  $x$ -axis with an angle  $\theta$  by adjusting the pulse length  $t_p$ :

$$\theta = \omega_1 \tau_p \quad (2.35)$$

In case of a spin-1/2 system at equilibrium state, the populations  $p_{\pm 1/2}$  of two states can be manipulated by using an RF-pulse with the duration  $\omega_1 t_p = \pi/2$  resulting in two equally populated states according to  $p_{+1/2}(t_p) = p_{-1/2}(t_p)$ . Hence, the net magnetization along  $z$ -axis is zero; this manipulation is known as a  $\pi/2$ -pulse. In case of using an RF-pulse with the duration  $\omega_1 t_p = \pi/\omega_1$ , the initial magnetization will be inverted, this is then known as a  $\pi$ -pulse.

## Dipolar coupling

Each nuclear spin has a magnetic moment,  $\hat{\boldsymbol{\mu}} = \gamma \hat{\boldsymbol{I}}$ , and these can interact through space with each other - this interaction is known as *dipole-dipole coupling* or *direct dipolar coupling*. This type of

coupling is different from scalar (J) coupling, which is an *indirect dipolar coupling* mediated by local electrons.

The dipole-dipole interaction strongly depends on the internuclear distance  $1/r^3$  with  $r$  being the internuclear distance. The interaction energy between two point magnetic dipoles,  $\boldsymbol{\mu}_1$  and  $\boldsymbol{\mu}_2$ , is given by:

$$U = \left\{ \frac{\boldsymbol{\mu}_1 \cdot \boldsymbol{\mu}_2}{r^3} - 3 \frac{(\boldsymbol{\mu}_1 \cdot \mathbf{r})(\boldsymbol{\mu}_2 \cdot \mathbf{r})}{r^5} \right\} \frac{\mu_0}{4\pi}, \quad (2.36)$$

where  $\mathbf{r}$  denotes the vector between the point magnetic dipoles and  $\mu_0$  being the vacuum permeability. Quantum mechanically, the magnetic moment operator  $\hat{\boldsymbol{\mu}}$  can be written in terms of the nuclear spin operator  $\hat{\mathbf{I}}$  as  $\hat{\boldsymbol{\mu}} = \gamma \hbar \hat{\mathbf{I}}$ , according to equation 2.18. Hence, the hamiltonian for dipole-dipole coupling,  $\hat{H}_{dd}$ , between two nuclear spins,  $k$  and  $l$ , can be expressed as:

$$\hat{H}_{dd} = \frac{\mu_0}{4\pi} \frac{\gamma_k \gamma_l}{r_{kl}^3} (\hat{\mathbf{I}}_k \hat{\mathbf{I}}_l - 3[(\hat{\mathbf{I}}_k \mathbf{e}_{kl})(\hat{\mathbf{I}}_l \mathbf{e}_{kl})]), \quad (2.37)$$

where  $r_{kl}$  is the distance and  $\mathbf{e}_{kl}$  being the unit vector between the spins  $k$  and  $l$ . By expanding the scalar products of equation 2.37 and switching to spherical coordinates, the hamiltonian can be rewritten as:

$$\hat{H}_{dd} = \frac{\mu_0}{4\pi} \frac{\gamma_k \gamma_l}{r_{kl}^3} [A + B + C + D + E + F], \quad (2.38)$$

with the terms  $A$  to  $F$ :

$$\begin{aligned} A &= \hat{I}_k^z \hat{I}_l^z (1 - 3\cos^2\theta_{kl}), \\ B &= -\frac{1}{4}(\hat{I}_k^+ \hat{I}_l^- + \hat{I}_k^- \hat{I}_l^+) (1 - 3\cos^2\theta_{kl}), \\ C &= -\frac{3}{2}(\hat{I}_k^+ \hat{I}_l^z + \hat{I}_k^z \hat{I}_l^+) \sin\theta_{kl} \cos\theta_{kl} e^{-i\phi_{kl}}, \\ D &= -\frac{3}{2}(\hat{I}_k^- \hat{I}_l^z + \hat{I}_k^z \hat{I}_l^-) \sin\theta_{kl} \cos\theta_{kl} e^{-i\phi_{kl}}, \\ E &= \frac{3}{4} \hat{I}_k^+ \hat{I}_l^+ \sin^2\theta_{kl} e^{-i2\theta_{kl}}, \\ F &= -\frac{3}{4} \hat{I}_k^- \hat{I}_l^- \sin^2\theta_{kl} e^{-i2\theta_{kl}}. \end{aligned} \quad (2.39)$$

$\hat{I}_k^+$ ,  $\hat{I}_l^+$  and  $\hat{I}_k^-$ ,  $\hat{I}_l^-$  are the raising and lowering operators for the spin  $k$  and  $l$ . The terms  $C$  to  $F$  can be neglected from equation 2.38 and resulting secular part of the hamiltonian can be rewritten for homonuclear interaction according to:[30, 34]

$$\hat{H}_{dd,sec}^{homo} = -\frac{1}{2} \frac{\mu_0}{4\pi} \frac{\gamma_k^2}{r_{kl}^3} (\hat{\mathbf{I}}_k \hat{\mathbf{I}}_l - 3\hat{I}_k^z \hat{I}_l^z) (1 - 3\cos^2\theta_{kl}), \quad (2.40)$$

where the identities  $\gamma_k = \gamma_l = \gamma_I$  and  $\hat{I}_k^+ \hat{I}_l^- + \hat{I}_k^- \hat{I}_l^+ = 2(\hat{\mathbf{I}}_k \hat{\mathbf{I}}_l - \hat{I}_k^z \hat{I}_l^z)$  have been used. In case of heteronuclear interaction only the term  $A$  contributes and the hamiltonian can be written by using the identify  $\gamma_k \neq \gamma_l$  as:[30, 34]

$$\hat{H}_{dd}^{hetero} = \frac{\mu_0}{4\pi} \frac{\gamma_k \gamma_l}{r_{kl}^3} \hat{I}_k^z \hat{I}_l^z (1 - 3\cos^2\theta_{kl}). \quad (2.41)$$

The direct dipole-dipole coupling is a short-range interaction between ( $\hat{H}_{dd} \propto r^{-3}$ ) direct neighbors. In general, it is several orders of magnitude weaker compared to the Zeeman interaction and is responsible for the line-broadening of the resonance line as well as relaxation processes.

### Quadrupolar coupling

All NMR active nuclei with a spin  $I \geq 1$  are termed *quadrupolar*. Such nuclei possess a nuclear quadrupole moment  $eQ$ , that is able to interact with an electric field gradient EFG present at the nuclear site. An EFG arises from the local electronic structure of nuclei with a non-cubic symmetry. The quadrupole hamiltonian to describe the interaction between a nuclear electric quadrupole and an EFG  $\mathbf{V}$  can be written as:

$$\hat{H}_Q = \frac{eQ}{2I(2I-1)\hbar} \hat{\mathbf{I}} \cdot \mathbf{V} \cdot \hat{\mathbf{I}}, \quad (2.42)$$

with  $\mathbf{V}$  being the EFG tensor at the nuclear site,  $Q$  being the electric quadrupole moment,  $e$  being the proton charge and  $\hat{\mathbf{I}}$  is the nuclear spin vector. In its principal axis frame (PAF),  $\mathbf{V}$  can be described by using a  $3 \times 3$  by its the diagonal entries  $V_{XX}, V_{YY}$  and  $V_{ZZ}$  as principal values. Since the EFG tensor is traceless, *i.e.*  $V_{XX} + V_{YY} + V_{ZZ} = 0$ ,  $\mathbf{V}$  can be described by using two parameters, namely  $eq$ , the anisotropy of the EFG tensor, and  $\eta_Q$ , the (*quadrupolar*) *asymmetry parameter*.

$$eq = V_{ZZ} \quad \text{and} \quad \eta_Q = \frac{V_{XX} - V_{YY}}{V_{ZZ}}, \quad (2.43)$$

where  $e$  is the proton charge. In turn, the quadrupole coupling constant  $C_Q$  can be used as a parameter instead of  $eq$ :

$$C_Q = \frac{V_{ZZ}eQ}{\hbar} = \frac{e^2qQ}{\hbar}, \quad (2.44)$$

with  $\hbar$  being the reduced Planck constant and  $C_Q$  being given in angular frequency units. By expanding the tensor product of equation 2.42, the hamiltonian can be expressed in the PAF frame by using equation 2.43 and 2.44 as:

$$\hat{H}_Q = \frac{C_Q}{4I(2I-1)} [3\hat{I}_Z^2 - \hat{\mathbf{I}}^2 + \eta_Q(\hat{I}_X^2 - \hat{I}_Y^2)]. \quad (2.45)$$

In general, the Zeeman interaction dominates over the quadrupolar interaction, *i.e.*  $\|\hat{H}_z\| \gg \|\hat{H}_Q\|$ . Hence, only the secular part of the Hamilton operator is important for the determination of the quadrupole coupling. In order to use  $\hat{H}_Q$ , the quadrupolar hamiltonian has to be expressed in the laboratory frame by rotating the principle axis frame ( $X, Y$  and  $Z$ ) into the frame of the Zeeman hamiltonian ( $x, y, z$ ). Polar coordinates ( $\theta$  and  $\phi$ ) are used to describe to orientation of the PAF with respect to the external magnetic field  $B_0$ .

$$\hat{H}_Q^{sec} = \frac{C_Q}{8\hbar I(2I-1)} (3\hat{I}_z^2 - \hat{\mathbf{I}}^2) (3\cos^2\theta - 1 + \eta_Q \sin^2\theta \cos 2\phi). \quad (2.46)$$

The energy of the Zeeman level shift for a given  $I$  can be expressed by using the time-dependent Schrödinger equation  $\hat{H}_Q^{sec}|I, M\rangle = E_Q^m|I, m\rangle$  as:

$$E_Q^m = \frac{\hbar C_Q}{8I(2I-1)} (3m^2 - I(I+1)) f(\theta, \phi). \quad (2.47)$$

The orientation of the EFG is abbreviated by:

$$f(\theta, \phi) = 3\cos^2\theta - 1 + \eta_Q \sin^2\theta \cos 2\phi. \quad (2.48)$$

For nuclei with  $I = 3/2$  the Zeeman levels are shifted as follows:

$$E_Q^{\pm 3/2} = \frac{\hbar C_Q f(\theta, \phi)}{8} \quad \text{and} \quad E_Q^{\pm 1/2} = -\frac{\hbar C_Q f(\theta, \phi)}{8}. \quad (2.49)$$

In this case, the transition  $m = +1/2 \rightarrow -1/2$ , being the *central transition*, is unaffected by quadrupolar anisotropy, whereas the transitions from  $m = +3/2 \rightarrow +1/2$  and  $m = -1/2 \rightarrow -3/2$ , being the *satellite transition*, are raised or lowered by the quadrupole frequency  $\omega_Q$ . As a result of the quadrupole coupling, the satellite transitions are removed from the Larmor frequency by  $(2m - 1)\omega_Q$  with  $m$  being the initial Zeeman level of the transition, and  $\omega_Q$  - the quadrupole splitting can be described as:

$$\omega_Q = \frac{3e^2qQ}{4I(2I-1)} \frac{1}{2} [(3\cos^2\theta - 1) + \eta_Q \sin^2\theta \cos 2\phi]. \quad (2.50)$$

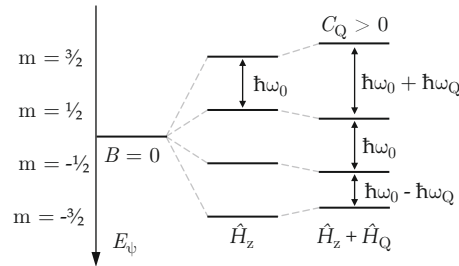


**Figure 2.8** – Schematic illustration of the Zeeman level splitting with and without quadrupole interaction for a spin- $3/2$  nucleus with  $C_Q > 0$ .

As for non-integer spin nuclei, the NMR spectra will show one central line with  $2I - 1$  additional satellite resonances. In a solid powder sample, a distribution of the EFG can be observed, since the crystallites are randomly orientated. This is the reason for occurrence of a so-called powder pattern, *e.g.* in figure 2.9b) for an uniaxial EFG tensor ( $\eta_Q \neq 0$ ). The satellite lines can be used to directly read off the value of the quadrupole coupling constant  $C_Q$ , since it is given by the distance between the outer shoulders. A single crystal will only give two satellite lines at the position  $\omega_0 \pm \omega_Q$ , *e.g.* in figure 2.9a) for a non-zero quadrupole frequency.

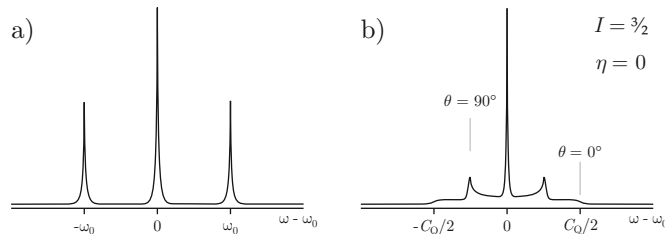


**Figure 2.9** – Schematic illustration of the NMR spectra of spin- $3/2$  nuclei for a) a single crystalline sample with a non-zero quadrupole frequency, *i.e.*  $f(\theta, \phi) \neq 0$ , and b) a powder sample with an uniaxial EFG tensor, *i.e.*  $\eta_Q = 0$ . Dipolar coupling is taken into account in both spectra.

### 2.4.2 NMR relaxation and diffusion

In an external magnetic field  $\mathbf{B}_0$ , a given spin system is in its thermal equilibrium with its surroundings, also known as the *lattice*, and the population of the Zeeman levels is given by the Boltzmann distribution. This population can be disturbed by applying a resonant RF pulse. After the perturbation of the spin system, interactions with the temporal fluctuations of the local field will have the system to return to thermal equilibrium. This process is known as *nuclear spin* (or NMR) *relaxation*. There are two different types of relaxation processes known, the first one is the *spin-lattice relaxation* (SLR) or *longitudinal relaxation*, which occurs with the characteristic time constant  $T_1$ . This relaxation type occurs along the direction of the applied field. The second process occurs perpendicular to the applied field and is concerned with the decay of single-quantum coherences. The relaxation process is called *spin-spin relaxation* (SSR) or *transverse relaxation* and occurs with the time constant  $T_2$ .

In general, field-fluctuations are induced by spin-carrying nuclei themselves in a static lattice, *i.e.*, as in this thesis, by moving  $\text{Li}^+$  ions. Hence, investigating NMR relaxation processes can help in gaining information on diffusion processes in solids.

#### Relaxation rates and spectral density functions

*Spectral density functions*  $J(\omega)$  are used to describe relaxation processes. An interaction Hamiltonian  $\hat{H}_1$  can be used to describe the interactions with fluctuating magnetic fields, and in case of spins  $I \geq 1$ , with the electric field gradient. This interactions can be referred to *direct dipole-dipole coupling* and *electric quadrupole coupling* respectively. Hence, by using the matrix elements of  $\hat{H}_1$ , the average ensemble of the transitions between the spin states  $|k\rangle$  and  $|l\rangle$  can be described by using a correlation function  $G(\tau)$ .

$$G_{kl}(\tau) = \overline{\langle k | \hat{H}_1(t - \tau) | l \rangle \langle l | \hat{H}_1(t) | k \rangle}, \quad (2.51)$$

where the bar denotes this ensemble average. The correlation function  $G(\tau)$  describes the correlation between the field at a later time  $\tau$  with the field at the time  $\tau = 0$ . In general the smaller  $\tau$ , the more similar the values will be. The mean time period between transition inducing fluctuations is quantified by the *correlation time*  $\tau_c$ . The correlation time is equal to the mean residence time  $\tau$  of a nuclei on its lattice site between two successful jumps. The spectral density function  $J_{kl}(\omega)$  of the fluctuating field is given by the Fourier transform of  $G_{kl}(\tau)$  according to:

$$J_{kl}(\omega) = \int_{-\infty}^{\infty} G_{kl}(\tau) \exp(-i\omega\tau) d\tau. \quad (2.52)$$

The spectral density is linked to the spin-lattice relaxation rate  $R_1$  *via* the proportionality  $T_1^{-1} = R_1 \propto J(\omega_0)$ . A relaxation processes will be induced in case of  $\omega = \omega_0$ . [28, 35] Hence, the rates for homonuclear dipolar relaxation can be written as:

$$T_{1,dd}^{-1} \equiv R_{1,dd} = \frac{3}{2} \gamma^4 \hbar^2 I(I+1) [J_{dd}^{(1)}(\omega_0) + J_{dd}^{(2)}(2\omega_0)], \quad (2.53)$$

$$T_{2,dd}^{-1} \equiv R_{2,dd} = \frac{3}{8} \gamma^4 \hbar^2 I(I+1) [J_{dd}^{(0)}(0) + 10J_{dd}^{(1)}(\omega_0) + J_{dd}^{(2)}(2\omega_0)], \quad (2.54)$$

where  $I$  denotes the spin of relaxing nuclei,  $\gamma$  their gyromagnetic ration and  $\hbar$  is the reduced Planck constant.  $J_{dd}^{(q)}$  are the spectral densities describing the spin transitions with  $\Delta m = \pm q$ , where  $q = 0, 1, 2$  denotes the changing of the angular momentum.[36] In analogy, the relaxation rates for quadrupolar interaction can be written as:[28, 35]

$$T_{1,Q}^{-1} \equiv R_{1,Q} = \frac{9}{160} \left( \frac{eQ}{\hbar I} \right)^2 \frac{2I+3}{2I-1} [J_Q^{(1)}(\omega_0) + J_Q^{(2)}(2\omega_0)], \quad (2.55)$$

$$T_{2,Q}^{-1} \equiv R_{2,Q} = \frac{9}{128} \left( \frac{eQ}{\hbar} \right)^2 [J_Q^{(0)}(0) + 10J_Q^{(1)}(\omega_0) + J_Q^{(2)}(2\omega_0)], \quad (2.56)$$

with  $eQ$  being the electric quadrupole moment of the nuclei. Relaxation rates gained from  $T_2$  measurements are only appropriate in case of sufficiently narrowed NMR lines; in the so-called *motional-narrowing regime*, where  $J^{(0)}(0)\tau_c \ll 1$  holds. Here, the jump rates are in the order of the inverse SSR rates. In case of  $J^{(0)}(0)\tau_c \gg 1$ , in the so-called *rigid-lattice regime*, a constant SSR rate  $R_2$  is obtained:

$$R_2 = R_{20} \equiv \sqrt{\langle \Delta\omega^2 \rangle}, \quad (2.57)$$

where  $\langle \Delta\omega^2 \rangle$  denotes the second moment.[28, 30, 37–39] The relaxation rates (equations 2.53 to 2.56) are describing NMR relaxation rates in the laboratory frame of reference.

The spin-lattice relaxation SLR in the rotating frame of reference is a NMR technique for measuring very slow ionic motion.[40, 41] As for a spin-locking NMR experiment, a weak locking field  $B_1$  ( $\sim 10^{-4}$  T) formally replaces the static external field  $B_0$ . The equilibrium magnetization  $M_{\rho,eq}$  is rotated into the  $x$ - $y$  plane where the magnetization is "locked" by the locking pulse for the duration  $t$ . The relaxation rate (SLR $\rho$ ) in the rotating frame of reference can be obtained in a relatively simple way by using a method introduced by Kelly and Sholl.[35] The spin-lattice relaxation rates for dipolar and quadrupolar interactions take the form:

$$T_{1\rho,dd}^{-1} \equiv R_{1\rho,dd} = \frac{3}{8} \gamma^4 \hbar^2 I(I+1) [J_{dd}^{(0)}(2\omega_1) + 10J_{dd}^{(1)}(\omega_0) + J_{dd}^{(2)}(2\omega_0)], \quad (2.58)$$

$$T_{1\rho,Q}^{-1} \equiv R_{1\rho,Q} = \frac{9}{640} \left( \frac{eQ}{\hbar I} \right)^2 \frac{2I+3}{2I-1} [J_Q^{(0)}(2\omega_1) + 10J_Q^{(1)}(\omega_0) + J_Q^{(2)}(2\omega_0)]. \quad (2.59)$$

with  $\omega_1 = \gamma B_1$  as the locking frequency.

### BPP-Model for 3D diffusion

In order to describe spectral density functions and relaxation rates, a suitable model has to be used to determine the time-dependency of the correlation functions  $G(\tau)$ . A well-established model for three-dimensional diffusion is the BPP model proposed by Bloembergen, Purcell and Pound.[39] The model describes the isotropic, three-dimensional motion of nuclei by a single exponential decay of the autocorrelation function  $G(\tau)$ :

$$G^{(q)}(\tau) = G^{(q)}(0) \exp\left(\frac{-|\tau|}{\tau_c}\right), \quad (2.60)$$

where  $\tau_c$  denotes the correlation time. After Fourier transformation of equation 2.60, the resulting Lorentzian-shaped spectral density function is given as:

$$J^{(q)}(\omega) = G^{(q)}(0) \frac{2\tau_c}{1 + \omega^2\tau_c^2}. \quad (2.61)$$

For short correlation times and for an isotropic distribution of the spins, the ratio of the correlation functions is:

$$G^{(0)}(0) : G^{(1)}(0) : G^{(2)}(0) = 6 : 1 : 4. \quad (2.62)$$

Hence, the relaxation rates in the laboratory and in the rotating frame of reference can be expressed as:

$$R_1 = C'_1 \left[ J^{(1)}(\omega_0) + 4J_Q^{(1)}(2\omega_0) \right], \quad (2.63)$$

$$R_2 = C'_2 \left[ 6J^{(1)}(0) + 10J^{(1)}(\omega_0) + 4J^{(1)}(2\omega_0) \right], \quad (2.64)$$

$$R_{1\rho} = C'_{1\rho} \left[ 6J^{(1)}(2\omega_1) + 10J^{(1)}(\omega_0) + 4J^{(1)}(2\omega_0) \right]. \quad (2.65)$$

By combining equation 2.61 with equations 2.63 to 2.65 and by simplifying the prefactors  $C'_n$  to  $C_n$  with  $n = 1, 2, \rho$  via the relation  $C_n = 2G^{(1)}(0)C'_n$ , the rates can be rewritten according to:

$$R_1 = C_1 \left[ \frac{\tau_c}{1 + (\omega_0\tau_c)^2} + \frac{4\tau_c}{1 + (2\omega_0\tau_c)^2} \right], \quad (2.66)$$

$$R_2 = C_2 \left[ 6\tau_c + \frac{10\tau_c}{1 + (\omega_0\tau_c)^2} + \frac{4\tau_c}{1 + (2\omega_0\tau_c)^2} \right], \quad (2.67)$$

$$R_{1\rho} = C_{1\rho} \left[ \frac{6\tau_c}{1 + (\omega_1\tau_c)^2} + \frac{10\tau_c}{1 + (2\omega_0\tau_c)^2} + \frac{4\tau_c}{1 + (2\omega_0\tau_c)^2} \right]. \quad (2.68)$$

The correlation time  $\tau_c$  is used to describe the temperature-dependence of the rates by an Arrhenius law according to:

$$\tau_c^{-1} = \tau_{c0}^{-1} \exp \left[ \frac{-E_a}{k_B T} \right], \quad (2.69)$$

with  $\tau_c^{-1}$  being in the same order of magnitude as the jump rate  $\tau^{-1} \approx \tau_c^{-1}$  governing the diffusion process.  $E_a$  is denoting the activation energy of the diffusion process,  $\tau_0^{-1}$  is denoting the pre-exponential factor,  $k_B$  is the Boltzmann constant and  $T$  the temperature. Equations 2.66 to 2.68 in combination with equation 2.57, can be used to fit experimental obtained  $R_1$ ,  $R_2$  and  $R_{1\rho}$  data with appropriate mathematical functions. Hence, the fitting functions can be used to gain information on diffusion parameters such as activation energy  $E_a$  and the attempt frequency  $\tau_0^{-1} \approx \tau_{c0}^{-1}$ . Figure 2.10a illustrates schematically the temperature dependence of the relaxation rates from dipole-dipole interactions for three different resonance frequencies. At a given Larmor frequency  $\omega_0$ , the rates increase with the temperature. By plotting the logarithm of the rate  $R_1$  against the inverse temperature,

the rate will pass through a peak maximum at  $T_{max}$  where the maximum condition  $\omega_0\tau_c = 1$ <sup>3</sup> approximately holds (schematically illustrated in figure 2.10b).

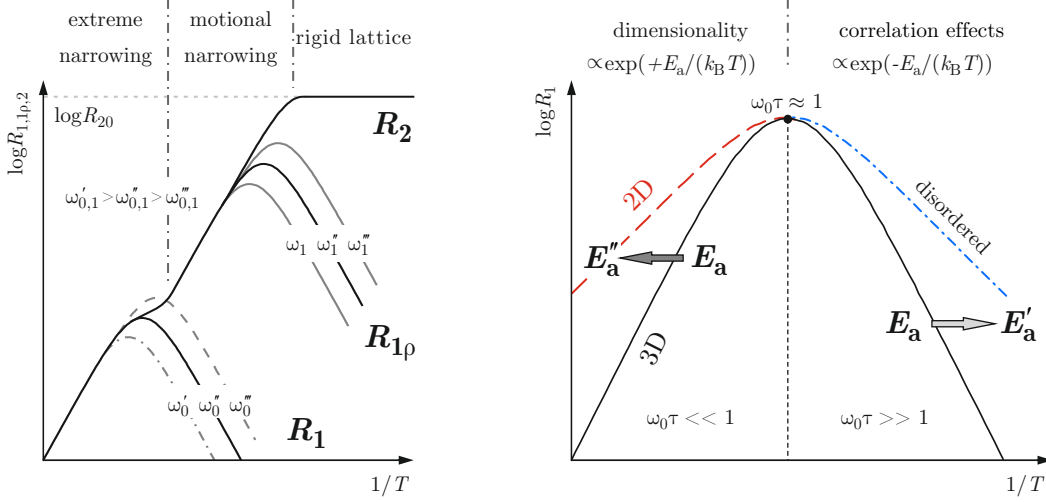


**Figure 2.10** – a) Schematic illustration of the temperature-dependency of the spin-lattice and spin-spin relaxation rates,  $R_1$ ,  $R_{1\rho}$  and  $R_2$ . In case of  $R_1$  and  $R_{1\rho}$ , the maximum of the relaxation peak is shifted towards lower temperatures with decreasing resonance frequency  $\omega$ . b) Schematic illustration of the relaxation rate  $R_1$  for different diffusion models. Three dimensional BPP-type behavior results in symmetrical high- and low-temperature flanks, whereas two-dimensional will give a deviation at the high-temperature flank and, in case of disordered systems, at the low-temperature flank.

The flank on each side of the maximum feature indicate a symmetrical peak due to the following proportionalities:

$$\begin{aligned} R_1 &\propto \tau_c && \text{for } \omega_0\tau_c \ll 1, \\ R_1 &\propto \tau_c^{-1}\omega_0^{-2} && \text{for } \omega_0\tau_c \gg 1. \end{aligned} \quad (2.70)$$

In the Arrhenius representation, the slope of the flank on either side ( $\pm E_a/k_B$ ) can be used to calculate the activation energy for the diffusion process. The first limit, where  $\omega_0\tau_c \gg 1$  holds, is known as the so-called *low-temperature LT limit* (or *low-frequency limit*) and the second limit, where  $\omega_0\tau_c \ll 1$  holds, is known as the so-called *high-temperature HT limit* (or *high-frequency limit*). The LT flank stands for short range (or local) diffusion, whereas the HT is representing the long range transport in a material. Analogous to the  $R_1$  rate in the laboratory frame of reference is the behavior of  $R_{1\rho}$  in the rotating frame of reference. Compared to  $R_1$ , the rate peak of  $R_{1\rho}$  is shifted towards lower temperatures and diffusion processes are probed on a longer time as well as length scale. The maximum condition is fulfilled at  $\omega_1\tau_c = 0.5$ <sup>4</sup> according to equation 2.68. The linear progression of  $R_2$  is only valid in the motional narrowing regime. According to equation 2.57, the rates are limited by the NMR line width at lower temperatures.

Since NMR measurements of real materials only in the rarest of cases show an ideal behavior of the rates, the measurement of SLR rates often results in asymmetrical line peaks, where the LT flanks

<sup>3</sup>If only the first term in the brackets of equation 2.66 is considered, the maximum condition is given by  $\omega_0\tau_c = 1$ . In case of taking the whole expression, the maximum condition is given by  $\omega_0\tau_c \approx 0.62$ .

<sup>4</sup>If only order-of-magnitude approximations are considered, the maximum condition can be still assumed as  $\omega_1\tau_c \approx 1$ .

possess different slopes compared to the HT flanks -  $E_a^{\text{LT}} \neq E_a^{\text{HT}}$ . Especially structurally disordered systems, *e.g.* glasses, exhibit this behavior. The ion dynamics present in the systems can no longer be assumed to be isotropic and random. This behavior is not only limited to structurally disordered systems since it can also be found in structurally ordered systems, where the asymmetry of the rate peak is associated with the correlated motion of mobile spins.[42, 43] Here, a modified BPP-model can be used to describe correlated jump diffusion:

$$J(\omega) = G(0) \frac{2\tau_c}{1 + (\omega\tau_c)^\beta}, \quad (2.71)$$

where  $1 < \beta < 2$  characterizes correlation effects; in the ideal case the correlation parameter  $\beta$  equals 2. In turn, the expression for  $R_1$  from equation 2.66 can be rewritten as:

$$R_1 = C_1 \left[ \frac{\tau_c}{1 + (\omega_0\tau_c)^\beta} + \frac{4\tau_c}{1 + (2\omega_0\tau_c)^\beta} \right]. \quad (2.72)$$

The slope of the HT flank ( $\omega_0\tau_c \ll 1$ ) remains unchanged for correlated diffusion, whereas the slope of LT flank ( $\omega_0\tau_c \gg 1$ ) is reduced.

$$\begin{aligned} R_1 &\propto \tau_c && \text{for } \omega_0\tau_c \ll 1, \\ R_1 &\propto \tau_c^{1-\beta} \omega_0^{-\beta} && \text{for } \omega_0\tau_c \gg 1. \end{aligned} \quad (2.73)$$

Here, the alteration of the slope will result in two different activation energies. From equation 2.73 and 2.69 the reduction of the activation energy is given by:

$$E_a^{\text{LT}} = (\beta - 1)E_a^{\text{HT}}. \quad (2.74)$$

As mentioned above, the LT limit is linked to diffusion processes on short time and length scales, whilst the HT limit is linked to long-range ion diffusion.[44]

### The model of Richards for 2D diffusion

Diffusion can also occur confined to two dimensions, *e.g.* for layered structured material such as covered in this work 2H-Li<sub>x</sub>NbS<sub>2</sub> (see section 3.1.2). Since this confinement is reflected in NMR measurements, information on the dimensionality of the diffusion process can be experimentally obtained by *frequency-dependent* SLR NMR measurements.

Since diffusivity of the spins is thermally activated and due to the fact that the LT limit describes short range motion of the ions (spins perform only few jumps), as a consequence, the structurally confined ionic motion in the LT regime has only little effect on the rates, or rather spectral densities. However, in the HT regime at temperatures  $T > T_{max}$ , where many successful jumps occur, the confined ionic motion will influence the HT flank of the rate peak. The temperature limits for uncorrelated 2D-diffusion can be described as following:[45]

$$\begin{aligned} J^{2D}(\omega, \tau_c) &\propto \tau_c \ln(1/\omega\tau_c) && \text{for } \omega\tau_c \ll 1, \\ J^{2D}(\omega, \tau_c) &\propto \tau_c^{-1} \omega^{-2} && \text{for } \omega\tau_c \gg 1. \end{aligned} \quad (2.75)$$

This results in the same expression in the high-frequency limit as that from the BPP model as stated above in equation 2.73. In other words, the same behavior of the relaxation rates is observed in this regime for both three-dimensional isotropic diffusion and two-dimensional structurally confined motion, respectively. The empirical spectral density function introduced by Richards combines both expressions from equation 2.75:[45]

$$J^{2D}(\omega, \tau_c) \propto \tau_c \ln \left( 1 + \frac{1}{(\omega \tau_c) 2} \right), \quad (2.76)$$

In turn, the two-dimensional spin-lattice relaxation rates in the laboratory frame of reference can be written as:

$$R_1^{2D} = C_1^{2D} \left[ \tau_c \ln \left( 1 + \frac{1}{(\omega_0 \tau_c)^\beta} \right) + 4 \tau_c \ln \left( 1 + \frac{1}{(2\omega_0 \tau_c)^\beta} \right) \right], \quad (2.77)$$

and for the rotating frame of reference:

$$R_{1\rho}^{2D} = C_{1\rho}^{2D} \left[ 6 \tau_c \ln \left( 1 + \frac{1}{(2\omega_1 \tau_c)^\beta} \right) + 10 \tau_c \ln \left( \frac{1}{(\omega_0 \tau_c)^2} \right) + 4 \tau_c \ln \left( \frac{1}{(2\omega_0 \tau_c)^2} \right) \right]. \quad (2.78)$$

For both, the exponent  $\beta \leq 2$  is employed for potential correlation effects.[46] Figure 2.11 shows a contrasting juxtaposition of the 3D BPP model (dashed grey lines) and the 2D model of Richards (solid black lines). In contrast to the coinciding rates in the LT regime, there is a distinct frequency dependence observable in the HT regime compared to the three-dimensional case, this dependence is characteristic for lower-dimensional diffusion processes. This dependence can be used to differentiate between two-dimensional and three-dimensional diffusion *via* frequency-dependent  $R_{1\rho}$  measurements at a constant temperature in the HT regime as a function of  $\omega_0$ .

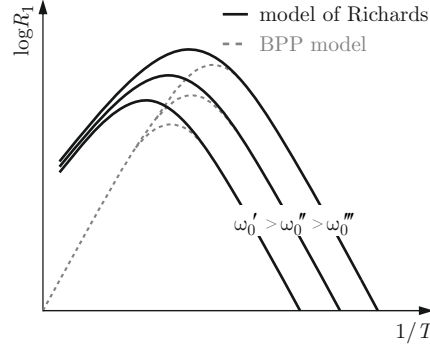


**Figure 2.11** – Schematic comparison between the SLR rates using different models for diffusion in solids. Solid lines are referred to rates derived from using the model of Richards for two-dimensional diffusion and dashed lines are referred to rates derived from using the BPP model for three-dimensional diffusion. Here, the rates for uncorrelated motion ( $\beta = 2$ ) are illustrated schematically for three different resonance frequencies  $\omega_0' > \omega_0'' > \omega_0'''$ . Proportionality constants were chosen such that  $C_1 = C_1^{2D}$ .

### Diffusion coefficient

The correlation rate (see equation 2.69) is linked to the jump rate  $\tau^{-1}$  of a diffusion progress, the maximum condition  $\omega_0 \tau \approx 1$ , in the laboratory frame of reference, can be used to assume the jump rate of a nucleus at the temperature of the rate peak maximum ( $T_{max}$ ) as  $\tau^{-1} \approx \omega_0$ . In turn, the

Einstein-Smoluchowski equation can be employed to calculate the diffusion coefficient for uncorrelated motion according to:[47–49]

$$D^{uc} = \frac{na^2}{2d\Delta t} = \frac{\langle a^2 \rangle}{2d\bar{\tau}}, \quad (2.79)$$

where  $a$  denotes the jump length (distance between the lattice sites),  $d$  is the dimensionality of the diffusion process and  $\bar{\tau} = \Delta t/n$  denotes the mean residence time of a nucleus on its lattice site with  $\bar{\tau}^{-1}$  being the mean jump rate. In order to calculate diffusion coefficients from NMR experiments in the rotating frame of reference, the maximum condition  $\omega_1\tau = 0.5$  has to be used.

### 2.4.3 Spin-alignment echo NMR

The most straight-forward method for the determination of diffusion parameters by NMR experiments is the recording of SLR rates. The spin-alignment echo (SAE) NMR is a special technique that allows us to probe the jump rates of diffusing particles in the order of the respective resonance frequency (in the order of  $10^8 \text{ s}^{-1}$  and  $10^4 \text{ s}^{-1}$  in the laboratory and rotating frame of reference respectively). This technique is a well-established method to investigate slow ion dynamics in solids.[9, 50–52] Here, the correlation of the quadrupole frequency at the beginning of the mixing time ( $t_m = 0$ ) with the frequency at the end of the mixing time  $t_m$  is measured. By increasing the interval time between these two points, the decay of the correlation function can be determined.[9, 53] SAE NMR experiments are performed by using the well-known Jeener-Broekaert pulse sequence:[54]

$$\beta_{1,\phi_1} - t_p - \beta_{2,\phi_2} - t_m - \beta_{3,\phi_3} - t - \text{echo}, \quad (2.80)$$

where  $\beta_i$  denotes the angle of the pulses ( $\beta_1 = 90^\circ$  and  $\beta_2 = \beta_3 = 45^\circ$ ) and  $\phi_i$  their phase. The time  $t_p$  is the preparation time and  $t_m$  is the mixing (or evolution) time. The Fourier transformation of the echo (occurring at  $t = t_p$ ) will result in the corresponding SAE spectra. Starting from an equilibrium longitudinal magnetization a quadrupolar alignment state can be generated by the first two pulses  $\beta_1$  and  $\beta_2$  by choosing their phases such as  $|\phi_1 - \phi_2| = \pi/2$ . This state is able to store the phase information  $\omega_Q(t_m = 0)t_p$  with  $\omega_Q$  being the quadrupolar angular frequency. During the mixing process with the defined duration  $t_m$ , the particles can diffuse on sites in the lattice driven by different EFG. The third pulse  $\beta_3$  is then used to tilt the state into an observable direction by multiplying it at the end of the mixing time  $t_m$  with a second phase information  $\omega_Q(t_m)t$ . After the time  $t$  the echo can be recorded (the echo is maximal at  $t = t_p$ ). The amplitude of the echo signal (using the above mentioned pulse angles) can be described by using a two-time correlation function according to:[38, 50, 55, 56]

$$S_2(t_p, t_m, t) = \frac{9}{20} \sin[\omega_Q(0)t_p] \sin[\omega_Q(t_m)t]. \quad (2.81)$$

Since powder samples are mathematically described by an ensemble average (here by  $\langle \dots \rangle$ ) the echo amplitude of the relaxation process can be written as:

$$S_2(t_p, t_m, t) = \frac{9}{20} \langle \sin[\omega_Q(0)t_p] \sin[\omega_Q(t_m)t] \rangle \exp\left(-\frac{2t_p}{T_2}\right) \exp\left(-\frac{t_m}{T_1}\right). \quad (2.82)$$

The echo damping *via* NMR relaxation can be described by using single (or stretched) exponential functions. The correlation time  $\tau_{\text{SAE}}$  of the echo damping is limited by  $T_2 \leq \tau_{\text{SAE}} \leq T_1$ . Since a SAE experiment consists of several parameters (pulses, phased, times), the right setup of these values

plays a crucial role to the generation of quadrupolar spin-alignment states; a right phase cycling is essential. The phase cycling used in the experiments in this work is given in appendix B.2. Here again, the corresponding diffusion coefficient can be determined from the correlation times by using the Einstein-Smoluchowski equation.

#### 2.4.4 Magic-angle spinning NMR

Magic-angle spinning (MAS) NMR is a special technique in the field of solid-state NMR. As solid-state implies, we are generally dealing with solid powder samples containing many random orientated crystallites. The orientation of the crystallites affects nuclear spin interactions, and further, the NMR spectra, chemical shielding, dipole-dipole coupling and quadrupole coupling. The dependence on the orientation is called *anisotropy*. The task of MAS NMR is the removal of chemical shift anisotropy and heteronuclear dipolar coupling effects. In addition, this technique can be used to narrow lines from quadrupolar nuclei, and if the spinning rates are high enough, it can be used to remove homonuclear decoupling effects. In liquid NMR spectra, these phenomena are rarely observed due to rapid isotropic tumbling of the molecules. The experimental setup of an MAS NMR experiment is illustrated in figure 2.12.

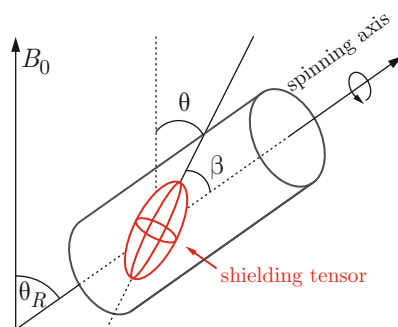


**Figure 2.12** – Illustration of the magic-angle spinning (MAS) experiment. The sample is spun rapidly (up to 40 kHz) in a *rotor* about an axis orientated at the magic angle  $\theta_R = 54.74^\circ$  with respect to the applied field  $B_0$ . Hence, effects of chemical shielding anisotropy and heteronuclear dipolar coupling are removed due to the magic-angle spinning. Here, the chemical shielding tensor of a randomly oriented molecule in the sample is illustrated by an ellipsoid. The angles  $\theta$  and  $\beta$  denote the angle between the principal  $z$ -axis of the shielding tensor and applied magnetic field  $B_0$  and the spinning axis, respectively. Figure adapted from reference [34].

The molecular orientation dependence is given by  $3\cos^2\theta - 1$ , where  $\theta$  denotes the orientation of the spin interaction tensor. As stated above, powder samples are anisotropic, the angle  $\theta$  can take on all possible values. If the sample is spun about an axis inclined to the applied field  $B_0$  at the angle  $\theta_R$ , the molecular orientation  $\theta$  varies with time. The averaged orientation dependence of  $3\cos^2\theta - 1$  is given as:

$$\langle 3\cos^2\theta - 1 \rangle = \frac{1}{2}(3\cos^2\theta_R - 1)(3\cos^2\beta - 1), \quad (2.83)$$

where the angles  $\beta$  and  $\theta_R$  are defined in figure 2.12. As stated before, the angle  $\theta$  is between the principal  $z$ -axis of the shielding tensor and applied field  $B_0$ . The angle  $\beta$  denotes the angle between the principal  $z$ -axis of the shielding tensor and the spinning axis, whereas  $\theta$  is the so-called *magic angle* between the applied field  $B_0$  and the spinning axis. In case of  $\theta_R$  being fixed to  $54.74^\circ$ , the

averaged orientation dependence  $\langle 3\cos^2\theta - 1 \rangle$  is zero due to  $\langle 3\cos^2\theta_R - 1 \rangle = 0$ . At sufficient high spinning rates,  $\theta$  is averaged rapidly compared to the interaction anisotropy.

Spinning at slow rates leads to the appearance of *spinning sidebands* symmetrically in addition to the isotropic line. These sidebands are sharp lines on the left and right side of the line at the isotropic chemical shift separated by a distance equal to the spin rate. The isotropic line is not affected in its position with changing spinning rates; it is not necessarily the most intense line in the spectrum. Today, spinning rates of 30 kHz are routine on modern NMR devices and rates up to 50 kHz can be achieved by using small rotors with a diameter of 1.2 mm. If spun at these rates, spinning sidebands will rarely occur as more than one (or two) in a spectrum.

## 2.5 Impedance spectroscopy

Impedance spectroscopy (IS) is a well-established and relatively simple method for the investigation of ion diffusion in solids. Ionic conductivity ( $\sigma$ ) is measured as a function of frequency (ranging from mHz to GHz) and as a function of temperature. Multiple microscopic processes (including transport of electrons) occur throughout the cell if electrically stimulated and these processes create an overall electrical response. Impedance measurements give access to short- and long-range diffusion mechanisms. The general approach is to apply an alternating voltage the electrodes and to observe the resulting current  $I(\omega)$  (see figure 2.13 for an illustration of a basic experimental setup).[57]

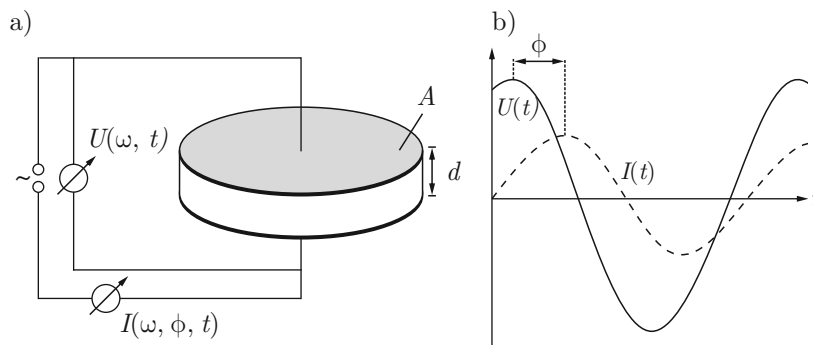


**Figure 2.13** – a) Illustration of a basic IS experiment setup for ion conductors. An AC-voltage ( $\sim$ ) is applied to the electrodes of the sample and the resulting current is measured by an ammeter. The sample is well-placed between two electrodes with an area  $A$  separated by the distance  $d$ . b) Illustration of a phase shift  $\phi$  between sinusoidal voltage ( $U(t)$ ) and current ( $I(t)$ ) as a function of time. A phase shift can be observed when a dielectric material is placed between the electrodes.

### 2.5.1 Basics of impedance spectroscopy

The principle of impedance spectroscopy is based on the application of a sinusoidal voltage with a frequency  $\nu = \omega/2\pi$  to the investigated material:

$$U(t) = U_0 \sin(\omega t). \quad (2.84)$$

The current response  $I$  will be linear resulting in a sinus-shaped current with same frequency. The differences between the initial current and the resulting current are a phase shift  $\phi$  and a different

amplitude  $I_0$  when compared to the voltage:

$$I(\omega) = I_0 \sin(\omega t - \phi(\omega)). \quad (2.85)$$

In case of a purely electrical resistance the phase shift  $\phi$  is zero and the resistance  $R$  can be described using *Ohm's law*  $R = U/I$ . The concept of a complex resistance is used to address a displacement of the phase. In order to address this concept mathematically a switch to the complex plane, indicated by a tilde in the upcoming section, is necessary. Thus, Equation 2.84 and 2.85 are expressed as

$$\tilde{U}(t) = U_0 \exp(i\omega t), \quad (2.86)$$

$$\tilde{I}(t) = I_0 \exp(i(\omega t - \phi)). \quad (2.87)$$

Here,  $i$  is an imaginary number defined by  $i^2 = -1$ . Analogous to Ohm's law, the *impedance*  $\tilde{Z}$  can be expressed

$$\tilde{Z}(\omega) = \frac{\tilde{U}(\omega)}{\tilde{I}(\omega)} = |\tilde{Z}(\omega)| \exp(i\phi), \quad (2.88)$$

with an absolute value of  $\tilde{Z}$  being  $|\tilde{Z}(\omega)| = \nu_0/I_0$ . The reciprocal of the *impedance* is known as *admittance*  $\tilde{Y}$  and can be described by using  $\tilde{Y} = 1/\tilde{Z}$  as:

$$\tilde{Y} = |\tilde{Z}(\omega)|^{-1} \exp(-i\phi). \quad (2.89)$$

Using *Euler's formula*  $\exp(i\phi) = \cos(\phi) + i\sin(\phi)$  for the correlation between real- and imaginary part the *impedance* and *admittance* can be rewritten as:

$$\tilde{Z} = |\tilde{Z}|(\cos(\phi) + i\sin(\phi)) \equiv Z' + iZ'', \quad (2.90)$$

$$\tilde{Y} = |\tilde{Y}|(\cos(\phi) - i\sin(\phi)) \equiv Y' + iY'', \quad (2.91)$$

where the real part of the impedance  $Z' = |\tilde{Z}|\cos(\phi)$  as of the *admittance*  $Y' = |\tilde{Y}|\cos(\phi)$  and the corresponding imaginary part  $Z'' = |\tilde{Z}|\sin(\phi)$  and  $Y'' = |\tilde{Y}|\sin(\phi)$  are marked by primes or double primes respectively. There are four parameters significant for impedance spectroscopy. The other two parameters, besides the impedance and admittance, are the *dielectric permittivity* (2.92) and the *modulus function* (2.93).

$$\tilde{\epsilon} = \epsilon' - i\epsilon'' \equiv \tilde{M}^{-1} = \frac{\tilde{Y}}{i\omega C_0}. \quad (2.92)$$

The modulus function  $M = \epsilon^{-1}$  is defined as the inverse of the permittivity, thus giving

$$\tilde{M} \equiv M' + iM'' = i\omega C_0 \tilde{Z}. \quad (2.93)$$

Here, the capacitance of an empty cell  $C_0$  is described by  $C_0 = \epsilon A/d$  where  $A$  is the surface area of the electrodes and  $d$  is the distance between electrodes.

A really important parameter for the characterization of solid ion conductors accessible by IS is the DC-conductivity  $\sigma_{DC}$  on condition of conductivity caused exclusively by moving ions. This parameter

can be accessed by an evaluation of conductivity spectra, where the real part of the conductivity is plotted against the frequency  $\omega$ . Conductivity is a material specific parameter, and therefore independent of the geometry of the sample, and is given by the sum of real- and imaginary part  $\tilde{\sigma} = \sigma' + i\sigma''$ . It can be calculated by introducing a geometry constant  $\kappa$  and the admittance  $\tilde{Y}$  according to:

$$\tilde{\sigma} = \tilde{Y} \cdot \frac{d}{A}, \quad (2.94)$$

where  $A$  is the area and  $d$  the thickness of the sample. An overview on the relation of these four parameters (also known as *immittances*) is provided in table 2.1.

**Table 2.1** – Overview on the relations between the four commonly used parameters of impedance spectroscopy.

	$M$	$Z$	$Y$	$\epsilon$
$M$	$M$	$\mu Z$	$\mu Y^{-1}$	$\epsilon^{-1}$
$Z$	$\mu^{-1} M$	$Z$	$Y^{-1}$	$\mu^{-1} \epsilon^{-1}$
$Y$	$\mu M^{-1}$	$Z^{-1}$	$Y$	$\mu \epsilon$
$\epsilon$	$M^{-1}$	$\mu^{-1} Z^{-1}$	$\mu^{-1} Y$	$\epsilon$

## 2.5.2 Conductivity spectra and diffusion

As mentioned at the beginning of this section impedance spectroscopy can be carried out over a wide range of frequencies (ranging from mHz up to GHz) and temperatures (110 K up to 620 K). In this work, the data gained from IS is processed in the form of conductivity spectra. The real part of the conductivity  $\sigma'$  measured at various temperatures is plotted against the frequency  $\nu$  in a double logarithmic plot. An example of an impedance spectrum of a solid is provided in figure 2.14, where the measurement of glassy petalite serves as a model for the demonstration of the most common features of conductivity spectra. A conductivity spectrum can be divided into the following domains:

- (i) At low frequencies and moderate temperatures, a frequency independent plateau, with the value  $\sigma_{\text{DC}} = \sigma'(0)$  (also known as DC-conductivity or DC-plateau), can be found in conductivity spectra. In solids,  $\sigma_{\text{DC}} T$  exhibits an Arrhenius-like behavior:  $\sigma_{\text{DC}} T \propto \exp(-E_a^{\text{DC}}/k_b T)$ , with the activation energy  $-E_a^{\text{DC}}$  and the Boltzmann's constant  $k_b$ .
- (ii) At higher frequencies, there is a monotonic increase of the impedance  $\sigma'$  with the frequency  $\nu$  up to the range of phonon frequencies. This behavior of the impedance is caused by various correlation effects evoked by lattice defects, the interaction of ions or from the response of the lattice to ion hopping.
- (iii) The number of moving ions increases with temperature. At lower frequencies, polarization effects at the blocking electrodes can be observed, which leads to a drop of  $\nu'$ .
- (iv) At very high frequencies (above 100 GHz, not shown in figure 2.14), the conductivity reaches a regime governed by lattice vibration. In this regime,  $\nu'$  is solely determined by phononic contributions and shows square dependence of the frequency  $\sigma' \propto \omega^2$ .

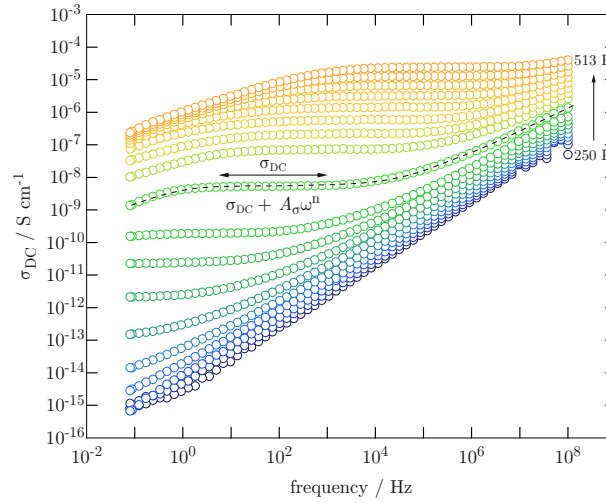


**Figure 2.14** – Selected conductivity spectra of glassy petalite ( $\text{LiAlSi}_4\text{O}_{10}$ ) to illustrate the common features found in impedance spectroscopy.

The transition of the DC-plates into the dispersive region (see figure 2.14) can be reasonably well described by the *Jonscher power law*:

$$\sigma'(\omega) = \sigma_{\text{DC}} + A\omega^n, \quad (2.95)$$

where  $\sigma'$  denotes the real part of the conductivity and  $A$  and  $n$  are constants with  $n$  usually in the range of 0.6 to 0.7. In general,  $\sigma_{\text{DC}} = \sum_i \sigma_{\text{DC}}^i$  is the sum of conductivities of all ionic species  $i$  present in the sample. In this work, only materials with a single diffusing species were investigated, meaning that  $\sigma_{\text{DC}}$  is only governed by Li ions. A diffusion coefficient  $D^\sigma$  can be obtained from IS by using the *Nernst-Einstein Equation*: [58–62]

$$D^\sigma = \frac{\sigma_{\text{DC}} k_B T}{Nq^2}, \quad (2.96)$$

where  $N$  denotes the charge carrier density and  $q$  the charge of the ions.



# 3

## Results

In this section, the results of all studies on Li ion conductors are presented in a cumulative form; either as submitted or published articles in peer-reviewed journals. The articles are arranged into four sections defined by the diffusion properties, or rather, class of the material, *viz.* lithium ion diffusion in low-dimensional materials (section 3.1), three-dimensional diffusion in garnet-type Li-ion conductors (section 3.2), the influence of mechanical treatment on lithium diffusivity in the aluminosilicate mineral petalite (section 3.3) and ionic liquids (section 3.4). Each subsection provides a brief introduction and, in some cases, additional data not included in the already published article.

The first section deals with lithium ion diffusion in low-dimensional materials. Thus, a start is made by an article investigating the diffusion properties of one-dimensional  $\text{LiBi}_3\text{S}_5$  with the title "*LiBi<sub>3</sub>S<sub>5</sub> - A lithium bismuth sulfide with strong cation disorder*" (see section 3.1.1).[63] The two distinct Li positions in the structure of the electric conductor  $\text{LiBi}_3\text{S}_5$  were successfully determined by using  $^6\text{Li}$  MAS spectroscopy.  $^7\text{Li}$  SLR measurements in the laboratory frame of reference revealed an activation energy of 0.44 eV for short range Li ion hopping. The obtained relaxation rates show high Li ion diffusivity at higher temperatures ( $T > 400$  K). The second article with the title "*Li ion dynamics along the inner surfaces of layer-structured 2H-Li<sub>x</sub>NbS<sub>2</sub>*" covers a comprehensive NMR characterization of the compound  $2\text{H-Li}_x\text{NbS}_2$  with  $x = 0.1, 0.3$  and  $1$  (see section 3.1.2).[64] Here, information on the dimensionality of the diffusion process in the material was experimentally determined by frequency-dependent  $R_{1\rho}$  NMR measurements carried out at  $T = 444$  K. A slight, but measurable frequency-dependence within the HT limit is found; the result is in good agreement with predictions from relaxation models developed to approximate low-dimensional (2D) jump diffusion. The work of both articles was done in collaboration with the group of Prof. Martin Lerch (Berlin, Germany), where the sample material, in both cases, was synthesized and the structural properties were determined (XRD-analysis, chemical characterization, crystal structure determination, *etc.*).

The next section focuses on lithium ion diffusion in three-dimensional garnet-type Li ion conductors, which are an interesting class of materials due to their potential application as a solid electrolyte in all-solid Li ion batteries. The work presented in this section originated from previous and ongoing collaboration with Dr. Daniel Rettenwander (Salzburg, Austria). In the first part of the subsection temperature-variable  $^7\text{Li}$  NMR relaxometry measurements using both laboratory and spin-lock techniques to probe Li jump rates in single-crystalline  $\text{Li}_6\text{La}_3\text{ZrTaO}_{12}$  are presented. It was determined, that the material is a very fast Li ion conductor and the gained data perfectly mirror a modified BPP-type relaxation response. The second part of the subsection is assigned to Li ion dynamic studies of Bi-doped garnet-type  $\text{Li}_{7-x}\text{La}_3\text{Zr}_{2-x}\text{Bi}_x\text{O}_{12}$  (see section 3.2.1). The results are discussed in detail in the article "*Synthesis, crystal structure, and stability of cubic  $\text{Li}_{7-x}\text{La}_3\text{Zr}_{2-x}\text{Bi}_x\text{O}_{12}$* " (see section 3.2.2).[65] The motional narrowing of  $^7\text{Li}$  NMR line width (FWHM = full width at half maximum) was used to predict the influence of Bi-doping on Li ion dynamics. Additional  $^7\text{Li}$  SLR NMR measurements shows that fast translational Li ion dynamics are only observed for samples with large amounts of Bi incorporated ( $x > 0.8$ ).

This section describes the influence of mechanical treatment, and thus nanostructuring and the introduction of defects, on Li ion dynamics in both, crystalline and glassy, petalite  $\text{LiAlSi}_4\text{O}_{10}$ . The samples were comprehensively investigated by solid-state  $^7\text{Li}$  NMR and impedance spectroscopy (see section 3.3.1). The various nanostructured samples were prepared by high-energy ball milling. Ball-milling of crystalline petalite results in an enhancement of long-range ion transport by several orders of magnitude. The opposite trend, however, is found when  $\text{LiAlSi}_4\text{O}_{10}$  glass is treated for several hours in a planetary mill. The Li ion conductivities of the two samples, *viz.* the crystalline and glassy forms, head towards each other with increasing milling time.

The last section contains an article on a novel electrolyte system with the title "*Ionic liquids-in-salt*" - a promising electrolyte concept for high-temperature lithium batteries?" (see section 3.4.1).[66]  $^7\text{Li}$  NMR spectroscopy was employed to study both local electronic structures and  $\text{Li}^+$  self-diffusion in pure LiTFSI and in the mixture of an ionic liquid with a lithium salt -  $\text{Li}_x\text{EMIM}_{(1-x)}\text{TFSI}$  with  $x = 0.9$ . The work was done in collaboration with the group of Prof. Patrik Johansson (Göteborg, Sweden), where the samples were prepared and characterized.

## **3.1 Lithium ion diffusion in low-dimensional materials**

### **3.1.1 One-dimensional Li diffusion in $\text{LiBi}_3\text{S}_5$**

#### **$\text{LiBi}_3\text{S}_5$ - A lithium bismuth sulfide with strong cation disorder**

Suliman Nakhil, Dennis Wiedermann, Bernhard Stanje, Oleksandr Dolotko, Martin Wilkening, Emmanuelle Suard and Martin Lerch. *Journal of Solid State Chemistry*, DOI: 10.1016/j.jssc.2016.03.010 (2016), 60 - 67





Contents lists available at ScienceDirect

Journal of Solid State Chemistry

journal homepage: [www.elsevier.com/locate/jssc](http://www.elsevier.com/locate/jssc)LiBi<sub>3</sub>S<sub>5</sub>—A lithium bismuth sulfide with strong cation disorderSuliman Nakhal<sup>a</sup>, Dennis Wiedemann<sup>a,\*</sup>, Bernhard Stanje<sup>b</sup>, Oleksandr Dolotko<sup>c</sup>, Martin Wilkening<sup>b</sup>, Martin Lerch<sup>a</sup><sup>a</sup> Institut für Chemie, Technische Universität Berlin, Straße des 17. Juni 135, 10623 Berlin, Germany<sup>b</sup> Christian Doppler Laboratory for Lithium Batteries and Institute for Chemistry and Technology of Materials (Member of NAWI Graz), Graz University of Technology, Stremayrgasse 9, 8010 Graz, Austria<sup>c</sup> Heinz Maier-Leibnitz Zentrum (MLZ), Technische Universität München, Lichtenbergstraße 1, 85748 Garching b. München, Germany

## ARTICLE INFO

## Article history:

Received 29 January 2016  
 Received in revised form  
 29 February 2016  
 Accepted 3 March 2016  
 Available online 4 March 2016

## Keywords:

Lithium bismuth sulfide  
 Crystal structure  
 Neutron powder diffraction  
 Topological analysis  
 Lithium NMR  
 Lithium diffusion pathways

## ABSTRACT

Among chalcogenide semiconductors for thermoelectric applications, alkali-metal bismuth compounds occur in many complex compositions favorable for high performance. Although LiBi<sub>3</sub>S<sub>5</sub> had been announced in 1977, the potential 1D lithium-ion conductor has hitherto eluded selective synthesis and structure determination. In this study, we present a solid-state route to phase-pure LiBi<sub>3</sub>S<sub>5</sub> powder starting from LiBiS<sub>2</sub> and Bi<sub>2</sub>S<sub>3</sub>. Neutron diffractograms and lithium NMR spectra reveal its crystal structure to be a cation-disordered variety of the AgBi<sub>3</sub>S<sub>5</sub> type (synthetic pavonite; monoclinic, C2/m). Topological analyses and lithium NMR relaxometry suggest that correlated lithium-ion diffusion with activation energies up to 0.66(2) eV occurs along the channels in *b* direction including tetrahedral voids. Because of cation disorder, immobile bismuth(III) ions clog these pathways, making LiBi<sub>3</sub>S<sub>5</sub> a moderate to poor ionic conductor. The synthesis route reported is nonetheless promising for new lithium bismuth sulfides with, possibly ordered, structure types of the pavonite homologous series.

© 2016 Elsevier Inc. All rights reserved.

## 1. Introduction

Semiconducting chalcogenide compounds have been receiving much attention because of their wide range of applications in various fields of science and technology. One of the most promising areas is their use in thermoelectric refrigeration or portable power generation [1]. Various solid solutions of M<sub>2</sub>X<sub>3</sub> phases (M = As, Sb, Bi; X = S, Se, Te), which are excellent for thermoelectric applications near room temperature, have been the most investigated materials during the last half century [2].

In recent years, intense efforts focused on discovering new materials amongst ternary and quaternary alkali-metal bismuth chalcogenides. This class of compounds has proven to be remarkably large and has contributed many complex compositions and structures favorable for high thermoelectric performance [3], e.g., K<sub>2.5</sub>Bi<sub>8.5</sub>Se<sub>14</sub> [4], β-K<sub>2</sub>Bi<sub>8</sub>Se<sub>13</sub> [4], A<sub>2</sub>Bi<sub>8</sub>Se<sub>13</sub> (A = Rb, Cs) [5], and CsBi<sub>4</sub>Te<sub>6</sub> [6]. In comparison to selenides and tellurides, most of the alkali-metal bismuth sulfides exhibit wide energy band gaps and strong ionic interactions between the alkali-metal ions and the [Bi<sub>x</sub>S<sub>y</sub>]<sup>z-</sup> framework, e.g., in β- and γ-CsBiS<sub>2</sub> [7], γ-RbBi<sub>3</sub>S<sub>5</sub> [8], and KBi<sub>3</sub>S<sub>5</sub> [9]. Because of these characteristics, further compounds of this class are sought after. As KBi<sub>3</sub>S<sub>5</sub> has the potential to act as a

host for ion exchange, Chondroudis and Kanatzidis used a low temperature solid-state route to exchange the potassium ions for a variety of other ions. Reaction of the host material with RbCl, LiI, NaI, or (NH<sub>4</sub>)I yielded the isostructural compounds β-RbBi<sub>3</sub>S<sub>5</sub>, Li<sub>0.82</sub>K<sub>0.18</sub>Bi<sub>3</sub>S<sub>5</sub>, Na<sub>0.66</sub>K<sub>0.33</sub>Bi<sub>3</sub>S<sub>5</sub>, and (NH<sub>4</sub>)Bi<sub>3</sub>S<sub>5</sub> [10]. KBi<sub>3</sub>S<sub>5</sub> was, however, not completely converted to the corresponding lithium and sodium compound using this route, whereas the synthesis of pure (NH<sub>4</sub>)Bi<sub>3</sub>S<sub>5</sub> has been reported to be possible.

In this work, we present the selective synthesis of LiBi<sub>3</sub>S<sub>5</sub>, a compound that has been announced, but hitherto very poorly characterized. Lazarev *et al.* assumed its existence on the basis of differential thermal analysis (DTA) and provided a list of the strongest reflections in X-ray diffraction as well as temperature-dependent conductivity measurements [11]. Unfortunately, the lack of experimental and evaluative descriptions makes these pieces of information rather vague and difficult to interpret. So far, lithium bismuth disulfide LiBiS<sub>2</sub> (NaCl type with statistical cation distribution) had been the only well-known ternary compound in the system Li-Bi-S. We describe LiBi<sub>3</sub>S<sub>5</sub> as a second member, supplying crystal-structure refinements based on neutron diffraction, nuclear magnetic resonance (NMR) investigations on lithium-ion dynamics, and topological analyses of possible lithium-diffusion pathways. Since LiBi<sub>3</sub>S<sub>5</sub> is expected to show both electronic and ionic conduction, lithium NMR was chosen to selectively [12] probe lithium-ion dynamics in the mixed conductor.

\* Corresponding author.

E-mail address: [dennis.wiedemann@chem.tu-berlin.de](mailto:dennis.wiedemann@chem.tu-berlin.de) (D. Wiedemann).

## 2. Materials and methods

### 2.1. Syntheses

All reactants have been used in their naturally occurring isotope mixture.

**LiBiS<sub>2</sub>**: Li<sub>2</sub>CO<sub>3</sub> and Bi<sub>2</sub>O<sub>3</sub> powders (molar ratio 1:1) were shaken together and the mixture was thoroughly ground in an agate mortar. It was then heated under H<sub>2</sub>S flow in an alumina crucible at 600 °C for 4 h to give lithium bismuth disulfide as a black powder.

**Bi<sub>2</sub>S<sub>3</sub>**: Bi<sub>2</sub>O<sub>3</sub> was reacted in an alumina crucible under H<sub>2</sub>S flow at 400 °C for 4 h to give dibismuth trisulfide as a black powder.

**LiBi<sub>3</sub>S<sub>5</sub>**: Samples were prepared via two different routes:

- 1) LiBiS<sub>2</sub> and Bi<sub>2</sub>S<sub>3</sub> powders (molar ratio 1:1) were shaken together and the mixture was thoroughly ground in an agate mortar. It was then heated under H<sub>2</sub>S flow in an alumina crucible at 600 °C for 4 h to give lithium tribismuth pentasulfide. Excess sulfur from catalytic decomposition of H<sub>2</sub>S was removed at 150 °C *in vacuo* within 24 h. As the grey-black powders prepared in this way contained small amounts of side phases (Bi<sub>2</sub>S<sub>3</sub> or bismuth), the following route was chosen for further studies.
- 2) LiBiS<sub>2</sub> and Bi<sub>2</sub>S<sub>3</sub> powders were dried *in vacuo* at 150 °C within 24 h. A mixture of them (molar ration 1:1) was sealed in an evacuated silica-glass ampoule and heated to 600 °C with a gradient of 25 °C/h. It was kept at that temperature for 48 h and then rapidly quenched to ambient temperature. Excess sulfur (from catalytic decomposition of H<sub>2</sub>S during precursor synthesis) was removed at 150 °C *in vacuo* within 24 h to leave lithium tribismuth pentasulfide as a grey-black powder.

Anal. found: Bi, 79.15; Li, 0.90; S, 20.44. Calc. for Bi<sub>3</sub>LiS<sub>5</sub> (794.18): Bi, 78.94; Li, 0.87; S, 20.35 wt%. Void of silicon, aluminum (ampoule materials), and oxygen.

### 2.2. Chemical characterization

The absence of oxygen compounds was verified using a “Leco EF-TC 300” N<sub>2</sub>/O<sub>2</sub> analyzer (hot-gas extraction). The sulfur content was determined using a “Thermo Finnigan Flash EA 1112” analyzer. Determination of the bismuth and sulfur contents as well as checks for the absence of silicon and aluminum were accomplished via X-ray fluorescence (XRF) analysis on a “PANalytical Axios PW4400/24” spectrometer equipped with a rhodium tube and a wavelength-dispersive detector. Lithium determinations were carried out with an “Agilent 7500ce ICPMS” (Agilent Technologies, Waldbronn, Germany).

### 2.3. Crystal structure determination

Neutron diffraction was carried out at the neutron facility FRM II (Maier-Leibnitz Zentrum, Garching b. München) using the high-resolution powder diffractometer SPODI with Ge(551)-monochromated radiation ( $\lambda = 154.831$  pm) in Debye–Scherrer geometry [13]. The compacted powder sample was mounted in a vanadium cylinder ( $d = 9$  mm,  $h = 40$  mm) at r.t. and exposed for 12 h. Data were recorded with an array of 80 position-sensitive <sup>3</sup>He tubes ( $2\theta_{\max} = 160^\circ$ , effective height: 300 mm) and reduced using a variable-height algorithm as implemented in the in-house parser [14], yielding a final range of  $0.95^\circ \leq 2\theta \leq 151.90^\circ$  with  $\Delta(2\theta) = 0.05^\circ$ . X-ray diffraction was carried out on a “PANalytical X’Pert PRO MPD” diffractometer equipped with a “PIXcel” detector using nickel-filtered Cu-K $\alpha$  radiation ( $\lambda_1 = 154.056$  pm,  $\lambda_2 = 154.439$  pm) in Bragg–Brentano ( $\theta$ – $\theta$ ) geometry.

For Rietveld refinements, a known model for AgBi<sub>3</sub>S<sub>5</sub> [15] from the Inorganic Crystal Structure Database (ICSD) [16] was imported, adjusted to reflect the actual cell parameters and contents, and refined against net intensities with FULLPROF [17] using the full-matrix least-squares algorithm with fixed elements per cycle. Neutron data were analytically corrected for absorption (cylindrical sample) and stripped of the inclined inset between 0° and 4°. The background was defined manually with 20 (neutrons) or 17 (X-rays) points of refined height. Peak profiles were fitted with a pseudo-Voigt function (Gaussian parameters  $U$ ,  $V$ , and  $W$ ; Lorentzian parameter  $X$ ; mixing parameter  $\eta$ ). Asymmetry was corrected for using the Bérar–Baldinazzi method with two (neutrons) or four parameters (X-rays) [18]. A scale factor and a zero-shift correction (neutrons) or displacement and transparency corrections (X-rays) were applied.

Same-position and same-ADP constraints were applied to bismuth and lithium ions sharing approximately same positions. The isotropic displacement parameters of Bi4/Li4 and Bi5/Li5 were fixed at the average of those of the other ions. All other ions were refined with individual anisotropic (neutrons) or isotropic (X-rays) atomic displacement. All positions included were constrained to be fully occupied. As the occupation of Bi3 refined to a value only insignificantly lower than 0.5 for neutron data, it was fixed at this value. Furthermore, the sum of bismuth occupations was found to be very close to the one given by the chemical composition and was thus restrained to equal it. Tables 1 and S1 list further experimental details, Figs. 1 and S1 show the neutron and X-ray diffractogram, respectively.

Structure graphics were produced using DIAMOND 3.2 [19]. Analysis of the Hirshfeld surface under exclusion of lithium ions was performed using CRYSTAL EXPLORER 3.1 [20]. For Voronoi–Dirichlet partitioning analysis, TOPOS PRO 5.1 [21] was employed in a standard procedure: After detection, too small elementary voids (spherical-domain radius  $R_{sd} < 158$  pm for lithium ions in sulfide environments [22]) and channels (adjacency radius  $R_{ad} < 219$  pm, 90% of sum of ionic radii [23]) as well as those not only determined by sulfide ions (solid angle of interaction with bismuth ions  $\Omega > 10\% \times 4\pi$ ) were discarded [24].

Further details of the crystal structure investigations may be obtained from FIZ Karlsruhe, 76344 Eggenstein-Leopoldshafen, Germany (fax: +49 7247 808-666; e-mail: [crysddata@fiz-karlsruhe.de](mailto:crysddata@fiz-karlsruhe.de)), on quoting the deposition numbers CSD-430770 (neutrons) and -430769 (X-rays).

**Table 1**  
Details of neutron powder diffraction at LiBi<sub>3</sub>S<sub>5</sub>.

Sum formula	LiBi <sub>3</sub> S <sub>5</sub>
$T/K$	298
Crystal system	Monoclinic
Space group	$C2/m$
$\lambda/\text{pm}$	154.831
$Z$	4
$M/\text{g mol}^{-1}$	794.2
$a/\text{pm}$	1310.79(2)
$b/\text{pm}$	400.070(7)
$c/\text{pm}$	1650.85(3)
$\beta/^\circ$	94.0723(12)
$V/10^6 \text{ pm}^3$	863.53(3)
$\rho_{\text{calc}}/\text{g cm}^{-3}$	6.109
$\mu/\text{mm}^{-1}$	0.0297
$R_p$	0.0160
$R_{\text{wp}}$	0.0190
$R_{\text{exp}}$	0.0125
$R_B$	0.0367
$R_F$	0.0216
$S$	1.52

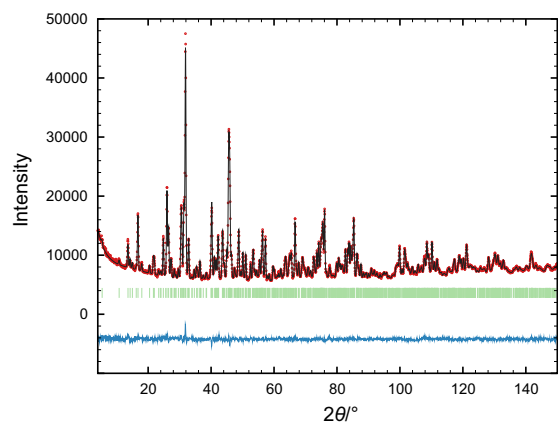


**Fig. 1.** Neutron powder diffractogram of  $\text{LiBi}_3\text{S}_5$  with the results of the Rietveld refinement (black: measured, red: calculated intensities, green: Bragg positions, blue: intensity difference; for interpretation of the references to color in this figure legend, the reader is referred to the web version of this article).

#### 2.4. Lithium NMR

For the  $^7\text{Li}$  NMR measurements under static, *i.e.*, non-rotating conditions, the  $\text{LiBi}_3\text{S}_5$  powder prepared was fire-sealed under vacuum in DURAN<sup>®</sup> glass ampoules (*ca.* 4 cm in length and 0.5 cm in diameter) to permanently protect the sulfide from any moisture or air.

$^7\text{Li}$  NMR measurements were performed using a “Bruker Avance III” spectrometer, which was connected to a shimmed cryomagnet with a nominal external magnetic field of  $B_0=7.04\text{ T}$ , which corresponds to a  $^7\text{Li}$  resonance frequency of  $\omega_0/2\pi=116.4\text{ MHz}$ . A ceramic high-temperature NMR probe (Bruker BioSpin) was employed that allows  $\pi/2$  pulse lengths of *ca.* 6–7.5  $\mu\text{s}$  at 200 W. The exact  $\pi/2$  pulse length depends on temperature. The temperature in the sample chamber (223–573 K) was adjusted via a “Eurotherm” controller and a stream of freshly evaporated dinitrogen.  $^7\text{Li}$  NMR spectra and  $^7\text{Li}$  spin-lattice relaxation (SLR) rates ( $1/T_1=R_1$ ) in the laboratory frame of reference were recorded with the well-known saturation recovery pulse sequence. In our case, this sequence consists of ten  $\pi/2$  pulses destroying any longitudinal magnetization  $M$  followed by an evolution period allowing for the recovery of  $M(t_d)$ :  $10 \times \pi/2 - t_d - \pi/2 - \text{acq}$ . The last pulse is used for detection of the free induction decay (FID). In addition, we used spin-lock NMR relaxometry to probe slower ion dynamics.  $^7\text{Li}$  SLR rates in the so-called rotating frame of reference ( $1/T_{1\rho}=R_{1\rho}$ ) were recorded with the following pulse sequence:  $\pi/2_{\text{X}} - \text{spin-locking pulse } (t_{\text{lock}}) - \text{acq}$ . The first pulse flips the equilibrium magnetization  $M$  into the ( $xy$ )-plane; the spin-lock pulse, directly following the pulse to prepare the spin-system, is used to hold the transversal component of  $M$ . During the locking pulse, which is generated via the  $B_1$  field characterized by  $\omega_1/2\pi$  in the kilohertz range,  $M$  has to adopt a new equilibrium value that is much smaller than that corresponding to  $B_0$ . Hence, a transversal decay of  $M(t_{\text{lock}})$  is monitored that is influenced by lithium-ion diffusion at sufficiently high  $T$ . Here, we used a spin-lock frequency of *ca.* 20 kHz. Between the acquisitions of each spin-lock FID, a recycle delay of at least  $5T_1$  was applied.

To gather information on local magnetic structures around the lithium nuclei,  $^6\text{Li}$  magic-angle spinning (MAS) NMR was used. The corresponding spectra were recorded at 296 K using a “Bruker Avance III” 500 MHz spectrometer, which was connected to a shimmed 11.7 T cryomagnet, resulting in a nominal  $^6\text{Li}$  resonance

frequency of 73.6 MHz. Spinning was carried out using 2.5-mm rotors (Bruker) that are able to rotate the samples at speeds as high as 30 kHz.

### 3. Results and discussion

#### 3.1. Structure determination

We started structure determination by recording and interpreting an X-ray diffractogram (see Fig. S1). A first inspection showed it to be roughly reconcilable with the interplanar spacings and corresponding intensities tabulated before [15], so that we assume to have the same compound in our hands. The comparison to X-ray diffractograms of other known compounds collected in the ICSD suggested that  $\text{LiBi}_3\text{S}_5$  is of the  $\text{AgBi}_3\text{S}_5$  (synthetic pavonite) type. Subsequent Rietveld refinement using a model of this structure type and inspection of difference electron-density maps revealed ample occupation of the positions originally attributed to silver(I) ions by bismuth(III) ions (see Tables S1–S2). A free refinement of bismuth occupancies led to an empirical formula of approximately  $\text{Bi}_{2.9}\text{S}_5$ , so that we restrained the bismuth content to 3.0—also in accordance with chemical analysis. No significant residual electron-density maxima were found after this procedure.

As lithium ions are notoriously weak X-ray scatterers, we have performed powder neutron diffraction to unambiguously locate them in the crystal structure. Results of the Rietveld refinement are shown in Fig. 1 and summarized in Tables 1–3. Starting with the model acquired from X-ray data, difference maps of scattering-length density revealed occupation of most cation positions (especially Bi4 and Bi5) with lithium ions. As free refinement led to site occupation factors (s.o.f.) greater than one, all positions were constrained to be fully occupied either by bismuth or lithium ions. The s.o.f. of Bi3 was found to be insignificantly smaller than unity and thus constrained to reflect full bismuth occupation. The data then allowed for refinement of all positions, except for Bi4/Li4 and Bi5/Li5, with anisotropic displacement parameters (ADPs). Even in the isotropic case—as also noticed in the fitting to X-ray data before—, negative or huge displacement parameters resulted for Bi4/Li4 and Bi5/Li5, respectively. Neither the shift of these ions to general positions nor the permission of anharmonic contributions to displacement led to physically sensible models and stable refinements at the same time. Consequently, we fixed their  $U_{\text{iso}}$  at the average of all other  $U_{\text{eq}}$ . Notably, these complications occur at the only two positions with (a) considerable lithium occupation and (b) the highest site symmetry possible in this space group. In our opinion, the misfit between lithium(I) and bismuth(III) may

**Table 2**  
Atomic coordinates and site occupation factors (s.o.f.) for  $\text{LiBi}_3\text{S}_5$  at ambient temperature as derived from neutron powder diffraction.

Atom	Wyckoff site	x	y	z	s.o.f.
Bi1	4i	0.23805(16)	½	0.11122(10)	0.821(3)
Li1	4i	0.23805(16)	½	0.11122(10)	0.179(3)
Bi2	4i	0.47179(14)	0	0.21890(10)	0.876(3)
Li2	4i	0.47179(14)	0	0.21890(10)	0.124(3)
Bi3	4i	0.21539(12)	0	0.39076(8)	1
Bi4	2a	0	0	0	0.450(3)
Li4	2a	0	0	0	0.550(3)
Bi5	2d	0	½	½	0.156(3)
Li5	2d	0	½	½	0.844(3)
S1	4i	0.3716(4)	0	0.0535(3)	1
S2	4i	0.1069(4)	0	0.1534(3)	1
S3	4i	0.3411(3)	½	0.2580(3)	1
S4	4i	0.0706(3)	½	0.3631(3)	1
S5	4i	0.3536(3)	½	0.4656(2)	1

**Table 3**  
Displacement parameters (in  $10^4 \text{ pm}^2$ ) for  $\text{LiBi}_3\text{S}_5$  at ambient temperature as derived from neutron powder diffraction.

Atom	$U_{\text{iso}}$	$U_{\text{eq}}$	$U_{11}$	$U_{22}$	$U_{33}$	$U_{12}$	$U_{13}$	$U_{23}$
Bi1	–	0.0162(11)	0.0110(10)	0.0123(11)	0.0254(12)	0	0.0011(9)	0
Li1	–	0.0162(11)	0.0110(10)	0.0123(11)	0.0254(12)	0	0.0011(9)	0
Bi2	–	0.0190(11)	0.0192(10)	0.0178(10)	0.0200(12)	0	–0.0030(10)	0
Li2	–	0.0190(11)	0.0192(10)	0.0178(10)	0.0200(12)	0	–0.0030(10)	0
Bi3	–	0.0254(9)	0.0309(9)	0.0224(8)	0.0230(10)	0	0.0068(7)	0
Bi4	0.01825	–	–	–	–	–	–	–
Li4	0.01825	–	–	–	–	–	–	–
Bi5	0.01825	–	–	–	–	–	–	–
Li5	0.01825	–	–	–	–	–	–	–
S1	–	0.018(2)	0.034(3)	0.0101(19)	0.010(2)	0	0.009(2)	0
S2	–	0.020(2)	0.011(2)	0.023(2)	0.027(3)	0	0.007(2)	0
S3	–	0.016(2)	0.012(2)	0.013(2)	0.024(2)	0	0.011(2)	0
S4	–	0.016(2)	0.020(2)	0.0122(20)	0.017(2)	0	–0.0100(19)	0
S5	–	0.015(2)	0.019(2)	0.0109(19)	0.017(2)	0	–0.0045(17)	0

well lead to a disorder over these positions that is unresolvable because of severe reflection overlap. This problem is especially prominent in the high-angle regime, thus leading to difficulties evaluating displacement parameters. The final model led to an empirical formula very close to  $\text{Bi}_3\text{LiS}_5$ ; occupation sums were then restrained to equal it.

### 3.2. Structure description

$\text{LiBi}_3\text{S}_5$  crystallizes in cation-disordered variant of the  $\text{AgBi}_3\text{S}_5$  type, the eponym of which is a member ( $N=5$ ) of the so-called pavonite homologous series with the general formula  $[\text{Bi}_2\text{S}_3]_2 \cdot [\text{AgBiS}_2]_{(N-1)/2}$  [15]. The different members of the pavonite homologues series are usually denoted by the symbol  ${}^N\text{P}$ , where  $N$  is the number of the octahedra per diagonal octahedral chain of the thicker slabs in the structure (see Fig. 2).

Four of the bismuth and all of the lithium ions present in the crystal structure are octahedrally coordinated by six sulfide ions. The remaining Bi3 is coordinated by five close sulfide ions in the fashion of a square pyramid. This position is not accidentally unoccupied by lithium, as a square pyramidal coordination would be unfavorable. The crystal structure of  $\text{LiBi}_3\text{S}_5$  is composed of two types of alternating slabs parallel to (001), which can be described as assembly of blocks excised from a distorted NaCl-type structure. The thinner slabs are composed of single  $\text{MS}_6$  octahedra ( $M=\text{Bi5, Li5}$ ) sandwiched by two square ( $\text{Bi3}$ ) $\text{S}_5$  pyramids along [100]. In the thicker slabs (thickness varying with  $N$  in the  ${}^N\text{P}$ -pavonite series), the arrangement of the sulfide ions deviates only slightly from a cubic close packing. In our case, they consist of five  $\text{MS}_6$  octahedra ( $M=\text{Bi1, Li1, Bi2, Li2, Bi4, Li4}$ ) per diagonal chain. The two types of slabs are connected via vertices at S4, which is part of the polyhedra around Bi2/Li2, Bi3, and Bi5/Li5.

The individual and average bond lengths, volumes, and continuous shape measure for all coordination polyhedra are listed in Table 4. The latter quantifies the minimal distance movement that the ions would have to undergo to be transformed into an ideal shape (e.g., an octahedron or a square pyramid) [25]. All average bond lengths in  $\text{LiBi}_3\text{S}_5$  are close to the reported values for  $\text{AgBi}_3\text{S}_5$  [15]. It is noteworthy that Bi3 binds to only five sulfide ions, thus forming a distorted square pyramid, and interacts with two additional anions in the thicker slab at a long distance of 346.9 (4) pm. If these were included into the coordination polyhedron, it would be considered an augmented triangular prism. Amongst the positions partially occupied by lithium ions, Bi5/Li5 holds a somewhat special place: the smallest bond lengths in the structure (only ca. 250 pm) are found here and lead to an average, which is

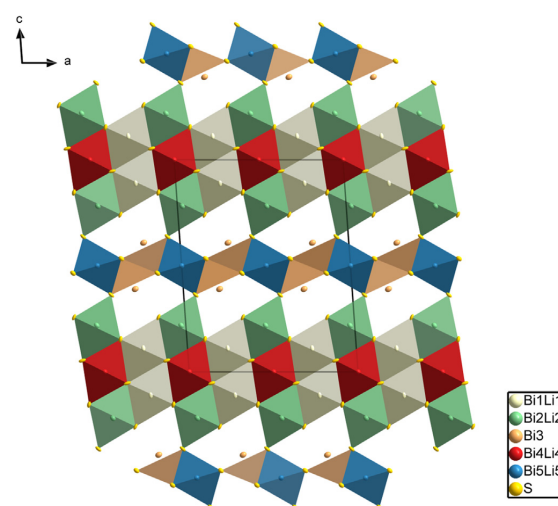


**Fig. 2.** Unit cell of  $\text{LiBi}_3\text{S}_5$  and polyhedral representation of the crystal structure (ellipsoids for probability of 50%).

by ca. 10 pm smaller than those for the other cation positions. This causes a way smaller and much more strongly distorted coordination octahedron, making it particularly unfavorable for hosting bismuth(III) ( $r_{\text{eff}}=103 \text{ pm}$ ) instead of lithium(I) ions ( $r_{\text{eff}}=76 \text{ pm}$  [23]). Disorder between these two species itself is well known, e.g., in the sulfidic  $\text{LiBiS}_2$  [26] or in various oxidic materials [27,28].

### 3.3. Topological analysis

Even though  $\text{LiBi}_3\text{S}_5$  will be shown to be an, at best, moderate lithium-ion conductor (*vide infra*), we were interested in the migration paths that are generally possible in pavonite-like materials. For an experimental mapping of lithium diffusion pathways in crystalline solids, neutron diffraction at—preferably multiple—high temperatures is the method of choice [30,31]. In the present case, however, effective evaluation of powder data would be severely hampered by cation disorder and low symmetry. To gain insight into probable migration paths nonetheless, we have used two topological methods only requiring the solid-state structure (and tabulated empirical parameters) as input: the Hirshfeld-surface

**Table 4**  
Bond lengths in LiBi<sub>3</sub>S<sub>5</sub> at ambient temperature as derived from neutron powder diffraction.

Atom1	Atom2	Count	d/pm	V <sub>cp</sub> /10 <sup>6</sup> pm <sup>3a</sup>	S(cp) <sup>b</sup>
Bi1/Li1	S3	1 ×	268.9(5)	67.75	0.05
	S2	2 ×	275.9(4)		
	S1	2 ×	286.5(4)		
	S1	1 ×	298.4(5)		
	Average		282(11)		
Bi2/Li2	S4	1 ×	262.8(5)	62.28	0.11
	S3	2 ×	274.0(3)		
	S2	2 ×	292.9(4)		
	S1	1 ×	294.5(5)		
	Average		282(14)		
Bi3	S5	1 ×	259.7(4)	79.87	0.87
	S4	2 ×	277.3(3)		
	S5	2 ×	291.4(3)		
	Average		279(14)		
Bi4/Li4	S1	4 ×	279.7(4)	52.16	0.01
	S2	2 ×	280.6(5)		
	Average		280.0(5)		
Bi5/Li5	S4	2 ×	250.2(5)	34.62	0.67
	S5	4 ×	280.2(3)		
	Average		270(16)		

<sup>a</sup> Volume of the coordination polyhedron (calculated with ToposPro 5.1 [21]).

<sup>b</sup> Continuous shape measure for the idealized coordination polyhedron (square pyramid for Bi3, octahedron for all others; calculated on CSM website [29]).

analysis (HSA) and the Voronoi–Dirichlet partitioning (VDP) of the Bi<sub>3</sub>S<sub>5</sub><sup>−</sup> void structure, which have been used successfully in studies on battery materials and fast ion conductors before [29,32]. Note that the conclusions drawn from the room temperature structure are transferable to high temperature only if no phase transformation or significant thermal dilation of voids takes place. A prerequisite for lithium-ion diffusion is the availability of vacancies or accessible voids (*i.e.*, space to induce Frenkel defects) in the crystal structure. As the former is not the case in stoichiometric LiBi<sub>3</sub>S<sub>5</sub>, the latter have to be shown to be present.

For the HSA of crystal voids, one is restricted to ordered models. We have thus chosen three cases: a stoichiometric model (Bi1–Bi3, Li4, Li5) representing a probable configuration, an all-bismuth model (Bi1–Bi5) as worst case (*i.e.*, bulkiest framework), and a defective model (Bi1–Bi3) to investigate accessibility to moving lithium ions. In spite of its quite spacious appearance, the stoichiometric model contains only small voids with a distorted tetrahedral, anionic environment (S3, S4, S4', S5) at the junction of the slabs. Their isosurfaces connect to very narrow channels along [010] at a value of 0.0045 a.u., indicating an unlikely migration path (see Fig. 3a). In the all-bismuth model, the voids stay isolated up to a high isovalue of 0.006 a.u., albeit being accessible from the positions of Li2 and Li5 (see Fig. 3b). The presence of bismuth ions effectively blocks all paths. The defective model shows the largest voids at the vacancies. These voids connect to ample channels along [010] at isovalues of 0.0045 a.u./0.0035 a.u. and above for the deletion of Li4/Li5, respectively (see Fig. 3c). This means that two crystallographically inequivalent, isolated 1D migration pathways along direction *b* may exist. The less preferable one (for reasons of size) includes Li4, the favored one includes Li5. Any of them would be clogged by bismuth ions Bi4 or Bi5. (In an additional experiment, we heated LiBi<sub>3</sub>S<sub>5</sub> to 600 °C and slowly cooled down to 130 °C with 0.5 °C/h. As evidenced by X-ray diffractograms, this did not lead to cation ordering).

The VDP approach offers further insight, as it includes more detailed information about the size of voids, of the migrating ions, and chemical environment of the pathway. Taking into account the

results of the HSA, we have chosen the stoichiometric model with bismuth ions Bi1, Bi2, Bi3 and lithium ions Li4 and Li5 for this analysis of a best-case scenario. Of the 34 major elementary voids found, 14 were large and regular enough for lithium ions. Of these, five were only determined by sulfide ions and thus significant (fit to host a cation), including the abovementioned tetrahedral void and the position of Li4. Elimination of insignificant (too small) elementary channels between those five left the void at Li4 isolated and the tetrahedral position connected to only one elementary void. Thus, they may host interstitial lithium ions, but are not part of the conduction pattern, which is formed by a single migration channel consisting of four elementary voids (see Fig. 4). One (ZA1) is in proximity of the tetrahedral void's center. The two remainders are very close to the position of Li5 and, by symmetry equivalence, form a four-membered ring around it. This may be the reason for a disorder causing the problems that were experienced during refinement of the displacement parameters of Li5/Bi5.

### 3.4. Lithium NMR spectra

To collect information on local magnetic as well as electric structures in LiBi<sub>3</sub>S<sub>5</sub>, we recorded both <sup>6</sup>Li and <sup>7</sup>Li NMR spectra. High-resolution lithium spectra are usually recorded by taking advantage of lithium-6 (7.5% natural abundance); this practice is because of the much lower quadrupole moment *q*(<sup>6</sup>Li) (spin quantum number *I*=1) as compared to lithium-7 with *I*=3/2: *q*(<sup>6</sup>Li)/*q*(<sup>7</sup>Li)=1/50. Considering diamagnetic compounds, this circumstance reduces second-order quadrupole broadening being responsible for the low resolution of the corresponding <sup>7</sup>Li MAS NMR spectra. In the present case, the <sup>6</sup>Li MAS NMR spectrum was acquired at a spinning speed of 30 kHz (see Fig. 5a). The total signal is composed of at least two overlapping NMR lines representing the chemically and magnetically inequivalent lithium sites in the sulfide. Large paramagnetic shifts are clearly absent. When referenced to aqueous LiCl (*c*=1 mol L<sup>−1</sup>), the resonances appear at +0.27 ppm and −1.30 ppm, respectively. Because of very similar chemical shifts, it turned out to be rather difficult to resolve all four different lithium environments as deduced from neutron-diffraction data (see above).

If analyzed using two Voigt functions (see Fig. 5a), the area ratio of the two lines is *ca.* 1:0.9. Most likely, the line at lower chemical shift includes the lithium ions Li5 in the smaller octahedral voids (Wyckoff position: 2*d*). The smaller the octahedra, the better the shielding and the larger the up-field shift. The ions residing in larger voids might be characterized by larger chemical shifts.

In general, first insights on lithium-ion dynamics can be deduced from variable-temperature NMR line-shape measurements [33]. The static <sup>7</sup>Li NMR spectrum of LiBi<sub>3</sub>S<sub>5</sub> is composed of a single, Lorentzian-shaped central line (see Fig. 5b) with widths (full width at half maximum, fwhm) ranging from 3.1 kHz at 213 K down to 1.2 kHz at 613 K. While dipole-dipole interactions govern the line width at low *T*, lithium-ion self-diffusion (*i.e.*, exchange of the ions among the magnetically distinct crystallographic sites) increasingly averages magnetic dipolar interactions. Consequently, the line narrows. Plotting the width as a function of *T* yields the so-called motional narrowing (MN) curve as shown in the inset of Fig. 6. Line narrowing sets in at *ca.* 290 K and is pronounced with increasing temperature. Full narrowing, however, is not reached within the temperature range covered. Interestingly, motional narrowing spans a rather large *T* regime. This behavior indicates a relatively broad distribution of lithium jump rates.

By evaluating the narrowing curve, a mean lithium-ion jump rate  $\tau_{MN}^{-1}$  can be roughly estimated from the inflection point located at *ca.* 500 K. At this temperature,  $\tau_{MN}^{-1} \approx 2 \times \nu_{H1}$  holds ( $\nu_{H1}$ :

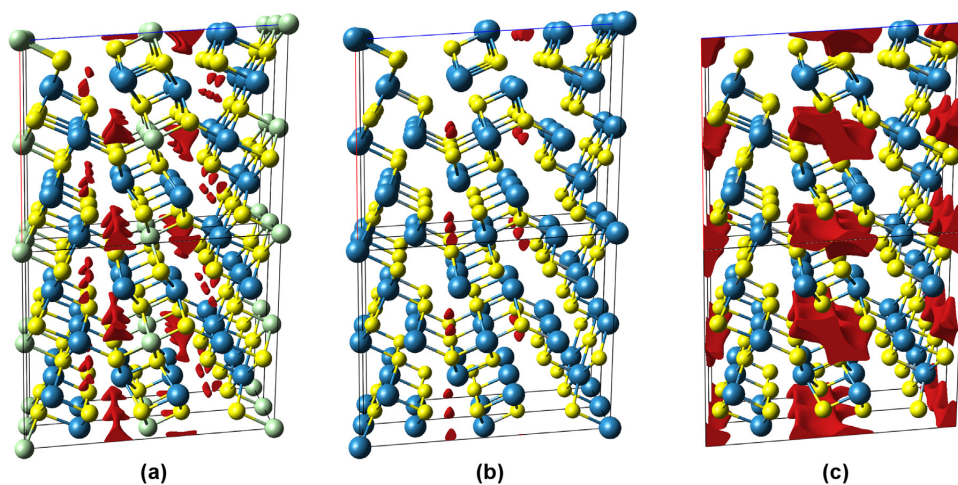


**Fig. 3.** Details of  $\text{LiBi}_3\text{S}_5$  framework models with void surfaces at 0.0045 a.u. (blue: bismuth ions, green: lithium ions, yellow: sulfide ions, red: void surfaces; ions with arbitrary radii, unit cell in black, view approximately along  $b$ ). (a) Stoichiometric model, (b) all-bismuth model, (c) defective model. (For interpretation of the references to color in this figure legend, the reader is referred to the web version of this article.)

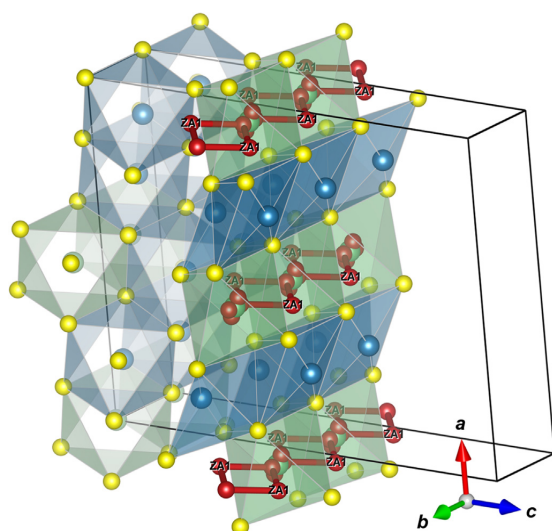


**Fig. 4.** Detail of ordered model of  $\text{LiBi}_3\text{S}_5$  with migration channel (blue: bismuth ions, green: lithium ions, yellow: sulfide ions, red: elementary voids and channels; ions with arbitrary radii, unit cell in black; for interpretation of the references to color in this figure legend, the reader is referred to the web version of this article).

rigid-lattice line width, *i.e.*, the width at sufficiently low  $T$ ) [34]. Here, we obtain jump rates in the order of  $\tau_{\text{MN}}^{-1} \approx 2 \times 10^4 \text{ s}^{-1}$ . Such a value points to slow ion diffusion in channel-structured  $\text{LiBi}_3\text{S}_5$ .

As can be seen in Fig. 5b, a shallow quadrupole powder-pattern (two humps next to the central line, each one marked by a circle) shows up at sufficiently low temperature. The humps represent the  $90^\circ$  singularities of the powder pattern. The spectral separation of  $\Delta\nu_q \approx 50 \text{ kHz}$  points to a mean quadrupole coupling constant in the order of 100 kHz. Besides magnetic dipolar interactions, also electric quadrupolar interactions are expected to be influenced by rapid lithium diffusion [35]. Indeed, the quadrupole intensities vanish at  $T \geq 613 \text{ K}$ , meaning that, at this temperature,  $\tau^{-1}$  is expected to exceed  $\Delta\nu_q$  by many times.

### 3.5. Diffusion-induced relaxation rates

In order to quantify lithium diffusion in terms of activation energies,  $^7\text{Li}$  SLR NMR measurements were performed in both the laboratory and rotating frame of reference, *i.e.*, at frequencies of  $\omega_0/2\pi = 116.4 \text{ MHz}$  and  $20 \text{ kHz}$  [36–39]. The corresponding rates  $R_1$  and  $R_{1\rho}$  were obtained by parameterizing the resulting magnetization transients,  $M_z(t_d)$  and  $M_\rho(t_{\text{lock}})$ , by means of stretched exponentials of the form  $M_z(t_d) \propto 1 - \exp[-(t_d/T_1)^\gamma]$  and  $M_\rho(t_{\text{lock}}) \propto \exp[-(t_{\text{lock}}/T_{1\rho})^\gamma]$ . As an example, the stretching exponent  $\gamma$  varies only slightly with temperature (0.57–0.71). In Fig. S2, some selected  $R_{1\rho}$  transients are shown to illustrate the quality of the curves recorded at a locking frequency of 20 kHz. Depending on temperature and stretching, most of the transients could be monitored over a dynamic range of two to three orders of magnitude.

In Fig. 6, the rates  $R_1$  and  $R_{1\rho}$  vs. the inverse temperature are shown as an Arrhenius plot. By increasing the temperature  $T$ , the rates pass over into the so-called low- $T$  flank of a diffusion-induced peak. Because of slow lithium-ion diffusion, the high- $T$  flank cannot be accessed below 600 K. While the latter flank would entail information on long-range diffusion, the low- $T$  flank is affected by local, within-site ion dynamics, which can additionally be influenced by correlation effects such as Coulomb interactions and structural disorder [40]. Below *ca.* 400 K, a non-diffusive background is observed, as indicated by the dotted line in Fig. 6. Most likely, it is caused by coupling of the lithium spins with conduction electrons, lattice vibrations, or by paramagnetic impurities. For  $R_{1\rho}$ , the same two regions can be seen. Noticeably, almost temperature-independent background relaxation of spin-lock NMR shows up below 250 K. Between temperatures of 250 and 400 K, a slight increase of  $R_{1\rho}$  is observed that is, however, absent in  $R_1$ .

The solid lines in Fig. 6 represent Arrhenius fits. The range of data points used for the fitting procedure is marked by the arrows drawn. While in the case of  $R_1$  the activation energy turned out to be  $E_a = 0.43(2) \text{ eV}$ , a value of  $E_a = 0.66(2) \text{ eV}$  is obtained for  $R_{1\rho}$ . As mentioned above, the rates  $R_{1\rho}$  are more sensitive to long-range lithium-ion motions rather than to short-range ion dynamics. The discrepancy seen in  $E_a$  hints at correlated ion dynamics and multiple-jump pathways the ions have access to.

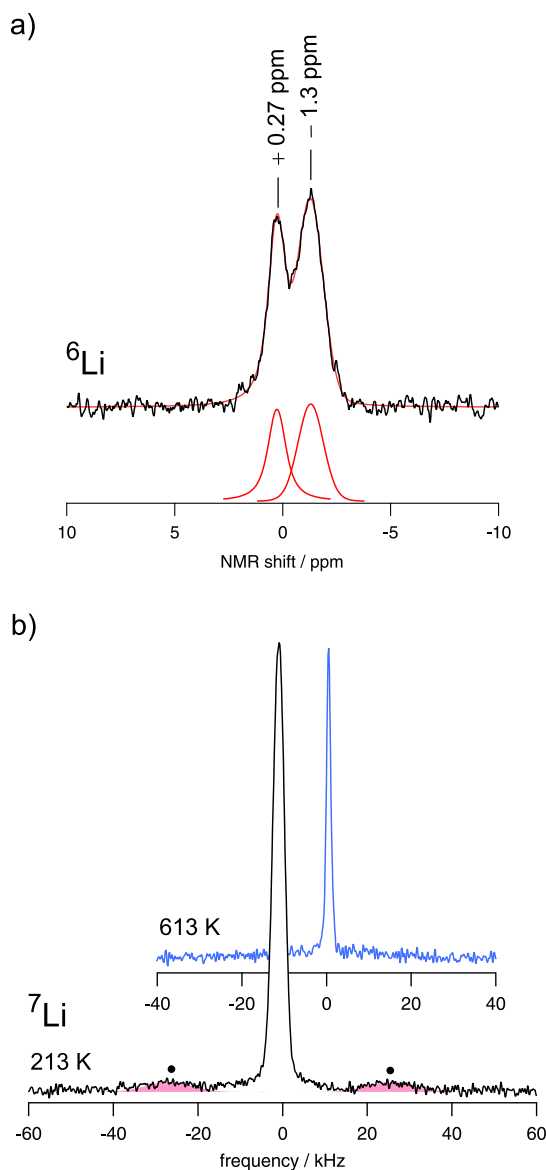


**Fig. 5.** (a)  ${}^6\text{Li}$  MAS spectrum of  $\text{LiBi}_3\text{S}_5$  recorded with a single-pulse experiment. The  $90^\circ$  pulse length was  $3.33\ \mu\text{s}$ . The rotation frequency was set to 30 kHz. The lithium signal is referenced to aqueous  $\text{LiCl}$  ( $c=1\ \text{mol}\cdot\text{L}^{-1}$ ). (b) Static  ${}^7\text{Li}$  NMR spectra of  $\text{LiBi}_3\text{S}_5$  recorded at 213 K and 613 K. The black circles mark the  $90^\circ$  singularities of the quadrupole powder pattern.

Compared to investigations of other lithium-containing sulfides (see, e.g., refs. [11,41]), the  ${}^7\text{Li}$  NMR measurements identified  $\text{LiBi}_3\text{S}_5$  as a poor lithium-ion conductor. The activation energy of 0.66 eV is two to three times larger than the ones usually found for sulfides exhibiting extremely fast ion exchange (0.2–0.3 eV) [40,42]. Slow ion dynamics also manifests in rather low  $R_1$  rates measured near ambient temperature: rates in the order of  $0.025\ \text{s}^{-1}$  in combination with the temperature independence seen in this  $T$  range clearly indicate slow lithium-ion diffusivity. Of course, the absolute value depends on the number density of

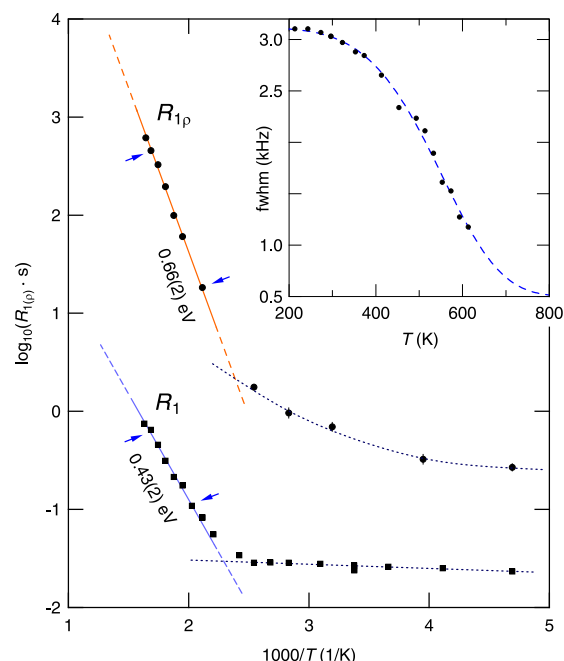


**Fig. 6.** Arrhenius plot of the  ${}^7\text{Li}$  NMR SLR rates of  $\text{LiBi}_3\text{S}_5$  recorded in both the laboratory frame ( $R_1$ , ■) and in the rotating frame of reference ( $R_{1p}$ , ●). Data were measured at  $\omega_0/2\pi=116.4\ \text{MHz}$ . The locking frequency was  $\omega_1/2\pi=20\ \text{kHz}$ . Inset:  ${}^7\text{Li}$  NMR line width (fwhm) as a function of temperature  $T$ . The dashed blue line is drawn to guide the eye. See text for further explanation. (For interpretation of the references to color in this figure legend, the reader is referred to the web version of this article.)

paramagnetic impurities of the sample, which, in our case, seems to be rather low.

The very slow ion dynamics can be understood in terms of spatially restricted lithium diffusion. As already suggested above,  $\text{LiBi}_3\text{S}_5$  proved to conduct lithium-ion along the  $b$  direction. Any blockade of these by immobile bismuth ions, as verified to be present by neutron diffraction, greatly slows down lithium self-diffusivity in the material. Such a decrease is expected for 1D ion conductors, which are prone to clogging [43]. Even in the case of accessible channels, highly correlated motion is anticipated for materials only offering spatially restricted 1D pathways, i.e., single-file diffusion in narrow channels.

#### 4. Conclusions

We have successfully synthesized grey-black  $\text{LiBi}_3\text{S}_5$  as pure-phase material using a solid-state reaction. The ternary sulfide crystallizes in a variant of the known  $\text{AgBi}_3\text{S}_5$  type with a highly disordered cation sublattice. A closer look at the coordination polyhedra in this quite complex material offers explanations, why some positions are preferred by one or the other type of cation.

Topological methods based on the Rietveld-refined model suggest that  $\text{LiBi}_3\text{S}_5$  is indeed a 1D lithium-ion conductor. Defects in the cation lattice can be formed by displacement of lithium ions into tetrahedral voids. Migration can only occur along channels in the  $b$  direction that are situated in the transition zone between the slabs and comprise the positions  $\text{Bi}5/\text{Li}5$ . The curved migration pathway traverses a tetrahedral void and is blocked in the presence of a bismuth ion. As seen *via* NMR, spatial restriction results

in low lithium-ion diffusivity. Motional processes occurring on long-range as well as short-range scales were probed through  $^7\text{Li}$  NMR relaxometry. In particular, activation energies as high as 0.66 (2) eV were extracted from spin-lock NMR. This finding is in line with results from NMR motional line narrowing hinting at a lithium jump-rate in the order of  $ca. 2 \times 10^4 \text{ s}^{-1}$  at 500 K. Such values clearly identify  $\text{LiBi}_3\text{S}_5$  as a moderate, if not poor ionic conductor. These findings are in line with studies on the channel-structured quaternary sulfide  $\text{LiPbSb}_3\text{S}_6$ , in which cation disorder accounts for low thermal diffusivity and conductivity [44].

In general, synthesis starting from  $\text{LiBiS}_2$  and  $\text{Bi}_2\text{S}_3$  can be considered a promising route to new lithium bismuth sulfides with structure types known from the pavonite homologous series.

### Acknowledgments

The authors would like to thank Dr. Rafał Zubrzycki and Dipl.-Chem. Steven Orthmann (Technische Universität Berlin) for performing XRF and oxygen analyses, respectively. M.W. would like to thank Oliver Steiner and Dr. Walter Gössler for the metal determination as well as the Austrian Federal Ministry of Economy, Family and Youth, and the Austrian National Foundation for Research, Technology and Development for financial support.

This work is based upon experiments performed at the SPODI instrument [13] operated by FRM II at the Heinz Maier-Leibnitz Zentrum (MLZ), Garching b. München, Germany. Financial support by the Deutsche Forschungsgemeinschaft (FOR 1277: “Mobilität von Lithiumionen in Festkörpern [molife]”) is gratefully acknowledged.

### Appendix A. Supporting information

Supplementary data associated with this article can be found in the online version at <https://dx.doi.org/10.1016/j.jssc.2016.03.010>.

### References

- [1] D.M. Rowe (Ed.), *Thermoelectrics Handbook: Macro to Nano*, CRC Press, Boca Raton, USA, 2006.
- [2] (a) M.J. Smith, R.J. Knight, C.W. Spencer, *J. Appl. Phys.* **33** (1962) 2186–2190; (b) L.R. Testardi, J.N. Bierly Jr., F.J. Donahoe, *J. Phys. Chem. Solids* **23** (1962) 1209–1217; (c) C.H. Champness, P.T. Chiang, P. Parekh, *Can. J. Phys.* **43** (1965) 653–659; (d) W.M. Yim, E.V. Fitzke, *J. Electrochem. Soc.* **115** (1968) 556–560.
- [3] (a) M.G. Kanatzidis, *Semicond. Semimet.* **69** (2001) 51–100; (b) D.-Y. Chung, L. Iordanidis, K.-S. Choi, M.G. Kanatzidis, *Bull. Korean Chem. Soc.* **19** (1998) 1283–1293; (c) M.G. Kanatzidis, S.D. Mahanti, T.P. Hogan, *Chemistry, Physics and Materials Science of Thermoelectric Materials: Beyond Bismuth Telluride*, Kluwer Academic/Plenum Publishers, New York, USA 2003, p. 35; (d) A. Mrotzek, M.G. Kanatzidis, *Acc. Chem. Res.* **36** (2003) 111–119.
- [4] D.-Y. Chung, K.-S. Choi, L. Iordanidis, J.L. Schindler, P.W. Brazis, C.R. Kannewurf, B. Chen, S. Hu, C. Uher, M.G. Kanatzidis, *Chem. Mater.* **9** (1997) 3060–3071.
- [5] L. Iordanidis, P.W. Brazis, T. Kyratsi, J. Ireland, M. Lane, C.R. Kannewurf, W. Chen, J.S. Dyck, C. Uher, N.A. Ghelani, T. Hogan, M.G. Kanatzidis, *Chem. Mater.* **13** (2001) 622–633.
- [6] D.-Y. Chung, T. Hogan, P.W. Brazis, C.R. Kannewurf, M. Bastea, C. Uher, M. G. Kanatzidis, *Science* **287** (2000) 1024–1027.
- [7] T.J. McCarthy, S.-P. Ngeyi, J.-H. Liao, D. DeGroot, T. Hogan, C.R. Kannewurf, M. G. Kanatzidis, *Chem. Mater.* **5** (1993) 331–340.
- [8] L. Iordanidis, D. Bilc, S.D. Mahanti, M.G. Kanatzidis, *J. Am. Chem. Soc.* **125** (2003) 13741–13752.
- [9] T.J. McCarthy, T.A. Tanzer, M.G. Kanatzidis, *J. Am. Chem. Soc.* **117** (1995) 1294–1301.
- [10] K. Chondroudis, M.G. Kanatzidis, *J. Solid State Chem.* **136** (1998) 328–332.
- [11] V.B. Lazarev, S.I. Berul', A.F. Trippel', *Russ. J. Inorg. Chem.* **22** (1977) 1218–1220.
- [12] V. Epp, O. Gün, H.-J. Deiseroth, M. Wilkening, *J. Phys. Chem. Lett.* **4** (2013) 2118–2123.
- [13] M. Hoelzel, A. Senyshyn, O. Dolotko, *J. Large-Scale Res. Facil* **1** (2015) A5, <http://dx.doi.org/10.17815/jlsrf-1-24>.
- [14] M. Hoelzel, A. Senyshyn, N. Juenke, H. Boysen, W. Schmah, H. Fuess, *Nucl. Instrum. Methods Phys. Res. Sect. A* **667** (2012) 32–37.
- [15] E. Makovicky, W.G. Mumme, J.A. Watts, *Can. Miner.* **15** (1977) 339–348.
- [16] G. Bergerhoff, I.D. Brown, *Inorganic crystal structure database*, in: F.H. Allen, G. Bergerhoff, R. Sievers (Eds.), *Crystallographic Databases, International Union of Crystallography*, Chester, UK, 1987, pp. 77–95.
- [17] J. Rodríguez-Carvajal, *Phys. B: Condens. Matter* **192** (1993) 55–69.
- [18] J.-F. Béjar, G. Baldinozzi, *J. Appl. Crystallogr.* **26** (1993) 128–129.
- [19] K. Brandenburg, H. Putz, *Diamond 3.2 – Crystal and Molecular Structure Visualization, Crystal Impact*, Bonn, Germany, 2014.
- [20] S.K. Wolff, D.J. Grimwood, J.J. McKinnon, M.J. Turner, D. Jayatilaka, M.A. Spackman, *CrystalExplorer 3.1 – Crystal Structure Analysis with Hirshfeld Surfaces*, University of Western Australia, Perth, Australia, 2012.
- [21] V.A. Blatov, A.P. Shevchenko, D.M. Proserpio, *Cryst. Growth Des.* **14** (2014) 3576–3586.
- [22] As the spherical-domain radius for lithium ions in sulfides has not yet been established, it was estimated enlarging the value for oxides ( $R_{\text{sd}}=138 \text{ pm}$ ) by 20 pm, an average difference for other cations known in both environments; V.A. Blatov, *Crystallogr. Rev.* **10**, 2004, 249–318.
- [23] R.D. Shannon, *Acta Crystallogr. Sect. A: Cryst. Phys. Diffr. Theor. Gen. Crystallogr.* **32** (1976) 751–767.
- [24] V.A. Blatov, G.D. Ilyushin, O.A. Blatova, N.A. Anurova, A.K. Ivanov-Schits, L. N. Dem'yanets, *Acta Crystallogr. Sect. B: Struct. Sci.* **62** (2006) 1010–1018.
- [25] H. Zabrodsky, S. Peleg, D. Avnir, *J. Am. Chem. Soc.* **114** (1992) 7843–7851.
- [26] O. Glemser, M. Filcek, *Z. Anorg. Allg. Chem.* **279** (1955) 321–323.
- [27] C. Long, H. Fan, M. Li, *Dalton Trans.* **42** (2013) 3561–3570.
- [28] B. Hamdi, H.E. Feki, J.-M. Savariault, A.B. Salah, *Mater. Res. Bull.* **42** (2007) 299–311.
- [29] A. Zayit, M. Pinsky, H. Elgavi, C. Dryzun, D. Avnir, *Chirality* **23** (2011) 17–23.
- [30] D. Wiedemann, M.M. Islam, S. Nakhil, A. Senyshyn, T. Bredow, M. Lerch, *J. Phys. Chem. C* **119** (2015) 11370–11381.
- [31] D. Wiedemann, S. Nakhil, J. Rahn, E. Witt, M.M. Islam, S. Zander, P. Heitjans, H. Schmidt, T. Bredow, M. Wilkening, M. Lerch, *Chem. Mater.* **28** (2016) 915–924.
- [32] M.Ø. Filso, M.J. Turner, G.V. Gibbs, S. Adams, M.A. Spackman, B.B. Iversen, *Chem. Eur. J.* **19** (2013) 15535–15544.
- [33] M. Wilkening, V. Epp, A. Feldhoff, P. Heitjans, *J. Phys. Chem. C* **112** (2008) 9291–9300.
- [34] M. Wilkening, A. Kuhn, P. Heitjans, *Phys. Rev. B* **78** (2008) 054303.
- [35] A. Kuhn, S. Narayanan, L. Spencer, G. Goward, V. Thangadurai, M. Wilkening, *Phys. Rev. B* **83** (2011) 094302.
- [36] D. Ailion, C. Slichter, *Phys. Rev. Lett.* **12** (1964) 168–171.
- [37] C. Slichter, D. Ailion, *Phys. Rev. A* **135** (1964) 1099–1110.
- [38] D. Wolf, *Phys. Rev. B* **10** (1974) 2724–2732.
- [39] W. Schmidt, P. Bottke, M. Sternad, P. Gollub, V. Hennige, M. Wilkening, *Chem. Mater.* **27** (2015) 1740–1750.
- [40] M. Wilkening, P. Heitjans, *Chem. Phys. Chem.* **13** (2012) 53–65.
- [41] B. Stanje, V. Epp, S. Nakhil, M. Lerch, M. Wilkening, *ACS Appl. Mater. Interfaces* **7** (2015) 4089–4099.
- [42] D. Wohlmuth, V. Epp, M. Wilkening, *ChemPhysChem* **16** (2015) 2582–2593.
- [43] V. Epp, M. Wilkening, *Phys. Rev. B* **82** (2010) 020301.
- [44] E.C. Agha, C.D. Malliakas, J. Im, H. Jin, L.-D. Zhao, A.J. Freeman, M.G. Kanatzidis, *Inorg. Chem.* **53** (2014) 673–675.

### **3.1.2 Two-dimensional Li diffusion of 2H-Li<sub>x</sub>NbS<sub>2</sub>**

#### **Li ion dynamics along the inner surfaces of layer-structured 2H-Li<sub>x</sub>NbS<sub>2</sub>**

Bernhard Stanje, Viktor Epp, Suliman Nakhil, Martin Lerch and Martin Wilkening. *ACS Applied Materials and Interfaces*, DOI: 10.1021/am5078655 (2015), 4089 - 4099



# Li Ion Dynamics along the Inner Surfaces of Layer-Structured 2H-Li<sub>x</sub>NbS<sub>2</sub>

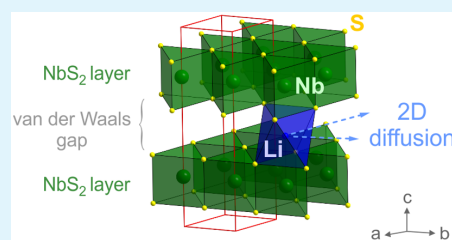
B. Stanje,<sup>\*,†</sup> V. Epp,<sup>†</sup> S. Nakhal,<sup>‡</sup> M. Lerch,<sup>‡</sup> and M. Wilkening<sup>†</sup>

<sup>†</sup>Christian Doppler Laboratory for Lithium Batteries, and Institute for Chemistry and Technology of Materials (Member of NAWI Graz), Graz University of Technology, Stremayrgasse 9, A-8010 Graz, Austria

<sup>‡</sup>Technische Universität Berlin, Institut für Chemie, Straße des 17. Juni 135, D-10623 Berlin, Germany

**ABSTRACT:** Layer-structured materials, such as graphite (LiC<sub>6</sub>) or Li<sub>x</sub>(Co,Ni,Mn)O<sub>2</sub>, are important electrode materials in current battery research that still relies on insertion materials. This is due to their excellent ability to reversibly accommodate small alkali ions such as Li<sup>+</sup> and Na<sup>+</sup>. Despite of these applications, microscopic information on Li ion self-diffusion in transition metal sulfides are relatively rare. Here, we used <sup>7</sup>Li nuclear magnetic resonance (NMR) spectroscopy to study translational Li ion diffusion in hexagonal (2H) Li<sub>x</sub>NbS<sub>2</sub> ( $x = 0.3, 0.7, \text{ and } 1$ ) by means of variable-temperature NMR relaxometry. <sup>7</sup>Li spin–lattice relaxation rates and <sup>7</sup>Li NMR spectra were used to determine Li jump rates and activation barriers as a function of Li content. Hereby, NMR spin–lattice relaxation rates recorded with the spin-lock technique offered the possibility to study Li ion dynamics on both the short-range and long-range length scale. Information was extracted from complete diffusion-induced rate peaks that are obtained when the relaxation rate is plotted vs inverse temperature. The peak maximum of the three samples studied shifts toward higher temperatures with increasing Li content  $x$  in 2H-Li<sub>x</sub>NbS<sub>2</sub>. Information on the dimensionality of the diffusion process was experimentally obtained by frequency dependent  $R_p$  measurements carried out at  $T = 444$  K, that is in the high-temperature regime of the rate peaks. A slight, but measurable frequency-dependence within this limit is found for all samples; it is in good agreement with predictions from relaxation models developed to approximate low-dimensional (2D) jump diffusion.

**KEYWORDS:** NMR, relaxation, dimensionality, insertion materials, jump diffusion



## 1. INTRODUCTION

The principle of lithium-ion<sup>1,2</sup> (or sodium-ion) batteries that use insertion compounds as electrode materials is based on the highly reversible accommodation of the ionic charge carriers. In the case of layered transition metal dichalcogenides (TMDs), titanium disulfide, TiS<sub>2</sub>, belongs to one of the first anode materials whose topotactic reaction with lithium has been studied in detail. Still TMDs play an important role in battery technology;<sup>2,3</sup> in general, their chemical versatility as compared to graphene makes them fundamentally and technologically intriguing.<sup>4–6</sup> It has been shown that besides the composition and positioning of atoms in such materials, understanding the low dimensional diffusion processes, also in terms of jump rates and hopping barriers, is key to developing new electrode materials and those with tunable electronic properties.<sup>7,8</sup>

Recently, Goodenough and co-workers reinvestigated the electrochemical insertion behavior and battery performance of the intercalation hosts 2H-NbS<sub>2</sub> and 3R-NbS<sub>2</sub> and showed the usability of niobium disulfide as potential cathode material in secondary Li-ion batteries.<sup>9,10</sup> While usually the electrochemical properties of potential candidates are extensively evaluated, only few experimental studies take up the challenge to describe the underlying Li diffusion mechanisms in detail from an atomic scale point of view. Here, Li<sub>x</sub>NbS<sub>2</sub> served as a low-dimensional model system for a comprehensive <sup>7</sup>Li NMR

relaxation study to gain insight into the Li ion dynamics between the van der Waals gap of the NbS<sub>2</sub> sheets. In particular, activation energies ( $E_a$ ) and Li correlation times ( $\tau_c$ ) have been determined. Besides NMR, also neutron scattering can be used to evaluate ion dynamics and diffusion pathways. In contrast to neutron scattering that, which is sensitive to ion dynamics with residence times on the ps time scale, NMR, however, is able to probe much slower ion dynamics. Using the appropriate NMR relaxation method, ion dynamics near ambient conditions can be probed as it is done here.

There are two different polytype hexagonal structures for niobium disulfide with different stacking order of the NbS<sub>6</sub> prisms known.<sup>11–13</sup> The first, 2H-NbS<sub>2</sub>, is composed of two NbS<sub>2</sub> layers per unit cell (space group:  $P6_3/mmc$ ) whereas the second one, 3R-NbS<sub>2</sub>, consists of three layers per unit cell (space group:  $R3m$ ) as shown in Figure 1.

Whereas the 2D Li self-diffusion process of the 3R modification was already studied by our group recently,<sup>14</sup> almost no NMR data could be found for the 2H modification. Here, we focused on the 2H polymorph and took advantage of variable-temperature <sup>7</sup>Li NMR relaxation measurements and

Received: November 17, 2014

Accepted: January 29, 2015

Published: January 29, 2015

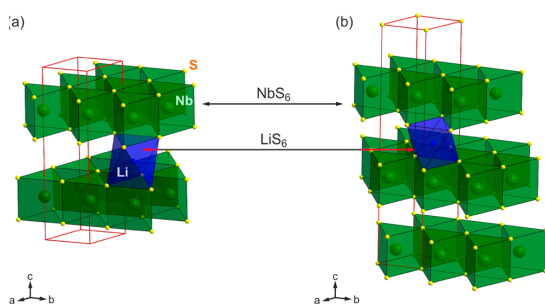


**Figure 1.** Crystal structures of (a) 2H-NbS<sub>2</sub> and (b) 3R-NbS<sub>2</sub> with LiS<sub>6</sub> octahedral sites (blue) and NbS<sub>6</sub> trigonal prismatic sites (green).<sup>12,13</sup>

line shape studies to collect information on ion dynamics of three fully homogenized samples with different Li contents, namely, 2H-Li<sub>x</sub>NbS<sub>2</sub> with  $x = 0.3, 0.7, \text{ and } 1$ . Spin-lattice relaxation measurements in both the laboratory ( $R_1$ ) and rotating frame of reference ( $R_\rho$ ) were carried out as a function of temperature to investigate short-range as well as long-range Li ion dynamics.<sup>15</sup> While the first are sensitive to ion hopping on the Ångström length scale, the latter is comparable to that usually probed via conductivity spectroscopy in the low frequency limit.<sup>16</sup> In particular, even if powder samples are used in NMR relaxometry, the method allows to deduce information on the dimensionality of the relevant diffusion process via frequency-dependent measurements.<sup>17–24</sup>

In the present study, we were able to precisely correlate the Li self-diffusion parameters with the change of the Li content  $x$  and the lattice parameters of the samples studied. We used chemically lithiated samples in order to avoid the influence of binders, conductive additives and the formation of passivation layers if Li insertion is carried out electrochemically. Additives usually needed to prepare electrodes might also influence the diffusion properties; regarding a similar study on Li<sub>4</sub>Ti<sub>5</sub>O<sub>12</sub> we do not expect significant differences for bulk properties.<sup>25</sup> This is, however, beyond the scope of the present study. Fortunately, since complete diffusion-induced relaxation rate peaks in the rotating frame of reference were accessible, we reached the so-called high-temperature flank of the corresponding rate peaks containing information on the dimensionality of the diffusion

process.<sup>23,26</sup> The results were compared with predictions of NMR relaxation models developed for low-dimensional diffusion.<sup>27</sup>

## 2. EXPERIMENT

2H-NbS<sub>2</sub> was prepared by direct synthesis from the elements in an evacuated silica ampule. The ampule was heated at 400 °C for 10 days to achieve complete reaction of the elemental sulfur, afterward it was kept at 700 °C for 7 days. Chemical lithiation of 2H-NbS<sub>2</sub> was carried out by stirring the powder in a 2.5 M solution of *n*-butyllithium in hexane at room temperature for 7 days under dry nitrogen atmosphere. Subsequently, the samples were heated at 400 °C for homogenization, that is, Li ion distribution, in sealed quartz ampules for 1 week. Due to their air-sensitivity they were fire-sealed under vacuum in DURAN glass ampules (~4 cm in length and 0.5 cm in diameter) to permanently exclude moisture and air. The ampules were placed inside the NMR probe.

Prior to our NMR measurements the powders were chemically characterized by combustion analysis (Thermo Finnigan FlashEA 1112 NC analyzer) for hydrogen content. The amount of oxygen was determined using a LECO EF-TC 300 N<sub>2</sub>/O<sub>2</sub> analyzer according to the hot gas extraction method. In addition, X-ray fluorescence analysis (PANalytical Axios PW4400/24 X-ray fluorescence spectrometer with an Rh-tube and wavelength dispersive detection) was used to check the niobium metal and sulfur content, respectively.

A PANalytical X'Pert PRO MPD diffractometer (Cu K<sub>α</sub> radiation, Bragg-Brentano ( $\theta$ - $\theta$ ) geometry) with a PIXcel detector was used for the powder XRD measurements. The program package FULL PROF 2006 was used for structural refinements.<sup>28</sup> The reflection profiles were fitted with a pseudoVoigt function.

<sup>7</sup>Li NMR measurements were performed using a Bruker Avance III spectrometer connected to a shimmed cryo-magnet  $B_0 = 7.04$  T with a nominal <sup>7</sup>Li resonance frequency of  $\omega_0/2\pi = 116.4$  MHz. A ceramic high-temperature NMR probe (Bruker BioSpin) was used that allows  $\pi/2$  pulse lengths of about 6 to 7.5  $\mu$ s at 200 W. The temperatures, adjusted via a Eurotherm controller and a stream of N<sub>2</sub> gas, ranged from 223 to 573 K.

Variable-temperature <sup>7</sup>Li NMR spectra and <sup>7</sup>Li spin-lattice relaxation NMR rates ( $1/T_1 = R_1$ ) in the laboratory frame of reference were acquired under static, i.e., nonrotating conditions.  $R_1$  rates were recorded with the saturation recovery pulse sequence ( $10 \times \pi/2 - t_d - \pi/2$ -acquisition (acq.)).<sup>29</sup> The initial sequence of ten  $\pi/2$  pulses was used to destroy any longitudinal magnetization  $M_z$ . Then, the recovery of  $M_z(t_d)$  was recorded after the final  $\pi/2$  pulse as a function of the delay time  $t_d$ . While Li diffusion is expected to govern longitudinal recovery in Li<sub>x</sub>NbS<sub>2</sub> at sufficiently high temperatures,

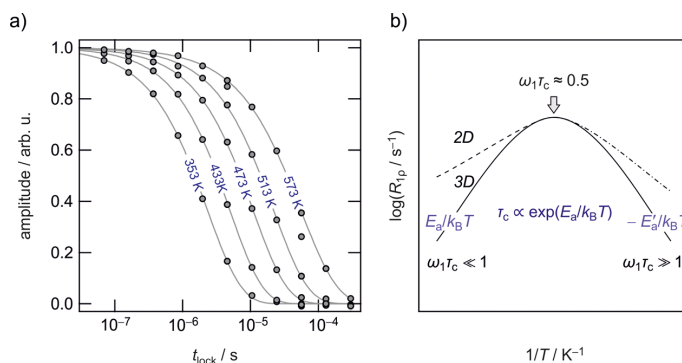


**Figure 2.** (a) <sup>7</sup>Li transversal decay of the spin-locked magnetization  $M_\rho(t_{\text{lock}})$  recorded at the temperatures indicated ( $\omega_1/2\pi = 20$  kHz). The solid lines represent fits according to stretched exponentials yielding the parameters  $R_{1\rho}$  and  $\gamma'$ ; note that the  $x$ -axis is scaled logarithmically. (b) Schematic representation of the diffusion induced NMR  $R_{1\rho}$  rate peaks.

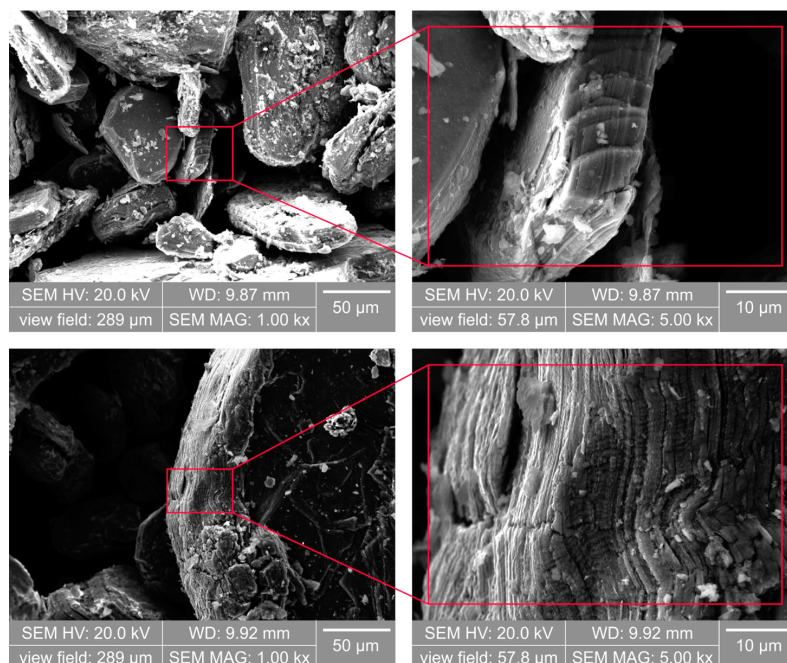


**Figure 3.** SEM images of powdered 2H-Li<sub>x</sub>NbS<sub>2</sub> (after Li insertion,  $x = 0.7$ ). Red squares indicate a zoom into the rectangular area marked on the left.

nondiffusive recovery because of lattice vibrations or coupling to conduction electrons will influence the  $R_1$  rates at lower temperatures.

<sup>7</sup>Li spin-lattice relaxation NMR rates in the rotating frame of reference ( $1/T_{1\rho} = R_{1\rho}$ ) were recorded by using the spin-locking technique ( $\pi/2_{x'} - \text{spin locking pulse } (t_{\text{lock}}) - \text{acq.}$ ) at an angular locking frequency  $\omega_1/2\pi$  of  $\sim 20$  kHz.<sup>29–32</sup> This technique is sensitive to much slower Li diffusion processes compared to  $R_1$  NMR measurements in the lab frame. First, the equilibrium magnetization  $M_z$  is flipped onto the  $y'$  axis by applying a  $\pi/2_{y'}$  pulse along the  $x'$  axis. The pulse is followed by a  $90^\circ$  phase-shifted locking pulse being in parallel to the resulting magnetization vector  $M_{y'}$ . The corresponding magnetic  $B_1$  field formerly replaces the external one  $B_0$  and represents a new reference point for spin relaxation. The initial, transversal magnetization has to adapt itself to the much smaller  $B_1$  field. Accordingly, a transversal decay of the amplitude of the  $M_{y'}$  vector can be observed. After switching off the locking pulse,  $M_{y'}$  ( $= M_\rho$ ) is measured as a function of the duration of the spin-lock  $t_{\text{lock}}$  pulse by recording the resulting FID. The longer the locking pulse, the smaller the amplitude of the  $M_{y'}$  vector. Here, the  $R_\rho$  rates  $R_{1\rho}$  at the given locking frequency were obtained from the transversal transients recorded by varying the duration of  $t_{\text{lock}}$  from 30  $\mu\text{s}$  to 300 ms. The recycle delay for  $R_\rho$  measurements was at least 5 times  $T_1$ .  $R_1$  and  $R_{1\rho}$  were obtained by parametrizing the resulting magnetic transients  $M_z(t_d)$  and  $M_\rho(t_{\text{lock}})$ , respectively, by stretched exponentials of the form  $M_z(t_d) \propto 1 - \exp[-(t_d/T_1)^\gamma]$  and  $M_\rho(t_{\text{lock}}) \propto \exp[-(t_{\text{lock}}/T_{1\rho})^{\gamma'}]$  with the stretching exponents,  $\gamma$  and  $\gamma'$ , ranging from 0.7 to 1.0, respectively (cf. Figure 2a) for some selected  $R_{1\rho}$  transients).

### 3. BASICS OF NMR RELAXOMETRY

Fortunately, via the temperature-variable NMR SLR measurements described above we were able to record so-called diffusion-induced rate peaks from which activation energies and jump rates can be deduced. In addition, frequency-dependent NMR  $R_\rho$  rates were recorded at fixed temperature (444 K) on the high- $T$  flank of the diffusion-induced rate peaks (see Figure

2b). In this  $T$  range the condition  $\omega_1\tau_c \ll 1$  approximately holds. The locking frequency  $\omega_1/2\pi$  was varied in from 5 to 20 kHz. While the peak maximum, for which the relation  $\omega_1\tau_c \approx 0.5$  holds, can be used to extract the correlation time  $\tau_c$  if  $\omega_1/2\pi$  is known, the flanks yield the activation energies  $E_a$  and  $E'_a$ . Here,  $E'_a$  is usually influenced by correlation effects whereas  $E_a$ , if directly extracted from the slope of the flank, can be identified with the long-range activation energy provided a 3D diffusion process is given.<sup>23,33–35</sup> For 1D and 2D diffusion a relaxation model has to be used to deduce  $E_a$  from the relaxation peak.<sup>27,30–32</sup>

In Figure 2b, a diffusion induced rate peak is plotted against the inverse temperature indicating the maximum condition (indicated by an arrow) as well as the low-temperature and high-temperature limits. Only for uncorrelated, 3D isotropic diffusion  $E'_a = E_a$  applies yielding a fully symmetric rate peak.<sup>36</sup> If correlation effects influence short-range ion hopping (see the dashed-dotted line),  $E'_a$  becomes smaller than  $E_a$ , both values are linked via  $E'_a{}^{3D} = E_a{}^{3D} \times (\beta - 1)$  while  $\beta$  ( $1 < \beta \leq 2$ ) denotes the frequency dependence of  $R_1$  in the low- $T$  limit. The parameter  $\beta$ , which has been introduced by Küchler et al.,<sup>37</sup> describes any asymmetry of the rate peak  $R_{1\rho}$  caused by correlation effects in the low- $T$  limit. Simultaneously, it is also a measure of the asymmetry of the rate peaks.<sup>23</sup> The activation energy  $E_a{}^{2D,\text{slope}}$ , which can be obtained from the slope of the rate in the limit  $\omega_1\tau_c \gg 1$  (see dashed line), is linked with  $E_a{}^{2D}$  via  $E_a{}^{2D,\text{slope}} = 0.75 \times E_a{}^{2D}$ , provided  $\beta$  equals 2.<sup>38</sup>

## 4. RESULTS AND DISCUSSION

### 4.1. Crystal Structure and Morphology of 2H-Li<sub>x</sub>NbS<sub>2</sub>

Before we present the results on spin-lattice relaxation NMR we would like to draw the reader's attention to the crystal

structure and morphology of the  $\text{Li}_x\text{NbS}_2$  samples studied and to the results from temperature-variable line shape measurements. NMR motional line narrowing (MN) gives first insights into how fast the ions are exchanged via self-diffusion among the crystallographic sites occupied.

In 2H- $\text{NbS}_2$  the niobium atoms occupy trigonal prismatic voids formed by the sulfur anions; each  $\text{NbS}_2$  site shares edges with six nearest  $\text{NbS}_2$  neighbors. In this structure lithium ions can be intercalated into the empty octahedral voids located in the van der Waals gap between the  $\text{NbS}_2$  sheets. Li-centered octahedra stack along the  $c$  axis and alternate with layers of  $\text{NbS}_2$ . In the 2H polymorph each  $\text{LiS}_6$  octahedra shares two common faces with an  $\text{NbS}_6$  prism. This is different for the 3R form where the Li ions are located between an  $\text{NbS}_6$  prism and an empty prism. Because of this difference, distinct diffusion pathways for the Li ions might be expected.

**Morphology as Seen via SEM.** The morphology and particle size of 2H- $\text{Li}_x\text{NbS}_2$  is presented in Figure 3 showing SEM images of the intercalated sample with  $x = 0.7$ . Large particles with a plate-like texture and a mean diameter of ca.  $13 \mu\text{m}$  were found. In contrast to the synthesis starting from  $\text{Li}_2\text{S}$ , elemental niobium and Sulfur as reported by Goodenough and co-workers, chemical intercalation of Li ions in  $\text{NbS}_2$  with *n*-butyllithium, as it is done here, results in no bouquet-like agglomerates of the primary particles as was observed recently.<sup>10</sup> The SEM images resemble that of nonlithiated 2H- $\text{NbS}_2$ ; this indicates that the Li has been inserted into the van der Waals gap between the  $\text{NbS}_2$  layers without noticeable structural change of the intercalation host.<sup>39</sup> As is visible in the enlargements of the SEM pictures (see Figure 3, right) each larger primary particle consists of several layers of  $\text{Li}_x\text{NbS}_2$ .

**Powder X-ray diffraction.** Phase purity of the  $\text{Li}_x\text{NbS}_2$  samples with  $x = 0.3, 0.7$ , and 1 was checked by powder X-ray diffraction carried out at room temperature (see Figures 4 and 5). The refined structural parameters and coordinates of the three samples investigated are listed in Tables 1 and 2.

As shown by Salyer et al.,<sup>12</sup> the lattice parameter  $c$  increases strongly with increasing lithium content for  $x = 0$  to  $x \approx 0.5$ . For larger amounts of  $x$  the  $c$  parameter increases slightly with  $x$ . Our refined lattice parameters are in good agreement with values reported by Omloo and Jellinek.<sup>38</sup> Both the  $a$  and  $c$  lattice parameters of  $\text{Li}_{0.7}\text{NbS}_2$  are slightly smaller than those reported by Salyer obtained from X-ray diffraction measurements of a single crystal.<sup>16</sup> A detailed investigation of lattice parameter variation with nominal composition for  $\text{Li}_x\text{NbS}_2$  is already presented in ref 12, together with a detailed discussion of the behavior observed.

#### 4.2. Static $^7\text{Li}$ NMR Spectra, Motional Narrowing.

Temperature-variable NMR line shape measurements allow getting first insights into the jump processes of Li ions in solids in a relatively easy way. Here, all of the static  $^7\text{Li}$  NMR spectra were recorded at various temperatures at a resonance frequency of 116.4 MHz. Independent of  $x$ , at lower temperatures (see Figure 6a) the spectra are composed of a single Gaussian shaped and slightly asymmetric central line with widths (full width at half-maximum, fwhm) ranging from 6.2 kHz ( $x = 0.3$ ) up to 7.7 kHz ( $x = 0.7$ ); considering the shape no distinct differences are seen. At the bottom of the lines tails of a quadrupole powder pattern are visible. This is due to the electric quadrupole interaction of the quadrupole moment of Li (spin-3/2) with a nonvanishing electric field gradient (EFG) at the Li site in  $\text{Li}_x\text{NbS}_2$ .<sup>40</sup> The interaction, which can be

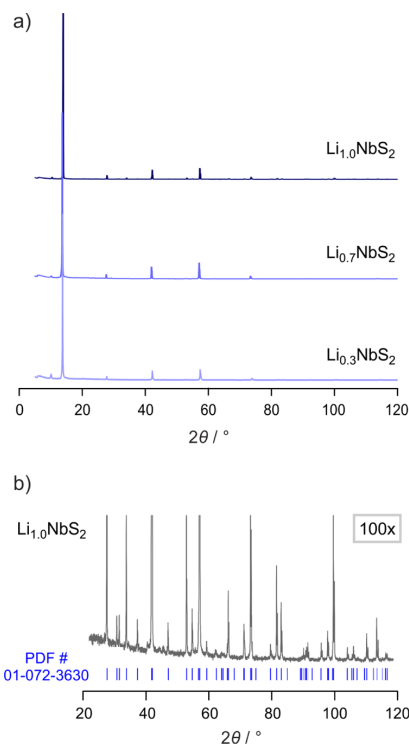


**Figure 4.** (a) Normalized X-ray powder diffractograms of the three samples investigated. For the sake of clarity, the larger reflections are reduced in their intensity. The patterns recorded indicate  $\text{Li}_x\text{NbS}_2$  with high purity. (b) Magnification of the low-intensity reflections of the XRD pattern of  $\text{Li}_{1.0}\text{NbS}_2$ . Vertical bars indicate the positions of reflections expected for  $\text{Li}_x\text{NbS}_2$ .

described by first order perturbation theory for  $^7\text{Li}$ , alters the Zeeman levels leading to three different spin transitions.<sup>40</sup>

In Figure 6b, spectra are presented that were measured at  $T = 475 \text{ K}$ . With increasing  $T$  the central line, which is dipolarly broadened at low  $T$ , transforms into a Lorentzian shaped and asymmetric signal. Since dipole–dipole interactions are averaged due to rapid Li exchange with values in the kHz range, now a well visible quadrupole pattern shows up with sharp  $90^\circ$  singularities. For 2H- $\text{Li}_x\text{NbS}_2$  with  $x = 1$  we observe a single quadrupole pattern indicating a single set of electrically equivalent Li positions.<sup>40,41</sup> If we assume axially symmetric EFGs, from the fully developed quadrupole powder pattern (410 K), which starts to emerge at  $T > 330 \text{ K}$ ,  $C_Q(^7\text{Li}, 384 \text{ K}) \approx 17 \text{ kHz}$  can be easily estimated from the frequency distance  $\Delta\nu_Q$  between the most intense satellite lines.

In contrast to  $\text{Li}_{1.0}\text{NbS}_2$ , the spectra of the samples with an intercalation degree of  $x = 0.3$  and  $0.7$ , respectively, indicate the presence of more than one inequivalent Li position occupied. For the sample with  $x = 0.7$  besides the main pattern with  $C_{Q1}(^7\text{Li}, 413 \text{ K}) \approx 16.5 \text{ kHz}$  (see Figure 6b) another set of singularities with very low intensity shows up that is characterized by  $C_{Q2}(^7\text{Li}, 384 \text{ K}) \approx 7.2 \text{ kHz}$ . For  $x = 0.3$  we obtain  $C_Q(^7\text{Li}, 413 \text{ K}) \approx 11 \text{ kHz}$ . Obviously, at intermediate values of  $x$  the Li ions have access to more than one crystallographic position in 2H- $\text{NbS}_2$ . In agreement with two sets of quadrupole powder patterns, the line of  $\text{Li}_{0.7}\text{NbS}_2$  (see

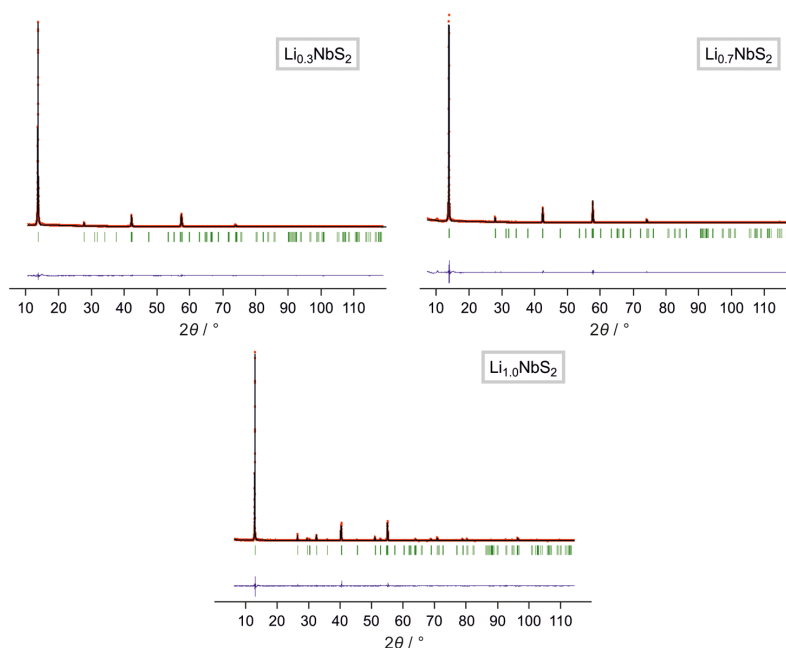


Figure 5. X-ray powder diagrams of  $\text{Li}_{0.3}\text{NbS}_2$  (left),  $\text{Li}_{0.7}\text{NbS}_2$  (right), and  $\text{Li}_{1.0}\text{NbS}_2$  (bottom) with the results of the Rietveld refinements.

Table 1. Refined Structural Parameters for  $\text{Li}_x\text{NbS}_2$  with  $x = 0.3, 0.7$ , and  $1.0$  at Ambient Temperature

	$x = 1.0$	$x = 0.7$	$x = 0.3$
space group	$P6_3/mmc$	$P6_3/mmc$	$P6_3/mmc$
lattice parameter	$a = 335.300$ (8) pm $c = 1290.23$ (2) pm	$a = 334.03$ (5) pm $c = 1288.02$ (3) pm	$a = 333.080$ (14) pm $c = 1281.79$ (2) pm
unit cell volume	$V = 125.622(4) \times 10^6 \text{ pm}^3$	$V = 124.46(3) \times 10^6 \text{ pm}^3$	$V = 123.153(7) \times 10^6 \text{ pm}^3$
formula units	$Z = 2$	$Z = 2$	$Z = 2$
$2\theta$ range	$5-120^\circ$	$5-120^\circ$	$5-120^\circ$
$R_{\text{wp}}$	0.0688	0.0704	0.0546
$R_{\text{Bragg}}$	0.0606	0.0213	0.0213
$R_{\text{exp}}$	0.0266	0.0264	0.0266
$S$	2.58	2.66	2.05

Table 2. Refined Atomic Coordinates for  $\text{Li}_x\text{NbS}_2$  with  $x = 0.3, 0.7$ , and  $1.0$  at Ambient Temperature

atom	Wyck. site	$x$	$y$	$z^a$	occ. for $\text{Li}_{1.0}\text{NbS}_2$	occ. for $\text{Li}_{0.7}\text{NbS}_2$	occ. for $\text{Li}_{0.3}\text{NbS}_2$
Li	$2a$	0	0	0	0.08333	0.05833	0.025
Nb	$2b$	0	0	0.25	0.08333	0.08333	0.08333
S	$4f$	$1/3$	$2/3$	$z$	0.16666	0.16666	0.16666

<sup>a</sup> $z = 0.12514(9)$  in  $\text{Li}_{0.3}\text{NbS}_2$ ;  $z = 0.12520(12)$  in  $\text{Li}_{0.7}\text{NbS}_2$ ;  $z = 0.12546(13)$  in  $\text{Li}_{1.0}\text{NbS}_2$ .

Figure 6b) also reveals a second central line that is characterized by its own chemical shift value. This feature is also seen for  $x = 0.3$ . We anticipate, however, that mainly the octahedral voids in the van der Waals gap are occupied, note that the intensity of the powder pattern leading to  $C_{\text{Q2}}$  ( $x = 0.7$ ) is much weaker than that associated with  $C_{\text{Q1}}$ .

Independent of  $x$ , the central lines with the largest intensity show the typical asymmetry as expected for Li spins exposed to a spatially confined environment,<sup>42</sup> which is found in layer structured materials. The change of the corresponding

quadrupole coupling constant from 11 kHz ( $x = 0.3$ ) to 16.5 kHz ( $x = 0.7$ ) and 17 kHz ( $x = 1$ ) observed resembles the variation in the lattice constant  $c$ , see Table 1.

The change of the shape of the  $^7\text{Li}$  NMR spectra over the temperature range covered here is illustrated in Figure 7, which presents exemplarily the line shapes of  $2\text{H-Li}_{1.0}\text{NbS}_2$ . The spectra meet the expectations for a pure  $\text{Li}_{1.0}\text{NbS}_2$  phase with the Li ions located inside the van der Waals gap. The fact that there is no averaging of the quadrupole intensities seen indicates spatially confined (two-dimensional) Li diffusion between the  $\text{NbS}_2$  sheets; thus, this diffusion process is restricted to an exchange process between the electrically equivalent Li sites ( $2a$ ) in the van der Waals gap of  $\text{NbS}_2$ .<sup>42</sup>

To collect quantitative information on Li ion dynamics, in Figure 6c the line width of the central transition was plotted vs temperature. Here, we focus on the most intense central line associated with the largest quadrupole powder pattern. The asymmetry is a clear indication of NMR chemical anisotropy being due to the layered structure of the material; similarly, this has been observed for  $\text{Li}_x\text{TiS}_2$  by the NMR study of Prigge et al.<sup>42</sup> At  $T = 420$  K it has already reached its full narrowing,

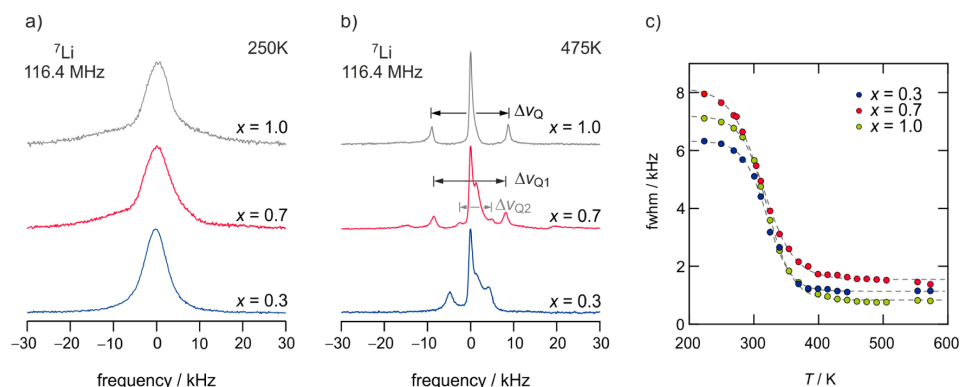


**Figure 6.** (a) <sup>7</sup>Li NMR spectra of annealed (that is, homogenized) layer-structured 2H-Li<sub>x</sub>NbS<sub>2</sub> ( $x = 0.3, 0.7,$  and  $1.0$ ) recorded at  $\omega_0/2\pi = 116.4$  MHz and 250 K. See text for further explanation. (b) <sup>7</sup>Li NMR spectra of the samples shown in (a) but recorded at  $T = 475$  K. (c) <sup>7</sup>Li NMR line width (full width at half-maximum, fwhm) as a function of temperature  $T$ . The dashed lines are to guide the eye.

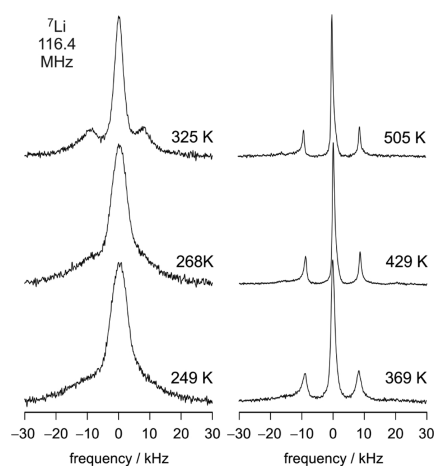


**Figure 7.** <sup>7</sup>Li NMR spectra of 2H-Li<sub>1.0</sub>NbS<sub>2</sub> recorded at the temperatures indicated. With increasing  $T$  the line width of the central line, which is slightly anisotropic, undergoes a motional narrowing due to averaging of (homonuclear) <sup>7</sup>Li dipole–dipole interactions. At  $T > 320$  K, a distinct quadrupole pattern appears that is fully developed at  $T > 420$  K. By using a Hahn echo that overcomes dead-time receiver effects, the powder pattern can be enhanced in intensity.

therefore, the contribution of the second line was not taken into account to construct the MN curves. The fwhm was read off manually; no fitting functions were used because of the observed chemical shift asymmetry. The line width in the rigid lattice regime,  $\nu_{il}(x)$ , depends on  $x$ ; it takes a value of 7.9 kHz for  $x = 0.7$  and 6.3 kHz for  $x = 1$ , respectively. The rigid lattice regime is reached at approximately 230 K.

Independent of Li content, the sulfides undergo a pronounced motional narrowing with increasing temperature due to increasing Li motions that are responsible for averaging of homonuclear dipole–dipole (<sup>7</sup>Li–<sup>7</sup>Li) interactions.<sup>43</sup> When the jump rate  $\tau_{MN}^{-1}$  reaches the order of the rigid lattice line width notable diffusion-controlled line narrowing is expected. Here, narrowing sets in at approximately 260 K. The Li ion jump rate  $\tau_{MN}^{-1}$  can be roughly estimated from the inflection point at approximately 320 K of the MN curves for all three

samples according to  $\tau_{MN}^{-1} \approx 2\pi \times \nu_{il}$ . For all three samples the Li jump rates  $\tau_{MN}^{-1}$  turn out to be in the order of  $\sim 5 \times 10^4$  s<sup>-1</sup>. Quite interestingly, although the intercalation degree  $x$  has been increased from  $x = 0.3$  up to  $x = 1$ , no significant shift of the onset of motional narrowing is observed (see Figure 6c). Clear distinctions in Li diffusivity, however, can be revealed by  $R_p$  NMR as is shown below. NMR line narrowing seems to be less sensitive to the differences that can be observed with the spin-lock technique.

At first glance, we would expect that  $\nu_{il}(x)$  increases with  $x$  because of increasing homonuclear dipole–dipole interactions as is quantified by the van Vleck formalism.<sup>40</sup> Here, however, the change in lattice constant  $c$ , which is the largest for  $x = 1$ , likely leads to a smaller rigid-lattice line width for Li<sub>1.0</sub>NbS<sub>2</sub> than expected.

**4.3. <sup>7</sup>Li NMR Spin–Lattice Relaxation Measurements, Frequency Dependence, 2D Diffusion.** To study Li diffusion parameters in more detail we measured both <sup>7</sup>Li  $R_1$  and  $R_{1\rho}/R$  rates at a Larmor frequency of  $\omega_0/2\pi = 116.4$  MHz and a locking frequency of 20 kHz (223 and 573 K), see refs 29 and 44–46 for an introduction into the basics of spin-lock measurements. In Figure 8 the rates  $R_1(1/T)$  and  $R_{1\rho}(1/T)$  together with the corresponding stretching exponents  $\gamma(R_{1\rho})$  of the transients analyzed (see Figure 2) are shown in an Arrhenius plot.<sup>47</sup>

Whereas the  $R_1$  transients  $M_z(t_d)$  can be best represented with exponential functions (see the equation mentioned above), the corresponding magnetization curves and  $M_\rho(t_{lock})$  need to be parametrized with  $M_\rho(t_{lock}) \propto \exp[-(t_{lock}/T_{1\rho})^{\gamma'}$  (see above) with  $\gamma'$  ranging between 0.7 and 1.0. The exact physical meaning of the stretching exponents is, in general, very difficult to explain; admittedly, in many cases no clear interpretation can be given. It is expected to be related to the shape of the underlying motional correlation function. In our opinion, intrinsic or extrinsic origins have to be considered: An intrinsically nonexponential motional correlation function might be expected for, for example, low-dimensional diffusion. Frequently, nonexponential decay behavior is related to a distribution of correlation rates being the direct consequence of a distribution of hopping barriers the ions have to overcome. Such extrinsic conditions would result in a superposition of distinct functions finally producing a stretched magnetization transient whose shape might change with temperature. In the

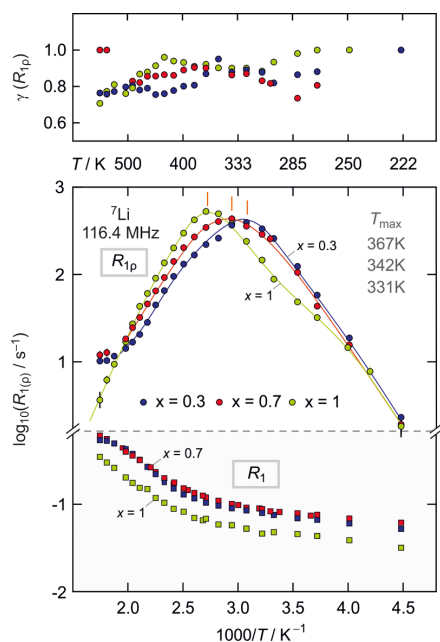


**Figure 8.** Arrhenius plot of the  ${}^7\text{Li}$  NMR  $R_1$  rates of  $2\text{H-Li}_x\text{NbS}_2$  recorded in the laboratory frame ( $R_1$  (■), see bottom part of the figure) and in the rotating frame of reference ( $R_{1p}$  (●), see upper part of the figure) measured at  $\omega_0/2\pi = 116.4$  MHz and at  $\omega_1/2\pi = 20$  kHz. The colors (see key) refer to the intercalation degree  $x$  of the samples ( $x = 0.3$  (blue),  $x = 0.7$  (red), and  $x = 1$  (green)). The upper graph shows the dependence of the stretching exponents  $\gamma(R_{1p})$  on  $T$ ; the error margins of the exponents range from 0.1 to 0.2.

case of  ${}^7\text{Li}$ , being a quadrupole nucleus, the interaction of its quadrupole moment with EFGs is expected to give complex nonexponential transients,<sup>48</sup> especially in the case of  $R_{1p}$ . Additionally, the latter are characterized by  $\gamma' = 0.5$  if induced by the interactions of Li spins with paramagnetic centers.<sup>49</sup> Thus, there are various reasons that lead to the observation of stretched exponentials. Since no large change of  $\gamma'$  is observed in the present case, error margins are within  $\pm 0.2$ , and since many of the values range from 0.8 to 1.0, the stretched transients most likely reflect Li diffusion in a relatively regular potential landscape as it has been observed for  $\text{Li}_{x=0.7}\text{TiS}_2$ .<sup>50</sup> In particular, this holds for the sample with  $x = 0.3$  ( $\beta = 1.8$ , see below), for which very similar activation energies are derived from  $R_1$  and  $R_{1p}$ .

Coming back to the rates extracted from the transients measured, below approximately 300 K the rates  $R_1$  are influenced by nondiffusive effects rather than by Li jump diffusion; at very low temperatures background relaxation is present that does only weakly depend on  $T$ . The corresponding relaxation rate ( $R_{1,\text{nd}}$ ) is presumed to be caused by coupling of the Li spins with conduction electrons, paramagnetic impurities and/or by lattice vibrations. To separate its influence on the purely diffusion-induced relaxation, which shows up at elevated  $T$ , an empirical power law,

$$R_{1,\text{nd}} \propto T^\kappa \quad (1)$$

was used to extrapolate the background rates toward higher temperatures. With increasing  $T$  the rates  $R_1$  pass into the low- $T$  flank of a diffusion-induced rate peak. The high- $T$  side, however, could not be reached since our NMR setup allows measurements up to 580 K only. For  $\text{Li}_{0.3}\text{NbS}_2$ , however, the rates seem to approach a maximum value at  $\sim 570$  K; compared to the other two samples this is a first indication that Li diffusivity in  $\text{Li}_{0.3}\text{NbS}_2$  is faster than that for  $x = 0.7$  and  $x = 1.0$ .

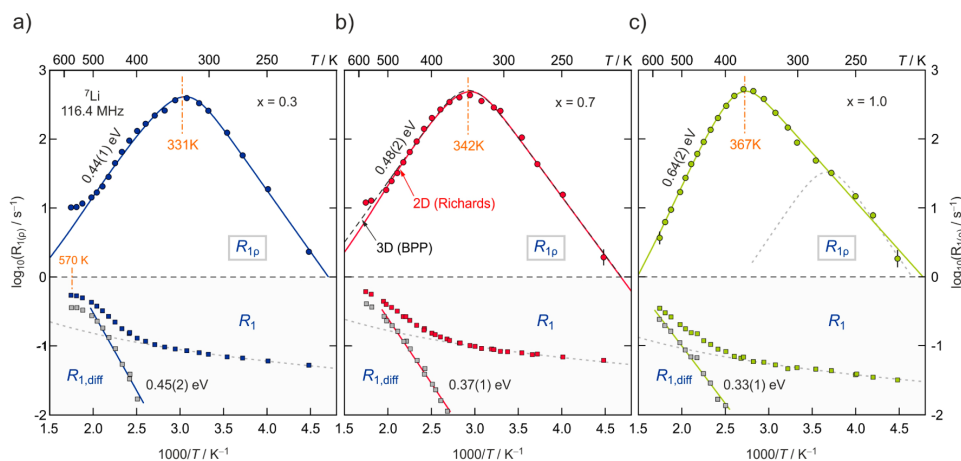


**Figure 9.** (a, b, and c) Detailed view of Arrhenius plot of the  ${}^7\text{Li}$  NMR  $R_p$  rates of  $2\text{H-Li}_x\text{NbS}_2$  recorded at 166.4 MHz; the locking frequency set was 20 kHz. Solid lines show fits with an NMR model taking the 2D diffusion into account. The dashed line in panel (b) represents a modified BPP fit. Activation energies are obtained from the fits and are linked to long-range diffusion. Short-range activation energies  $E_a^{2D}$  were calculated using  $E_a^{2D} = E_a^{2D} \times (\beta - 1)$  where  $E_a^{2D}$  denotes the activation energy obtained from the fits according to the model of Richards.<sup>27</sup> They are in agreement with those values that can directly be obtained from the slopes of the low- $T$  flanks (see text for further information). In order to obtain the purely diffusion-induced rates  $R_{1,\text{diff}}$ , nondiffusive background effects showing up at lower  $T$  have been taken into account by using an appropriate power law  $R_{1,\text{nd}} \propto T^\kappa$  (with  $\kappa_{x=0.3} = 1.34(1)$ , see panel (a),  $\kappa_{x=0.7} = 1.88(1)$ , see panel (b), and  $\kappa_{x=1} = 1.27(8)$ , see panel (c), represented by gray dashed lines).  $R_{1,\text{diff}}$  values were obtained by subtraction  $R_{1,\text{diff}}$  from the overall rates. Activation energies  $E_{a,\text{diff}}$  were calculated from the slope of the linear fits shown (cf. the solid lines in the lower parts of the figures).

In Figure 9a–c, the  $R_1(1/T)$  as well as  $R_{1,\text{diff}}(1/T)$  are shown, which have been calculated according to<sup>50</sup>

$$R_1 = R_{1,\text{diff}} + R_{1,\text{nd}} \quad (2)$$

A fit according to eq 1 is also presented in Figure 9 yielding  $\kappa = 1.34(1)$  for  $x = 0.3$ ,  $\kappa = 1.88(1)$  for  $x = 0.7$ , and  $\kappa = 1.27(8)$  for  $x = 1$ . The purely diffusion-induced rates  $R_{1,\text{diff}}$  are represented by gray squares. The activation energies  $E'_{a,\text{diff}}$  were obtained from the slope of a linear fit of the corrected rates. Since  $R_1$  (and so  $R_{1,\text{diff}}$ ) varies only slightly with  $T$ , the influence of  $R_{1,\text{nd}}$  is rather large resulting in activation energies that should be regarded as rough values. Here, we found 0.45(2) eV for  $x = 0.3$ ; 0.37(1) eV for  $x = 0.7$  and 0.33(1) eV for  $x = 1$ .  $E'_{a,\text{diff}}$  since it has been deduced in the limit  $\omega_1\tau_c \gg 1$ , is usually ascribed to short-range Li diffusion that is, in general, influenced by correlation effects such as Coulomb interactions and/or structural disorder.<sup>23</sup> Long-range ion dynamics, on the other hand, can only be inferred from the high-temperature flank of a diffusion-induced rate peak.<sup>34,35</sup> The intercalation degree  $x$  seems to have an impact on the activation energies characterizing short-range Li ion diffusion; the energies decrease from 0.45(2) eV for  $x = 0.3$  to 0.33(1) eV for  $x = 1$ .

In our case, complete relaxation rate peaks can be obtained if the spins relax in a magnetic field  $B_1$ , the spin-lock field, that is much lower than the external one characterized by 116 MHz. In the upper part of the Arrhenius plot that is shown in Figure 8 the NMR  $R_\rho$  rates obtained are presented. The rates  $R_{1\rho}$  pass through well-defined maxima showing up at different temperatures  $T_{\text{max}}$ . In contrast to  $R_1$  (as well as to the line widths measurements, vide supra), the  $R_{1\rho}$  data do reveal a clear influence of the intercalation degree  $x$  on Li diffusivity, that is, the position of the rate maximum on the  $1/T$  scale. According to the maximum condition,  $\omega_1\tau_c \approx 0.5$ , which is generally valid, the more the respective rate peak is shifted toward lower  $T$ , the higher the Li diffusivity. The latter is directly expressed by the correlation rate  $\tau_c^{-1}$  being in the same order of magnitude as the Li jump rate  $\tau^{-1}$ . Here, the highest diffusivity is found for the sample with  $x = 0.3$  (see Figure 8). Note that the  $R_{1\rho}$  rates follow a clear trend for  $x = 0.3$ , 0.7, and 1 which corroborates the above-mentioned indication of a  $R_1$  peak maximum in the case of 2H–Li<sub>0.3</sub>NbS<sub>2</sub>. The temperatures  $T_{\text{max}}$  are as follows: 331 K for  $x = 0.3$ , 342 K for  $x = 0.7$  and 367 K for  $x = 1$ . Inserting  $\omega_1/2\pi = 20$  kHz,  $\tau_c^{-1}$  is given by  $\tau_c^{-1} \approx \tau_{(\rho)}^{-1} = 3 \times 10^5 \text{ s}^{-1}$  at  $T_{\text{max}}$ . This value is slightly larger than the jump rate obtained from MN measurements,  $\tau_{\text{MN}}^{-1} \approx 5 \times 10^4 \text{ s}^{-1}$ .

To deduce activation energies from the  $R_{1\rho}(1/T)$  peaks and to gain information on the underlying dimensionality of the diffusion process, the rates were analyzed with an appropriate relaxation model introduced by Richards.<sup>27,38</sup>

The influence of  $x$  on the Li diffusivity can also be clearly rediscovered in the long-range activation energies  $E_a$  obtained from the appropriate fits that are shown in Figure 9a–c as solid lines. As is well-known for NMR relaxometry, the rate  $R_{1\rho}$  is linked to the spectral density function  $J(n\omega)_{n=1,2}$  via

$$R_{1\rho,\text{diff}} = C_\rho \left( J(2\omega_1) + \frac{5}{3}J(\omega_0) + \frac{2}{3}J(2\omega_0) \right) \quad (3)$$

where  $\omega_1$  denotes the angular locking frequency,  $\omega_0$  the Larmor frequency and  $k_B$  the Boltzmann constant. Here, the spectral density function introduced by Richards<sup>27</sup> for 2D diffusion  $J^{2D}(\omega,\tau_c) \propto \tau_c \ln(1 + 1/(1 + \omega_1\tau_c)^\beta)$  was used. It entails a logarithmic frequency dependence of the relaxation rate on the

high- $T$  side of the diffusion-induced rate peak. The rates were recorded at temperatures where the first term of eq 3 is sufficient to describe the relaxation rates adequately. Since the Li jump rate  $\tau^{-1}$  is of the order of the correlation rate  $\tau_c^{-1}$ , we obtain the following activation energies being characteristic for long-range ion transport that obeys the Arrhenius relation

$$\tau_c^{-1} \approx \tau_\rho^{-1} = \tau_0^{-1} \exp\left(\frac{-E_a^{2D}}{k_B T}\right) \quad (4)$$

The lowest activation energy  $E_a^{2D}$  of 0.44 eV is found for the sample with the lowest Li metal content ( $x = 0.3$ ). A slightly higher energy of 0.48 eV is found for  $x = 0.7$ , while the highest activation energy of 0.65 eV is obtained for the fully intercalated sample with  $x = 1$ . This is in excellent agreement with the increase of  $T_{\text{max}}$  with increasing Li content  $x$ . The validity of the fits is supported by the results for the pre-exponential factor  $\tau_0^{-1}$ , which is in the typical range of phonon frequencies;<sup>50</sup> here, we obtained  $\tau_0^{-1} \approx 10^{13} \dots 10^{15} \text{ s}^{-1}$ .

**Table 3. Results for the Pre-exponential Factor  $\tau_0^{-1}$  and Activation Energies  $E_a$**

	$x = 0.3$	$x = 0.7$	$x = 1$
$E_a^{2D}$	0.44 eV	0.48 eV	0.65 eV
$\tau_0^{-1}$	$3.44 \times 10^{13} \text{ s}^{-1}$	$1.96 \times 10^{13} \text{ s}^{-1}$	$4.28 \times 10^{15} \text{ s}^{-1}$

Let us note that it is good to know about the effective locking frequency used to carry out the fitting procedure. The fits shown here use the locking frequency that can be determined via the pulse power used to lock the spin system. The fact that for  $x = 0.3$ , a shallow  $R_1$  maximum is seen, gives us the chance to use a joint fit to parametrize both the  $R_1$  and  $R_{1\rho}$  rates; by leaving the fitting parameter  $\omega_1$  free, we can estimate a value for  $\omega_{\text{effective}}$  that takes into account local fields. Here, it turned out that  $\omega_{\text{effective}}$  is only about 2–3 times larger than  $\omega_1$ . This difference has almost no influence on the position and shape of the fits shown; its influence on the resulting  $E_a$  and the prefactor is quite small. Of course, the diffusion coefficient derived via the maximum condition is influenced by the same factor. Compared to other sources of error, this is quite small.

Using the fits shown in Figure 9a–c, the short-range activation energies  $E'_a$ , which describe the slope in the low-temperature limit  $\omega_0\tau_c \gg 1$ , can be easily estimated according to  $E'_a{}^{2D} = E_a^{2D} \times (\beta - 1)$  with the correlation parameter  $\beta$  ( $1 < \beta \leq 2$ ).<sup>23,34,35</sup> Interestingly,  $E'_a{}^{2D}$  behaves the other way round; the highest value (0.35 eV) is found for  $x = 0.3$  ( $\beta = 1.80$ ). Whereas for  $x = 0.7$  ( $\beta = 1.71$ ) an activation energy of 0.34 eV and for  $x = 1$  ( $\beta = 1.43$ ) the lowest value (0.28 eV) is found. Since  $E'_a{}^{2D}$  is governed by repulsive Coulomb interactions, its decrease with  $x$  (or the increase of  $\beta$  being a measure of these interactions) reflects Li–Li correlation effects rather than a reduction in local energy barriers. The larger the Li density, the more distinct correlated motion.<sup>33,34</sup> For  $x = 0.3$ , no large correlation effects are seen, since  $E'_a$  equals  $E_a^{2D}$  we assume that the Li ions are exposed to a regular, uniform potential landscape with almost no difference between short-range and long-range hopping motion, see also ref 50.

Moreover, frequency-dependent  $R_\rho$  measurements have been carried out at a constant temperature to differentiate between two-dimensional (2D) and three-dimensional (3D) diffusion, see Figure 10a.<sup>20</sup>

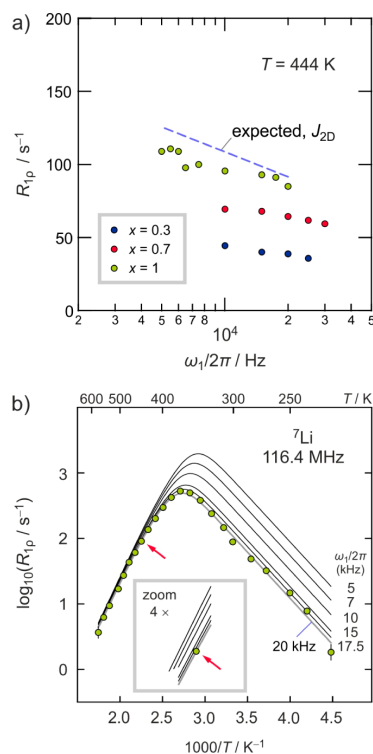


**Figure 10.** (a)  ${}^7\text{Li}$  NMR  $R_p$  rates of  $2\text{H-Li}_x\text{NbS}_2$  as a function of the locking frequency  $\omega_1/2\pi$ . The frequency axis is scaled logarithmically.  $R_p$  was recorded at 444 K on the high-temperature flank of the relaxation rate peak where the condition  $\omega_1\tau_c \ll 1$  approximately holds. The solid line indicates the expected frequency dependence according to the semiempirical model for 2D diffusion by Richards ( $R_p \propto -\tau_c \ln(\omega_1\tau_c)$ ).<sup>27</sup> (b) Simulation of the expected frequency dependence for  $\text{Li}_{1.0}\text{NbS}_2$  by varying the locking frequency from 5 to 20 kHz. As is visible in the inset a rather shallow dependence is expected at  $T = 444$  K; the values predicted are in good agreement with those found experimentally.

In Figure 10b, the spectral density function  $J^{2D}(\omega, \tau_c)$  (see above)<sup>27</sup> was used to calculate the expected frequency dependence  $R_{1p,\text{diff}} \propto -\tau_c \ln(\omega_1\tau_c)$  of  $\text{Li}_{1.0}\text{NbS}_2$  at 444 K (solid line), that is, within the high-temperature limit  $\omega_1\tau_c \ll 1$ .<sup>38,51</sup> Here,  $R_{1p,\text{diff}}$  denotes the diffusion-induced  $R_p$  rate.<sup>34</sup> Most importantly, in contrast to 2D hopping motion, 3D diffusion would result in no frequency dependence of the  $R_{1p,\text{diff}}$  rates in the limit  $\omega_1\tau_c \ll 1$ .<sup>23</sup> As it can be seen in the inset of Figure 10b, varying  $\omega_1/2\pi$  in a rather small range, *viz* from 5 to 17 kHz only, needs highly precise  $R_p$  measurements to attest 2D diffusion in  $\text{Li}_x\text{NbS}_2$ . Despite of the narrow frequency range accessible via  $R_p$  NMR, the rates measured at 444 K indeed reveal a small frequency dependence being indicative of 2D diffusion. Comparing the present findings for the 2H-modification with previous measurements on  $3\text{R-Li}_{0.7}\text{NbS}_2$ , it turned out, however, that the logarithmic frequency dependence is not as large as it was deduced from the frequency-dependent  $R_p$  measurements of the 3R-modification.<sup>14</sup> This difference might be due to differences in local crystal structure between the two polymorphs, especially when the connection of the  $\text{LiS}_6$  and  $\text{NbS}_6$  polyhedra is regarded (see above).

Possibly, the free prismatic voids located above the  $\text{LiS}_6$  octahedra in  $2\text{H-Li}_x\text{NbS}_2$  might lead to wavelike 2D diffusion, *i.e.*, an oscillating trajectory which results if we consider sites within the van der Waals gap that act as transition states. Such transition states might be the tetrahedral sites connecting two octahedral voids by sharing common faces; a similar/please add semicolon after faces diffusion pathway has been found for  $\text{Li}_x\text{TiS}_2$ .<sup>50,52,53</sup>

Ultimately, although a characteristic 2D frequency dependence was found, we also fitted the diffusion-induced rate peak  $R_{1p}$  by using the spectral density function developed for 3D diffusion introduced by Bloembergen, Purcell, and Pound (BPP).<sup>36,37,54</sup> In Figure 9b, the corresponding fit for the sample with  $x = 0.7$  is shown as a dashed line. Since there is almost no difference between the 2D fit according to Richards (red line) and the 3D BPP fit (dashed line), without the frequency dependent measurements carried out here it would be very difficult to distinguish 2D from 3D motion just by analyzing the temperature dependence of  $R_{1p}$ . Most importantly, disregarding the dimensionality of the diffusion process, 3D fits generally lead to lower activation energies and prefactors  $\tau_0^{-1}$ . Here, however, the logarithmic frequency dependence found serves as a good indication for 2D diffusion. This is strongly supported by the chemical shift anisotropy observed, which does not disappear with increasing temperature; thus even in the regime of fast Li motion the ions sense the spatially confined environment of the van der Waals gap. In line with this observation, no averaging or change of quadrupole intensities is seen at higher  $T$ . Consequently, to extract the correct activation energies  $E_a^{2D}$  the  $R_{1p}(1/T)$  rate peaks have to be analyzed in terms of spectral density functions  $J^{2D}$  introduced for 2D jump diffusion.<sup>27</sup>

For the sake of completeness, a possible second  $R_{1p}$  peak maximum for  $x = 1$  has to be mentioned here (indicated as a dashed line in Figure 9c). Since no obvious second maximum was found for the other samples only the clearly observable rate peak was taken into account for the analysis of the samples studied.

Here, we found strong evidence for 2D diffusion, that is,  $\text{Li}^+$  diffusion along the buried interfaces formed by the van der Waals gap of layer-structured  $\text{Li}_x\text{NbS}_2$ . For low Li contents,  $x = 0.3$ , Li diffusion turns out to be less influenced by correlation effects. In contrast to samples with larger values of  $x$ , activation energies from both  $R_L$  and  $R_p$  measurements (0.44 eV) indicate Li hopping within a regular potential landscape with almost no difference between short-range motion and long-range ion transport.

## 5. CONCLUSIONS

$2\text{H-Li}_x\text{NbS}_2$  turned out to be a suitable and intriguing model system with a layered structure to study both dimensionality effects in spatially confined dimensions as well as the influence of Li intercalation on local hopping and long-range ion transport.  ${}^7\text{Li}$  NMR line shapes, as well as  $R_p$  measurements, have been used to get insights into both the Li ion dynamics and the geometry of Li motion in  $\text{NbS}_2$ .

(i) Frequency-dependent  $R_p$  measurements were successfully used to identify two-dimensional diffusion in  $2\text{H-Li}_x\text{NbS}_2$  taking place along the buried interfaces in the host material. The  $R_p$  rates of all samples show a small but clearly noticeable logarithmic frequency dependence within the high temperature limit characterized by  $\omega_1\tau_c \ll 1$ ; the rates measured are in good agreement with the values expected for a 2D diffusion process if

the semiempirical spectral density function introduced by Richards is used for the prediction. (ii) As has been shown via  $R_p$  NMR, the intercalation degree  $x$  influences Li ion diffusion in  $2\text{H-Li}_x\text{NbS}_2$  as expected. The larger  $x$  is chosen, the less the vacancy concentration, which slows down Li diffusivity in the van der Waals gap. This manifests itself in a characteristic shift of the rate  $R_{1\rho}(1/T)$  peaks toward higher temperatures if  $x$  is increased from 0.3 to 1. Moreover, the slow-down of Li diffusivity is confirmed by a significant increase of the long-range activation energy that is raised from 0.44 ( $x = 0.3$ ) to 0.64 eV ( $x = 1$ ) if deduced from the fits for 2D jump diffusion, that is, Li ion diffusion along the inner van der Waals interface in  $\text{NbS}_2$ .

### AUTHOR INFORMATION

#### Corresponding Author

\*Webmail: bernhard.stanje@tugraz.at.

#### Notes

The authors declare no competing financial interest.

### ACKNOWLEDGMENTS

We thank our colleagues at the TU Graz for valuable discussions; in particular, Dr. I. Hanzu for assistance with scanning electron microscopy. We thank the Deutsche Forschungsgemeinschaft (DFG) for financial support within the DFG Research Unit 1277 (subproject 1, WI 3600 2-2). Additional support from the Austrian Federal Ministry of Science, Research and Economy, and the Austrian National Foundation for Research, Technology and Development is also greatly appreciated.

### REFERENCES

- (1) Goodenough, J. B.; Park, K.-S. The Li-Ion Rechargeable Battery: A Perspective. *J. Am. Chem. Soc.* **2013**, *135*, 1167–1176.
- (2) Whittingham, M. S. Lithium Batteries and Cathode Materials. *Chem. Rev.* **2004**, *104*, 4271–4302.
- (3) Whittingham, M. Chemistry of Intercalation Compounds: Metal Guests in Chalcogenide Hosts. *Prog. Solid State Chem.* **1978**, *12*, 41–99.
- (4) Wang, Q. H.; Kalantar-Zadeh, K.; Kis, A.; Coleman, J. N.; Strano, M. S. Electronics and Optoelectronics of Two-Dimensional Transition Metal Dichalcogenides. *Nat. Nanotechnol.* **2012**, *7*, 699–712.
- (5) Ramakrishna Matte, H. S. S.; Gomathi, A.; Manna, A. K.; Late, D. J.; Datta, R.; Pati, S. K.; Rao, C. N. R.  $\text{MoS}_2$  and  $\text{WS}_2$  Analogues of Graphene. *Angew. Chem., Int. Ed.* **2010**, *49*, 4059–4062.
- (6) Splendiani, A.; Sun, L.; Zhang, Y.; Li, T.; Kim, J.; Chim, C.-Y.; Galli, G.; Wang, F. Emerging Photoluminescence in Monolayer  $\text{MoS}_2$ . *Nano Lett.* **2010**, *10*, 1271–1275.
- (7) Chhowalla, M.; Shin, H. S.; Eda, G.; Li, L.-J.; Loh, K. P.; Zhang, H. The Chemistry of Two-Dimensional Layered Transition Metal Dichalcogenide Nanosheets. *Nat. Chem.* **2013**, *5*, 263–275.
- (8) Dahn, D.; Carolan, J.; Haering, R. Low-Temperature Specific Heat of  $\text{Li}_x\text{NbS}_2$  Intercalation Compounds. *Phys. Rev. B* **1986**, *33*, 5214–5220.
- (9) Kumagai, N.; Tanno, K.; Kumagai, N. Charge–Discharge Characteristics and Structural Change in Various Niobium Sulfide Cathodes for Lithium–Nonaqueous Secondary Batteries. *Electrochim. Acta* **1982**, *27*, 1087–1092.
- (10) Liao, Y.; Park, K.-S.; Singh, P.; Li, W.; Goodenough, J. B. Reinvestigation of the Electrochemical Lithium Intercalation in  $2\text{H-}$  and  $3\text{R-NbS}_2$ . *J. Power Sources* **2014**, *245*, 27–32.
- (11) Lévy, F. *Intercalated Layered Materials*; D. Reidel Publishing Company: Dordrecht, the Netherlands, 1979.
- (12) Salyer, P. A.; Barker, M. G.; Gregory, D. H.; Jones, M. O.; Wilson, C.  $\text{Li}_{0.7}\text{NbS}_2$ : Structural Effects of Increased Alkali Metal Content. *Acta Crystallogr., Sect. E: Struct. Rep. Online* **2003**, *59*, i112–i115.
- (13) Jellinek, F.; Brauer, G.; Müller, H. Molybdenum and Niobium Sulphides. *Nature* **1960**, *185*, 376–377.
- (14) Epp, V.; Nakhal, S.; Lerch, M.; Wilkening, M. Two-Dimensional Diffusion in  $\text{Li}_{0.7}\text{NbS}_2$  as Directly Probed by Frequency-Dependent  $^7\text{Li}$  NMR. *J. Phys.: Condens. Matter* **2013**, *25*, 195402–1–7.
- (15) Kuhn, A.; Narayanan, S.; Spencer, L.; Goward, G.; Thangadurai, V.; Wilkening, M. Li Self-Diffusion in Garnet-Type  $\text{Li}_7\text{La}_3\text{Zr}_2\text{O}_{12}$  as Probed Directly by Diffusion-Induced  $^7\text{Li}$  spin-Lattice Relaxation NMR Spectroscopy. *Phys. Rev. B* **2011**, *83*, 094302–1–11.
- (16) Wilkening, M.; Küchler, W.; Heitjans, P. From Ultraslow to Fast Lithium Diffusion in the 2D Ion Conductor  $\text{Li}_{0.7}\text{TiS}_2$  Probed Directly by Stimulated-Echo NMR and Nuclear Magnetic Relaxation. *Phys. Rev. Lett.* **2006**, *97*, No. 065901.
- (17) McDowell, A.; Fedders, P.; Conradi, M. Spin Relaxation for Motion Restricted to Two Dimensions. *Phys. Rev. B* **1998**, *58*, 248–253.
- (18) MacDonald, D. H.; Sholl, C. A.; Stephenson, P. C. L. Nuclear Magnetic Resonance Magnetic Dipolar Spectral Density Functions for Two-Dimensional Lattice Diffusion: Hexagonal Systems. *J. Phys.: Condens. Matter* **1998**, *10*, 417–428.
- (19) Wilkening, M.; Heitjans, P. From Micro to Macro: Access to Long-Range  $\text{Li}^+$  Diffusion Parameters in Solids via Microscopic  $^6, ^7\text{Li}$  Spin-Alignment Echo NMR Spectroscopy. *ChemPhysChem* **2012**, *13*, 53–65.
- (20) McDowell, A.; Mendelsohn, C.; Conradi, M.; Bowman, R.; Maeland, A. Two-Dimensional Diffusion of Hydrogen in  $\text{ZrBe}_2\text{H}_{1.4}$ . *Phys. Rev. B* **1995**, *51*, 6336–6342.
- (21) Epp, V.; Wilkening, M. Fast Li Diffusion in Crystalline  $\text{LiBH}_4$  Due to Reduced Dimensionality: Frequency-Dependent NMR Spectroscopy. *Phys. Rev. B* **2010**, *82*, No. 020301.
- (22) Kuhn, A.; Sreeraj, P.; Pöttgen, R.; Wiemhöfer, H.-D.; Wilkening, M.; Heitjans, P. Li Ion Diffusion in the Anode Material  $\text{Li}_{12}\text{Si}_7$ : Ultrafast Quasi-1D Diffusion and Two Distinct Fast 3D Jump Processes Separately Revealed by  $^7\text{Li}$  NMR Relaxometry. *J. Am. Chem. Soc.* **2011**, *133*, 11018–11021.
- (23) Heitjans, P.; Schirmer, A.; Indris, S. In *Diffusion in Condensed Matter*; Heitjans, P., Kärger, J., Eds.; Springer: Berlin, 2005; pp 367–415.
- (24) Epp, V.; Wilkening, M. Motion of  $\text{Li}^+$  in Nanoengineered  $\text{LiBH}_4$  and  $\text{LiBH}_4\cdot\text{Al}_2\text{O}_3$  Comparison with the Microcrystalline Form. *ChemPhysChem* **2013**, *14*, 3706–3713.
- (25) Wilkening, M.; Amade, R.; Iwaniak, W.; Heitjans, P. Ultraslow Li Diffusion in Spinel-Type Structured  $\text{Li}_4\text{Ti}_5\text{O}_{12}$ —A Comparison of Results from Solid State NMR and Impedance Spectroscopy. *Phys. Chem. Chem. Phys.* **2007**, *9*, 1239–1246.
- (26) Wilkening, M.; Kuhn, A.; Heitjans, P. Atomic-Scale Measurement of Ultraslow Li Motions in Glassy  $\text{LiAlSi}_2\text{O}_6$  by Two-Time  $^6\text{Li}$  Spin-Alignment Echo NMR Correlation Spectroscopy. *Phys. Rev. B* **2008**, *78*, No. 054303.
- (27) Richards, P. M. In *Topics in Current Physics*; Salomon, M. B., Ed.; Springer: Berlin, 1979; pp 141–174.
- (28) Rodriguez-Carvajal, J. FULLPROF: A Program for Rietveld Refinement and Pattern Matching Analysis. *Abstr. Satell. Meet. Powder Diffr. XV Congr. IUCr* **1990**, 127.
- (29) Fukushima, E.; Roeder, S. B. W. *Experimental Pulse NMR: A Nuts and Bolts Approach*; Perseus Books, Advanced Book Program: Reading, MA, 1981.
- (30) Ailion, D.; Slichter, C. Observation of Ultra-Slow Translational Diffusion in Metallic Lithium by Magnetic Resonance. *Phys. Rev.* **1965**, *137*, A235–A245.
- (31) Look, D. C. Nuclear Magnetic Dipole–Dipole Relaxation Along the Static and Rotating Magnetic Fields: Application to Gypsum. *J. Chem. Phys.* **1966**, *44*, 2995–3000.
- (32) Redfield, A. Nuclear Magnetic Resonance Saturation and Rotary Saturation in Solids. *Phys. Rev.* **1955**, *98*, 1787–1809.

- (33) Meyer, M.; Maass, P.; Bunde, A. Spin-Lattice Relaxation: Non-Bloembergen-Purcell-Pound Behavior by Structural Disorder and Coulomb Interactions. *Phys. Rev. Lett.* **1993**, *71*, 573–576.
- (34) Bunde, A.; Dieterich, W.; Maass, P.; Meyer, M. In *Diffusion in Condensed Matter—Methods, Materials, Models*, 2nd ed.; Heitjans, P., Kärger, J., Eds.; Springer: Berlin, 2005; pp 813–856.
- (35) Funke, K. Jump Relaxation in Solid Electrolytes. *Prog. Solid State Chem.* **1993**, *22*, 111–195.
- (36) Bloembergen, N.; Purcell, E.; Pound, R. Relaxation Effects in Nuclear Magnetic Resonance Absorption. *Phys. Rev.* **1948**, *73*, 679–712.
- (37) Küchler, W.; Heitjans, P.; Payer, A.; Schöllhorn, R.  $^7\text{Li}$  NMR Relaxation by Diffusion in Hexagonal and Cubic  $\text{Li}_x\text{TiS}_2$ . *Solid State Ionics* **1994**, *70–71*, 434–438.
- (38) Richards, P. M. Effect of Low Dimensionality on Prefactor Anomalies in Superionic Conductors. *Solid State Commun.* **1978**, *25*, 1019–1021.
- (39) Omluo, W.; Jellinek, F. Intercalation Compounds of Alkali Metals with Niobium and Tantalum Dichalcogenides. *J. Less-Common Met.* **1970**, *20*, 121–129.
- (40) Abragam, A. *The Principles of Nuclear Magnetism*; Clarendon Press: Oxford, U.K., 1961.
- (41) Bredow, T.; Heitjans, P.; Wilkening, M. Electric Field Gradient Calculations for  $\text{Li}_x\text{TiS}_2$  and Comparison with  $^7\text{Li}$  NMR Results. *Phys. Rev. B* **2004**, *70*, No. 115111.
- (42) Prigge, C.; Müller-Warmuth, W.; Schöllhorn, R. NMR Studies of Lithium Intercalated in the Host Compounds 1T-TiS<sub>2</sub>, c-TiS<sub>2</sub> and VSe<sub>2</sub>. *Z. Phys. Chem.* **1995**, *189*, 153–168.
- (43) Wilkening, M.; Epp, V.; Feldhoff, A.; Heitjans, P. Tuning the Li Diffusivity of Poor Ionic Conductors by Mechanical Treatment: High Li Conductivity of Strongly Defective  $\text{LiTaO}_3$  Nanoparticles. *J. Phys. Chem. C* **2008**, *112*, 9291–9300.
- (44) Ailion, D.; Slichter, C. Study of Ultraslow Atomic Motions by Magnetic Resonance. *Phys. Rev. Lett.* **1964**, *12*, 168–171.
- (45) Slichter, C.; Ailion, D. Low-Field Relaxation and the Study of Ultraslow Atomic Motions by Magnetic Resonance. *Phys. Rev.* **1964**, *135*, A1099–A1110.
- (46) Wolf, D. Effect of Correlated Self-Diffusion on the Low-Field Nuclear-Spin Relaxation in the Rotating Reference Frame. *Phys. Rev. B* **1974**, *10*, 2724–2732.
- (47) Epp, V.; Gün, Ö.; Deiseroth, H.-J.; Wilkening, M. Long-Range  $\text{Li}^+$  Dynamics in the Lithium Argyrodite  $\text{Li}_x\text{PSe}_6$  as Probed by Rotating-Frame Spin–Lattice Relaxation NMR. *Phys. Chem. Chem. Phys.* **2013**, *15*, 7123–2132.
- (48) Hubbard, P. Nonexponential Nuclear Magnetic Relaxation by Quadrupole Interactions. *J. Chem. Phys.* **1970**, *53*, 985–987.
- (49) Tse, D.; Hartmann, S. Nuclear Spin-Lattice Relaxation via Paramagnetic Centers without Spin Diffusion. *Phys. Rev. Lett.* **1968**, *21*, 511–514.
- (50) Wilkening, M.; Heitjans, P. Li Jump Process in  $h\text{-Li}_{0.7}\text{TiS}_2$  Studied by Two-Time  $^7\text{Li}$  Spin-Alignment Echo NMR and Comparison with Results on Two-Dimensional Diffusion from Nuclear Magnetic Relaxation. *Phys. Rev. B* **2008**, *77*, No. 024311.
- (51) Avogadro, A.; Villa, M. Nuclear Magnetic Resonance in a Two-Dimensional System. *J. Chem. Phys.* **1977**, *66*, 2359–2367.
- (52) Bensch, W.; Bredow, T.; Ebert, H.; Heitjans, P.; Indris, S.; Mankovsky, S.; Wilkening, M. Li Intercalation and Anion/Cation Substitution of Transition Metal Chalcogenides: Effects on Crystal Structure, Microstructure, Magnetic Properties, and  $\text{Li}^+$  Ion Mobility. *Prog. Solid State Chem.* **2009**, *37*, 206–225.
- (53) Van der Ven, A.; Thomas, J.; Xu, Q.; Swoboda, B.; Morgan, D. Nondilute Diffusion from First Principles: Li Diffusion in  $\text{Li}_x\text{TiS}_2$ . *Phys. Rev. B: Condens. Matter Mater. Phys.* **2008**, *78*, No. 104306.
- (54) Böhmer, R.; Jeffrey, K. R.; Vogel, M. Solid-State Li NMR with Applications to the Translational Dynamics in Ion Conductors. *Prog. Nucl. Magn. Reson. Spectrosc.* **2007**, *50*, 87–174.



## 3.2 Lithium ion diffusion in three-dimensional Li oxides

### 3.2.1 Extremely fast charge carriers in garnet-type $\text{Li}_6\text{La}_3\text{ZrTaO}_{12}$

The development of all-solid-state electrochemical energy storage systems (*e.g.* lithium-ion batteries with solid electrolytes) requires stable, electronically insulating compounds with exceptionally high ionic conductivities. The realization of next-generation and game-changing all-solid-state lithium-based batteries, able to reversibly store electricity from, *e.g.*, renewable but intermittent sources, requires powerful lithium-ion conductors with exceptionally high ionic conductivities and negligible electronic conduction. Such electrolytes would open the door to safe storage systems with high-energy densities. If flammable liquid electrolytes can successfully be replaced by solid electrolytes, expected to offer a wide electrochemical stability window, all-solid-state batteries could take advantage of using high-voltage cathode materials and lithium metal on the anode side. Of course, their success will depend on low interfacial resistances, including grain boundaries, and negligible degradation processes at the electrode-electrolyte interface. The latter might be inhibited by using additional protective layers consisting of moderate but inert Li ion conductors with a thickness of just a few nm. Considering oxides, garnet-type  $\text{Li}_6\text{La}_3\text{Zr}_2\text{O}_{12}$  (LLZO) and derivatives, see Zr-exchanged  $\text{Li}_6\text{La}_3\text{ZrTaO}_{12}$  (LLZTO), have attracted great attention because of their high  $\text{Li}^+$  ionic conductivities of up to  $10^{-3} \text{ S cm}^{-1}$ .

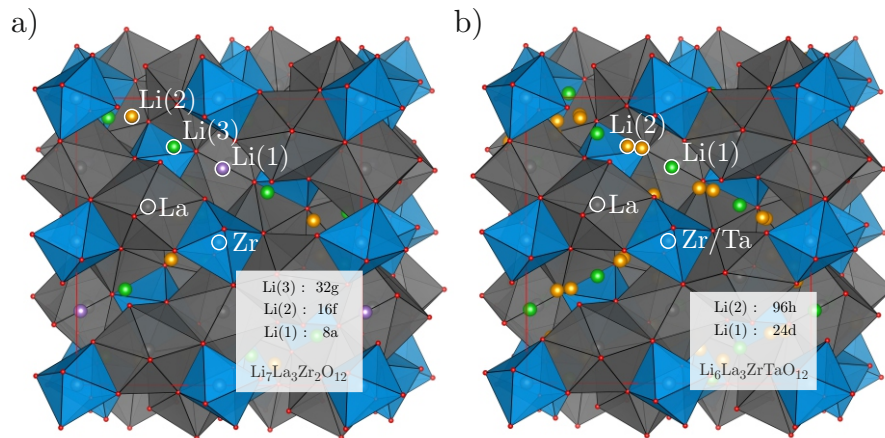


**Figure 3.1** – a) Crystal structure of tetragonal  $\text{Li}_6\text{La}_3\text{Zr}_2\text{O}_{12}$ , space group  $I4_1/acd$ . The Li ions are distributed over three different sites, 32g, 16f and 8a. This low-temperature modification possesses poor Li ion dynamics due to a "clogged" diffusion pathway b) Crystal structure of cubic  $\text{Li}_6\text{La}_3\text{ZrTaO}_{12}$ , space group  $Ia\bar{3}d$ . While La ions reside on the 24c sites, Zr and Ta share the 16c site. The Li ions are distributed over the 24d and 96h site. The latter is a split-atom site; only one of the closely neighbored positions can be occupied by a single Li ion. The Li ions form a three-dimensional network of fast diffusion pathways due to a large fraction of the 24d and 96h sites being vacant. The  $\text{ZrO}_6$  octahedral sites are represented by gray polyhedra and the  $\text{LaO}_8$  dodecahedral sites are represented by green polyhedra.

Pure LLZO occurs in two structural polymorphs: a low-temperature tetragonal (space group  $I4_1/acd$ ) and a high-temperature cubic phase (space group  $Ia\bar{3}d$ ) (see figure 3.1a)). At room temperature the thermodynamically stable phase of LLZO is the tetragonal modification.[67, 68] In order to stabilize the cubic modification at ambient temperatures, a variety of metals can be used as a dopant to do so, *e.g.* germanium, tantalum, aluminium or niobium *etc.*[69–73] Compared to the tetragonal modification, the cubic HT modification exhibits a disorder in the Li ion distribution. The

cubic garnet structure is composed of a framework of 8-fold coordinated  $\text{LaO}_8$  dodecahedra (24c) and 6-fold  $\text{ZrO}_6$  octahedra (16a).  $\text{Li}^+$  is located at interstitial sites, showing tetrahedral (24d), octahedral (48g) and distorted 4-fold (96h) coordination (see figure 3.1b). The 96h site is a so-called split-atom site; only one of the closely neighbored positions can be occupied by a single Li ion. The Li ions form a three-dimensional network of fast diffusion pathways due to the fact that a large fraction of the 24d and 96h sites are vacant. Here, single crystalline  $\text{Li}_6\text{La}_3\text{Zr}_2\text{O}_{12}$  served as a model system for a comprehensive  $^7\text{Li}$  NMR relaxation study to gain insight into the Li ion dynamics. In particular, activation energies ( $E_a$ ) and Li correlation times ( $\tau_c$ ) have been determined.

LLZTO single crystals with the nominal composition  $\text{Li}_6\text{La}_3\text{ZrTaO}_{12}$  were grown by the conventional Czochralski technique. The starting materials were  $\text{Li}_2\text{CO}_3$ ,  $\text{La}_2\text{O}_3$ ,  $\text{ZrO}_2$  and  $\text{Ta}_2\text{O}_5$ . The carbonates and oxides were dried and mixed in the required stoichiometry with a 10% excess of  $\text{Li}_2\text{CO}_3$ . Afterwards the powders were uniaxial pelletized, isostatically pressed at 2800 kbar and finally sintered at 1373 K for 16h in air. Capped magnesia crucibles were used, while covering the pellets with the respective LLZTO powder, to avoid Li-loss during the sintering process.

Because of the high melting temperatures, the sintered LLZTO samples were molten by radio frequency induction heating using a 25 kW microwave generator. An iridium seed (pulling rate 1.5 mm  $\text{h}^{-1}$ , rotation speed 1 rpm) was used for the crystal growth performed under dinitrogen atmosphere. An active afterheater was applied to adjust the temperature gradient in the set up. Thermal insulation was established by an outer alumina ceramic tube filled with zirconia granules. Inductively coupled plasma optical emission spectroscopy corroborated that the LLZTO single crystal obtained has indeed the composition  $\text{Li}_6\text{La}_3\text{ZrTaO}_{12}$ . Results are presented in tables 3.1 and 3.2.

**Table 3.1** – Data collection and results of structure refinement of garnet-type  $\text{Li}_6\text{La}_3\text{ZrTaO}_{12}$ .

parameter		parameter	
composition XRD	$\text{Li}_{5.28}\text{La}_{2.92}\text{Ta}_{1.09}\text{Zr}_{0.91}\text{O}_{12}$	space group	$Ia\bar{3}d$
diffractometer	Bruker SMART APEX	radiation	Mo $K\alpha$
wavelength (Å)	0.71073	crystal system	cubic
$a$ (Å)	12.8768(2)	volume (Å <sup>3</sup> )	914.94(2)
$Z$	8	density $D_x$ (mg/m <sup>3</sup> )	5.693
crystal size (mm)	$0.21 \times 0.18 \times 0.17$	theta range (°)	3.876 - 38.910
index range $h / K / l$	-22 ... 22	resolution $d_{min}$ (Å)	0.57
reflections collected	313473	independent reflections	523
$R_{int}$	4.69	R1 (all data)	2.03
wR2 (all data)	3.83	Goof on $F^2$	1.492
extinction coefficient	0.00087(4)	largest diff. peak/hold	0.713/-0.813 $\text{e}\text{Å}^{-3}$

**Table 3.2** – Fractional atomic coordinates and anisotropic and equivalent isotropic atomic displacement parameters.

atom	x/a	y/b	z/c	Occ.	$U_{11}$	$U_{22}$	$U_{33}$	$U_{23}$	$U_{13}$	$U_{12}$	$U_{eq}$
O1 (96h)	0.10299(17)	0.19773(17)	0.28027(17)	1	0.0092(8)	0.0117(9)	0.0120(9)	0.0012(6)	0.0004(6)	-0.0005(6)	0.0110(4)
La1 (24c)	0.125	0	0.25	0.9748(8)	0.00958(13)	0.0070(1)	0.0070(1)	0.00295(9)	0	0	0.00786(9)
Zr1 (16a)	0	0	0	0.455(8)	0.00499(11)	0.00499(11)	0.00499(11)	-0.00003(5)	-0.00003(5)	-0.00003(5)	0.00499(11)
Ta1 (16a)	0	0	0	0.545(8)	0.00499(11)	0.00499(11)	0.00499(11)	-0.00003(5)	-0.00003(5)	-0.00003(5)	0.00499(11)
Li1 (24d)	0.375	0	0.25	0.75(2)	0.025(12)	0.056(13)	0.056(13)	0	0	0	0.046(10)
Li2 (96h)	0.1470(16)	0.1760(17)	0.4387(17)	0.25(3)							0.011(6)

A well-established method for getting first insights into the jump processes of Li ions in solids in a relatively easy way is the measurement of temperature-variable NMR line shapes. Line shapes

measurements are sensitive to both local and long-range Li ion hopping processes. In addition to possible quadrupolar effects at low temperatures, dipolar interactions broaden the spectra; such interactions are averaged with increasing diffusivity of the spin-carrying ions. For this purpose, static  ${}^7\text{Li}$  NMR spectra of single-crystalline garnet-type  $\text{Li}_6\text{La}_3\text{ZrTaO}_{12}$  were recorded as a function of temperature (see figure 3.2).

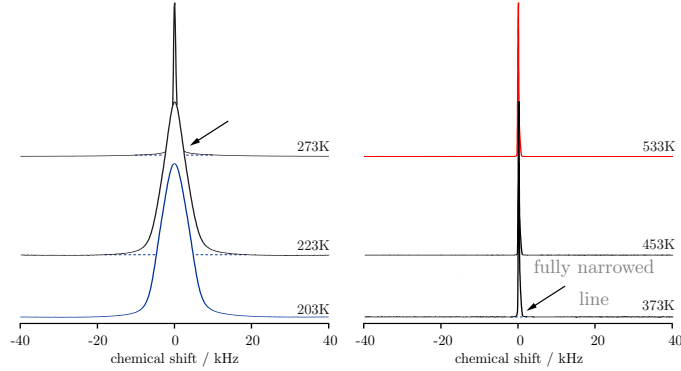


**Figure 3.2** – Static  ${}^7\text{Li}$  NMR spectra of single-crystalline garnet-type  $\text{Li}_6\text{La}_3\text{ZrTaO}_{12}$  recorded at  $\omega_0/2\pi = 116.4$  MHz. With increasing temperature  $T$  the line width of the central line, which is slightly anisotropic at higher  $T$ , undergoes a pronounced motional narrowing due to averaging of (homonuclear) dipole-dipole ( ${}^7\text{Li}$ – ${}^7\text{Li}$ ) interactions. Quadrupole intensities are significantly averaged due to lithium jump processes.

The spectrum of  $\text{Li}_6\text{La}_3\text{ZrTaO}_{12}$  is composed of a single Lorentzian-shaped central line with a width (full width at half-maximum, FWHM) of *ca.* 800 Hz at room temperature. At lower temperatures ( $T < 220$  K), the NMR lines exhibit a Gaussian-like shape. With increasing  $T$ , the central line transforms into an asymmetric Lorentzian-shaped line. The NMR line undergoes pronounced motional narrowing (MN) with increasing temperature due to averaging of dipole–dipole ( ${}^7\text{Li}$ – ${}^7\text{Li}$ ) interactions caused by increasing Li motions. As shown in figure 3.3, the central line of the garnet is already fully narrowed at ambient temperatures indicating very fast lithium ion diffusivity. The rigid lattice regime was not reached within the temperature range of the used setup (180 K to 400 K), meaning that MN already sets in at temperatures below 180 K.

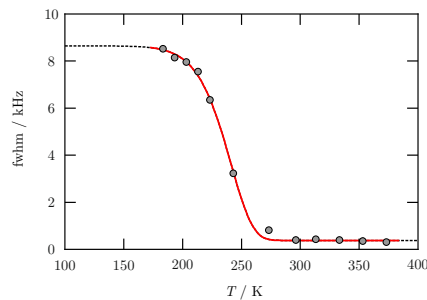


**Figure 3.3** – NMR line width (full width at half-maximum, FWHM) as a function of temperature  $T$ . The solid line is to guide the eye. See text for further explanation.

In addition to the NMR line shape analysis, variable-temperature  ${}^7\text{Li}$  spin-lattice relaxation (SLR) NMR rates in both the laboratory frame and the rotating frame of reference were recorded.  ${}^7\text{Li}$

SLR NMR rates in the laboratory frame of reference ( $1/T_1 = R_1$ ) were acquired under static, *i.e.*, nonrotating conditions and  $^7\text{Li}$  SLR NMR rates in the rotating frame of reference ( $1/T_{1\rho} = R_{1\rho}$ ) were recorded by using the well-established spin-locking technique at an angular locking frequency  $\omega_1/2\pi$  of 20 kHz. The latter is *per se* sensitive to slower Li diffusion processes compared to NMR measurements in the laboratory frame of reference. Both rates,  $R_1$  and  $R_{1\rho}$ , were obtained by parameterizing the resulting magnetic transients  $M_z(t_d)$  and  $M_\rho(t_{lock})$ , respectively, by stretched exponentials. (see figure 3.4 for some selected  $R_1$  and  $R_{1\rho}$  transients).

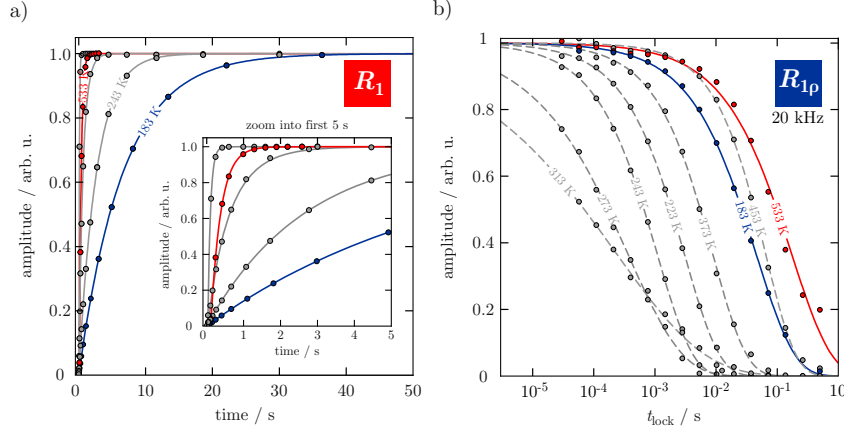


**Figure 3.4** – Selected temperature-variable magnetization transients containing the  $^7\text{Li}$  SLR NMR rates in the laboratory (a) and rotating frame of reference (b). The colored transients indicate the highest and lowest temperature measured. Solid and dashed lines show the fits using stretched exponentials of the form  $M_z(t_d) \propto 1 - \exp[-(t_d/T_1)^\gamma]$  and  $M_\rho(t_{lock}) \propto \exp[-(t_{lock}/T_{1\rho})^{\gamma'}]$  with stretching exponents,  $\gamma_1$  and  $\gamma_{1\rho}$ , ranging from 0.3 to 1.0, respectively (see upper graph in figure 3.5).

$^7\text{Li}$  SLR rates, recorded in both the laboratory frame ( $R_1$ ) and the rotating frame of reference ( $R_{1\rho}$ ), are shown as a function of the inverse temperature in an Arrhenius plot in figure 3.5. Both rates,  $R_1$  and  $R_{1\rho}$ , increase with the temperature  $T$  and pass through a maximum at approximately 430 K and 280 K, respectively. A full diffusion-induced SLR rate peak was obtained for  $R_{1\rho}$  by using the aforementioned spin-locking technique. The rate maximum of the  $R_{1\rho}$  rate peak is shifted towards lower temperatures; the maximum occurs if the maximum condition  $\omega_1\tau_c = 0.5$  is fulfilled. Lithium diffusivity is directly expressed by the correlation rate  $\tau_c^{-1}$  being in the same order of magnitude as the Li jump rate  $\tau^{-1}$ . This allows the direct determination of the Li jump rate  $\tau^{-1}$  which can be estimated by using the above mentioned maximum condition. It is worth mentioning that this estimation is based on an exponential correlation function for 3D diffusion. Here, at  $T_{max}$ , the jump rate  $\tau^{-1}$  is in the order of  $3 \times 10^5 \text{ s}^{-1}$ .

To deduce activation energies from the  $R_1(1/T)$  and  $R_{1\rho}(1/T)$  peaks and dynamic information on the elementary jump processes, the rates were analyzed with modified BPP-type spectral density functions  $J(\omega_0, \tau_c)$  and  $J(\omega_0, \omega_1, \tau_c)$  that are based on exponential motional correlation functions  $G(t')$  to describe the temperature dependence of  $R_1(1/T)$  and  $R_{1\rho}(1/T)$ , respectively.[12, 39, 44, 67, 74] Since the Lorentzian-shaped function  $J$  is directly proportional to  $R_1$  and  $R_{1\rho}$ , it can be derived from  $G$  by Fourier transformation.[28] For three-dimensional diffusion processes at higher temperatures in the limit  $\omega_{0(\rho)}\tau \ll 1$ , the spectral density function  $J$  is inverse proportional to the lithium residence time  $\tau$  according to  $J \propto \tau$ . Whereas in the LT limit where  $\omega_{0(\rho)}\tau \gg 1$  holds, the proportionality is given by

$J \propto \tau^{-1} \omega_{0(\rho)}^{-\beta}$  with  $1 < \beta \leq 2$ . Correlation effects are not taken into account in the original BPP-type behavior and a  $\beta = 2$  is predicted resulting in symmetrical relaxation rate peaks.[12, 39, 44, 75] Asymmetrical peaks are usually found for structurally complex ion conductors.[67, 76] These materials possess a broad range of short- and long-range motional processes affected by correlation effects resulting from, e.g. Coulomb interactions.[42] For the investigated garnet-type  $\text{Li}_6\text{La}_3\text{ZrTaO}_{12}$ , both the  $R_1(1/T)$  and  $R_{1\rho}(1/T)$ , BPP-type fits yield an asymmetry parameter  $\beta_{(\rho)} \approx 1.4$ .

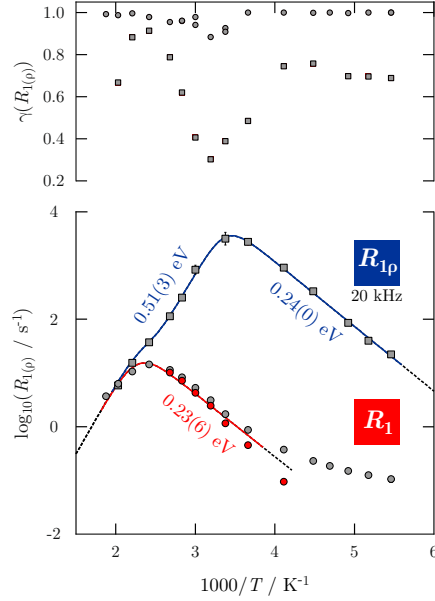


**Figure 3.5** – Detailed view of the Arrhenius plot of the  $^7\text{Li}$  SLR NMR rates of single crystalline LLZTO recorded at a Larmor frequency of  $\omega_0/2\pi = 116.4$  MHz. The upper graph shows the corresponding stretching exponents used to fit the transients with stretched exponentials. The solid lines represent a joint fit based on the BPP model. The rates measured were parameterized with a single set of diffusion parameters.

The data perfectly mirror a modified BPP-type relaxation response being based on a Lorentzian-shaped relaxation function. The NMR peaks  $R_1(1/T)$  and  $R_{1\rho}(1/T)$  of  $\text{Li}_6\text{La}_3\text{ZrTaO}_{12}$  are analyzed in terms of a global fit (solid lines in figure 3.5), that is, linking the fitting parameters such as  $\omega_0$ , the activation energies, and coupling constants. In the present case, the best fit is obtained when  $\beta \neq \beta_\rho$ . The nondiffusive background relaxation of the  $R_1(1/T)$  rates, which occurs below 240 K, was taken into account by using an appropriate power law:  $R_1 \propto T^\kappa$ .

An apparent activation energy of  $E_a = 0.23(6)$  eV and  $E_a = 0.24(0)$  eV was determined from the LT flank from the slopes of  $R_1$  and  $R_{1\rho}$  respectively of the fits shown in figure 3.5. These values, since they are deduced in the LT limit of a diffusion-induced rate peak, reflect short range Li ion dynamics being predominant in this temperature range. In the HT regime, where  $\omega_{0(\rho)}\tau \ll 1$  holds, an activation energy of  $0.51(3)$  eV was determined from the corresponding flank of the fit. The activation energies, determined in the limit  $\omega_{0(\rho)}\tau \ll 1$  of the NMR peak, are expected to be governed by an activation energy being similar to that found by DC-conductivity measurements. The activation energy from SLR NMR are in excellent agreement with results deduced from ongoing conductivity studies. *In concreto*, impedance spectroscopy revealed an activation energy  $E_a^{\text{DC}}$  of 0.47 eV and a conductivity in the order of  $2.9 \times 10^{-4}$  S  $\text{cm}^{-1}$  at room temperature.

In conclusion, single-crystalline garnet-type  $\text{Li}_6\text{La}_3\text{ZrTaO}_{12}$  is a material with a noteworthy high Li diffusivity. The long-range jump process is characterized by an activation energy of 0.5 eV, whereas the short-range jump process only has a hopping activation energy of 0.2 eV. The high diffusivity of the material is manifested in the  $R_{1\rho}(1/T)$  rate peak maximum showing up at a very low temperature of 280 K. The high Li diffusivity found makes the material a potential candidate for all-solid-state lithium battery.

### 3.2.2 Li ion dynamics in Bi-doped garnet-type $\text{Li}_{7-x}\text{La}_3\text{Zr}_{2-x}\text{Bi}_x\text{O}_{12}$

For more detailed information on the properties of  $\text{Li}_{7-x}\text{La}_3\text{Zr}_{2-x}\text{Bi}_x\text{O}_{12}$ , the reader is referred to the hereafter publication. First insights on lithium-ion dynamics were deduced from variable-temperature NMR line-shape measurements. The motional narrowing of  $^7\text{Li}$  NMR line width (full width at half maximum, FWHM) was used to predict the influence of Bi-doping on Li ion dynamics. At elevated temperatures, motional narrowing of the NMR line sets in as a result from averaged dipole–dipole interactions due to increased Li exchange processes. A closer look at the NMR lines of both samples  $x = 0.1$  and  $x = 0.9$ , respectively, reveals that the central line of  $\text{Li}_{6.1}\text{La}_3\text{Zr}_{0.1}\text{Bi}_{0.9}\text{O}_{12}$  is almost fully narrowed at ambient temperatures (see insert in figure 3.6), whereas the line of  $\text{Li}_{6.9}\text{La}_3\text{Zr}_{0.9}\text{Bi}_{0.1}\text{O}_{12}$  reaches full narrowed lines at much higher temperatures, around 460 K.

In addition,  $^7\text{Li}$  SLR NMR was employed to study Li diffusion parameters in more detail. Here,  $^7\text{Li}$   $R_1$  rates were measured at a Larmor frequency of  $\omega_0/2\pi = 116.4$  MHz to quantify lithium diffusion in terms of activation energies. The  $R_1$  rates were determined by parameterizing the resulting magnetization transients with exponential functions. The NMR spectra showed that fast translational Li ion dynamics are only observed for samples with large amounts of Bi incorporated ( $x > 0.8$ ); therefore, two samples of  $\text{Li}_{7-x}\text{La}_3\text{Zr}_{1-x}\text{Bi}_x\text{O}_{12}$  with  $x = 0.1$  and  $x = 0.9$  were investigated in more detail with SLR NMR measurements. In figure 3.6, the rates  $R_1$  ( $1/T$ ) vs. the inverse temperature are shown as an Arrhenius plot; together with an inset containing the motional narrowing.[77]

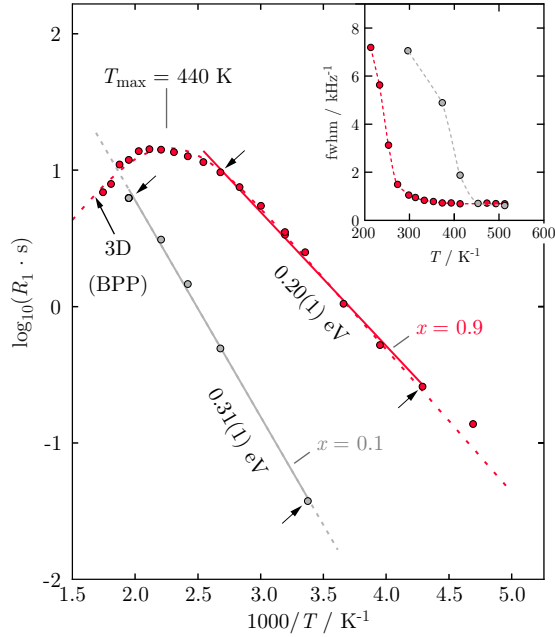


**Figure 3.6** – Arrhenius plot of the  $^7\text{Li}$  NMR  $R_1$  rates of  $\text{Li}_{7-x}\text{La}_3\text{Zr}_{1-x}\text{Bi}_x\text{O}_{12}$  with  $x = 0.1$  and  $x = 0.9$  recorded in the laboratory frame of reference measured at  $\omega_0/2\pi=16.4$  MHz. The colors refer to the intercalation degree  $x$  of the samples ( $x = 0.9$  - red  $\bullet$  and  $x = 0.1$  - gray  $\bullet$ ). Inset:  $^7\text{Li}$  NMR line width (FWHM) as a function of temperature  $T$ . The dashed line is drawn to guide the eye.

By increasing the temperature  $T$ , the rates for  $x = 0.9$  pass over into the so-called LT flank of a diffusion-induced peak and pass through a well-defined maximum showing up at the temperature  $T_{max} = 440\text{K}$ . However, because of slow lithium-ion diffusion, the HT flank could not be reached by the

rates of the sample with  $x = 0.1$ . Since our NMR setup allows only measurements up to 600 K, it was not possible to reach the maximum. While the HT flank entails information on long-range diffusion, the LT flank is affected by local, within-site ion dynamics, which can be additionally influenced by correlation effects such as Coulomb interactions and structural disorder. By comparing both rates to each other, the results reveal that Li diffusivity in  $\text{Li}_{7-x}\text{La}_3\text{Zr}_{1-x}\text{Bi}_x\text{O}_{12}$  with  $x = 0.9$  is faster than for  $x = 0.1$ . This is in perfect agreement with the preliminary results of temperature-variable NMR line shape measurements published (see following publication for more detail).

Ultimately, the diffusion-induced rate peak  $R_1$  of  $x = 0.9$  was fitted by using the spectral density function developed for three-dimensional diffusion introduced by Bloembergen, Purcell and Pound (BPP).[39] In figure 3.6, the corresponding BPP-type fit for  $x = 0.9$  is shown as a dashed red line. The measured SLR NMR rates ( $\beta = 1.93$ ) seem to follow the classical BPP relaxation behavior given by  $R_{1\rho} \propto \omega_1^{-2} \tau_c^{-1}$  for  $\omega_1 \tau_c \gg 1$ . The solid lines in figure 3.6 represent Arrhenius fits; from the slope of the flanks the activation energy for both samples was determined. The range of data points used for the fitting procedure is marked by the arrows drawn. An activation energy  $E_a^{\text{LT}}$  of 0.20(1) eV was extracted from the LT flank of the rate peak. A higher activation energy of 0.31(1) eV is found for  $\text{Li}_{7-x}\text{La}_3\text{Zr}_{1-x}\text{Bi}_x\text{O}_{12}$  with  $x = 0.1$ .

The  $^7\text{Li}$  SLR NMR measurements in the laboratory frame of reference confirmed the initial prediction that fast translational Li ion dynamics are only observed for samples with higher bismuth content.

## **Li ion dynamics in Bi-doped garnet-type $\text{Li}_{7-x}\text{La}_3\text{Zr}_{2-x}\text{Bi}_x\text{O}_{12}$**

### **Synthesis, crystal structure, and stability of cubic $\text{Li}_{7-x}\text{La}_3\text{Zr}_{2-x}\text{Bi}_x\text{O}_{12}$**

Reinhard Wagner, Daniel Rettenwander, Günther j. Redhammer, Gerold Tippelt, Gebhard Sabathi, Maurizio E. Musso, Bernhard Stanje, Martin Wilkening, Emmanuelle Suard and Georg Amthauer. *Inorganic Chemistry*, DOI: 10.1021/acs.inorgchem.6b01825 (2017), 12211 - 12219



This is an open access article published under a Creative Commons Attribution (CC-BY) License, which permits unrestricted use, distribution and reproduction in any medium, provided the author and source are cited.



## Synthesis, Crystal Structure, and Stability of Cubic $\text{Li}_{7-x}\text{La}_3\text{Zr}_{2-x}\text{Bi}_x\text{O}_{12}$

Reinhard Wagner,<sup>\*,†</sup> Daniel Rettenwander,<sup>†,||</sup> Günther J. Redhammer,<sup>†</sup> Gerold Tippelt,<sup>†</sup> Gebhard Sabathi,<sup>†</sup> Maurizio E. Musso,<sup>†</sup> Bernhard Stanje,<sup>‡</sup> Martin Wilkening,<sup>‡</sup> Emmanuelle Suard,<sup>§</sup> and Georg Amthauer<sup>†</sup>

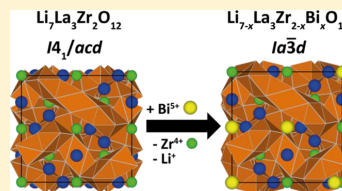
<sup>†</sup>Department of Chemistry and Physics of Materials, University of Salzburg, 5020 Salzburg, Austria

<sup>‡</sup>Christian Doppler Laboratory for Lithium Batteries, Institute for Chemistry and Technology of Materials, Graz University of Technology, 8010 Graz, Austria

<sup>§</sup>Diffraction Group, Institut Laue-Langevin (ILL), 71 avenue des Martyrs, 38000 Grenoble, France

### Supporting Information

**ABSTRACT:** Li oxide garnets are among the most promising candidates for solid-state electrolytes in novel Li ion and Li metal based battery concepts. Cubic  $\text{Li}_7\text{La}_3\text{Zr}_2\text{O}_{12}$  stabilized by a partial substitution of  $\text{Zr}^{4+}$  by  $\text{Bi}^{5+}$  has not been the focus of research yet, despite the fact that  $\text{Bi}^{5+}$  would be a cost-effective alternative to other stabilizing cations such as  $\text{Nb}^{5+}$  and  $\text{Ta}^{5+}$ . In this study,  $\text{Li}_{7-x}\text{La}_3\text{Zr}_{2-x}\text{Bi}_x\text{O}_{12}$  ( $x = 0.10, 0.20, \dots, 1.00$ ) was prepared by a low-temperature solid-state synthesis route. The samples have been characterized by a rich portfolio of techniques, including scanning electron microscopy, X-ray powder diffraction, neutron powder diffraction, Raman spectroscopy, and  $^7\text{Li}$  NMR spectroscopy. Pure-phase cubic garnet samples were obtained for  $x \geq 0.20$ . The introduction of  $\text{Bi}^{5+}$  leads to an increase in the unit-cell parameters. Samples are sensitive to air, which causes the formation of  $\text{LiOH}$  and  $\text{Li}_2\text{CO}_3$  and the protonation of the garnet phase, leading to a further increase in the unit-cell parameters. The incorporation of  $\text{Bi}^{5+}$  on the octahedral  $16a$  site was confirmed by Raman spectroscopy.  $^7\text{Li}$  NMR spectroscopy shows that fast Li ion dynamics are only observed for samples with high  $\text{Bi}^{5+}$  contents.



## 1. INTRODUCTION

Li stuffed oxide garnets have received much scientific attention as fast Li ion conductors. In particular, cubic  $\text{Li}_7\text{La}_3\text{Zr}_2\text{O}_{12}$  (LLZO) with its excellent chemical and thermal stability as well as its electrochemical inertness against Li metal is perfectly suited to be used as solid electrolyte and protecting layer in the next generation of all-solid-state Li ion and Li metal battery concepts.<sup>1,2</sup>

Pure LLZO occurs in at least two structural polymorphs: a low-temperature tetragonal (space group  $I4_1/acd$ ) and a cubic "high-temperature" phase (space group  $Ia\bar{3}d$ ).<sup>1,3</sup> Since the Li ion conductivity of the cubic phase is at least 2 orders of magnitude higher ( $10^{-4}$  to  $10^{-3}$  S  $\text{cm}^{-1}$  at room temperature) in comparison to the tetragonal phase, the stabilization of the cubic phase at room temperature is highly needed.<sup>3–5</sup>

Fortunately, the cubic polymorph can be stabilized at room temperature by doping with supervalent cations such as  $\text{Al}^{3+}$ ,<sup>2,5–8</sup>  $\text{Fe}^{3+}$ ,<sup>9,10</sup> and  $\text{Ga}^{3+}$ ,<sup>11–14</sup> which are incorporated on the 4-fold coordinated  $24d/96h$  positions replacing  $\text{Li}^+$ ,  $\text{Ce}^{4+}$  replacing  $\text{La}^{3+}$  on the 8-fold coordinated  $24c$  position,<sup>15</sup> and  $\text{Mo}^{6+}$ ,<sup>16,17</sup>  $\text{Nb}^{5+}$ ,<sup>18</sup>  $\text{Ta}^{5+}$ ,<sup>12,13,19–21</sup>  $\text{Sb}^{5+}$ ,<sup>22</sup>  $\text{Te}^{6+}$ ,<sup>23</sup>  $\text{W}^{6+}$ ,<sup>24</sup> and  $\text{Y}^{3+}$ ,<sup>25</sup> replacing  $\text{Zr}^{4+}$  at the octahedrally coordinated  $16a$  position. It was recently shown by Xia et al. that a stabilization of the cubic  $Ia\bar{3}d$  modification can also be achieved by a partial substitution of  $\text{Zr}^{4+}$  with  $\text{Bi}^{5+}$ ; the end member  $\text{Li}_5\text{La}_3\text{Bi}_2\text{O}_{12}$  (LLBO) was already described by Murugan et al. and further discussed in several other studies.<sup>26–30</sup>

The Li ion conductivity of LLZO at room temperature is still 1–2 orders of magnitude lower than that of widely used liquid electrolytes or other superionic conductors: e.g.,  $\text{Li}_{10}\text{GeP}_2\text{S}_{12}$  and  $\text{Li}_{1+x}\text{Al}_x\text{Ti}_{2-x}(\text{PO}_4)_3$  (LATP).<sup>31–33</sup> Hence, there is great interest in further improving its Li ion conductivity by microstructural and crystal chemical engineering.

The Li ion conductivity of cubic LLZO depends on various factors, such as, e.g., (i) amount of mobile charge carriers, (ii) vacancy concentration, (iii) coordination number of Li ions, (iv) strength and length of Li–O bond, and (v) microstructure of samples.<sup>34–36</sup>

These factors are strongly influenced by the cations that are added to stabilize the cubic  $Ia\bar{3}d$  modification of LLZO. Since  $\text{Bi}^{5+}$  has a larger ionic radius in comparison to  $\text{Zr}^{4+}$ , the unit-cell parameter  $a_0$  for  $\text{Li}_5\text{La}_3\text{Bi}_2\text{O}_{12}$  (LLBO) is significantly larger in comparison to that of LLZO stabilized with other dopant elements (13.065 vs 12.97 Å).<sup>27,37</sup>

We decided to study the LLZO–LLBO solid solution, in order to systematically vary  $a_0$  and the Li content. Therefore, we synthesized  $\text{Li}_{7-x}\text{La}_3\text{Zr}_{2-x}\text{Bi}_x\text{O}_{12}$  (LLZBO) with varying Bi contents ( $x = 0.10, 0.20, \dots, 1.00$ ) by solid-state synthesis at comparatively low temperatures. By means of X-ray powder diffraction (XRPD) and neutron powder diffraction (NPD) we studied the exchangeability of  $\text{Zr}^{4+}$  by  $\text{Bi}^{5+}$  in the LLZO–LLBO solid solution (LLZBO) and its stabilization effect on the cubic

Received: July 28, 2016

Published: November 15, 2016

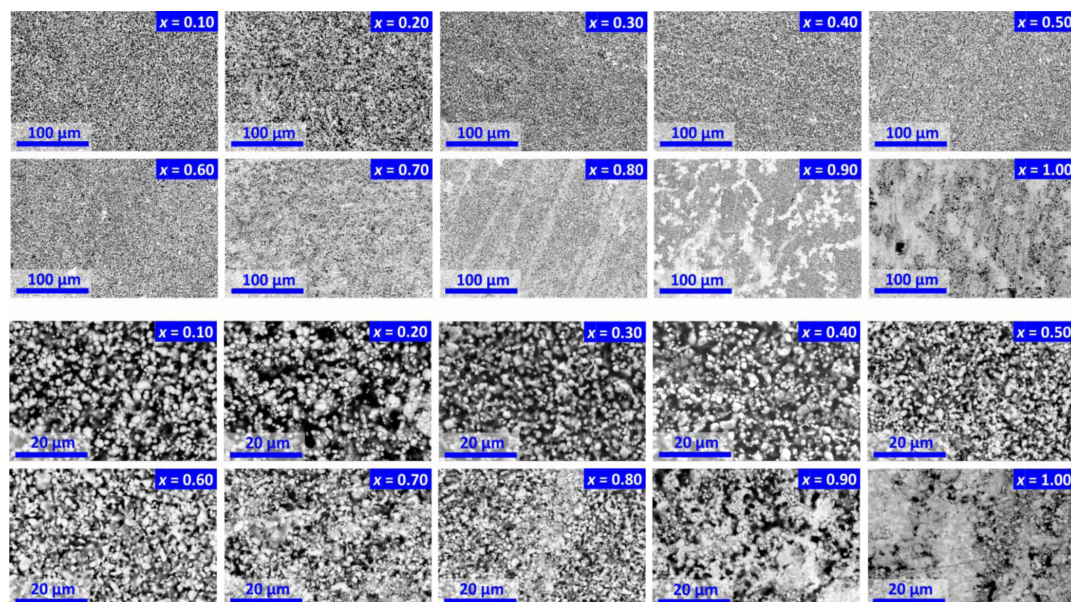


Figure 1. SEM-BSE images of  $\text{Li}_{7-x}\text{La}_3\text{Zr}_{2-x}\text{Bi}_x\text{O}_{12}$  with different magnifications.

LLZO structure. The influence of  $\text{Bi}^{5+}$  on the microstructure was evaluated by scanning electron microscopy (SEM) using backscattered electrons (BSE) and secondary electrons (SE). Energy-dispersive X-ray spectroscopy (EDX) measurements were performed to investigate the chemical composition of samples with regard to La, Zr, and Bi. Raman spectroscopy was applied to obtain information on the site occupation behavior of  $\text{Bi}^{5+}$ . Finally,  $^7\text{Li}$  nuclear magnetic resonance (NMR) line shape measurements were employed to study Li ion dynamics as a function of  $a_0$  and composition.

## 2. EXPERIMENTAL SECTION

**2.1. Synthesis.** A series of  $\text{Li}_{7-x}\text{La}_3\text{Zr}_{2-x}\text{Bi}_x\text{O}_{12}$  garnets with intended mole fractions of Bi ( $x_{\text{int}} = 0.10, 0.20, \dots, 1.00$ ) was synthesized by sintering in air. The starting materials were  $\text{Li}_2\text{CO}_3$  (99%, Merck),  $\text{La}_2\text{O}_3$  (99.99%, Roth),  $\text{ZrO}_2$  (99.0%, Roth), and  $\text{Bi}_2\text{O}_3$  (99.0%, Merck). The reagents were weighed out in their intended stoichiometric proportions with an excess of 10 wt % of  $\text{Li}_2\text{CO}_3$  to compensate for the loss of  $\text{Li}_2\text{O}$  during sintering. The reagents were mixed in an agate mortar and then cold-pressed into pellets with the help of a uniaxial press. The pellets were put into an alumina crucible. To avoid contamination with  $\text{Al}^{3+}$  from the crucible, the samples were placed on a pellet of pure LLZO. During the first sintering step, the samples were heated to  $850^\circ\text{C}$  at a rate of  $5^\circ\text{C min}^{-1}$  and calcinated for 4 h. The resulting pellets were then removed from the furnace, ground in an agate mortar, and ball-milled for 1 h in isopropyl alcohol (FRITSCH Pulverisette 7, 800 rpm, 2 mm  $\text{ZrO}_2$  balls). After drying in air, the powder was again cold-pressed into pellets. The sample pellets were again placed on a pellet of pure LLZO and then put into an alumina crucible. The final sintering step was performed at  $850^\circ\text{C}$  for 8 h in air. Small fragments of the sintered pellets were ground in an agate mortar and used for the XRPD, NPD, and NMR investigations. Material used for the last two characterization methods was stored under Ar. For SEM analysis, polycrystalline chips from the sample pellets were embedded in epoxy resin. The surface was ground and then polished using diamond paste. Relative densities of unaltered samples have been measured by pycnometry. The influence of the  $\text{Bi}^{5+}$

content and the unit-cell parameters on the theoretical densities has been considered by using theoretical densities obtained from Rietveld refinement of XRPD data. In addition, the presence of extra phases has also been taken into consideration.

**2.2. SEM.** Scanning electron microscopy investigations were performed using a Zeiss Ultra Plus device to determine the grain size and grain morphology of the samples. In particular, we put emphasis on the investigation of the phase composition and the chemical homogeneity, i.e. the distribution, of La, Zr, and Bi, using a backscattered electron detector (BSE) and energy-dispersive X-ray spectroscopy (EDX) measurements with an acceleration voltage of 20 kV.

**2.3. XRPD.** X-ray powder diffraction patterns were recorded with a Bruker D8 Advance DaVinci Design diffractometer with a Lynxeye solid-state detector using  $\text{Cu K}\alpha$  radiation to characterize the synthetic products in terms of all phases present and to determine the symmetry of the garnet. Data were collected in the range  $10^\circ \leq 2\theta \leq 80^\circ$ . For a precise determination of the unit-cell parameter  $a_0$ , separate measurements were performed with addition of a silicon standard with a well-known lattice constant ( $a_0 = 5.43088 \text{ \AA}$ ) to each sample. XRPD patterns were recorded on fresh samples immediately after synthesis as well as on samples that were stored in air for 1 and 3 weeks, respectively. The unit-cell parameter  $a_0$  was determined by Rietveld refinement using the program Topas V2.1 (Bruker).

**2.4. NPD.** Neutron powder diffraction measurements were performed at the Institut Laue-Langevin (ILL) in Grenoble, France. Powder diffraction data were collected at room temperature in constant wavelength mode with  $\lambda = 1.594 \text{ \AA}$  at the D2B diffractometer. Experiments were performed with a step width of  $0.04^\circ$  in the range  $5.8^\circ \leq 2\theta \leq 159.7^\circ$ . Data treatment and refinement were carried out with the FULLPROF suite of programs.<sup>38</sup> In all data evaluations, the La, (Zr + Bi), and O atom positions were refined using anisotropic atomic displacement parameters; the atomic displacement factor for the Li1 positions was refined isotropically while that of Li2 was set to 3.5 to avoid large correlations with the occupation factor. Site occupancies on Li sites were then allowed to refine unconstrained and (Zr + Bi) was fixed to full occupation of this site; however, the relative

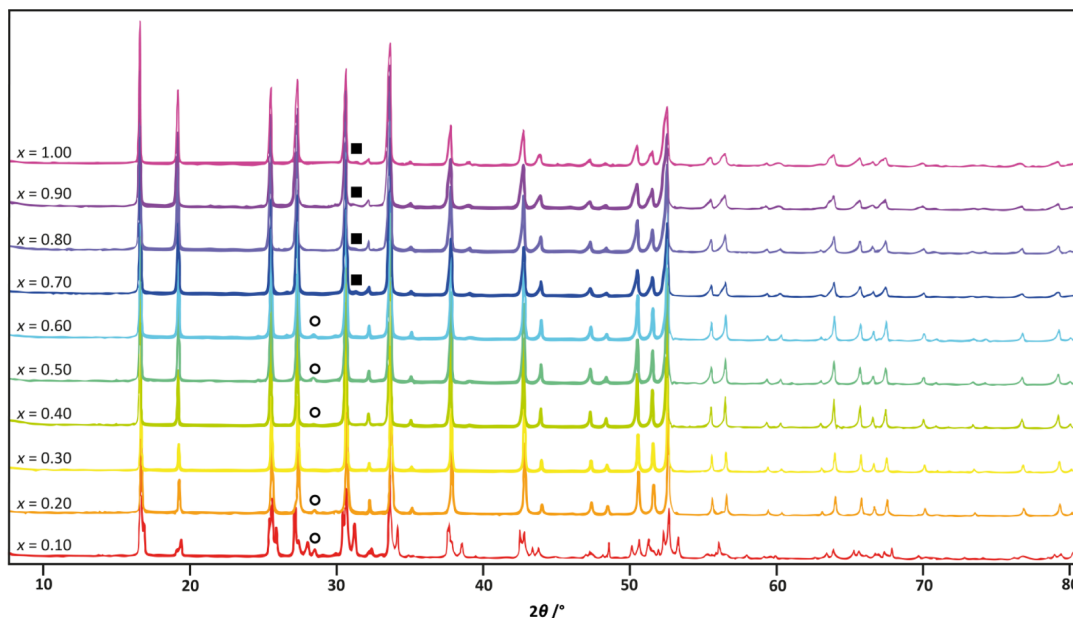


**Figure 2.** XRPD patterns of as-synthesized  $\text{Li}_{7-x}\text{La}_3\text{Zr}_{2-x}\text{Bi}_x\text{O}_{12}$  samples. Peaks at  $2\theta = 28.6^\circ$ , marked with open circles, are attributed to small amounts of  $\text{La}_2\text{Zr}_2\text{O}_7$ , while peaks at  $2\theta = 31.8^\circ$ , marked with black squares, are attributed to  $\text{Li}_2\text{CO}_3$ .

**Table 1.** Refined  $\text{Bi}^{3+}$  Content  $x_{\text{ref}}$ , Relative Density, and Unit-Cell Parameters  $a_0$  of LLZBO Derived from Rietveld Refinement of XRPD Data Collected Immediately after Synthesis as well as after Air Exposure for 1 and 3 Weeks, Respectively

$x_{\text{int}}$	$x_{\text{ref}}$	rel density (%)	$a_0$ (Å)		
			as synthesized	after 1 week	after 3 weeks
0.10	0.155	69	13.00265(57)	13.01189(23)	13.05982(40)
0.20	0.187	71	13.00222(27)	13.03072(31)	13.06170(43)
0.30	0.283	72	13.00547(48)	13.04424(33)	13.06736(39)
0.40	0.404	68	13.01373(53)	13.04441(28)	13.07248(47)
0.50	0.495	70	13.01896(72)	13.05463(25)	13.08688(20)
0.60	0.602	72	13.02295(17)	13.05933(33)	13.08769(12)
0.70	0.708	74	13.02912(29)	13.07479(23)	13.08501(18)
0.80	0.806	80	13.03307(31)	13.07065(23)	13.08578(15)
0.90	0.893	85	13.03699(37)	13.07647(23)	13.08517(21)
1.00	1.000	89	13.04522(31)	13.06803(33)	13.08144(25)

amounts of Bi and Zr were allowed to refine freely. The results for Bi and Zr occupancies agree well with those of XRPD refinements.

**2.5. Raman Spectroscopy.** Raman spectra of the sample pellets were collected at room temperature with a Thermo Scientific DXR Raman microscope using a 10 mW depolarized internal laser light source with an excitation wavelength of 780 nm. The Raman microscope was equipped with a high-resolution grating, allowing the collection of Raman spectra from 50 to 1800  $\text{cm}^{-1}$  with a spatial resolution (fwhm) of 2  $\text{cm}^{-1}$ .

**2.6.  $^7\text{Li}$  NMR Lines.** For the  $^7\text{Li}$  NMR line shape measurements under static, i.e., nonrotating, conditions the samples were ground in an agate mortar and fire-sealed under vacuum in DURAN glass ampules (ca. 4 cm in length and 0.5 cm in diameter) to permanently protect the powders from any moisture or air.  $^7\text{Li}$  NMR measurements were performed using a Bruker Avance III spectrometer, which was connected to a shimmed cryomagnet (Bruker) with a nominal external magnetic field of  $B_0 = 7.04$  T; the  $^7\text{Li}$  resonance frequency  $\omega_0/2\pi$  was 116.4 MHz.  $^7\text{Li}$  NMR spectra were recorded with the saturation recovery pulse sequence. In our case, this sequence contained 10  $\pi/2$

pulses to destroy any longitudinal magnetization  $M$ . After a constant waiting time, the magnetization recovered was flipped into the  $(xy)'$  plane via a final  $\pi/2$  pulse to detect the free induction decay. Fourier transformation and subsequent phase correction led to the spectra shown in this work.

### 3. RESULTS

**3.1. Crystal Size, Morphology, and Chemical Composition As Seen by SEM and SEM-EDX.** After the final sintering step, the sample pellets have a yellow color, the intensity of the color rising with increasing Bi content. Polished samples were examined by SEM-BSE. Figure 1 shows SEM-BSE images of samples with different Bi contents. The grain size of the samples is around 1–3  $\mu\text{m}$ . Single grains show an isometric shape. The Bi concentration does not have a significant effect on the grain size, but an improved densification is noted for samples with higher Bi concentrations. SEM-EDX measurements of La, Zr, and Bi show that

sample compositions for these elements are well in agreement with the intended stoichiometries. Very frequently, a fine-grained phase was found between single LLZBO grains. This phase is interpreted as a mixture of LiOH and  $\text{Li}_2\text{CO}_3$  that formed during processing and polishing of samples.

**3.2. Phase Composition and Unit-Cell Parameters As Seen via XRPD.** The XRPD patterns of the  $\text{Li}_{7-x}\text{La}_3\text{Zr}_{2-x}\text{Bi}_x\text{O}_{12}$  ( $x_{\text{int}} = 0.10\text{--}1.00$ ) are shown in Figure 2. The phase compositions of the samples were evaluated by Rietveld analysis. All samples exhibit reflections indicating cubic  $Ia\bar{3}d$  symmetry. For the sample with  $x_{\text{int}} = 0.10$ , Rietveld refinement shows about 66% of tetragonal LLZO and 34% of cubic garnet. Some samples show a small peak at  $2\theta = 28.6^\circ$  ( $d = 3.12 \text{ \AA}$ ), which can be attributed to  $\text{La}_2\text{Zr}_2\text{O}_7$ , while other samples show a reflection at  $2\theta = 31.8^\circ$  ( $d = 2.81 \text{ \AA}$ ), indicating the presence of small amounts of  $\text{Li}_2\text{CO}_3$ . If Zr and Bi contents on the octahedral 16a site are allowed to refine freely during Rietveld refinement, the refined Bi contents  $x_{\text{ref}}$  obtained from these refinements are well in accordance with the intended Bi contents  $x_{\text{int}}$  (see Table 1). Reflections show a relatively broad peak shape, especially at high  $2\theta$  angles.

As shown in Figure 3 and Table 1, the unit-cell parameters of LLZBO samples increase with increasing Bi content. For low Bi

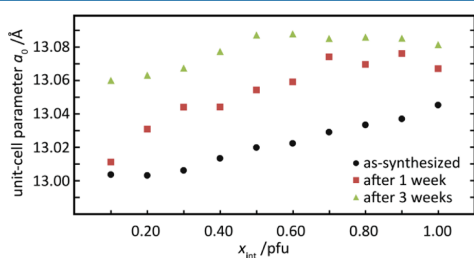


**Figure 3.** Unit-cell parameters  $a_0$  of as-synthesized LLZBO samples (black dots) and LLZBO samples after storage under air for 1 week (red squares) and 3 weeks (green triangles), respectively.

concentrations, the lattice parameter  $a_0$  is around  $13.00 \text{ \AA}$  and increases up to  $13.04 \text{ \AA}$  for the sample with  $x_{\text{int}} = 1.00$ . This observation is in agreement with Vegard's law, as 6-fold coordinated  $\text{Bi}^{5+}$  shows an ionic radius of  $0.76 \text{ \AA}$ , which is larger than that of 6-fold coordinated  $\text{Zr}^{4+}$  ( $0.72 \text{ \AA}$ ).<sup>37</sup> The correlation between the intended Bi content  $x_{\text{int}}$  and the unit-cell parameter  $a_0$  of LLZBO can be expressed by a simple linear regression:  $a_0 = 0.0494x_{\text{int}} + 12.994$ . A comparison with other studies on LLZBO shows that the unit-cell parameters obtained in this work are systematically higher; however, the slope of the linear regression is in agreement with other studies on LLZBO and LLBO.<sup>26–28</sup> The comparatively large unit-cell parameter might not only be attributed to the increase caused by the substitution of  $\text{Zr}^{4+}$  by  $\text{Bi}^{5+}$ ; it also seems to be related to a partial protonation of LLZBO due to a reaction of the garnet phase with moisture from the air, as this behavior was described for similar compounds as well.<sup>39,40</sup> This is also indicated by the presence of  $\text{Li}_2\text{CO}_3$  as mentioned above, as  $\text{Li}_2\text{CO}_3$  can result from the reaction of  $\text{CO}_2$  from air with LiOH, which is a side product of the protonation of LLZO-type materials.<sup>41–43</sup>

**3.3. Stability of LLZBO in Air.** To study the stability of LLZBO in air, samples were ground in an agate mortar and stored under air for 1 and 3 weeks, respectively. XRPD measurements including a silicon standard were performed to

investigate the formation of secondary phases as well as to determine the unit-cell parameters. The evolution of the unit-cell parameters as a function of the Bi content and the duration of exposure is shown in Figure 3 and Table 1. It is clearly visible that the unit-cell parameters increase if samples are stored under air. This increase is attributed to the protonation of the garnet phase, which was also reported by other studies on LLZO.<sup>39,40</sup> The protonation reaction also causes the formation of  $\text{Li}_2\text{CO}_3$ . The presence of small amounts of  $\text{Li}_2\text{CO}_3$  in aged samples was confirmed by XRPD measurements due to the presence of an additional reflection at  $d = 4.16 \text{ \AA}$ . The peak width of LLZO reflections, especially at high  $2\theta$  angles, increases even further in comparison to XRPD patterns of fresh samples; however, attempts to perform a fit using two different LLZBO garnets with different unit-cell parameters did not lead to a significant improvement. Attempts were also made to perform a structural refinement using the  $I\bar{4}3d$  model, which was recently reported for protonated Li oxide garnets and LLZO garnets stabilized with certain cations such as  $\text{Ga}^{3+}$  and  $\text{Fe}^{3+}$ .<sup>40,44–47</sup> As the characteristic 310 reflection of space group  $I\bar{4}3d$ , which appears at  $d = 4.10 \text{ \AA}$  ( $2\theta = 21.6^\circ$ ) for LLZO garnets with a unit-cell parameter of  $12.97 \text{ \AA}$ , would shift to larger  $d$  values due to the increasing unit-cell parameters of LLZBO, it might be possible that the additional reflection at  $d = 4.16 \text{ \AA}$  ( $2\theta = 21.35^\circ$ ) is related to the phase transformation to the  $I\bar{4}3d$  space group. Rietveld refinement showed that, even for strongly protonated LLZBO samples with large unit-cell parameters of  $13.08 \text{ \AA}$ , this characteristic 310 reflection of space group  $I\bar{4}3d$  would be located at  $d = 4.138 \text{ \AA}$  ( $2\theta = 21.45^\circ$ ). Therefore, the additional reflection at  $d = 4.16 \text{ \AA}$  ( $2\theta = 21.35^\circ$ ) is attributed to the 110 reflection of  $\text{Li}_2\text{CO}_3$  and not to a LLZBO garnet phase with space group  $I\bar{4}3d$ . In addition, the evolution of a small peak at  $2\theta = 31.8^\circ$  ( $d = 2.81 \text{ \AA}$ ) can also be related to  $\text{Li}_2\text{CO}_3$ . The presence of  $\text{Li}_2\text{CO}_3$  was also confirmed by evaluation of NPD measurements as well as by Raman spectroscopy.

**3.4. NPD.** Results of neutron powder diffraction generally confirmed the results obtained by XRPD. Refinement results of 2 different NPD measurements are shown in Figures S1 and S2 in the Supporting Information. As the samples were stored under an Ar atmosphere, NPD samples were only slightly affected by protonation and aging, in comparison to samples from XRPD measurements. The  $\text{Li}_2\text{CO}_3$  contents were quantified for all LLZBO samples, yielding about 2%  $\text{Li}_2\text{CO}_3$ . Small contents of LiOH were found as well. As determined by XRPD, the sample with  $x_{\text{int}} = 0.10$  still shows both tetragonal  $I4_1/acd$  and cubic  $Ia\bar{3}d$  garnet modifications. In contrast to the evaluation of XRPD data, a model with two different cubic (space group  $Ia\bar{3}d$ ) LLZBO phases was used for the evaluation of NPD data of samples with  $x_{\text{int}} \geq 0.30$ , as the data quality and resolution of data obtained from NPD are better than those obtained from XRPD. This model consists of an LLZBO phase that is unaffected or only slightly affected by protonation and a second LLZBO phase which is strongly affected by protonation on the  $96h$  site, therefore showing a larger unit-cell parameter. For this second phase only  $\text{H}^+$  was assumed to occupy  $96h$ ; fractional atomic coordinates are close to those reported recently for protonated LLZO with space group  $Ia\bar{3}d$ .<sup>48</sup> In the unprotonated material, the Li content decreases with increasing Bi content, for both the Li1 and Li2 sites to similar extents; however, data overlap is large so that no additional detailed structural parameters can be extracted. Unit-cell parameters of unprotonated and protonated LLZBO phases of different

samples obtained by Rietveld refinements of NPD data are shown in Table S1 and Figure S3 in the Supporting Information; the corresponding structural data of selected samples are given in Table S2 in the Supporting Information. Unit-cell parameter values for unprotonated LLZBO samples are similar to values of as-synthesized values obtained from XRPD; while the unit-cell parameters of protonated LLZBO phases are similar to XRPD-derived values of samples that have been stored in air for 1 week. The discontinuity of the unit-cell parameter between samples with  $x_{\text{int}} = 0.70$  and  $x_{\text{int}} = 0.80$  might be related to different alteration stages that could not be resolved. Rietveld refinements yield protonated garnet contents between 22% and 34%.

**3.5. Raman Spectroscopy.** Raman spectra of LLZBO samples are shown in Figure 4.

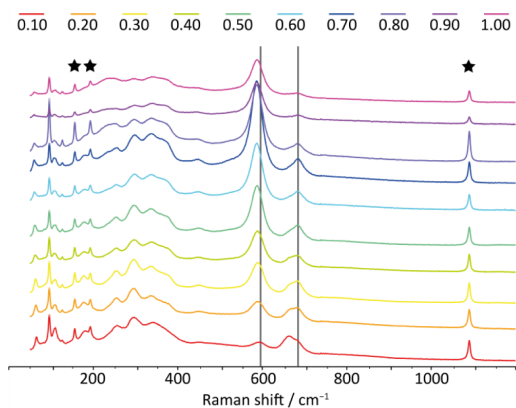


**Figure 4.** Raman spectra of  $\text{Li}_{7-x}\text{La}_3\text{Zr}_{2-x}\text{Bi}_x\text{O}_{12}$  samples ( $x = 0.10, 0.20, \dots, 1.00$ ). Bands at 156, 195, and 1090  $\text{cm}^{-1}$ , marked with stars, are attributed to  $\text{Li}_2\text{CO}_3$ . Two vertical lines have been added to highlight the shifting of bands.

In general, the obtained spectra show a good coincidence with other spectra of cubic LLZO stabilized with different aliovalent cations.<sup>16,19,43,49,50</sup> In addition to the characteristic LLZO bands, additional bands at 156, 195, and 1090  $\text{cm}^{-1}$  were observed for all samples. These bands can be assigned to  $\text{Li}_2\text{CO}_3$ .<sup>41,51–53</sup> Considering the evolution of the Raman spectra depending on the variation in the Zr/Bi ratio, the most prominent features are two bands at  $\sim 590$  and  $\sim 650$   $\text{cm}^{-1}$ , respectively, which show a distinct trend, depending on the Bi content. The band at  $\sim 590$   $\text{cm}^{-1}$  gets more intense and slightly shifts to lower wavenumbers with increasing Bi content, whereas at the same time the intensity of the band at  $\sim 650$   $\text{cm}^{-1}$  decreases and the band shifts toward higher wavenumbers. Bands in this region are interpreted as M–O breathing modes of the octahedral 16a position. Mukhopadhyay et al. observed that the Zr–O associated band appears at 640  $\text{cm}^{-1}$ , whereas a Ta–O associated band is present at 720  $\text{cm}^{-1}$ .<sup>19</sup> This effect was due to a shorter bond length of Ta–O in comparison to Zr–O. Rettenwander et al. observed an analogous effect for  $\text{Li}_{7-2x}\text{La}_3\text{Zr}_{2-x}\text{Mo}^{6+}_x\text{O}_{12}$ , as they observed the appearance and intensity increase of a band at  $\sim 770$   $\text{cm}^{-1}$  with increasing Mo content of the garnet.<sup>16</sup> The evolution of the Raman spectra of LLZBO can be explained similarly. The progression of the band at 590  $\text{cm}^{-1}$  is considered as an effect

of the extended bond length of Bi–O bonds in comparison to Zr–O bonds, as the ionic radius of  $\text{Bi}^{5+}$  is larger than that of  $\text{Zr}^{4+}$ , resulting in the appearance of a band at smaller wavenumbers, which slightly shifts to lower wavenumbers with increasing Bi contents, in accordance with the slightly increasing unit-cell parameters of the LLZBO samples with increasing Bi contents. Another interesting feature can be observed in the low-wavenumber region between 200 and 400  $\text{cm}^{-1}$ , in particular for samples with high  $\text{Bi}^{5+}$  contents ( $x_{\text{int}} = 0.80–1.00$ ). Raman spectra show a broadening of the bands in this region. The broad bands were also found in other studies and have been attributed to disorder caused by the migration of highly mobile  $\text{Li}^+$  ions along the  $\text{Li}^+$  diffusion pathways.<sup>43,49,54</sup> These observations are well in accordance with results of  $^7\text{Li}$  NMR spectroscopy.

**3.6. Static  $^7\text{Li}$  NMR Spectra: Line Narrowing.** NMR line shapes of the quadrupole  $^7\text{Li}$  nucleus (spin quantum number  $I = 3/2$ ) are sensitive to both local and long-range Li ion hopping processes. In addition to possible quadrupolar effects, at low temperatures dipolar interactions broaden the spectra; such interactions are averaged with increasing diffusivity of the spin-carrying ions. Thus, by a comparison of line shapes of samples with different compositions at the same temperature, preliminary information on Li ion dynamics can be deduced. For this purpose, static  $^7\text{Li}$  NMR spectra of  $\text{Li}_{7-x}\text{La}_3\text{Zr}_{2-x}\text{Bi}_x\text{O}_{12}$  ( $x_{\text{int}} = 0.10–1.00$ ) were recorded at three different temperatures at a Larmor frequency of  $\omega_0/2\pi = 116.4$  MHz (see Figures 5 and 6).

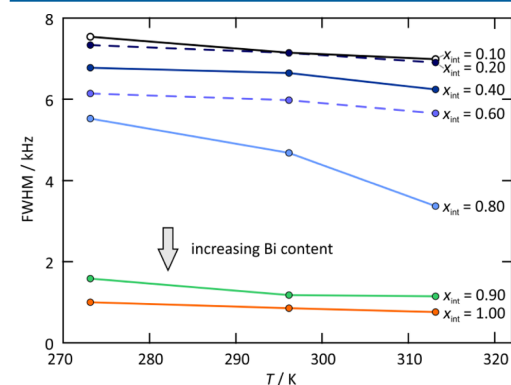


**Figure 5.**  $^7\text{Li}$  NMR line width (fwhm = full width at half-maximum, 116 MHz) as a function of temperature  $T$ . The lines are drawn to guide the eye. The higher the Bi content, the faster the Li ions exchange among the crystallographic sites in the garnets. See the text for further explanations.

While at a Bi content of  $x_{\text{int}} > 0.60$  the line width (full width at half-maximum), when read off at 273 K, ranges from approximately 6 to ca. 7 kHz, it clearly drops down to only 850 Hz when  $x_{\text{int}} = 1.00$  is reached (Figure 5). Importantly, already at  $x_{\text{int}} = 0.80$  a narrow top superimposes the broad Gaussian-shaped line which characterizes the central line of the other samples (see Figure 6). The narrow component is the first indication of a fast-diffusing spin subensemble having access to jump pathways with low activation barriers. At  $x_{\text{int}} = 1.00$  the narrow line governs almost the whole NMR spectrum (Figure 6), which reveals that almost all Li ions participate in fast ion

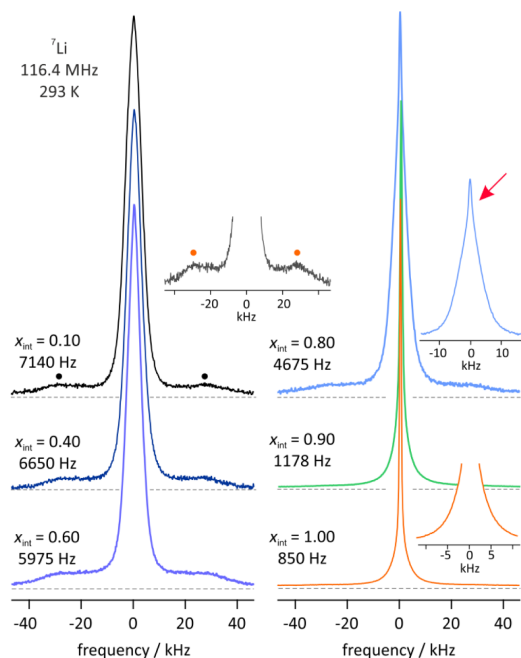


**Figure 6.** Static  ${}^7\text{Li}$  NMR spectra of  $\text{Li}_{7-x}\text{La}_3\text{Zr}_{2-x}\text{Bi}_x\text{O}_{12}$  ( $x_{\text{int}} = 0.10$ – $1.00$ ) recorded at  $\omega_0/2\pi = 116.4$  MHz and 273 K. Full line narrowing is reached at  $x_{\text{int}} = 0.90$ ; at this composition, quadrupole intensities are significantly averaged due to Li jump processes. The sample with  $x_{\text{int}} = 0.80$  already reveals a two-component line shape representing fast and slow Li ions. See the text for further explanation.

exchange. The central line of the sample with  $x_{\text{int}} = 1.00$  does not change further with increasing temperature; at  $T > 273$  K the shape of the spectra remains unchanged, demonstrating that the extreme narrowing regime was already reached at 273 K (Figure 5). On consideration of a rigid-lattice line width,  $\nu_{\text{rl}}$ , on the order of a few kilohertz, at 273 K (and also higher temperatures) the Li jump rate  $\tau^{-1}$  is estimated to be at least of the same order of magnitude. This is in contrast to the samples with  $x_{\text{int}} > 0.60$ : up to  $T \approx 310$  K only the rigid-lattice regime is detected (Figure 5). The corresponding mean Li jump rate turns out to be much lower than  $\nu_{\text{rl}}$  and, hence, has no effect on the line width. Hence, significant Li ion dynamics, able to average homonuclear dipole–dipole couplings, is only observed for samples with large amounts of Bi incorporated. The change in rigid-lattice line width with increasing  $x_{\text{int}}$ , cf. the samples with  $x_{\text{int}} < 0.60$ , presumably reflects a decreasing Li–Li distance to which  $\nu_{\text{rl}}$  is sensitive.

Li diffusivity averages not only magnetic dipolar but also electric quadrupolar interactions. These effects result from the interaction of the quadrupole moment of the Li nucleus with a nonvanishing electric field gradient at the nuclear site. In contrast to the situation with no electric field gradient, the four Zeeman levels are perturbed so that, in the case of a polycrystalline sample, a powder pattern shows up (Figure 6). Li diffusivity also affects this pattern, leading to averaged quadrupole satellite lines at sufficiently high temperatures. For  $x_{\text{int}} < 0.80$  the NMR lines reveal distinct patterns (see also the inset shown for the sample with  $x_{\text{int}} = 0.10$  in Figure 6). The

$90^\circ$  singularities, marked in Figure 6 with dots, point to coupling constants in the order of 60 kHz. The larger the  $x_{\text{int}}$  value, the higher the Li exchange among the electrically different Li sites. Sufficiently fast exchange causes the pattern to vanish. At  $T$  values much higher than those covered in this study, the emergence of a new, fully averaged quadrupole powder pattern is expected, characterized by a reduced coupling constant.

#### 4. DISCUSSION

The main goal of this study is to observe the influence of a partial substitution of  $\text{Zr}^{4+}$  by  $\text{Bi}^{5+}$  in LLZO and the stabilization of the cubic phase. Pure-phase cubic samples were obtained for Bi contents  $x_{\text{int}} \geq 0.20$ , which is consistent with the results of previous studies.<sup>26</sup> It has to be noted that pure-phase cubic garnet samples are obtained by comparatively low Bi contents, as much higher dopant concentrations are needed if other substituting cations, such as  $\text{Ta}^{5+}$  and  $\text{Nb}^{5+}$ , are used as substituents for  $\text{Zr}^{4+}$ .<sup>50,55</sup> Rietveld refinement of XRPD data confirms a systematic increase of the unit-cell parameter with increasing  $\text{Bi}^{5+}$  content; additionally, the increase of the unit-cell parameter is partially caused by a protonation of the garnet phase. The increase of the unit-cell parameter due to protonation and the observation of  $\text{Li}_2\text{CO}_3$  from NPD as well as from Raman spectroscopy indicate that LLZBO is unstable in air. As NPD samples, which have been stored under Ar directly after the synthesis, already show the first signs of protonation, the protonation might already start during the cooling of samples in the furnace. Reactions with  $\text{H}_2\text{O}$  and  $\text{CO}_2$  from the air cause the formation of  $\text{LiOH}$  and  $\text{Li}_2\text{CO}_3$  and lead to a protonation of the garnet, which has negative effects on the ionic conductivity.<sup>40–44,55–59</sup> Due to the small grain size of the samples and the high porosity of the pellets, both being side effects of the low sintering temperature, the samples provide a large surface for interactions with air. LLZBO samples from this study seem to be very prone to these reactions, as the increase of the lattice parameter was observed after less than 1 week of storage in air. Even samples characterized by XRPD immediately after synthesis show indications for the aging process mentioned above.  $\text{Li}_2\text{CO}_3$  was partially also documented from XRPD measurements of samples immediately after synthesis; however, small concentrations of  $\text{Li}_2\text{CO}_3$  are hardly observable by XRPD. LLZBO samples stored under Ar were less affected by the aging process, as the unit-cell parameters obtained by NPD, where samples have been stored under Ar, were lower than those obtained from XRPD. However, even NPD samples showed indications for the aging process such as the formation of  $\text{Li}_2\text{CO}_3$  and the presence of protonated LLZBO. Therefore, the exposure of LLZBO to air should be strictly avoided. In addition, an enhancement of the density of LLZBO samples would also be beneficial, as the surface area of LLZBO grains available for interaction with air would decrease. An increase in the density of LLZBO samples will also have positive effects on the Li ion conductivity.

Results from  ${}^7\text{Li}$  NMR spectroscopy show that fast Li ion diffusivity for LLZBO is only achieved for high Bi contents. As the samples have been stored under Ar, the samples have not been significantly affected by protonation and the results show a very clear trend as a function of the Bi content. Xia et al. studied the Li ion conductivity of cubic LLZBO with  $x = 0.20$  and obtained a Li ion conductivity of  $2.6 \times 10^{-5} \text{ S cm}^{-1}$ .<sup>26</sup> The results from this study indicate that higher Li ion conductivities might be achieved by using samples with higher Bi contents.

Also for Ta-stabilized LLZO, the highest conductivities were reported for Ta contents of 0.60 atoms per formula unit.<sup>60</sup> The results of Xia et al. also show that an increase of the density of samples, either by higher sintering temperatures or by the introduction of Al<sup>3+</sup> that acts as a sintering aid, are beneficial for the Li ion conductivity. As stated above, an improved preparation route for LLZBO will be necessary to obtain satisfying electrochemical performances. As Ga<sup>3+</sup> seems to be an even more effective sintering aid for LLZO in comparison to Al<sup>3+</sup>, it may be worth preparing and studying Ga-bearing LLZBO samples as well.

## 5. CONCLUSIONS

The cubic modification of LLZO can be stabilized by a substitution of Zr<sup>4+</sup> with Bi<sup>5+</sup>. Samples prepared by a low-temperature synthesis route show a broad peak shape in XRPD and are sensitive to moisture and CO<sub>2</sub> content in air, which leads to the protonation of LLZBO and the formation of LiOH and Li<sub>2</sub>CO<sub>3</sub>. This aging has been proven by NPD and Raman spectroscopy as well. The incorporation of Bi into the LLZO structure leads to the evolution of an additional band in the Raman spectra at ~590 cm<sup>-1</sup>. <sup>7</sup>Li NMR spectroscopy shows that fast translational Li ion dynamics are only observed for samples with large amounts of Bi incorporated.

## ■ ASSOCIATED CONTENT

### Supporting Information

The Supporting Information is available free of charge on the ACS Publications website at DOI: 10.1021/acs.inorgchem.6b01825.

Results of Rietveld refinement of NPD measurements of samples with  $x_{\text{int}} = 0.20$  and  $x_{\text{int}} = 0.90$ , respectively, unit-cell parameters of LLZBO obtained from Rietveld refinement of NPD measurements, unit-cell parameters of LLZBO obtained by Rietveld refinement of NPD measurements, and structural models of samples with  $x_{\text{int}} = 0.20$  and  $x_{\text{int}} = 0.80$  derived from Rietveld refinement of NPD data (PDF)

## ■ AUTHOR INFORMATION

### Corresponding Author

\*E-mail for R.W.: Reinhard.Wagner@sbg.ac.at.

### Present Address

<sup>||</sup>Center for Materials Science and Engineering, Massachusetts Institute of Technology, Cambridge, Massachusetts 02139, United States

### Notes

The authors declare no competing financial interest.

## ■ ACKNOWLEDGMENTS

This study was supported by the Austrian Science Fund (FWF), project number P25702. The authors thank the ILL for allocation of neutron beam time and financial support.

## ■ REFERENCES

- (1) Murugan, R.; Thangadurai, V.; Weppner, W. Fast lithium ion conduction in garnet-type Li<sub>7</sub>La<sub>3</sub>Zr<sub>2</sub>O<sub>12</sub>. *Angew. Chem., Int. Ed.* **2007**, *46*, 7778–7781.
- (2) Geiger, C. A.; Alekseev, E.; Lazic, B.; Fisch, M.; Armbruster, T.; Langner, R.; Fechtelkord, M.; Kim, N.; Petteke, T.; Weppner, W. Crystal Chemistry and Stability of "Li<sub>7</sub>La<sub>3</sub>Zr<sub>2</sub>O<sub>12</sub>" Garnet: A Fast Lithium-Ion Conductor. *Inorg. Chem.* **2011**, *50*, 1089–1097.

- (3) Awaka, J.; Kijima, N.; Hayakawa, H.; Akimoto, J. Synthesis and structure analysis of tetragonal Li<sub>7</sub>La<sub>3</sub>Zr<sub>2</sub>O<sub>12</sub> with the garnet-related type structure. *J. Solid State Chem.* **2009**, *182*, 2046–2052.

- (4) Thangadurai, V.; Narayanan, S.; Pinzaru, D. Garnet-type solid-state fast Li ion conductors for Li batteries: critical review. *Chem. Soc. Rev.* **2014**, *43*, 4714–4727.

- (5) Buschmann, H.; Dolle, J.; Berendts, S.; Kuhn, A.; Bottke, P.; Wilkening, M.; Heitjans, P.; Senyshyn, A.; Ehrenberg, H.; Lotnyk, A.; Duppel, V.; Kienle, L.; Janek, J. Structure and dynamics of the fast lithium ion conductor "Li<sub>7</sub>La<sub>3</sub>Zr<sub>2</sub>O<sub>12</sub>". *Phys. Chem. Chem. Phys.* **2011**, *13*, 19378–19392.

- (6) Rettenwander, D.; Blaha, P.; Laskowski, R.; Schwarz, K.; Bottke, P.; Wilkening, M.; Geiger, C. A.; Amthauer, G. DFT Study of the Role of Al<sup>3+</sup> in the Fast Ion-Conductor Li<sub>7-3x</sub>Al<sub>x</sub><sup>3+</sup>La<sub>3</sub>Zr<sub>2</sub>O<sub>12</sub> Garnet. *Chem. Mater.* **2014**, *26*, 2617–2623.

- (7) Jin, Y.; McGinn, P. Al-doped Li<sub>7</sub>La<sub>3</sub>Zr<sub>2</sub>O<sub>12</sub> synthesized by a polymerized complex method. *J. Power Sources* **2011**, *196*, 8683–8687.

- (8) Rangasamy, E.; Wolfenstine, J.; Sakamoto, J. The role of Al and Li concentration on the formation of cubic garnet solid electrolyte of nominal composition Li<sub>7</sub>La<sub>3</sub>Zr<sub>2</sub>O<sub>12</sub>. *Solid State Ionics* **2012**, *206*, 28–32.

- (9) Rettenwander, D.; Geiger, C. A.; Amthauer, G. Synthesis and Crystal Chemistry of the Fast Li-Ion Conductor Li<sub>7</sub>La<sub>3</sub>Zr<sub>2</sub>O<sub>12</sub> Doped with Fe. *Inorg. Chem.* **2013**, *52*, 8005–8009.

- (10) Rettenwander, D.; Geiger, C. A.; Tribus, M.; Tropper, P.; Wagner, R.; Tippelt, G.; Lottermoser, W.; Amthauer, G. The solubility and site preference of Fe<sup>3+</sup> in Li<sub>7-3x</sub>Fe<sub>x</sub>La<sub>3</sub>Zr<sub>2</sub>O<sub>12</sub> garnets. *J. Solid State Chem.* **2015**, *230*, 266–271.

- (11) Rettenwander, D.; Geiger, C. A.; Tribus, M.; Tropper, P.; Amthauer, G. A Synthesis and Crystal Chemical Study of the Fast Ion Conductor Li<sub>7-3x</sub>Ga<sub>x</sub>La<sub>3</sub>Zr<sub>2</sub>O<sub>12</sub> with  $x = 0.08$  to 0.84. *Inorg. Chem.* **2014**, *53*, 6264–6269.

- (12) Allen, J. L.; Wolfenstine, J.; Rangasamy, E.; Sakamoto, J. Effect of substitution (Ta, Al, Ga) on the conductivity of Li<sub>7</sub>La<sub>3</sub>Zr<sub>2</sub>O<sub>12</sub>. *J. Power Sources* **2012**, *206*, 315–319.

- (13) Wolfenstine, J.; Ratchford, J.; Rangasamy, E.; Sakamoto, J.; Allen, J. L. Synthesis and high Li-ion conductivity of Ga-stabilized cubic Li<sub>7</sub>La<sub>3</sub>Zr<sub>2</sub>O<sub>12</sub>. *Mater. Chem. Phys.* **2012**, *134*, 571–575.

- (14) El Shinawi, H.; Janek, J. Stabilization-of cubic lithium-stuffed garnets of the type "Li<sub>7</sub>La<sub>3</sub>Zr<sub>2</sub>O<sub>12</sub>" by addition of gallium. *J. Power Sources* **2013**, *225*, 13–19.

- (15) Rangasamy, E.; Wolfenstine, J.; Allen, J.; Sakamoto, J. The effect of 24c-site (A) cation substitution on the tetragonal-cubic phase transition in Li<sub>7-x</sub>La<sub>3-x</sub>A<sub>x</sub>Zr<sub>2</sub>O<sub>12</sub> garnet-based ceramic electrolyte. *J. Power Sources* **2013**, *230*, 261–266.

- (16) Rettenwander, D.; Welzl, A.; Cheng, L.; Fleig, J.; Musso, M.; Suard, E.; Doeff, M. M.; Redhammer, G. J.; Amthauer, G. Synthesis, Crystal Chemistry, and Electrochemical Properties of Li<sub>7-2x</sub>La<sub>3</sub>Zr<sub>2-x</sub>Mo<sub>x</sub>O<sub>12</sub> ( $x = 0.1$ – $0.4$ ): Stabilization of the Cubic Garnet Polymorph via Substitution of Zr<sup>4+</sup> by Mo<sup>6+</sup>. *Inorg. Chem.* **2015**, *54*, 10440–10449.

- (17) Bottke, P.; Rettenwander, D.; Schmidt, W.; Amthauer, G.; Wilkening, M. Ion Dynamics in Solid Electrolytes: NMR Reveals the Elementary Steps of Li<sup>+</sup> Hopping in the Garnet Li<sub>6.3</sub>La<sub>3</sub>Zr<sub>1.73</sub>Mo<sub>0.25</sub>O<sub>12</sub>. *Chem. Mater.* **2015**, *27*, 6571–6582.

- (18) Ohta, S.; Kobayashi, T.; Asaoka, T. High lithium ionic conductivity in the garnet-type oxide Li<sub>7-x</sub>La<sub>3</sub>(Zr<sub>2-x</sub>Nb<sub>x</sub>)O<sub>12</sub> ( $X = 0$ – $2$ ). *J. Power Sources* **2011**, *196*, 3342–3345.

- (19) Mukhopadhyay, S.; Thompson, T.; Sakamoto, J.; Huq, A.; Wolfenstine, J.; Allen, J. L.; Bernstein, N.; Stewart, D. A.; Johannes, M. D. Structure and Stoichiometry in Supervalent Doped Li<sub>7</sub>La<sub>3</sub>Zr<sub>2</sub>O<sub>12</sub>. *Chem. Mater.* **2015**, *27*, 3658–3665.

- (20) Li, Y. T.; Wang, C. A.; Xie, H.; Cheng, J. G.; Goodenough, J. B. High lithium ion conduction in garnet-type Li<sub>6</sub>La<sub>3</sub>ZrTaO<sub>12</sub>. *Electrochem. Commun.* **2011**, *13*, 1289–1292.

- (21) Buschmann, H.; Berendts, S.; Mogwitz, B.; Janek, J. Lithium metal electrode kinetics and ionic conductivity of the solid lithium ion conductors "Li<sub>7</sub>La<sub>3</sub>Zr<sub>2</sub>O<sub>12</sub>" and Li<sub>7-x</sub>La<sub>3</sub>Zr<sub>2-x</sub>Ta<sub>x</sub>O<sub>12</sub> with garnet-type structure. *J. Power Sources* **2012**, *206*, 236–244.

- (22) Cussen, E. J.; Yip, T. W. S. A neutron diffraction study of the  $d^0$  and  $d^{10}$  lithium garnets  $\text{Li}_3\text{Nd}_3\text{W}_2\text{O}_{12}$  and  $\text{Li}_3\text{La}_3\text{Sb}_2\text{O}_{12}$ . *J. Solid State Chem.* **2007**, *180*, 1832–1839.
- (23) Deviannapoorani, C.; Dhivya, L.; Ramakumar, S.; Murugan, R. Lithium ion transport properties of high conductive tellurium substituted  $\text{Li}_7\text{La}_3\text{Zr}_2\text{O}_{12}$  cubic lithium garnets. *J. Power Sources* **2013**, *240*, 18–25.
- (24) Dhivya, L.; Janani, N.; Palanivel, B.; Murugan, R.,  $\text{Li}^+$  transport properties of W substituted  $\text{Li}_7\text{La}_3\text{Zr}_2\text{O}_{12}$  cubic lithium garnets. *Aip Adv.* **2013**, *3*.
- (25) Murugan, R.; Ramakumar, S.; Janani, N. High conductive yttrium doped  $\text{Li}_7\text{La}_3\text{Zr}_2\text{O}_{12}$  cubic lithium garnet. *Electrochem. Commun.* **2011**, *13*, 1373–1375.
- (26) Xia, Y.; Ma, L.; Lu, H.; Wang, X.-P.; Gao, Y.-X.; Liu, W.; Zhuang, Z.; Guo, L.-J.; Fang, Q.-F. Preparation and enhancement of ionic conductivity in Al-added garnet-like  $\text{Li}_{6.8}\text{La}_3\text{Zr}_{1.8}\text{Bi}_{0.2}\text{O}_{12}$  lithium ionic electrolyte. *Front Mater. Sci.* **2015**, *9*, 366–372.
- (27) Murugan, R.; Weppner, W.; Schmid-Beurmann, P.; Thangadurai, V. Structure and lithium ion conductivity of bismuth containing lithium garnets  $\text{Li}_3\text{La}_3\text{Bi}_2\text{O}_{12}$  and  $\text{Li}_6\text{SrLa}_2\text{Bi}_2\text{O}_{12}$ . *Mater. Sci. Eng., B* **2007**, *143*, 14–20.
- (28) Gao, Y. X.; Wang, X. P.; Wang, W. G.; Zhuang, Z.; Zhang, D. M.; Fang, Q. F. Synthesis, ionic conductivity, and chemical compatibility of garnet-like lithium ionic conductor  $\text{Li}_3\text{La}_3\text{Bi}_2\text{O}_{12}$ . *Solid State Ionics* **2010**, *181*, 1415–1419.
- (29) Gao, Y. X.; Wang, X. P.; Sun, Q. X.; Zhuang, Z.; Fang, Q. F. Electrical properties of garnet-like lithium ionic conductors  $\text{Li}_{3+x}\text{Sr}_x\text{La}_{3-x}\text{Bi}_2\text{O}_{12}$  fabricated by spark plasma sintering method. *Front Mater. Sci.* **2012**, *6*, 216–224.
- (30) Gao, Y. X.; Zhuang, Z.; Lu, H.; Wang, X. P.; Fang, Q. F. Relaxation Model of Lithium Ions in the Garnet-like  $\text{Li}_3\text{La}_3\text{Bi}_2\text{O}_{12}$  Lithium-Ion Conductor. *Solid State Phenom.* **2012**, *184*, 116–121.
- (31) Aono, H.; Sugimoto, E.; Sadaoka, Y.; Imanaka, N.; Adachi, G. Ionic-Conductivity of Solid Electrolytes Based on Lithium Titanium Phosphate. *J. Electrochem. Soc.* **1990**, *137*, 1023–1027.
- (32) Knauth, P. Inorganic solid Li ion conductors: An overview. *Solid State Ionics* **2009**, *180*, 911–916.
- (33) Kamaya, N.; Homma, K.; Yamakawa, Y.; Hirayama, M.; Kanno, R.; Yonemura, M.; Kamiyama, T.; Kato, Y.; Hama, S.; Kawamoto, K.; Mitsui, A. A lithium superionic conductor. *Nat. Mater.* **2011**, *10*, 682–686.
- (34) Zeier, W. G. Structural limitations for optimizing garnet-type solid electrolytes: a perspective. *Dalton T* **2014**, *43*, 16133–16138.
- (35) Zeier, W. G.; Zhou, S. L.; Lopez-Bermudez, B.; Page, K.; Melot, B. C. Dependence of the Li-Ion Conductivity and Activation Energies on the Crystal Structure and Ionic Radii in  $\text{Li}_6\text{MLa}_2\text{Ta}_2\text{O}_{12}$ . *ACS Appl. Mater. Interfaces* **2014**, *6*, 10900–10907.
- (36) Miara, L. J.; Ong, S. P.; Mo, Y. F.; Richards, W. D.; Park, Y.; Lee, J. M.; Lee, H. S.; Ceder, G. Effect of Rb and Ta Doping on the Ionic Conductivity and Stability of the Garnet  $\text{Li}_{7+2xy}(\text{La}_{3-x}\text{Rb}_x)(\text{Zr}_{2-y}\text{Ta}_y)\text{O}_{12}$  ( $0 \leq x \leq 0.375$ ,  $0 \leq y \leq 1$ ) Superionic Conductor: A First Principles Investigation. *Chem. Mater.* **2013**, *25*, 3048–3055.
- (37) Shannon, R. D. Revised Effective Ionic-Radii and Systematic Studies of Interatomic Distances in Halides and Chalcogenides. *Acta Crystallogr., Sect. A: Cryst. Phys., Diffraction, Theor. Gen. Crystallogr.* **1976**, *32*, 751–767.
- (38) Rodriguez-Carvajal, J. Magnetic structure determination from powder diffraction using the program FullProf. *Applied Crystallography* **2000**, *30*–36.
- (39) Liu, C.; Rui, K.; Shen, C.; Badding, M. E.; Zhang, G. X.; Wen, Z. Y. Reversible ion exchange and structural stability of garnet-type Nb-doped  $\text{Li}_7\text{La}_3\text{Zr}_2\text{O}_{12}$  in water for applications in lithium batteries. *J. Power Sources* **2015**, *282*, 286–293.
- (40) Orera, A.; Larraz, G.; Rodriguez-Velamazán, J. A.; Campo, J.; Sanjuan, M. L. Influence of  $\text{Li}^+$  and  $\text{H}^+$  Distribution on the Crystal Structure of  $\text{Li}_{7-x}\text{H}_x\text{La}_3\text{Zr}_2\text{O}_{12}$  ( $0 \leq x \leq 5$ ) Garnets. *Inorg. Chem.* **2016**, *55*, 1324–1332.
- (41) Cheng, L.; Wu, C. H.; Jarry, A.; Chen, W.; Ye, Y. F.; Zhu, J. F.; Kostecki, R.; Persson, K.; Guo, J. H.; Salmeron, M.; Chen, G. Y.; Doeff, M. Interrelationships among Grain Size, Surface Composition, Air Stability, and Interfacial Resistance of Al-Substituted  $\text{Li}_7\text{La}_3\text{Zr}_2\text{O}_{12}$  Solid Electrolytes. *ACS Appl. Mater. Interfaces* **2015**, *7*, 17649–17655.
- (42) Jin, Y.; McGinn, P. J.  $\text{Li}_7\text{La}_3\text{Zr}_2\text{O}_{12}$  electrolyte stability in air and fabrication of a  $\text{Li}/\text{Li}_7\text{La}_3\text{Zr}_2\text{O}_{12}/\text{Cu}_{0.1}\text{V}_2\text{O}_5$  solid-state battery. *J. Power Sources* **2013**, *239*, 326–331.
- (43) Larraz, G.; Orera, A.; Sanjuan, M. L. Cubic phases of garnet-type  $\text{Li}_7\text{La}_3\text{Zr}_2\text{O}_{12}$ : the role of hydration. *J. Mater. Chem. A* **2013**, *1*, 11419–11428.
- (44) Larraz, G.; Orera, A.; Sanz, J.; Sobrados, I.; Diez-Gómez, V.; Sanjuán, M. L. NMR study of Li distribution in  $\text{Li}_{7-x}\text{H}_x\text{La}_3\text{Zr}_2\text{O}_{12}$  garnets. *J. Mater. Chem. A* **2015**, *3*, 5683–5691.
- (45) Wagner, R.; Redhammer, G. J.; Rettenwander, D.; Senyshyn, A.; Schmidt, W.; Wilkening, M.; Amthauer, G. Crystal Structure of Garnet-Related Li-Ion Conductor  $\text{Li}_{7-3x}\text{Ga}_x\text{La}_3\text{Zr}_2\text{O}_{12}$ : Fast Li-Ion Conduction Caused by a Different Cubic Modification? *Chem. Mater.* **2016**, *28*, 1861–1871.
- (46) Rettenwander, D.; Redhammer, G.; Preishuber-Pflügl, F.; Cheng, L.; Miara, L.; Wagner, R.; Welzl, A.; Suard, E.; Doeff, M. M.; Wilkening, M.; Fleig, J.; Amthauer, G. Structural and Electrochemical Consequences of Al and Ga Cosubstitution in  $\text{Li}_7\text{La}_3\text{Zr}_2\text{O}_{12}$  Solid Electrolytes. *Chem. Mater.* **2016**, *28*, 2384–2392.
- (47) Wagner, R.; Redhammer, G. J.; Rettenwander, D.; Tippelt, G.; Welzl, A.; Taibl, S.; Fleig, J.; Franz, A.; Lottermoser, W.; Amthauer, G. Fast Li-Ion-Conducting Garnet-Related  $\text{Li}_{7-3x}\text{Fe}_x\text{La}_3\text{Zr}_2\text{O}_{12}$  with Uncommon  $\bar{I}43d$  Structure. *Chem. Mater.* **2016**, *28*, 5943–5951.
- (48) Ma, C.; Rangasamy, E.; Liang, C.; Sakamoto, J.; More, K. L.; Chi, M. Excellent stability of a lithium-ion-conducting solid electrolyte upon reversible  $\text{Li}(+)/\text{H}(+)$  exchange in aqueous solutions. *Angew. Chem., Int. Ed.* **2015**, *54*, 129–33.
- (49) Tietz, F.; Wegener, T.; Gerhards, M. T.; Giarola, M.; Mariotto, G. Synthesis and Raman micro-spectroscopy investigation of  $\text{Li}_7\text{La}_3\text{Zr}_2\text{O}_{12}$ . *Solid State Ionics* **2013**, *230*, 77–82.
- (50) Thompson, T.; Wolfenstine, J.; Allen, J. L.; Johannes, M.; Huq, A.; David, I. N.; Sakamoto, J. Tetragonal vs. cubic phase stability in Al-free Ta doped  $\text{Li}_7\text{La}_3\text{Zr}_2\text{O}_{12}$  (LLZO). *J. Mater. Chem. A* **2014**, *2*, 13431–13436.
- (51) Pasierb, P.; Komornicki, S.; Rokita, M.; Rękas, M. Structural properties of  $\text{Li}_2\text{CO}_3$ - $\text{BaCO}_3$  system derived from IR and Raman spectroscopy. *J. Mol. Struct.* **2001**, *596*, 151–156.
- (52) Peltzer, D.; Múnera, J.; Cornaglia, L. Operando Raman spectroscopic studies of lithium zirconates during  $\text{CO}_2$  capture at high temperature. *RSC Adv.* **2016**, *6*, 8222–8231.
- (53) Koura, N.; Kohara, S.; Takeuchi, K.; Takahashi, S.; Curtiss, L. A.; Grimsditch, M.; Saboungi, M.-L. Alkali carbonates: Raman spectroscopy, ab initio calculations, and structure. *J. Mol. Struct.* **1996**, *382*, 163–169.
- (54) Afyon, S.; Krumeich, F.; Rupp, J. L. M. A shortcut to garnet-type fast Li-ion conductors for all-solid state batteries. *J. Mater. Chem. A* **2015**, *3*, 18636–18648.
- (55) Wang, Y. X.; Lai, W. Phase transition in lithium garnet oxide ionic conductors  $\text{Li}_7\text{La}_3\text{Zr}_2\text{O}_{12}$ : The role of Ta substitution and  $\text{H}_2\text{O}/\text{CO}_2$  exposure. *J. Power Sources* **2015**, *275*, 612–620.
- (56) Xia, W.; Xu, B.; Duan, H.; Guo, Y.; Kang, H.; Li, H.; Liu, H. Ionic Conductivity and Air Stability of Al-Doped  $\text{Li}_7\text{La}_3\text{Zr}_2\text{O}_{12}$  Sintered in Alumina and Pt Crucibles. *ACS Appl. Mater. Interfaces* **2016**, *8*, 5335–5342.
- (57) Galven, C.; Dittmer, J.; Suard, E.; Le Berre, F.; Crosnier-Lopez, M.-P. Instability of Lithium Garnets against Moisture. Structural Characterization and Dynamics of  $\text{Li}_{7-x}\text{H}_x\text{La}_3\text{Sn}_2\text{O}_{12}$  and  $\text{Li}_{5-x}\text{H}_x\text{La}_3\text{Nb}_2\text{O}_{12}$ . *Chem. Mater.* **2012**, *24*, 3335–3345.
- (58) Galven, C.; Fourquet, J. L.; Crosnier-Lopez, M. P.; Le Berre, F. Instability of the Lithium Garnet  $\text{Li}_7\text{La}_3\text{Sn}_2\text{O}_{12}$ :  $\text{Li}^+/\text{H}^+$  Exchange and Structural Study. *Chem. Mater.* **2011**, *23*, 1892–1900.
- (59) Gam, F.; Galven, C.; Bulou, A.; Le Berre, F.; Crosnier-Lopez, M. P. Reinvestigation of the Total  $\text{Li}^+/\text{H}^+$  Ion Exchange on the Garnet-Type  $\text{Li}_3\text{La}_3\text{Nb}_2\text{O}_{12}$ . *Inorg. Chem.* **2014**, *53*, 931–934.

(60) Li, Y. T.; Han, J. T.; Wang, C. A.; Xie, H.; Goodenough, J. B. Optimizing  $\text{Li}^+$  conductivity in a garnet framework. *J. Mater. Chem.* **2012**, *22*, 15357–15361.



### 3.3 The influence of mechanical treatment on lithium diffusivity

#### 3.3.1 Li ion diffusion and ionic conduction in aluminosilicate $\text{LiAlSi}_4\text{O}_{10}$

##### Experimental

The  $\text{LiAlSi}_4\text{O}_{10}$  glass was provided by Schott Glaswerke (Germany) and was prepared by mixing the appropriate amounts of  $\text{Li}_2\text{CO}_3$ ,  $\text{Al}_2\text{O}_3$  and  $\text{SiO}_2$ . The glass was obtained from the melt by roller quenching. The glass is fully x-ray amorphous (see figure 3.7). Microcrystalline  $\text{LiAlSi}_4\text{O}_{10}$  was prepared by devitrification of the glassy source material and subsequent grinding. The crystallization process was completed after heating the glass sample with a rate of  $5 \text{ K/min}$  up to  $1093 \text{ K}$  for  $300 \text{ h}$ . The material was cooled with a rate of  $3 \text{ K/min}$  down to  $303 \text{ K}$ . X-ray diffraction (XRD) measurements of the crystalline sample confirmed the phase purity and revealed, oddly, the pattern of  $\beta$ -spodumene. Additional ICP/MS measurements confirmed the nominal composition of  $\text{LiAlSi}_4\text{O}_{10}$  and led to the assumption that  $\text{SiO}_2$  is present in an amorphous state. In other words, we are speaking of a mixture of the crystalline aluminosilicate spodumene with amorphous quartz. XRD patterns were recorded under air with a Bruker D8 Advance diffractometer using Bragg Brentano geometry and  $\text{CuK}_\alpha$  radiation ( $10$  to  $100^\circ 2\theta$ , step size  $0.02^\circ 2\theta$ , step time  $1 \text{ s}$ ). Rietveld refinement was done with X-PertHighScorePlus (PANalytical). Nanocrystalline  $\text{LiAlSi}_4\text{O}_{10}$  was prepared by high-energy ball milling (HEBM) using a planetary ball mill (Fritsch Pulverisette 7 premium line) with  $\text{ZrO}_2$  beakers in combination with  $180$  balls of the same material ( $5 \text{ mm}$  in diameter). The ball-to-powder weight ratio was chosen to be about  $4:1$ . The glass was treated under the same conditions. In both cases, the total milling time was  $6 \text{ h}$  and  $24 \text{ h}$ , respectively. The time period does not include the cooling intervals in between.

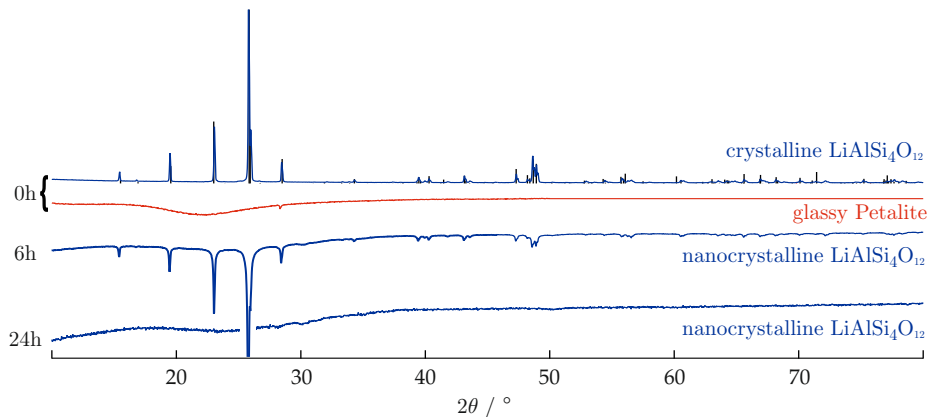


**Figure 3.7** – XRD patterns of micro- and nanocrystalline  $\text{LiAlSi}_4\text{O}_{10}$ . The coarse grained sample (micro) was prepared by devitrification of the  $\text{LiAlSi}_4\text{O}_{10}$  glass and subsequent extensive grinding of the material. The nanocrystalline samples were prepared by high-energy ball milling of the microcrystalline source material. In addition, the XRD pattern of the untreated  $\text{LiAlSi}_4\text{O}_{10}$  glass is shown (see text for further details).

## Results

The mobility of small ions, cations and anions, in solids depends on numerous factors. It is well-known that point defects and polyhedral connections play an important role in enabling local jump processes and bulk ion transport. Besides defects, the morphology of the whole material will determine migration of the charge carriers over long, *i.e.*, macroscopic distances. A convenient and well-established technique to introduce disorder into a sample is the treatment of the material in high-energy mills. Conveniently, high-energy ball milling is carried out at ambient temperature and it allows the preparation of large quantities. In many cases, if only one component is treated, phase pure nanocrystalline materials are obtained with large volume fractions of amorphous regions or at least disordered interfaces. The introduction of point defects and dislocations is, however, also expected for the crystalline cores of the nanocrystallites (a schematic illustration for the investigated petalite is proved in figure 3.8). Many examples have so far been reported documenting that the ionic conductivity of a poor conductor can be significantly enhanced when transforming the oxides or sulfides into a defect-rich nanocrystalline ceramics.[26, 78–81]

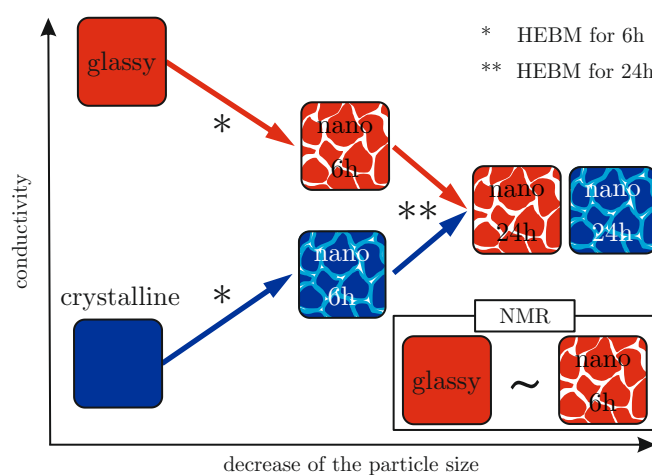


**Figure 3.8** – Schematic illustration on the effect of high energy ball milling (HEBM) on the conductivity of the studied aluminosilicate  $\text{LiAlSi}_4\text{O}_{10}$ .

Here, the influence of structural disorder generated through ball milling, and thus nanostructuring, on Li ion transport in both crystalline petalite  $\text{LiAlSi}_4\text{O}_{10}$  and its glassy form was comprehensively investigated by solid-state  $^7\text{Li}$  NMR and impedance spectroscopy. Milling of polycrystalline samples of petalite  $\text{LiAlSi}_4\text{O}_{10}$  causes, as expected, the ionic conductivity and diffusivity to increase.[82, 83] Before the results on spin-lattice relaxation NMR are presented, I would like to draw the reader’s attention to the results from temperature-variable line shape measurements of both, glassy and crystalline,  $\text{LiAlSi}_4\text{O}_{10}$  samples.

NMR motional line narrowing (MN) gives first insights into how fast the ions are exchanged by self-diffusion processes. Independent of the morphology, all samples undergo a pronounced motional narrowing with increasing temperature  $T$  due to increasing Li motions, which are responsible for averaging of homonuclear dipole-dipole ( $^7\text{Li}$ - $^7\text{Li}$ ) interactions.[81] When the jump rate  $\tau_{\text{MN}}^{-1}$  reaches the order of the rigid lattice line width, notable diffusion controlled line narrowing can be expected. Here, narrowing sets in for the glassy samples at approximately 300 K and for crystalline samples,

the onset point is shifted slightly towards higher temperatures 340 K (see figure 3.9). The Li ion jump rate  $\tau_{\text{MN}}^{-1}$  can be roughly estimated from the inflection point, at approximately 300 K and 340 K, respectively, of the MN curves according to  $\tau_{\text{MN}}^{-1} \approx 2\pi \times \nu_{\text{rl}}$ . For all samples, the Li jump rate was in the order of *ca.*  $2 - 3 \times 10^4 \text{ s}^{-1}$ . Quite interestingly, it seems that the morphology does not have a huge impact on the lithium jump rate. NMR line narrowing seems to be less sensitive to the differences that can be revealed by other NMR techniques and impedance spectroscopy.

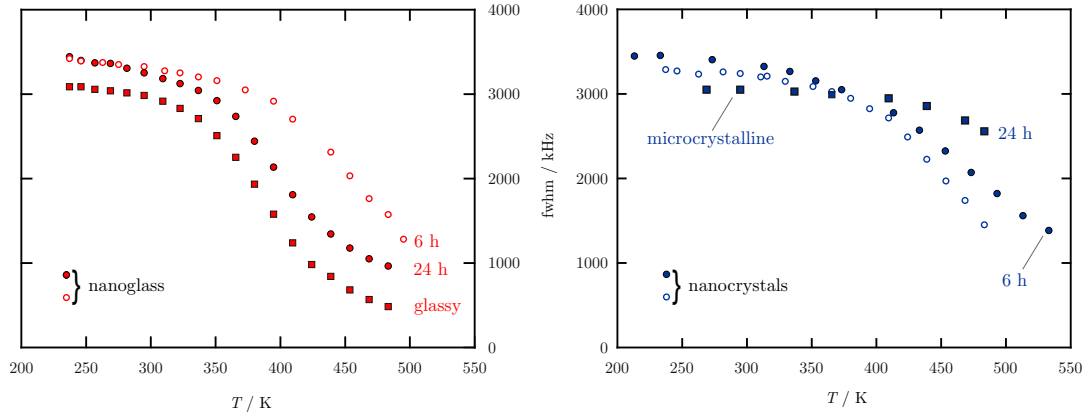


**Figure 3.9** –  ${}^7\text{Li}$  NMR line width (full width at half-maximum, FWHM) as a function of temperature  $T$ . On the left side, the values starting from glassy petalite, and on the right side, samples starting from crystalline material are presented. Explanation of symbols: unmilled samples are indicated by a filled square (■), 6h milled samples by a filled circle (●) and 24h milled samples by a empty circle (○).

In contrast to NMR line narrowing experiments, conductivity and SLR NMR experiments are able to reveal clear distinctions in Li diffusivity between both glassy and crystalline  $\text{LiAlSi}_4\text{O}_{10}$  samples. In figure 3.10a, the DC conductivities of micro- and nanocrystalline  $\text{LiAlSi}_4\text{O}_{10}$  are shown. High-energy ball-milling of crystalline petalite leads to an increase of the ionic conductivity by almost two orders of magnitude (330 K). Milling for 24h does not change the conductivity much further. Starting with micro- $\text{LiAlSi}_4\text{O}_{10}$ , the activation energy decreases from 0.95 eV down to 0.81 eV. The 24h sample is characterized by 0.85 eV revealing a slight increase in  $E_a$ . The opposite trend, however, is found when  $\text{LiAlSi}_4\text{O}_{10}$  glass is treated for several hours in a planetary mill. The Li ion conductivity of the glassy forms decreases with increasing milling time. A quite similar, but opposite, trend in the activation energy is observed if we start from the glass. Initially, the glass, whose ion conductivity exceeds that of the microcrystalline form by 4 orders of magnitude (330 K), is characterized by 0.72 eV. While nanoglassy  $\text{LiAlSi}_4\text{O}_{10}$  (6h) has to be characterized by  $E_a = 0.79$  eV, after milling the oxide for 24h, the activation has further increased to 0.84 eV and the resulting  $\sigma_{\text{DC}}$  values coincide with those of nanocrystalline  $\text{LiAlSi}_4\text{O}_{10}$  treated for the same period of time. The changes in long-range ion transport of glassy  $\text{LiAlSi}_4\text{O}_{10}$  seen *via* conductivity spectroscopy can also be recognized in rotating-frame  ${}^7\text{Li}$  NMR spin-lattice relaxometry (figure 3.10b).  $R_{1\rho}$  NMR measurements on nanoglassy samples have been carried out for the first time to confirm the changes in  $\sigma_{\text{DC}}$  by NMR. As compared to conductivity spectroscopy, NMR is a contactless method and no post-treatment of the samples to prepare pellets with conducting electrodes is required. For a reliable description of the effect observed, it is important to have a method, such as NMR, at hand that is insensitive to the porosity and density of the pressed pellets investigated by impedance spectroscopy. Note that in figure 3.10, except for

the glass, data of powder samples are shown. Originally, the diffusion-induced  $R_{1\rho}$  rates of glassy  $\text{LiAlSi}_4\text{O}_{10}$  pass through a broad  $R_{1\rho}$  ( $1/T$ ) peak which seems to be composed of at least two separate peaks. One of them is indicated by the small arrow in figure 3.10b; while this peak is located at 400 K, another one, the main peak, shows up at 440 K. As expected from conductivity measurements, the beginning of the LT flank is shifted towards higher  $T$  reflecting a decrease in Li ion diffusivity upon mechanical treatment. Correspondingly, the slope of nanoglassy  $\text{LiAlSi}_4\text{O}_{10}$  is steeper than that of the glass sample.

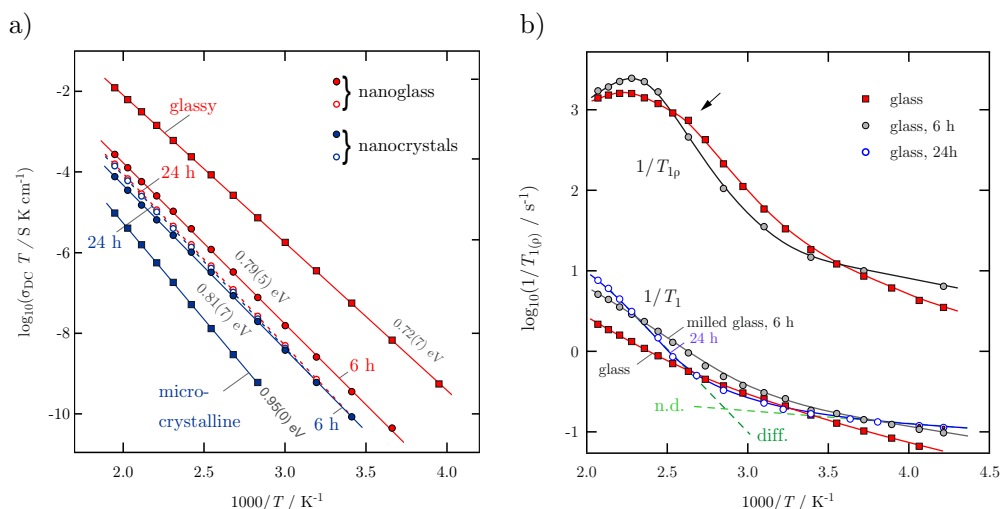


**Figure 3.10** – a) Conductivities of glassy and microcrystalline  $\text{LiAlSi}_4\text{O}_{10}$ . As expected, the ion conductivities of the glass (small plate) and the crystalline sample differ by several orders of magnitude. Milling the two materials for 6h in a planetary mill changes the transport parameters significantly. Upon milling, the conductivities head toward each other and the activation energies converge reaching ca. 0.8 eV. If the milling time is increased to 24h, the conductivities finally coincide. Interestingly,  $E_a$  slightly increases again (0.85 eV). b)  $^7\text{Li}$  NMR SLR rates recorded in both the laboratory and rotating frame of reference (194 MHz, 20 kHz); the NMR response of the untreated glass and the crystallized material is compared to those samples that were milled for 6h and 24h, respectively. The lines are to guide the eye. See text for further explanation.

A similar behavior, but much more subtle, can be observed if we regard the  $R_1$  rates of glassy and nanoglassy  $\text{LiAlSi}_4\text{O}_{10}$ . Keeping in mind that  $R_1$  rates are sensitive to short-range ion motions, the changes after mechanical treatment might be smaller than those for  $\sigma_{\text{DC}}$ . Whereas for the glass, the transition from non-diffusive (nd) relaxation to diffusion-induced spin-lattice relaxation is almost fluent, milling causes a separation of these regimes, see the dashed lines in 3.10b. The increase of  $R_1$  in the nd-regime might be the result of an increased number density of paramagnetic impurities introduced during milling. Alternatively, localized ion dynamics might have changed that originally caused a shallow  $T$ -dependence of the NMR rates. If we simply regard the onset of the diffusion-induced LT flank of the  $R_1$  rate peak, a shift toward higher  $T$  is observable, which would be in agreement with the results from both  $R_{1\rho}$ - and  $\sigma_{\text{DC}}$ -measurements. In agreement with this trend, the associated activation energy increases from 0.34 eV for the glass and 0.37 for the nanoglass (6h) to 0.49 eV for nanoglassy  $\text{LiAlSi}_4\text{O}_{10}$  obtained after 24h of mechanical treatment. Note that the relatively low value of 0.34 eV for the glass is, however, thought to be largely influenced by correlation effects that lead to

lower expected  $E_a$  values in this temperature regime. Thus, directly comparing the activation energies from LT flanks is not as straight-forward as it looks like at first glance.

The  $R_1$  rates in the diffusion-induced regime of the sample milled for 24h significantly exceed those of the glassy sample, see figure 3.10b. Interestingly, the opposite trend has been observed for  $\beta$ -spodumene. While for the 6h sample this feature points to an increased coupling constant in nanoglassy  $\text{LiAlSi}_4\text{O}_{10}$ , in the case of the sample milled for 24h, the steeper increase with  $1/T$  traitorously leads to the assumption that the corresponding peak will be passed through at lower  $T$ . Hence, from a point of view that focusses on short-range motions, local ion dynamics in nanoglassy  $\text{LiAlSi}_4\text{O}_{10}$  (24h), at least for some of the ions, seems to be enhanced. Obviously, the fast relaxing ensemble of spins, which is responsible for the relatively steep increase of the rates above 400 K (see 3.10b), is not able to significantly compensate for the decrease found in  $\sigma_{\text{DC}}$  as we finally obtain  $\sigma_{\text{DC}}(\text{nanocrystalline}) \approx \sigma_{\text{DC}}(\text{nanoglassy})$ . Most likely, also for nanoglassy samples, a heterogeneous structure consisting of bulk and interfacial regions is formed. For  $\text{LiAlSi}_4\text{O}_{10}$ , these interfacial regions, characterized by a higher degree of free volume, might act as hosts for some fast relaxing spins. The higher  $E_a$  (0.49 eV), as compared to that the glassy sample (0.34 eV), indicates (local) Li motions less influenced by correlation effects rather than a higher mean hopping barrier. Obviously, these regions do not form a through-going network to enable the ions to move over long distances as quickly as in the original glassy state obtained by quenching.

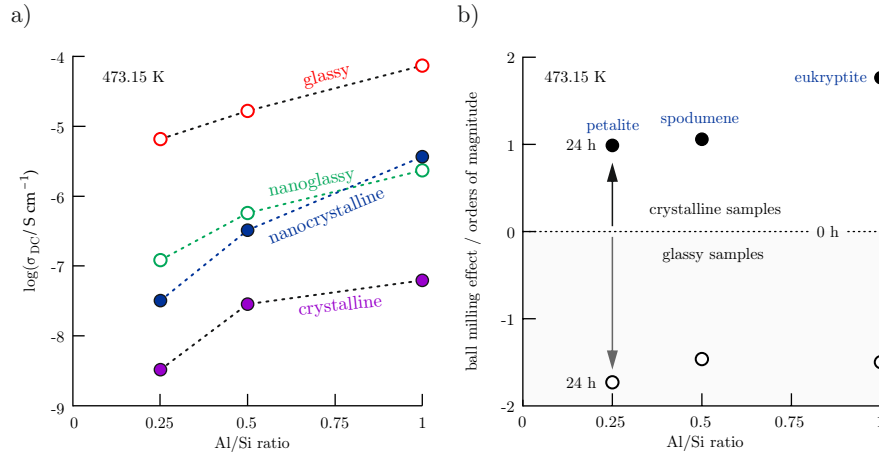


**Figure 3.11** – a) Overview of conductivities of a series of aluminosilicates as a function of Al/Si ratio. Here the conductivity at 473.15 K of eucryptite ( $\text{LiAlSiO}_4$ ), spodumene ( $\text{LiAlSi}_2\text{O}_6$ ) and petalite ( $\text{LiAlSi}_4\text{O}_{10}$ ) is presented.[83–86] b) Here, the ball milling effect for all three aluminosilicate minerals (eucryptite, spodumene and petalite) is compared to each other. The greater the value of the ball milling effect, the greater the impact of the mechanical treatment on diffusivity will be.

As a last remark, by comparing the effect seen in  $\sigma_{\text{DC}}$  for  $\text{LiAlSiO}_4$  (eucryptite),  $\text{LiAlSi}_2\text{O}_6$  (spodumene) and  $\text{LiAlSi}_4\text{O}_{10}$ , we notice that the ratio  $\sigma_{g:n} = \sigma_{\text{DC}}(\text{glassy}) : \sigma_{\text{DC}}(\text{nanoglassy})$  clearly increases with decreasing Al:Si ratio:  $\sigma_{g:n}(\text{LiAlSiO}_4) < \sigma_{g:n}(\text{LiAlSi}_2\text{O}_6) < \sigma_{g:n}(\text{LiAlSi}_4\text{O}_{10})$ . While for  $\text{LiAlSiO}_4$  and  $\text{LiAlSi}_2\text{O}_6$  the  $1/T_1$  response points to the same direction as was observed through conductivity measurements, for  $\text{LiAlSi}_4\text{O}_{10}$ , characterized by the lowest Al content and the largest  $\sigma_{g:n}$  ratio, the  $R_1$  rates reveal an exception.



## 3.4 A novel electrolyte concept for high-temperature Li ion batteries

### 3.4.1 "Ionic liquids-in-salt"-concept

For more detailed information on the diffusion parameters of the material the reader is referred to the hereafter publication. In addition to the results published,  $\text{Li}^+$  self-diffusion in pure LiTFSI and in the mixture of an ionic liquid with a lithium salt  $\text{Li}_x\text{EMIM}_{(1-x)}\text{TFSI}$  with  $x = 0.9$ , was investigated by recording  $^7\text{Li}$  NMR  $R_1$  rates as a function of temperature. The magnetization transients of the mixture show a two-component behavior, which can be approximated by a double exponential fitting function yielding two characteristic time constants for two distinct spin reservoirs. A diffusion-induced rate maximum could not be probed within the experimental temperature range (180 K to 400 K).

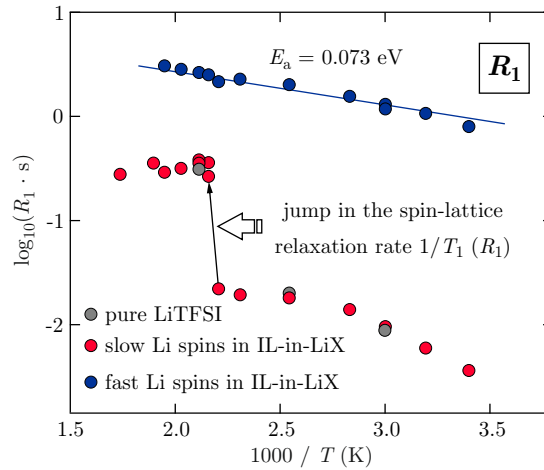


**Figure 3.12** – Arrhenius plot of  $^7\text{Li}$  NMR  $R_1$  rates of pure LiTFSI (gray dots) and  $\text{Li}_{0.9}\text{EMIM}_{0.1}\text{TFSI}$  (red and blue dots). The data was measured at  $\omega_0/2\pi = 194.3$  MHz. Two different rates were deduced from the corresponding relaxation transients of the sample material revealing two distinct spin reservoirs. The blue dots are assigned to fast Li ions located in the "ionic liquid-in-salt" phase, whereas the red dots show the rates of slow ions from the pure Li salt LiTFSI.

Pure LiTFSI is characterized by a solid-solid transition at 425 K. This known solid-state phase transformation of LiTFSI can be well recognized by a "jump" in low-temperature regime of the  $R_1$  NMR rate peak. This jump occurs at approximately 440 K (see rates for pure LiTFSI marked by gray dots in figure 3.12). Upon heating to 513 K, the mixture of the ionic liquid with the salt clearly reveals several double phase regions; as published, these double phase regions can be monitored by a change of the quadruple powder pattern of the  $^7\text{Li}$  NMR spectra of LiTFSI. The central line is composed of two components (see inset of Fig. 2b in the article). Whereas the broad line coincides with that of pure LiTFSI, the (motionally narrowed) NMR line on top can be attributed to Li ions being much more mobile than those in the IIa LiTFSI phase (see blue dots in figure 3.12). These two distinct spin reservoirs can be monitored by temperature-variable  $^7\text{Li}$  spin-lattice relaxation (SLR) NMR. The presence of highly mobile ions at ambient temperature can also be confirmed by  $R_1$  rates recorded under static nonrotating conditions. If recorded up to delay times of 1000s, the pronounced bi-exponential  $^7\text{Li}$  SLR NMR transients directly reveal a subset of highly mobile Li ions,

partly identified as  $[\text{Li}(\text{TFSI})_2]^-$ , which can be well discriminated from the response of pure LiTFSI (see figure 3.12). A quite low activation energy  $E_a$  of 0.073 eV was determined for the fast diffusion process. This sub-ensemble is regarded to be responsible for the enhancement in ion conductivity.

**"Tonic liquids-in-salt" - a promising electrolyte concept for high-temperature lithium batteries?**

Maciej J. Marczweski, Bernhard Stanje, Ilie Hanzu, Martin Wilkening and Patrik Johansson. *Physical Chemistry Chemical Physics*, DOI: 10.1039/c4cp01133c (2014), 12341 - 12349





PCCP

PAPER

View Article Online  
View Journal | View Issue

## “Ionic liquids-in-salt” – a promising electrolyte concept for high-temperature lithium batteries?

Cite this: *Phys. Chem. Chem. Phys.*, 2014, 16, 12341Maciej J. Marczewski,<sup>\*a</sup> Bernhard Stanje,<sup>b</sup> Ilie Hanzu,<sup>bc</sup> Martin Wilkening<sup>b</sup> and Patrik Johansson<sup>\*ac</sup>

A novel electrolyte concept for lithium-ion batteries, termed “ionic liquid-in-salt”, is introduced. Our feasibility study on  $(1-x)\text{EMIMTFSI}:(x)\text{LiTFSI}$ ,  $0.66 \leq x \leq 0.97$ , showed that at elevated temperatures the various dual liquid and solid phase regions are characterized by a wide thermal stability window, high ionic conductivities and appreciable mechanical integrity. The highest conductivity values are obtained for the compositions  $x = 0.70$  and  $x = 0.75$  ( $\sigma \approx 6 \times 10^{-3} \text{ S cm}^{-1}$ ) and are related to the final melting of the materials. Overall, high conductivities are observed for  $0.70 < x < 0.90$  while low ones are found for  $x > 0.90$ . Raman and NMR spectroscopies reveal the presence of highly mobile Li-containing species, partly identified as  $[\text{Li}(\text{TFSI})_2]^+$ , albeit rather unexpected for these high  $x$  values, which might explain the high ionic conductivities observed. To prove the general value of our concept in more detail, some first results on BMIMTFSI and PY<sub>13</sub>TFSI based systems are also presented.

Received 17th March 2014,  
Accepted 28th April 2014

DOI: 10.1039/c4cp01133c

www.rsc.org/pccp

### 1 Introduction

The last two decades have been the time of the omnipresent commercialization of rechargeable lithium-ion batteries. However, today's lithium-ion battery technology is a compromise between high performance and safety, with serious safety issues originating from electrolytes based on the metastable  $\text{LiPF}_6$  salt that demands stabilizing additives, and organic solvents, which are prone both to decompose and to inflame.<sup>1</sup> Especially for larger batteries, aimed at application in electric or hybrid electric vehicles as well as for load-levelling, intrinsically safer batteries, preferably based on thermally and electrochemically stable electrolytes with high ionic conductivities, *i.e.*, excellent ion transport properties, are urgently needed. One possibility to improve existing lithium-ion batteries is to develop electrolytes based on ionic liquids (ILs).<sup>2,3</sup> There are many groups developing and testing electrolytes based on ILs doped with lithium salts,  $\text{LiX}$ , with X being any anion. Most common are binary systems,  $\text{IL}_{(1-x)}\text{-LiX}_x$ , but ternary systems have also been thoroughly studied.<sup>4-6</sup> The focus has so far been on systems with low or medium  $\text{LiX}$  concentrations,  $0.01 < x < 0.5$ , (“ $\text{LiX-in-IL}$ ”), but a few papers report on systems with  $x > 0.5$ , up to 0.7 or even 0.8, systems for which we here coin the term “ionic liquid-in-salt” or specifically “ $\text{IL-in-LiX}$ ”.<sup>7,8</sup> Another possible

answer to the challenge of battery safety is to use electrolytes intrinsically designed for use at elevated or even at very high temperatures. These are often based on solid polymer electrolytes or molten salts<sup>9-11</sup> but here the potential of IL based electrolytes has also been recognized.<sup>12</sup>

Here, we combine the two notions by presenting high temperature studies (up to 180 °C) on “ionic liquid-in-salt” systems with large amounts of lithium salt ( $x \geq 0.66$ ) being in analogy with the “polymer-in-salt” and the very recent “solvent-in-salt” concepts.<sup>13,14</sup> Until now, systems with  $x \geq 0.66$  have not attracted any interest due to their very low ionic conductivities, low Li transference numbers at room and moderate temperatures as well as because of the poor reproducibility of the results obtained. This might change when they are used at elevated or high temperatures (*ca.* 90 °C to 120 °C). “ $\text{IL-in-salts}$ ” may become promising as intrinsically safe, thermally and electrochemically stable electrolytes with both high ionic conductivities and appreciable mechanical properties.

For this proof-of-concept study of “ $\text{IL-in-LiX}$ ” systems it is important to use a simple but also relevant model system. The IL should be characterized by high thermal stability, high ionic conductivity, and it should possess the same anion as the lithium salt. The lithium salt should be thermally stable as well. Furthermore, it should be able to form homogenous melts or solutions in organic solvents being compatible with the IL and the preparation method chosen. To enable a more complete study, knowledge about the entire possible phase behaviour of the IL and  $\text{LiX}$  is of importance; hence, a previously well-studied “ $\text{LiX-in-IL}$ ” system should preferably be selected. The reason for the latter is that local heterogeneities may occur, due to

<sup>a</sup> Department of Applied Physics, Chalmers University of Technology, SE-41296, Göteborg, Sweden. E-mail: m\_marczewski@ch.pw.edu.pl, patrik.johansson@chalmers.se

<sup>b</sup> Christian Doppler Laboratory for Lithium Batteries, Institute of Chemistry and Technology of Materials, Graz University of Technology, 8010 Graz, Austria

<sup>c</sup> ALISTORE-ERI European Research Institute, 33 rue Saint Leu, 80039 Amiens, France

preparation, cooling, and storage conditions, or even during employment inside an electrochemical cell. Thus, any phase which can potentially be formed is relevant, not only those being thermodynamically stable. Furthermore, to make the system more predictable, as few phases as possible within the temperature range, defined by the working temperature (*ca.* 90 °C) and room-temperature storage conditions (*ca.* 20 °C), are preferred.

With the above considerations applied, the IL and LiX pair selected is 1-ethyl-3-methyl-imidazolium bis(trifluoromethanesulfonyl)imide (EMIMTFSI) and the corresponding LiTFSI lithium salt. These together create the model system  $(1 - x)$ EMIMTFSI( $x$ )-LiTFSI, or shorter  $\text{Li}_x\text{EMIM}_{(1-x)}\text{TFSI}$ . Crystalline phases form for  $x < 0.25$  (solid EMIMTFSI) and for the composition with  $x = 0.67$  (1:2 EMIMTFSI/LiTFSI crystal) whereas between  $0.25 < x < 0.55$  this system is fully amorphous at room-temperature.<sup>8,15,16</sup> For other  $x$  variations and temperatures, however, the system exists in different double phase regions – each with its own characteristics of, for example, ionic conductivity and other properties relevant for practical battery electrolyte usage, such as mechanical strength and Al corrosion propensity.

To strengthen the fundamental understanding of this new concept, giving promise to further rational improvement, we also aim to arrive at a congruent picture of the structure-property relationship of these new electrolytes. This is done by connecting the macroscopic property performance observations with the molecular level origin in terms of local ion coordination, charge carrier concentration, anion conformation, mobility and diffusivity *etc.* For the latter there is indeed a wide bibliography of both calculated and measured NMR, IR and Raman spectra for EMIMTFSI and LiTFSI individually and for the “LiX-in-IL” systems.<sup>17–23</sup> Furthermore, to show the generality of the concept proposed, the  $\text{Li}_x\text{BMIM}_{(1-x)}\text{TFSI}$  and  $\text{Li}_x\text{PY}_{13(1-x)}\text{TFSI}$  systems are also presented.

## 2 Experimental section

### Materials

1-Ethyl-3-methylimidazolium bis(trifluoromethanesulfonyl)imide, EMIMTFSI (purity 99.9%), 1-butyl-3-methylimidazolium bis(trifluoromethanesulfonyl)imide, BMIMTFSI (purity 99.9%) and *N*-propyl-*N*-methylpyrrolidinium bis(trifluoromethanesulfonyl)imide,  $\text{PY}_{13}\text{TFSI}$  (purity 99.9%) were all purchased from Solvionic and used as received. In all cases the water amount was  $< 30$  ppm as determined by Karl Fischer titration. Lithium bis(trifluoromethanesulfonyl)imide, LiTFSI (purity 99.95%), was purchased from Sigma Aldrich and dried under vacuum for 72 h at 80 °C before use. All materials were stored in an argon filled glove box ( $\text{H}_2\text{O} < 1$  ppm,  $\text{O}_2 < 1$  ppm).

### Sample preparation

The samples were prepared in an argon filled glove-box, *i.e.*, under inert conditions. Materials were prepared by direct mixing of weighted appropriate quantities in glass tubes placed in an oven, heated to 250 °C and held at this temperature for 1 hour. After cooling to room temperature a spatula was used to

homogenize the samples, thereafter the procedure was repeated but with a shorter heating time (30 min). This way, (i) a set of eight  $(1 - x)$ EMIMTFSI( $x$ )-LiTFSI mixtures with  $x = 0.66, 0.70, 0.75, 0.80, 0.85, 0.90, 0.93,$  and  $0.97$ , (ii) a set of three  $(1 - x)$ BMIMTFSI( $x$ )-LiTFSI mixtures,  $x = 0.70, 0.80,$  and  $0.90$ , and (iii) a set of five  $(1 - x)$ PY<sub>13</sub>TFSI( $x$ )-LiTFSI mixtures,  $x = 0.75, 0.80, 0.85, 0.90,$  and  $0.96$ , were prepared.

### Differential scanning calorimetry

Thermal data were obtained by measuring about 10 mg of the sample placed in aluminum hermetic pans using a TA Instrument Q1000 Differential Scanning Calorimeter (DSC). The DSC scans were performed as follows. After equilibration at 40 °C the samples were cooled down to  $-150$  °C using a cooling rate of  $5$  °C  $\text{min}^{-1}$ . Subsequently, the samples were equilibrated at  $-150$  °C for three minutes and thereafter heated to 250 °C at a heating rate of  $5$  °C  $\text{min}^{-1}$ . After 3 minutes of equilibration at 250 °C, the samples were cooled down to  $-150$  °C using a cooling rate of  $5$  °C  $\text{min}^{-1}$  and equilibrated for at least 3 minutes. Finally, samples were heated from  $-150$  °C to 250 °C at a rate of  $5$  °C  $\text{min}^{-1}$ .  $(1 - x)$ EMIMTFSI( $x$ )-LiTFSI samples with  $x = 0.66, 0.70$  and  $0.75$  were heated up to 160 °C and 200 °C respectively. For the  $(1 - x)$ BMIMTFSI( $x$ )-LiTFSI samples only the first heating cycle was performed. Reported melting temperatures are peak temperatures.

### Ionic conductivity measurements

The temperature dependence of the ionic conductivity was measured by dielectric spectroscopy using a Novocontrol broadband dielectric spectrometer at frequencies ranging from  $10^{-1}$  to  $10^7$  Hz. The sample (about 0.3 g) was placed between two stainless steel electrodes with a Teflon spacer (13.2 mm in diameter and 0.99 mm in thickness) and loaded into a cryofurnace with nitrogen flow. The cell, “Liquid parallel plate cell BDS 1308” – Novocontrol, was assembled in an argon atmosphere. Data were collected during heating from 20 °C to 180 °C with a temperature step of 10 °C and a stabilization time of 30 min at each temperature. The DC conductivity was deduced from the low frequency plateau of the conductivity isotherms obtained by plotting the real part of the complex conductivity as a function of frequency.

### Raman spectroscopy

FT-Raman spectra were recorded on a Bruker MultiRAM Stand-Alone FT-Raman Spectrometer using a Nd-YAG laser (1064 nm). Typically, the recording time for a single spectrum was 3 to 4 h. The laser power was in the range of 100 to 350 mW for all samples. Raman spectra were measured over the frequency range 0 to  $3600$   $\text{cm}^{-1}$ . The spectra were normalized by integrating the intensity of the most intense Raman band between 720 and  $780$   $\text{cm}^{-1}$ . For measurements at 90 °C and 165 °C, the samples were placed on a glass plate in a hermetically sealed Linkam FTIR600 temperature controlled stage filled with dry argon gas. Before the measurements, each sample was held at 90 °C (or 165 °C) for 40 min.

### $^7\text{Li}$ NMR measurements

$^7\text{Li}$  NMR measurements were performed using a high-performance Bruker Avance III 500 MHz spectrometer which is permanently connected to a shimmed 11.7 T cryomagnet with a nominal  $^7\text{Li}$  resonance frequency of 194.3 MHz. A commercial broadband probe (Bruker Biospin) was employed to measure temperature-variable  $^7\text{Li}$  NMR line shapes under static, *i.e.*, non-rotating conditions.  $^7\text{Li}$  NMR lines were acquired by applying a saturation recovery pulse sequence ( $10 \times \pi/2 - t_d - \pi/2 -$  acquisition). The initial pulse train, consisting of ten  $\pi/2$  pulses, was used to destroy any longitudinal magnetization  $M_z$ . Immediately after,  $M_z$  recovers according to spin-lattice relaxation determined by the rate  $1/T_1$ . After a sufficiently long waiting period  $t_d$ ,  $M_z$  was flipped with a  $\pi/2$  pulse. In the rotating frame of reference,  $M_z$  decays due to spin-spin relaxation. Fourier transformation of the resulting free induction decay produces the spectra shown. Typically, the  $\pi/2$  pulse lengths ranged between 2.60 and 3.20  $\mu\text{s}$ , *i.e.*, the Li spins have been non-selectively excited. The WSolids software was used to estimate NMR coupling constants and asymmetry parameters.<sup>24</sup>

## 3 Results and discussion

### Thermal behaviour

First, the thermal behaviour of all compositions was studied and overall found to be in very good agreement with previous reports.<sup>5,7,8</sup> Pure LiTFSI is characterized by a solid-solid transition at 152 °C and a melting temperature at approximately 234 °C (Fig. 1). Whereas the crystal structure of the low-temperature solid phase (IIa) has been previously well described,<sup>25</sup> that of the high temperature solid phase (Ia) is still

not characterized. In Fig. 2a the corresponding temperature variable solid-state  $^7\text{Li}$  NMR spectra are shown. The spectrum of the low temperature phase IIa is composed of a central line with a width (full width at half maximum) of approximately 3.6 kHz. Next to the central transition satellite intensities show up which are due to the interaction of the quadrupole moment of the  $^7\text{Li}$  spin with an electric field gradient (EFG) at its site.<sup>26</sup> Note that  $^7\text{Li}$  is a spin-3/2 quadrupole nucleus, *i.e.*, in addition to the interaction with the external magnetic field, the Zeeman levels are altered by electric quadrupolar interactions. In general, a non-vanishing EFG is produced by the electric charge distribution in the direct neighborhood of the  $^7\text{Li}$  nucleus.<sup>26,27</sup> In LiTFSI the Li ions occupy a single crystallographic site. The NMR quadrupole powder pattern observed points to an EFG characterized by a quadrupole coupling constant  $C_q$  of approximately 50 kHz as estimated from the outer singularities whose position remains largely unaffected by the other NMR parameters influencing the overall spectrum. From the inner singularities in combination with a preliminary simulation we estimate the corresponding asymmetry parameter  $\eta$  of the EFG to be approximately 0.3. Note that the individual positions (and relative intensities) of all singularities (see the inset of Fig. 2a) with respect to the central line can be explained by taking into account a slight chemical anisotropy in combination with a proper choice of the corresponding Euler angles. The latter characterize the chemical shift tensor when going from the crystal frame to the principal axis system.

With increasing temperature  $C_q$  being characteristic for the EFG in the IIa phase of LiTFSI slightly increases which is most likely due to extremely small changes in the lattice parameters of this phase. The overall features of the NMR spectrum, however, remain untouched. At temperatures above

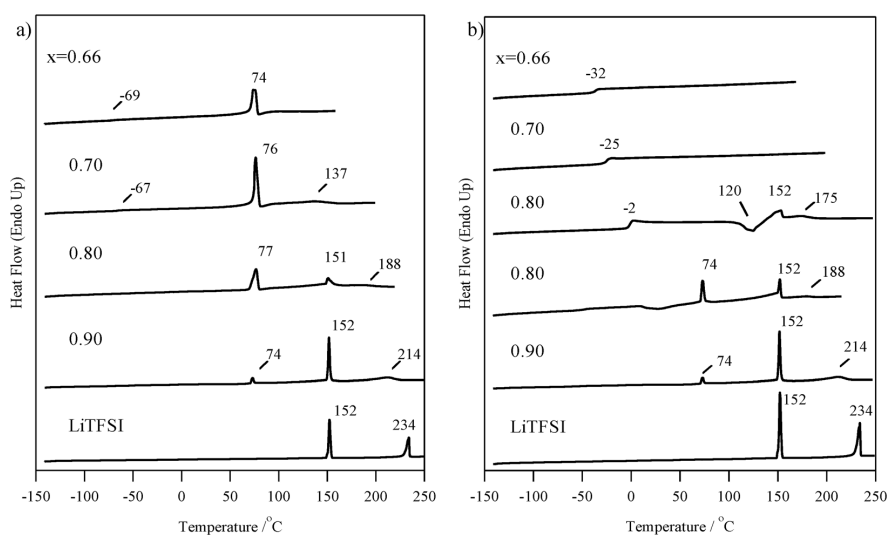


Fig. 1 DSC heating traces for the  $\text{Li}_x\text{EMIM}_{(1-x)}\text{TFSI}$  ( $0.66 \leq x \leq 1$ ) system; data collected during the first heating cycle (a), data collected during the second heating cycle (b).

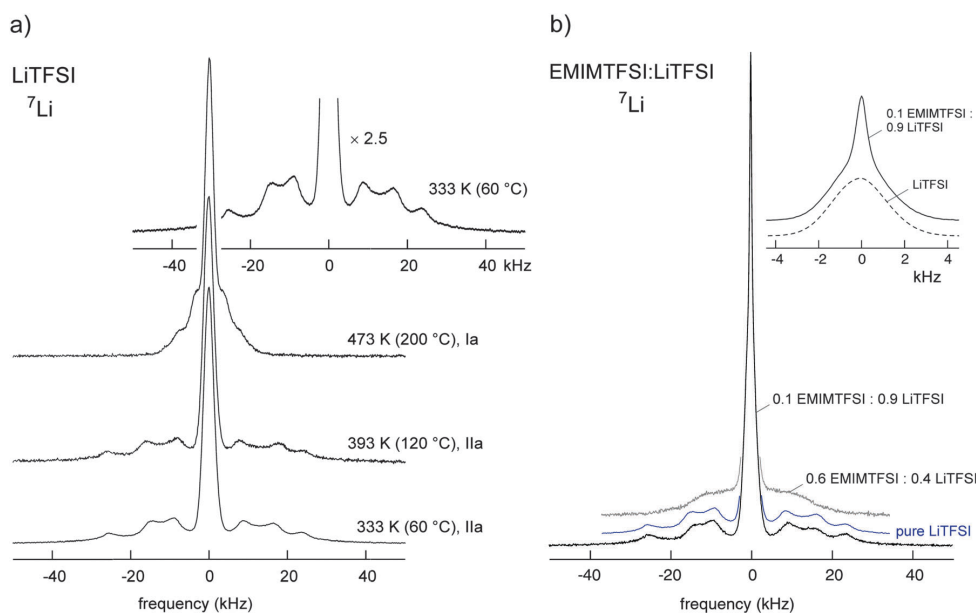


Fig. 2 Solid-state  ${}^7\text{Li}$  NMR spectra (194.3 MHz) of pure crystalline LiTFSI recorded at the temperatures indicated, the inset shows a magnification of the quadrupole powder pattern of the spectrum recorded at 333 K (phase IIa). (a) The corresponding  ${}^7\text{Li}$  NMR spectrum of  $\text{Li}_x\text{EMIM}_{(1-x)}\text{TFSI}$  with  $x = 0.9$ ; for comparison the quadrupole satellite intensities of the samples with  $x = 1$  (pure LiTFSI) and  $x = 0.6$  LiTFSI are also shown. (b) The inset illustrates the shape of the central NMR line of  $\text{Li}_{0.9}\text{EMIM}_{0.1}\text{TFSI}$  being composed of two components reflecting fast and slow Li ions. The central line drawn with a dashed line represents that of pure LiTFSI. See the text for further explanation.

the solid–solid phase transition, a major change occurs and  $C_q$  of the newly formed Ia phase is reduced by more than a factor of 2 compared to its initial value in the IIa phase. This perfectly agrees with the DSC based observations.

For the as prepared mixed samples, doping of LiTFSI with EMIMTFSI ( $0.66 < x < 1$ ) results in the formation of up to three dual phase regions before the samples finally melt (Fig. 1a).

Starting from low temperatures up to the phase transition at *ca.* 76 °C, a new double phase region is observed for  $x > 0.66$ , which can be attributed to crystalline 1/2 EMIMTFSI/LiTFSI (Ib) and solid LiTFSI (IIa).  ${}^7\text{Li}$  NMR (Fig. 2b) reveals that the spectrum of a sample with  $x = 0.9$  mainly resembles that of pure LiTFSI (IIa), particularly when the well-resolved quadrupole powder pattern is regarded. In contrast to pure LiTFSI, however, the central line is composed of two components (see inset of Fig. 2b). Whereas the broad one coincides with that of pure LiTFSI, the (motionally narrowed) NMR line on top can be attributed to Li ions being much more mobile than those in the IIa LiTFSI phase. In general, averaging of dipole–dipole interactions because of rapid diffusive motions of the Li spins causes narrowing of the dipolarly broadened  ${}^7\text{Li}$  NMR lines. Significant narrowing is expected when the mean Li jump rate becomes larger than the spectral width of the NMR line at low temperatures. The latter is often called the *rigid lattice* line width. In the present case, the motionally narrowed NMR components point to exchange rates of the order of  $10^3 \text{ s}^{-1}$  at ambient temperature. Most importantly, the highly mobile ions do already show up at room temperature.

They can be related to those forming the Ib phase with mixed cations. Since the overall conductivity is relatively low at ambient temperature (see below), the mobile ions might be involved in jump processes restricted to shorter length scales. Increasing the amount of EMIMTFSI further results in a quadrupole powder pattern being smeared out, indicating an increased structural disorder resulting in a broad distribution of EFGs (Fig. 2). Samples with  $x > 0.7$  also show high ionic conductivities at room temperature (Fig. 5 and below).

In the literature the melting of the Ib phase was reported to occur at approximately 82 °C.<sup>8</sup> For  $x \leq 0.70$  a small amount of an amorphous phase is also observed (with  $T_g \approx -69$  °C). Between 76 °C and 151 °C another double phase region, obtained from melting of the 1/2 EMIMTFSI/LiTFSI phase is present which consists of liquid (0.33–0.25)EMIMTFSI:(0.67–0.75)LiTFSI (L) together with solid LiTFSI (IIa). The melting temperatures of samples with  $0.70 < x < 0.75$  range from 137 °C to 151 °C. A high temperature liquid–solid double phase region is observed only for  $x > 0.75$  and exists at temperatures between 151 °C and the final melting point. The melting point depends on overall composition  $x$  and ranges from *ca.* 153 °C up to 230 °C. The phase consists of liquid (0.25–0.03)EMIMTFSI:(0.75–0.97)LiTFSI (L) together with solid LiTFSI (Ia). Temperature variable  ${}^7\text{Li}$  NMR spectra excellently agree with the structural changes outlined (Fig. 3). At low temperatures the quadrupole powder pattern stems from LiTFSI; with rising temperature the pattern changes and we observe the

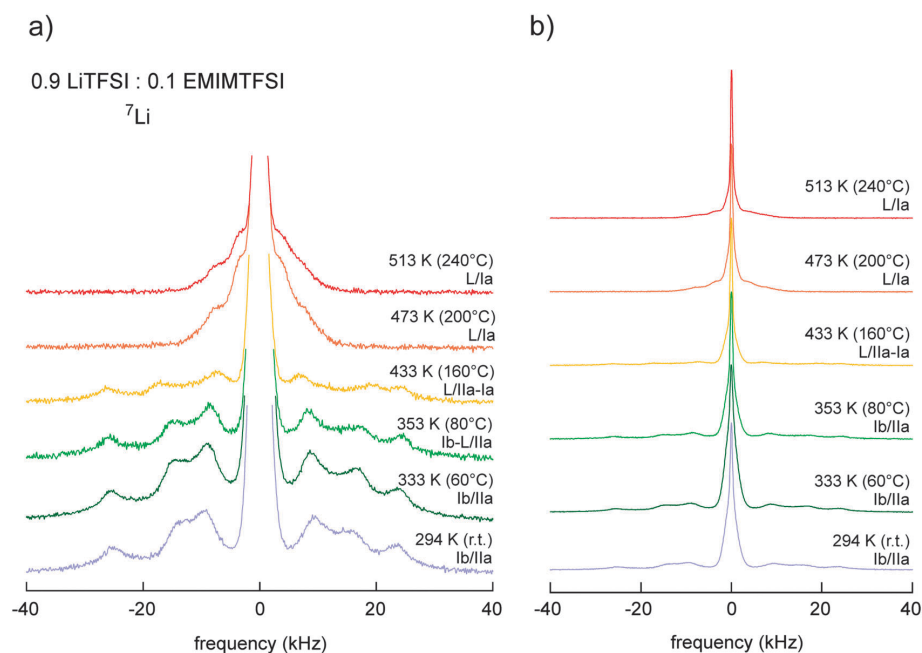


Fig. 3 Change in the solid-state  ${}^7\text{Li}$  NMR spectra (194.3 MHz) of  $\text{Li}_x\text{EMIM}_{(1-x)}\text{TFSI}$  with  $x = 0.9$  with increasing temperature; (a) the lower part of the spectra magnifying the quadrupole powder pattern, (b) full spectra revealing the two-component NMR central transition. The area fractions of the two NMR lines (see also the inset of Fig. 2b) are plotted in Fig. 4 as a function of temperature.

solid–solid I<sub>2</sub>a–I<sub>1</sub>a phase transition. Interestingly, melting of the Ib phase seems to partly affect the pattern of the I<sub>2</sub>a phase of LiTFSI as can be seen when the spectrum recorded at 80 °C (and 160 °C) is considered. At 200 °C the formation of the I<sub>1</sub>a phase has been completed. The spectrum recorded at 240 °C still has non-vanishing satellite intensities present, a signature of the crystalline LiTFSI phase (I<sub>1</sub>a). In Fig. 3b the complete NMR spectra are shown focusing on the central lines. With increasing  $T$  the number fraction of mobile Li ions, directly reflected by the area fraction of the narrowed NMR line, increases from 20 to 30% (see Fig. 4), in perfect agreement with the results mentioned above. This increase is directly in line with the increase of the overall conductivity of the sample with  $x = 0.9$  taking place between 30 and 70 °C which is below the melting point of the Ib phase (*cf.* Fig. 4 and 5). The correlation with the ionic conductivity indicates that the mobile ions seen by NMR increasingly start to participate in long-range ion transport also.

For the  $\text{Li}_x\text{BMIM}_{(1-x)}\text{TFSI}$  mixtures, in contrast to the EMIMTFSI based systems, the only equilibrium was between a liquid condensed phase of  $\text{Li}_x\text{BMIM}_{(1-x)}\text{TFSI}$ , being characterized by a high viscosity, and undissolved LiTFSI. Only the phase transitions of LiTFSI were detected (from I<sub>2</sub>a to I<sub>1</sub>a and melting of I<sub>1</sub>a). Even when the samples were stored for four weeks before any measurements had been carried out it was impossible to obtain any crystalline phase corresponding to 1/2 EMIMTFSI/LiTFSI (Ib). The data obtained for  $\text{Li}_x\text{PY}_{1.3(1-x)}\text{TFSI}$  are in very good agreement with those reported in the literature.<sup>5</sup>

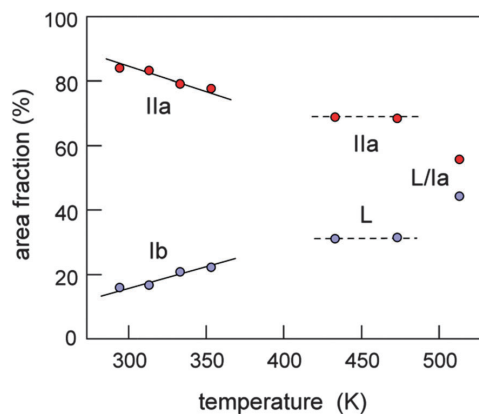


Fig. 4 Area fractions of the two dynamically distinct spin-reservoirs of  $\text{Li}_x\text{EMIM}_{(1-x)}\text{TFSI}$  with  $x = 0.9$ .

As the thermal behaviour of the materials dramatically depends on the thermal history as well as the composition, the 2nd DSC heating cycle gives a wealth of information. For  $x > 0.80$  all the phase transitions; Ib to L, I<sub>2</sub>a to I<sub>1</sub>a, and the melting of I<sub>1</sub>a are all reproducible. In addition, the crystallization during cooling is consistent with the 2nd heating cycle (Fig. 1b). Small heterogeneities of LiTFSI may here act as nucleation centres to facilitate crystallization. For  $x < 0.80$ ,

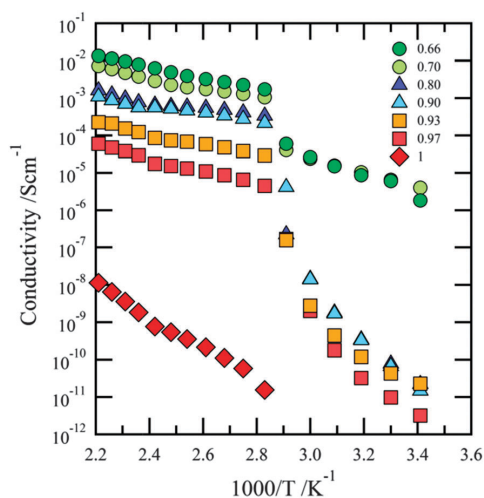


Fig. 5 Ionic conductivities obtained for the  $\text{Li}_x\text{EMIM}_{(1-x)}\text{TFSI}$  ( $0.66 \leq x \leq 1$ ) system; data collected during heating.

the 2nd cycle only records fully amorphous systems, characterized by increasing glass transition temperatures as a function of overall composition  $x$  ( $-32$  °C,  $-25$  °C, and  $-19$  °C for  $x = 0.66$ ,  $0.70$ , and  $0.75$ , respectively). In stark contrast, for  $x = 0.80$  thermal metastability is observed and different amounts of amorphous material have been formed characterized by a  $T_g$  of  $-2$  °C. Apart from causing the difference observed in *e.g.* the Ib to L transition temperature, it could also possibly provide different Li ion conductivities. The largest differences for the 2nd heating cycle were observed for the  $\text{Li}_x\text{PY}_{13(1-x)}\text{TFSI}$  system for which it was impossible to obtain reproducible results (not shown).

An important distinction to be made is that while the basic thermal behaviour as outlined above is fundamentally promising, the application of long-term high temperature electrochemical cycling using composite electrodes can be highly problematic, which is not investigated here. However, the next section points to the stability of the electrolytes during the high temperature conductivity measurements (with stabilization times of 30 min at each point) and all the materials are also stable during the synthesis procedure with mixing at  $250$  °C for 1 h.

### Ionic conductivity

Moving to a property of crucial importance for an electrolyte, *viz.* ionic conductivity, we observe for all compositions that ion dynamics are strongly correlated with the thermal behaviour of the samples. Previously, this has also been reported for pyrrolidinium (PY) based ILs doped with LiTFSI.<sup>7,16,28</sup> The three regimes being associated with the double phase regions Ib/IIa, L/IIa, and L/Ia, as seen in the DSC data, can also be straightforwardly recognized in the temperature dependent conductivity data (see Fig. 5 and 6).

The region corresponding to the existence of the dual phase Ib/IIa ( $20$  °C to  $70$  °C) is characterized by very low conductivities

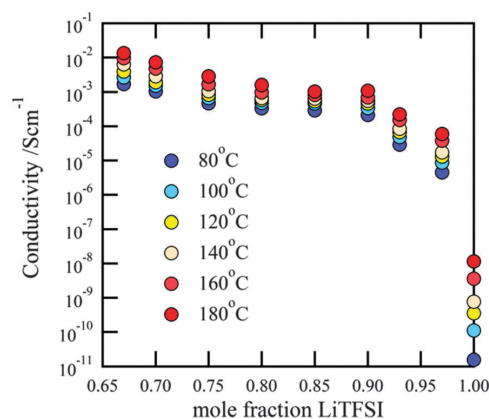


Fig. 6 Conductivity isotherms for the  $\text{Li}_x\text{EMIM}_{(1-x)}\text{TFSI}$  ( $0.66 \leq x \leq 1$ ) system as a function of composition; data collected during heating.

( $\sigma \approx 10^{-11}$  S  $\text{cm}^{-1}$ ) which is due to the presence of both crystalline 1:2 EMIMTFSI/LiTFSI and crystalline LiTFSI. The only exception is the sample with  $x = 0.70$  ( $\sigma \approx 10^{-6}$  S  $\text{cm}^{-1}$ ); very likely, this is due to the presence of some amorphous material. The fact that the  $^7\text{Li}$  NMR measurements reveal a sharp NMR line even at temperatures as low as room temperature is not in contradiction with the observation of low conductivities: in contrast to DC conductivity which probes long-range motions of the charge carriers, NMR is sensitive to dynamics on much shorter length scales.

Except for the sample with  $x = 0.7$ , between  $70$  °C and  $80$  °C a rapid increase in conductivity, *viz.* some orders of magnitudes, is observed, which is caused by the melting of the Ib phase. Since this process seem to also affect the  $^7\text{Li}$  NMR quadrupole powder pattern of the LiTFSI Ila phase (see Fig. 3a), this phase has potential to also somehow participate in enabling long-range ion transport.

Between  $80$  °C and  $140$  °C, that is the L/IIa region, charge carrier transport is characterized by relatively high and stable conductivities with values ranging from  $10^{-3}$  to  $10^{-5}$  S  $\text{cm}^{-1}$  and with a maximum in conductivity for  $x = 0.70$  ( $\sigma \approx 3 \times 10^{-3}$  S  $\text{cm}^{-1}$ ). Only slightly lower conductivities are observed in the compositional range  $0.75 \leq x \leq 0.90$  ( $\sigma \approx 10^{-4}$  S  $\text{cm}^{-1}$ ). Samples with  $x > 0.90$ , however, reveal a sudden drop in conductivity. In the last, the third conductivity region, corresponding to L/Ia ( $T > 140$  °C), the conductivity increases more rapidly with temperature. Once again, this might indicate that the LiTFSI phase takes part in facilitating ion transport over long distances. Despite the fact that the IIa-Ia phase transition is also detectable for pure LiTFSI in the conductivity measurements, the conductivity of pure LiTFSI is many orders of magnitude lower for the whole  $T$  range covered; it increases from  $10^{-11}$  S  $\text{cm}^{-1}$  at  $80$  °C to  $10^{-8}$  S  $\text{cm}^{-1}$  at  $180$  °C. The highest conductivity values are obtained for samples with  $x = 0.70$  and  $x = 0.75$  ( $\sigma \approx 3 \times 10^{-3}$  S  $\text{cm}^{-1}$ ) and are related to the final melting of the crystalline LiTFSI:EMIMTFSI phase Ib which occurs at  $138$  °C and  $151$  °C, respectively. Overall, high conductivities are observed for

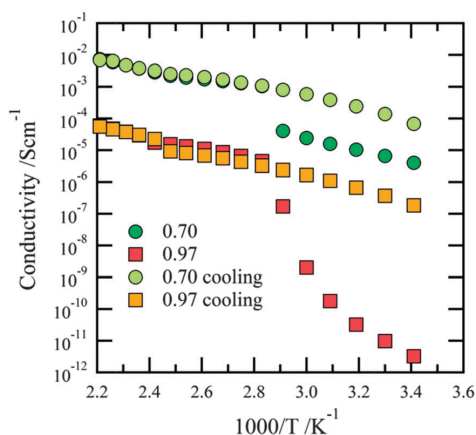


Fig. 7 Comparison of ionic conductivities obtained for the  $\text{Li}_x\text{EMIM}_{(1-x)}\text{TFSI}$  ( $x = 0.70$  and  $x = 0.97$ ) system; data collected during heating and cooling.

$0.70 < x < 0.90$  and lower conductivities for mixtures with overall compositions of  $x > 0.90$ .

Most likely, the results from the conductivity measurements and the thermal studies also correlate with the metastability of the different phases (see Fig. 7). Indeed, upon cooling, the Ia to IIa transition is well reproduced, with similar conductivity values as during heating. Similarly, also for the Ib to L transition there is no difference in the slope of the conductivity curves. The latter is in contradiction to the DSC data but can be explained by the tendency to create super-cooled liquid phases (even for  $x > 0.80$ ) and by the fact that the crystallization process is controlled by slow kinetics. Especially the different sizes and shapes of the samples for DSC (few mg, bulk) and conductivity (*ca.* 0.3 g, film) measurements should be taken into account.

A comparison of the temperature dependent ionic conductivity of  $\text{Li}_x\text{EMIM}_{(1-x)}\text{TFSI}$ ,  $\text{Li}_x\text{BMIM}_{(1-x)}\text{TFSI}$  and  $\text{Li}_x\text{PY}_{13(1-x)}\text{TFSI}$  for the different systems studied (Fig. 8) shows that between 20 °C and 70 °C the highest conductivities are obtained for the BMIMTFSI based samples. This can be explained by the presence of a liquid  $\text{Li}_x\text{BMIM}_{(1-x)'}\text{TFSI}$  phase rather than a solid–solid dual phase region being characteristic of both the  $\text{Li}_x\text{EMIM}_{(1-x)}\text{TFSI}$  and the  $\text{Li}_x\text{PY}_{13(1-x)}\text{TFSI}$  systems. The situation changes above 80 °C due to the melting of the Ib phase in the  $\text{Li}_x\text{EMIM}_{(1-x)}\text{TFSI}$  system leading to the highest conductivity observed. For  $x = 0.90$  the difference in ionic conductivity between the EMIMTFSI-based system and both the BMIMTFSI and the  $\text{PY}_{13}$ TFSI-based systems is about one order of magnitude above that at 80 °C. While the solvent-in-salt electrolytes can exhibit  $\text{Li}^+$  transference numbers as high as 0.73,<sup>14</sup> important for the inhibition of lithium dendrite growth, we have not determined these in this proof-of-concept study – but rely on the robustness of the materials. Further studies should of course properly address this property also. Moving to mechanical properties, the materials are powders at room temperature and easily handled as pellets, but depending on  $x$  may turn liquid at the working temperatures aimed at. If the materials will work in a

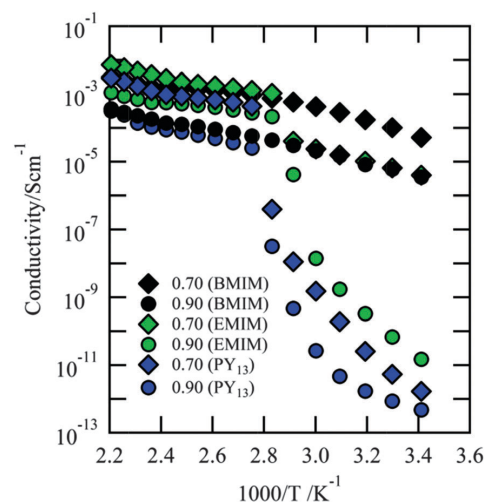


Fig. 8 Comparison of ionic conductivities obtained for the  $\text{Li}_x\text{EMIM}_{(1-x)}\text{TFSI}$ ,  $\text{Li}_x\text{BMIM}_{(1-x)}\text{TFSI}$ , and  $\text{Li}_x\text{PY}_{13(1-x)}\text{TFSI}$  ( $x = 0.70$  and  $x = 0.90$ ) systems; data collected during heating.

practical cell with respect to issues like electrode wettability is yet an open question calling for experimental evidence.

Adding to practical requirements, an EMIMTFSI-based electrolyte was previously shown to suppress Al current collector corrosion.<sup>29</sup> This was supported more recently when  $\text{PY}_{14}\text{TFSI}$  based electrolytes were also tested up to 60 °C; it was shown that even small amounts of ILs can suppress this phenomenon.<sup>30</sup> In addition, some very recent studies have revealed that by using electrolytes with (very) high concentrations of LiTFSI, even in organic solvents, the normally highly prevalent Al corrosion by TFSI can be hindered.<sup>14,31,32</sup> However, in contrast a very recent study showed that the electrochemical stability of  $\text{PY}_{14}$ -based electrolytes can be severely reduced at elevated temperatures such as 60 °C, even if TFSI-based ILs performed much better than the corresponding FSI-based ones.<sup>33</sup>

#### Raman spectroscopy studies

Finally, the macroscopic data for the  $\text{Li}_x\text{EMIM}_{(1-x)}\text{TFSI}$  system above are correlated with molecular level Raman spectroscopy data across all compositions and a wide range of temperatures. Raman spectra were collected at 23 °C, 90 °C and 165 °C to investigate the Ib, IIa, Ia, and L phases, respectively. The 735–760  $\text{cm}^{-1}$  region of the Raman spectra was chosen in order to obtain information about the anion coordination and thus the nature of the charge carrying species.<sup>16–23</sup>

The pure Ib phase ( $x = 0.66$ ) is useful as a starting point as the TFSI anion coordination is known<sup>11</sup> and, thus, can serve as an internal reference. Here, the TFSI anion exists in three different combinations of conformation and coordination environment; in two cases in  $C_1$  conformation and either coordinated by three lithium cations by four oxygen atoms or by two lithium cations by three oxygen atoms, and for the remaining case in  $C_2$  conformation and coordinated by two

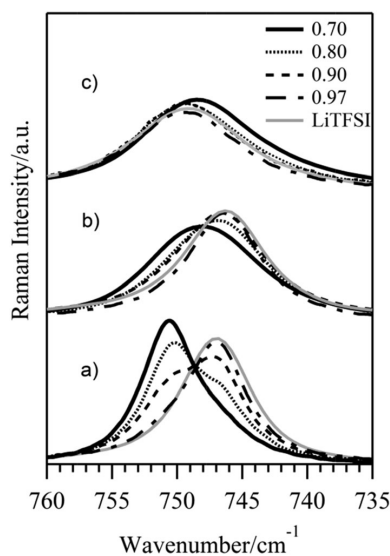


Fig. 9 Raman spectra of the  $\text{Li}_x\text{EMIM}_{(1-x)}\text{TFSI}$  ( $0.66 \leq x \leq 1$ ) system; collected at 23 °C (a), 90 °C (b) and 165 °C (c).

lithium cations by three oxygen atoms.<sup>15</sup> Likewise a known structure, in the I<sub>2a</sub> phase (pure LiTFSI) all TFSI anions are in  $C_2$  conformation and surrounded by four lithium cations each.<sup>25</sup> In general, at room temperature, two bands at *ca.* 747  $\text{cm}^{-1}$  and *ca.* 750.5  $\text{cm}^{-1}$  are observed for the  $\text{Li}_x\text{EMIM}_{(1-x)}\text{TFSI}$  systems (Fig. 9a). The first band can be correlated with the observations for the I<sub>2a</sub> phase, while the second corresponds to the I<sub>2b</sub> phase. This is further supported by the observation of an increasing  $x$  to continuously decrease the 750.5  $\text{cm}^{-1}$  band and increase the 747  $\text{cm}^{-1}$  band, until only the latter band remains. The Raman spectra collected at 90 °C (Fig. 9b), corresponding to the I<sub>2a</sub>/I<sub>2b</sub> phases, have wider and down-shifted bands as compared to the spectra collected at 23 °C. For the  $x = 0.70$  composition a broad band at 748  $\text{cm}^{-1}$  suggests at least two components; with increasing  $x$  the band maximum is shifted to 746  $\text{cm}^{-1}$ , but with a higher wavenumbers broadening. Adding an analysis of the 260–360  $\text{cm}^{-1}$  spectral range (Fig. 10) shows that, besides the bands characteristic of I<sub>2a</sub> (276  $\text{cm}^{-1}$ , 315  $\text{cm}^{-1}$ , 330  $\text{cm}^{-1}$  and 346  $\text{cm}^{-1}$ ) a group of signals being characteristic for  $[\text{Li}(\text{TFSI})_2]^-$  complexes appears upon melting of I<sub>2b</sub> (282  $\text{cm}^{-1}$ , 313  $\text{cm}^{-1}$ , 326  $\text{cm}^{-1}$ , and a shoulder at 338  $\text{cm}^{-1}$ ).<sup>22,23</sup> When the temperature is increased further (*i.e.*, up to 165 °C), hence above the I<sub>2a</sub> to I<sub>1a</sub> solid–solid phase transition, we observe a wide band located at approximately 749  $\text{cm}^{-1}$  for all compositions (Fig. 9c). For  $x = 0.70$  the maximum of this band is shifted towards lower wavenumbers by *ca.* 0.8  $\text{cm}^{-1}$ . Here, an analysis of the 260–360  $\text{cm}^{-1}$  spectral range shows no significant changes for the spectra with  $x = 0.70$  (Fig. 10c) *versus* data collected at 90 °C. The largest change occurs for the LiTFSI sample, where the I<sub>2a</sub> to I<sub>1a</sub> solid–solid phase transition takes place at 152 °C (Fig. 10c). The I<sub>1a</sub> phase is characterized by the following bands; 278  $\text{cm}^{-1}$  with a shoulder at 284  $\text{cm}^{-1}$ , 298  $\text{cm}^{-1}$ , 315  $\text{cm}^{-1}$  and

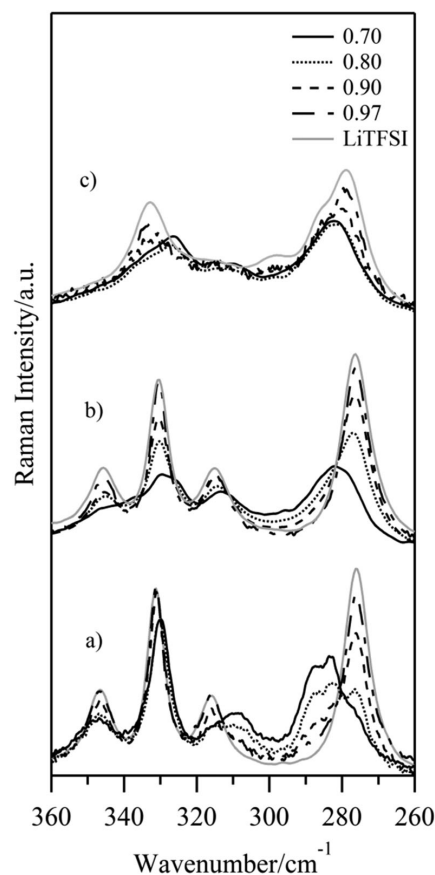


Fig. 10 Raman spectra of the  $\text{Li}_x\text{EMIM}_{(1-x)}\text{TFSI}$  ( $0.66 \leq x \leq 1$ ) system; collected at 23 °C (a), 90 °C (b) and 165 °C (c).

335  $\text{cm}^{-1}$ . This suggests a change in the conformation state of the TFSI anion in LiTFSI which simultaneously influences the EFG at the site of the  $^7\text{Li}$  nucleus, see above.

Considering also literature studies,<sup>17–23</sup> this indicates that the TFSI anion, compared with the pure I<sub>2a</sub> phase of LiTFSI (746  $\text{cm}^{-1}$ ) and with the existence in higher agglomerates or polymeric chains (*cf.* the molten I<sub>2b</sub> phase, 749  $\text{cm}^{-1}$ ), is also found in  $[\text{Li}(\text{TFSI})_2]^-$  triplets (746–749  $\text{cm}^{-1}$ ). The changed TFSI local coordination and charge carrier nature are clearly seen for  $x = 0.70$  with a large change in band area ratios upon heating. Indeed, the presence of highly mobile  $[\text{Li}(\text{TFSI})_2]^-$  can explain the high ionic conductivities observed, albeit rather unexpected for these high  $x$  values. As these complexes are largely responsible for the lithium transport in “LiX-in-IL” systems<sup>22,23</sup> the  $\text{Li}^+$  cation transport properties can also be arguably similar.

## 4 Conclusions

To conclude, a conceptually new class of electrolyte materials for high temperature lithium batteries has been studied. The

ionic liquid-in-salt samples studied show promising high ionic conductivities as well as appreciable mechanical strength. Fundamentally, the materials are truly multi-phase and easily super-cooled; they seem to benefit from charge carriers being of the same type as found in classic IL-based electrolytes.

## Acknowledgements

M.M. and P.J. are grateful to the Swedish Research Council (VR), the Swedish Research Council for Environment, Agricultural Sciences and Spatial Planning (FORMAS), and Chalmers Energy and Transport Areas of Advance for financial support. M.W. thanks the Austrian Federal Ministry of Economy, Family and Youth, and the Austrian National Foundation for Research, Technology and Development for financial support.

## Notes and references

- J.-M. Tarascon and M. Armand, *Nature*, 2001, **414**, 359.
- M. Armand, F. Endres, D. R. MacFarlane, H. Ohno and B. Scrosati, *Nat. Mater.*, 2009, **8**, 621.
- A. Lewandowski and A. Świdarska-Mocek, *J. Power Sources*, 2009, **194**, 601.
- D. R. MacFarlane, J. Huang and M. Forsyth, *Nature*, 1999, **402**, 792.
- W. A. Henderson and S. Passerini, *Chem. Mater.*, 2004, **16**, 2881.
- Q. Zhou, W. A. Henderson, G. Appetecchi and S. Passerini, *J. Phys. Chem. C*, 2010, **114**, 6201.
- M. Forsyth, J. Huang and D. R. MacFarlane, *J. Mater. Chem.*, 2000, **10**, 2259.
- Q. Zhou, K. Fitzgerald, P. D. Boyle and W. A. Henderson, *Chem. Mater.*, 2010, **22**, 1203.
- Q. Hu, S. Osswald, R. Daniel, Y. Zhu, S. Wesel, L. Ortiz and D. R. Sadoway, *J. Power Sources*, 2011, **196**, 5604.
- D. Munoz-Rojas, J.-B. Leriche, C. Delacourt, P. Poizot, M. R. Palacin and J.-M. Tarascon, *Electrochem. Commun.*, 2007, **9**, 708.
- F. Mestre-Aizpurua, S. Laruelle, S. Grugeon, J.-M. Tarascon and M. R. Palacin, *J. Appl. Electrochem.*, 2010, **40**, 1365.
- J. Mun, Y. S. Jung, T. Yim, H. H. Y. Lee, H.-J. Kim, Y. G. Kim and S. M. Oh, *J. Power Sources*, 2009, **194**, 1068.
- C. A. Angell, C. Liu and E. Sanchez, *Nature*, 1993, **362**, 137.
- L. Suo, Y.-S. Hu, H. Li, M. Armand and L. Chen, *Nat. Commun.*, 2013, **4**, 1481.
- K. Matsumoto, R. Hagiwara and O. Tamada, *Solid State Sci.*, 2006, **8**, 1103.
- Q. Zhou, P. D. Boyle, L. Malpezzi, A. Mele, J.-H. Shin, S. Passerini and W. A. Henderson, *Chem. Mater.*, 2011, **23**, 4331.
- M. Herstedt, M. Smirnov, P. Johansson, M. Chami, J. Grondin, L. Servant and J. C. Lassegues, *J. Raman Spectrosc.*, 2005, **36**, 762.
- J. C. Lassegues, J. Grondin, R. Holomb and P. Johansson, *J. Raman Spectrosc.*, 2007, **38**, 551.
- Y. Umebayashi, T. Mitsugi, S. Fukuda, T. Fujimori, K. Fujii, R. Kanzaki, M. Takeuchi and S. Ishiguro, *J. Phys. Chem. B*, 2007, **111**, 13028.
- L. J. Hardwick, M. Holzapfel, A. Wokaun and P. Novak, *J. Raman Spectrosc.*, 2007, **38**, 110.
- Y. Umebayashi, S. Mori, K. Fujii, S. Tsuzuki, S. Seki, K. Hayamizu and S. Ishiguro, *J. Phys. Chem. B*, 2010, **114**, 6513.
- J. C. Lassegues, J. Grondin and D. Talaga, *Phys. Chem. Chem. Phys.*, 2006, **8**, 5629.
- J. C. Lassegues, J. Grondin, C. Aupetit and P. Johansson, *J. Phys. Chem. A*, 2009, **113**, 305.
- K. Eichele, *WSolids1 software, version 1.20.21*, Universität Tübingen, 2013.
- J. L. Nowinski, P. Lightfoot and P. G. Bruce, *J. Mater. Chem.*, 1994, **4**, 1579.
- A. Abragam, *The Principles of Nuclear Magnetism*, Oxford University Press, 1961.
- D. Freude, in *Encyclopedia of Analytical Chemistry*, ed. R. A. Meyers, John Wiley & Sons Ltd, Chichester, 2000.
- W. A. Henderson, S. Passerini, H. C. De Long and P. C. Trulove, *ECS Trans.*, 2008, **11**, 115.
- B. Garcia and M. Armand, *J. Power Sources*, 2004, **132**, 206.
- R.-S. Kühnel, M. Lübke, M. Winter, S. Passerini and A. Balducci, *J. Power Sources*, 2012, **214**, 178.
- K. Matsumoto, K. Inoue, K. Nakahara, R. Yuge, T. Noguchi and K. Utsugi, *J. Power Sources*, 2013, **231**, 234.
- D. W. McOwen, D. M. Seo, O. Borodin, J. Vatamanu, P. D. Boyle and W. A. Henderson, *Energy Environ. Sci.*, 2014, **7**, 416.
- R.-S. Kühnel and A. Balducci, *J. Power Sources*, 2014, **249**, 163.



# 4

## Conclusion and Outlook

In the course of this dissertation, different materials have been investigated comprehensively by various solid-state NMR techniques and impedance spectroscopy. The combination of the two types of methods allows to probe ionic motion from both a microscopic and macroscopic point of view. The main focus of this work was the fundamental study of Li ion diffusivity (diffusion mechanisms and dynamical parameters) in various materials. The investigated materials in this work can be categorized as (*i*) study of lithium ion diffusion in low-dimensional materials ( $\text{Li}_3\text{BiS}_5$  and  $2\text{H-Li}_x\text{NbS}_2$ ), (*ii*) study of lithium ion diffusion in three-dimensional garnet-type Li oxides (LLZTO and LLZBO), (*iii*) study of the influence of mechanical treatment on lithium diffusivity in the aluminosilicate mineral petalite and (*iv*) study of lithium diffusion of a novel electrolyte concept "ionic liquids-in-salt" for high-temperature lithium batteries.

**$\text{Li}_3\text{BiS}_5$ .**  $\text{Li}_3\text{BiS}_5$  crystallizes with a channel-like structure and the Li ions, thus, have access to a spatially rather restricted diffusion pathway.  $^6\text{Li}$  MAS NMR spectroscopy was successfully employed to reveal the two distinct lithium positions present in the crystal structure of the mixed conductor  $\text{Li}_3\text{BiS}_5$ . In addition to the structural characterization, motional processes occurring on long-range as well as short-range scales were probed through  $^7\text{Li}$  NMR relaxometry. Bismuth and lithium nuclei share the same crystallographic site – bismuth atoms are blocking the diffusion pathway of lithium. Topological analyses and  $^7\text{Li}$  NMR relaxometry suggest that the lithium ions indeed diffuse one-dimensionally along the channels in the  $b$  direction involving tetrahedral voids. Activation energies as high as 0.66(2) eV were extracted from spin-lock NMR. A lithium jump rate in the order of *ca.*  $2 \times 10^4 \text{ s}^{-1}$  at 500 K identified the material as a moderate to poor ionic conductor, nonetheless the characterization and especially the synthetic pathway of  $\text{Li}_3\text{BiS}_5$  can be a potential foundation for the development of new lithium bismuth sulfides.

**$2\text{H-Li}_x\text{NbS}_2$ .** Two-dimensional Li ion diffusion was studied in  $2\text{H-Li}_x\text{NbS}_2$  as a function of the lithium content  $x$ .  $2\text{H-Li}_x\text{NbS}_2$  was a suitable and intriguing model system with a layered structure

to study both dimensionality effects in spatially confined dimensions, as well as the influence of Li intercalation on local hopping and long-range ion transport. Frequency-dependent  $R_\rho$  measurements were successfully employed to identify two-dimensional diffusion in 2H-Li<sub>x</sub>NbS<sub>2</sub> taking place along the buried interfaces in the host material. All samples show a small but clearly noticeable logarithmic frequency dependence in the  $R_\rho$  rates within the high temperature limit characterized by  $\omega_1\tau_c \ll 1$ . The experimental results are in excellent agreement with values predicted with the model of Richards for two-dimensional diffusion by using the semiempirical spectral density function.  $R_\rho$  NMR measurements showed that the Li intercalation degree  $x$  influences the Li ion diffusion in the material as expected. The larger that  $x$  is chosen, the less the vacancy concentration, which slows down Li diffusivity in the van der Waals gap. The  $R_{1\rho}$  rate peak maximum is shifted towards higher temperatures with increasing intercalation content  $x$ . Additionally, the slow-down of Li diffusion in the material is confirmed by a significant increase of the long-range activation energy ( $E_{a,x=0.3} = 0.44$  eV  $\rightarrow$   $E_{a,x=0.7} = 0.47$  eV  $\rightarrow$   $E_{a,x=1} = 0.64$  eV).

**Li<sub>6</sub>La<sub>3</sub>ZrTaO<sub>12</sub>.** For the first time, temperature-variable <sup>7</sup>Li NMR relaxometry measurements using both laboratory and spin-lock techniques were used to probe very fast lithium ion diffusivity in single crystalline Li<sub>6</sub>La<sub>3</sub>ZrTaO<sub>12</sub>. The data obtained from  $R_{1\rho}$  measurements perfectly mirror a modified BPP-type relaxation response being based on a Lorentzian-shaped relaxation function. The rates measured could be parameterized with a single set of diffusion parameters. A activation energy of 0.51 eV for long-range Li ion diffusion was calculated from the HT flank of the  $R_{1\rho}$  rate peak. Additionally to the NMR experiments, impedance spectroscopy experiments were carried out. The conductivity measurements identified Li<sub>6</sub>La<sub>3</sub>ZrTaO<sub>12</sub> as a very fast Li ion conductor with a high DC conductivity,  $\sigma_{DC}$  pf  $2.9 \times 10^{-4}$  S cm<sup>-1</sup>, and an activation energy of 0.47 eV at around ambient temperatures. Both NMR and IS methods are able to record the same diffusion process, which is reflected directly in the similar activation energies.

**Li<sub>7-x</sub>La<sub>3</sub>Zr<sub>2-x</sub>Bi<sub>x</sub>O<sub>12</sub>.** Motional narrowing of a series of bismuth doped LLZO ( $x_{int} = 0.10 - 1.00$ ) was measured by the evaluation of the FWHM of <sup>7</sup>Li solid-state NMR spectra. The results show that fast Li ion diffusivity for LLZBO is only achieved for high Bi contents. <sup>7</sup>Li NMR rates recorded in the laboratory frame of references confirms the assumed trend from motional narrowing measurements by a significant decrease of activation energy with increasing bismuth content  $x$ . The energies for short-range ion diffusion were obtained from the LT flank of  $R_1$  rates -  $E_{a,x=0.1} = 0.31(1)$  eV  $\rightarrow$   $E_{a,x=0.9} = 0.19(1)$ .

**LiAlSi<sub>4</sub>O<sub>10</sub>.** The influence of mechanical treatment, and thus nanostructuring, and the introduction of defects on Li ion dynamics in both crystalline petalite LiAlSi<sub>4</sub>O<sub>10</sub> and its glassy form, was comprehensively investigated by solid-state NMR and conductivity spectroscopy. Nanostructured samples were prepared by high-energy ball milling of the coarsely ground starting materials. As probed by conductivity spectroscopy, ball-milling of the crystalline LiAlSi<sub>4</sub>O<sub>10</sub> sample results in an enhancement of long-range ion transport by almost two orders of magnitude. Starting with micro-LiAlSi<sub>4</sub>O<sub>10</sub>, the activation energy decreased from 0.95 eV down to 0.81 eV. The opposite trend, however, is found when LiAlSi<sub>4</sub>O<sub>10</sub> glass is treated for several hours in a planetary mill. The Li ion conductivity of the glassy forms decreases with increasing milling and a reverse trend is observed regarding the activation energies since it increases from 0.73 eV to 0.85 eV. This decrease in conductivity is caused by mechanically induced structural relaxation of the glass. Importantly, with increasing milling time, the Li ion conductivities of both morphologies, *viz* crystalline and glassy, head towards each other.

---

**Li<sub>x</sub>EMIM<sub>1-x</sub>TFSI.** A conceptually new class of electrolyte materials usable for high temperature lithium batteries has been studied by solid state NMR; the mixture of an ionic liquid with a lithium salt. <sup>7</sup>Li NMR experiments were used to study both local electronic structures and Li<sup>+</sup> self-diffusion in LiTFSI and Li<sub>x</sub>EMIM<sub>(1-x)</sub>TFSI with  $x$  equals 0.9. Upon heating the mixture to 513 K, the relaxation transients clearly reveal several double phase regions; one phase can be assigned to the known solid-state phase transformation of lithium salt and can be well recognized by the change of the quadruple powder pattern of the <sup>7</sup>Li NMR spectra of LiTFSI. The change of the powder pattern was proved by examining the pure lithium salt in addition to the mixture. A rapid increase in long-range ion conductivity, within two orders of magnitudes, takes place when the 1/2 EMIMTFSI/LiTFSI phase starts to melt. This process can also be monitored by temperature-variable <sup>7</sup>Li SLR NMR. If recorded up to delay times of 1000s, the pronounced bi-exponential <sup>7</sup>Li SLR NMR transients directly reveal a subset of highly mobile Li ions, partly identified as [Li(TFSI)<sub>2</sub>]<sup>-</sup>, which can be well discriminated from the response of pure salt. This sub-ensemble is assumed to be responsible for the drastic boost of the ion conductivity.





## Supplemental material

Below, supplemental material to the articles "LiBi<sub>3</sub>S<sub>5</sub> - A lithium bismuth Sulfide with strong cation disorder" (see pp. 33) and "Synthesis, crystal structure, and stability of cubic Li<sub>7-x</sub>La<sub>3</sub>Zr<sub>2-x</sub>O<sub>12</sub>" (see pp. 63) is given. In addition, all conductivity spectra and the corresponding Arrhenius plot are shown as supplemental material to section 3.3.

# LiBi<sub>3</sub>S<sub>5</sub>—A Lithium Bismuth Sulfide with Strong Cation Disorder

## Supporting Information

*Suliman Nakhal<sup>a</sup>, Dennis Wiedemann<sup>a,\*</sup>, Bernhard Stanje<sup>b</sup>, Oleksandr Dolotko<sup>c</sup>, Martin Wilkening<sup>b</sup>, Martin Lerch<sup>a</sup>*

<sup>a</sup>Institut für Chemie, Technische Universität Berlin, Straße des 17. Juni 135, 10623 Berlin, Germany.

<sup>b</sup>Christian Doppler Laboratory for Lithium Batteries and Institute for Chemistry and Technology of Materials (Member of NAWI Graz), Graz University of Technology, Stremayrgasse 9, 8010 Graz, Austria.

<sup>c</sup>Heinz Maier-Leibnitz Zentrum (MLZ), Technische Universität München, Lichtenbergstraße 1, 85748 Garching b. München, Germany.

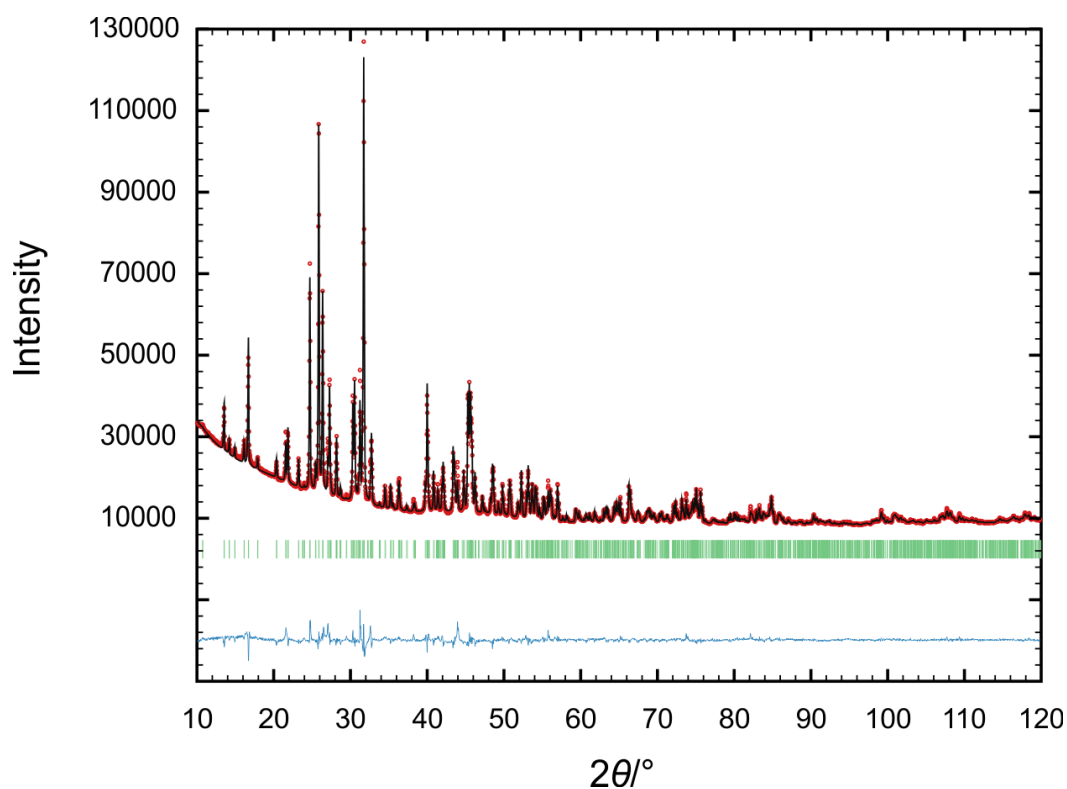


**Fig. S1.** X-ray powder diffractogram of LiBi<sub>3</sub>S<sub>5</sub> with the results of the Rietveld refinement (black: measured, red: calculated intensities, green: Bragg positions, blue: intensity difference).

**Table S1.** Details of X-ray powder diffraction at  $\text{LiBi}_3\text{S}_5$ .

Sum formula	$\text{LiBi}_3\text{S}_5$
$T/\text{K}$	298
Crystal system	monoclinic
Space group	$C2/m$
$\lambda_1/\text{pm}$	154.056
$\lambda_2/\text{pm}$	154.439
$Z$	4
$M/\text{g mol}^{-1}$	794.2
$a/\text{pm}$	1310.23(6)
$b/\text{pm}$	400.054(18)
$c/\text{pm}$	1650.92(7)
$\beta/^\circ$	94.0840(10)
$V/10^6 \text{ pm}^3$	863.15(7)
$\rho_{\text{calc}}/\text{g cm}^3$	6.112
$\mu/\text{mm}^{-1}$	128.51
$R_p$	0.0188
$R_{\text{wp}}$	0.0286
$R_{\text{exp}}$	0.0084
$R_B$	0.0658
$R_F$	0.0426
$S$	3.36

**Table S2.** Atomic coordinates, displacement parameters, and site occupation factors (s.o.f.) for LiBi<sub>5</sub>S<sub>5</sub> at ambient temperature as derived from X-ray powder diffraction.

Atom	Wyckoff site	<i>x</i>	<i>y</i>	<i>z</i>	<i>U</i> <sub>iso</sub> /10 <sup>4</sup> pm <sup>2</sup>	s.o.f.
Bi1	4 <i>i</i>	0.2378(2)	½	0.11120(14)	0.0223(13)	0.875(4)
Li1	4 <i>i</i>	0.2378(2)	½	0.11120(14)	0.0223(13)	0.125(4)
Bi2	4 <i>i</i>	0.4725(2)	0	0.21770(13)	0.0198(12)	0.862(3)
Li2	4 <i>i</i>	0.4725(2)	0	0.21770(13)	0.0198(12)	0.138(3)
Bi3	4 <i>i</i>	0.21592(16)	0	0.39037(13)	0.0180(11)	0.943(5)
Li3	4 <i>i</i>	0.21592(16)	0	0.39037(13)	0.0180(11)	0.057(5)
Bi4	2 <i>a</i>	0	0	0	0.019	0.467(4)
Li4	2 <i>a</i>	0	0	0	0.019	0.533(4)
Bi5	2 <i>d</i>	0	½	½	0.019	0.172(4)
Li5	2 <i>d</i>	0	½	½	0.019	0.828(4)
S1	4 <i>i</i>	0.3776(10)	0	0.0548(7)	0.010(4)	1
S2	4 <i>i</i>	0.1107(10)	0	0.1494(7)	0.013(4)	1
S3	4 <i>i</i>	0.3408(10)	½	0.2562(7)	0.019(4)	1
S4	4 <i>i</i>	0.0650(8)	½	0.3725(7)	0.007(4)	1
S5	4 <i>i</i>	0.3611(9)	½	0.4618(7)	0.017(4)	1

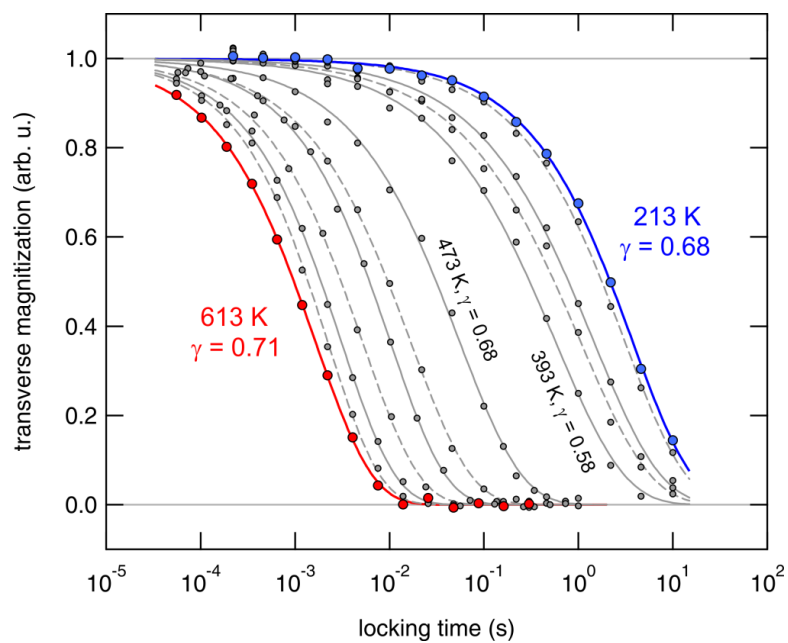


**Fig. S2.**  ${}^7\text{Li}$ -NMR  $R_{1\rho}$  magnetization transients recorded in the rotating frame of reference using a spin-lock frequency of 30 kHz; temperatures ranged from 213 to 613 K. The solid and dashed lines represent fits according to stretched exponentials yielding the parameters  $R_{1\rho}$  and  $\gamma$ . Note that the  $x$  axis is scaled logarithmically.

## Supporting Information

**Synthesis, crystal structure and stability of cubic  $\text{Li}_{7-x}\text{La}_3\text{Zr}_{2-x}\text{Bi}_x\text{O}_{12}$** 

Reinhard Wagner<sup>\*,†</sup>, Daniel Rettenwander<sup>†</sup>, Günther J. Redhammer<sup>†</sup>, Gerold Tippelt<sup>†</sup>, Gebhard Sabathl<sup>†</sup>, Maurizio E. Musso<sup>†</sup>, Bernhard Stanje<sup>‡</sup>, Martin Wilkening<sup>‡</sup>, Emmanuelle Suard<sup>§</sup>, Georg Amthauer<sup>†</sup>

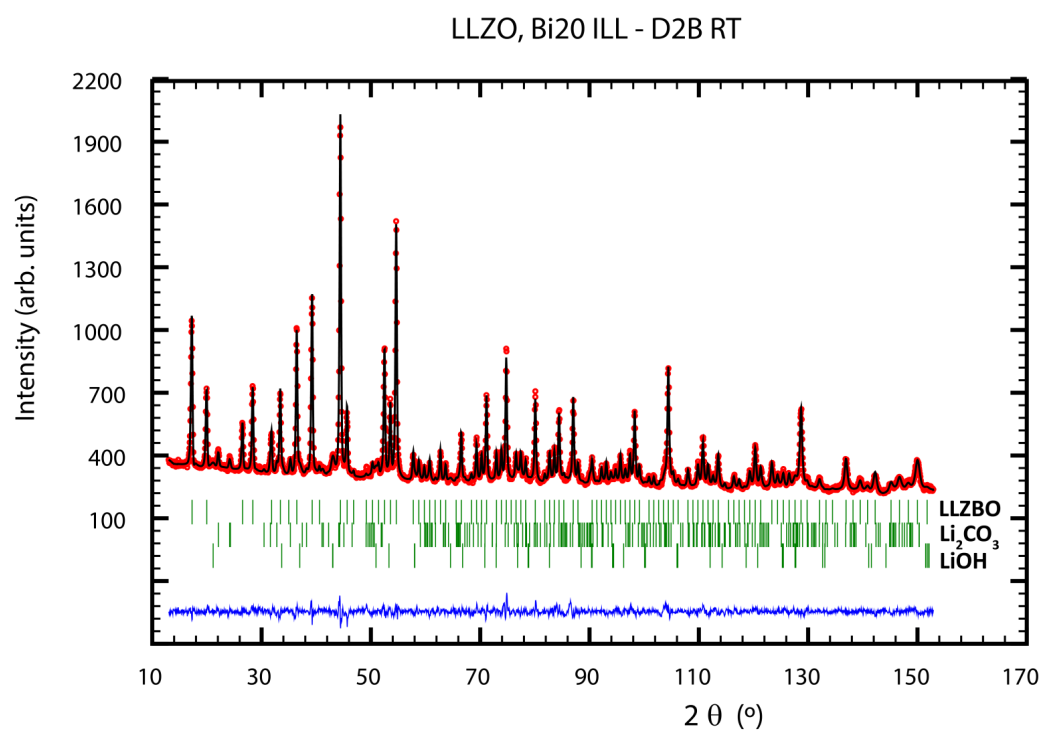


**Figure S1.** Rietveld refinement of NPD data of sample  $\text{Li}_{6.80}\text{La}_3\text{Zr}_{1.80}\text{Bi}_{0.20}\text{O}_{12}$ .

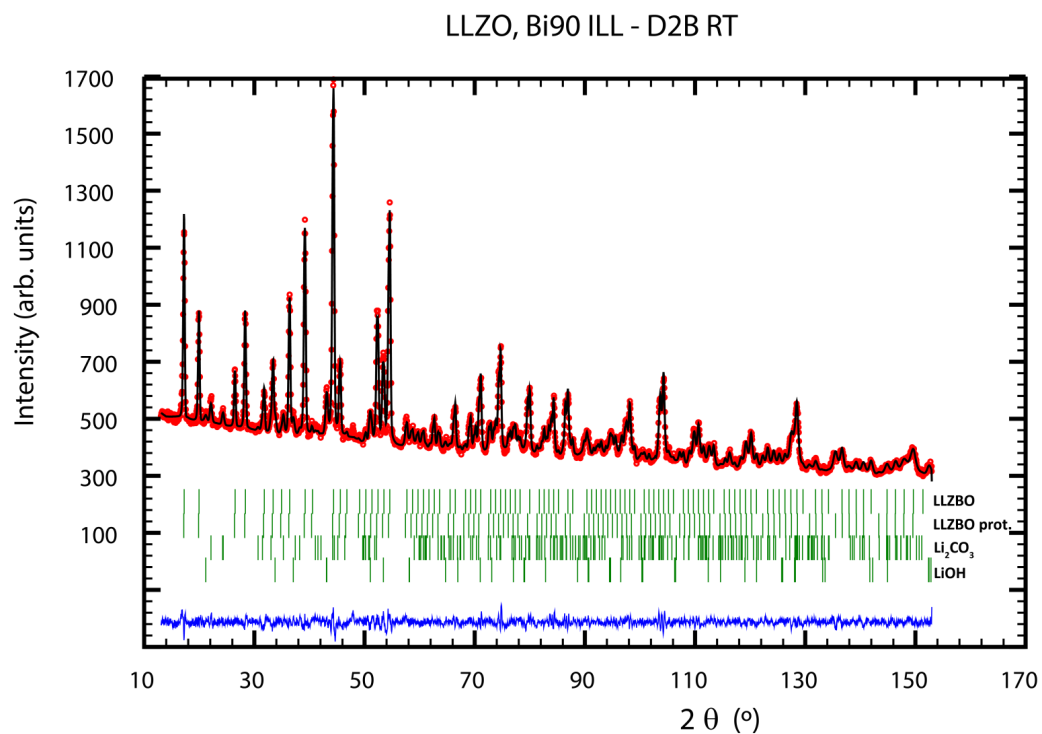


**Figure S2.** Rietveld refinement of NPD data of sample  $\text{Li}_{6.10}\text{La}_3\text{Zr}_{1.10}\text{Bi}_{0.90}\text{O}_{12}$ , using unprotonated LLZBO as well as protonated LLZBO.

**Table S1.** Unit-cell parameters  $a_0$  of  $\text{Li}_{7-x}\text{La}_3\text{Zr}_{2-x}\text{Bi}_x\text{O}_{12}$  as derived from NPD data.

$x$	$a_0$ [Å]	
	unprotonated LLZBO	protonated LLZBO
0.10	13.00541(11)	-
0.20	13.00396(10)	-
0.30	13.00790(13)	13.05130(35)
0.40	13.01106(09)	13.05581(35)
0.50	13.01373(12)	13.05951(31)
0.60	13.01767(21)	13.06724(26)
0.70	13.02165(24)	13.07348(25)
0.80	13.01118(10)	13.05684(29)
0.90	13.01544(20)	13.07028(23)
1.00	13.01692(19)	13.06627(24)

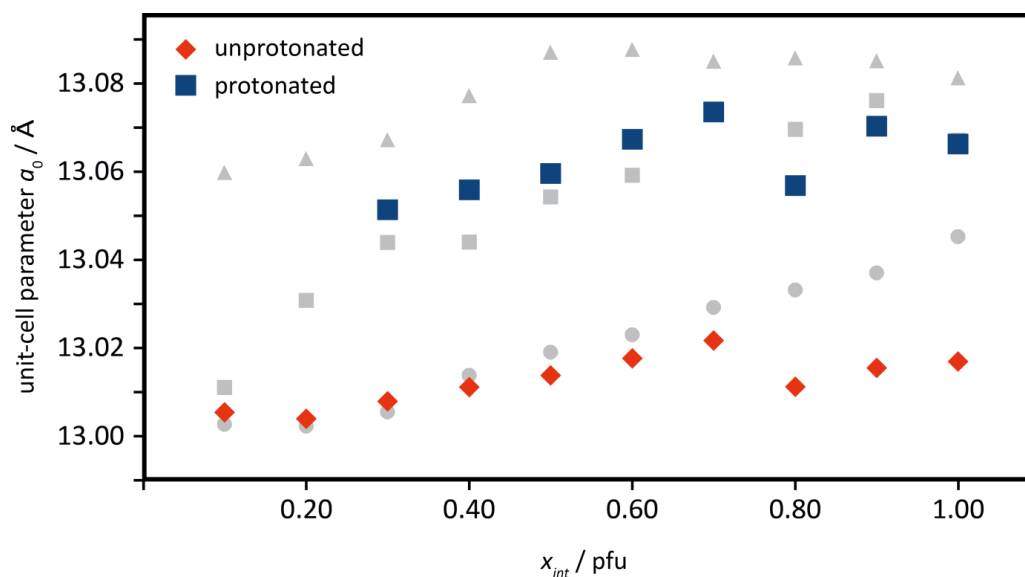


**Figure S3.** Unit-cell parameter of  $\text{Li}_{7-x}\text{La}_3\text{Zr}_{2-x}\text{Bi}_x\text{O}_{12}$  derived from NPD data. Red diamonds represent unit-cell parameters of unprotonated LLZBO phases, while blue squares represent unit-cell parameter values of protonated LLZBO phases. For comparison, unit-cell parameter values derived from XRPD are shown in grey (grey spheres: as-synthesized; grey squares: after 1 week under air; grey triangles: after 3 weeks under air).

**Table S2.** Structural data of  $\text{Li}_{6.80}\text{La}_3\text{Zr}_{1.80}\text{Bi}_{0.20}\text{O}_{12}$  (upper table) and  $\text{Li}_{6.20}\text{La}_3\text{Zr}_{1.20}\text{Bi}_{0.80}\text{O}_{12}$  (lower table), respectively, as derived from Rietveld refinement of NPD data.

**$\text{Li}_{6.80}\text{La}_3\text{Zr}_{1.80}\text{Bi}_{0.20}\text{O}_{12}$ :**

	<i>x</i>	<i>y</i>	<i>z</i>	<i>B</i>	<i>occ.</i>
La	0.125	0	0.25	1.60(4)	1
Zr	0	0	0	1.50(3)	0.91(1)
Bi	0	0	0	1.50(3)	0.09(1)
O	0	0.19477(13)	0.28108(11)	1.86(4)	1
Li1	0.375	0	0.25	3.7(4)	0.57(3)
Li2	0.0988(11)	0.1858(11)	0.4136(11)	3.5*	0.44(3)

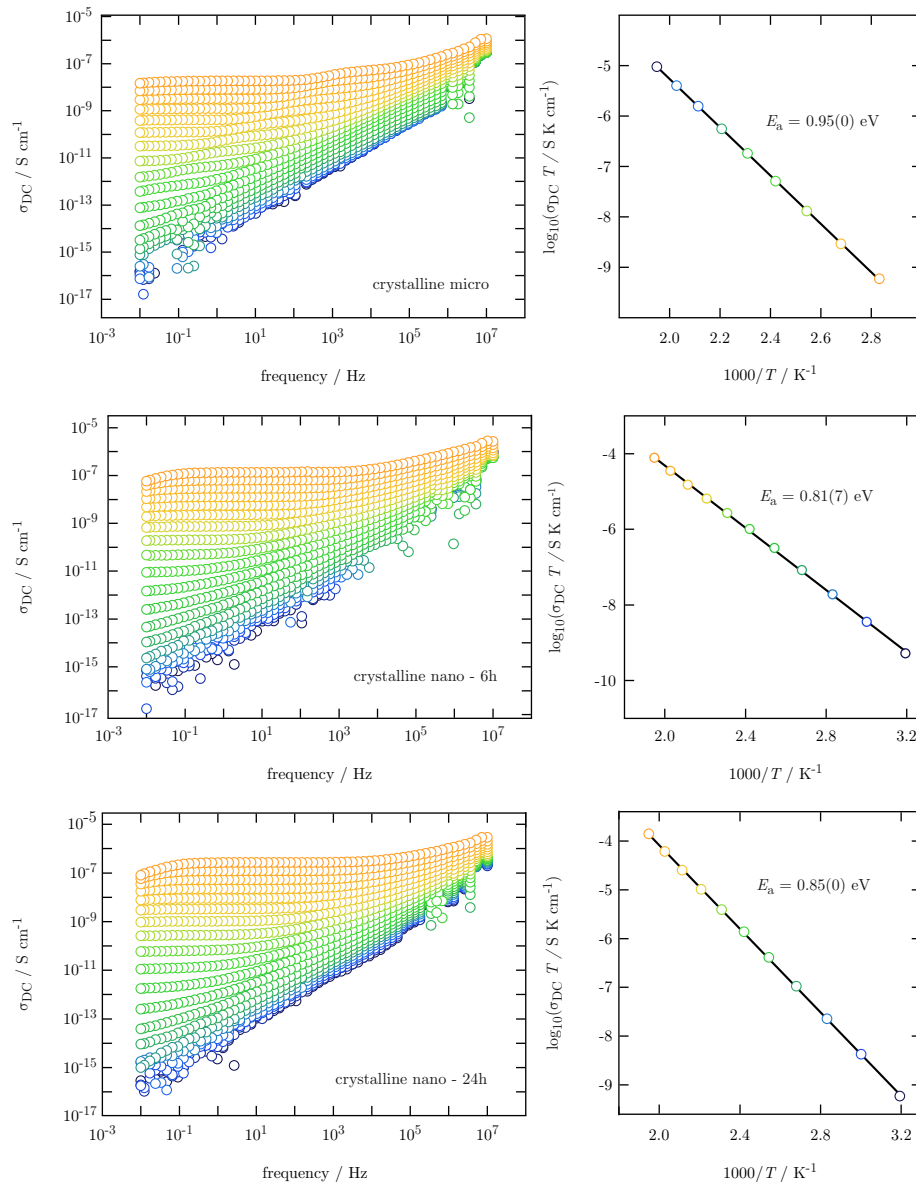
\* B value fixed during refinement

**$\text{Li}_{6.20}\text{La}_3\text{Zr}_{1.20}\text{Bi}_{0.80}\text{O}_{12}$ :**

	<i>x</i>	<i>y</i>	<i>z</i>	<i>B</i>	<i>occ.</i>
La	0.125	0	0.25	1.31(3)	1
Zr	0	0	0	1.21(4)	0.56(3)
Bi	0	0	0	1.21(4)	0.44(3)
O	0.10075(19)	0.1959(3)	0.28132(	1.62(3)	1
Li1	0.375	0	0.25	1.9(3)	0.51(4)
Li2	0.6849(24)	0.5924(25)	0.10666(	3.5*	0.32(2)

\* B value fixed during refinement

## Supporting information

Li ion diffusion & ionic conduction in aluminosilicate  $\text{LiAlSi}_4\text{O}_{10}$ 

**Figure A.1** – On the left hand side conductivity spectra for all crystalline petalite samples (0h, 6h and 24h milling time) and on the right hand side the corresponding Arrhenius plot are presented.

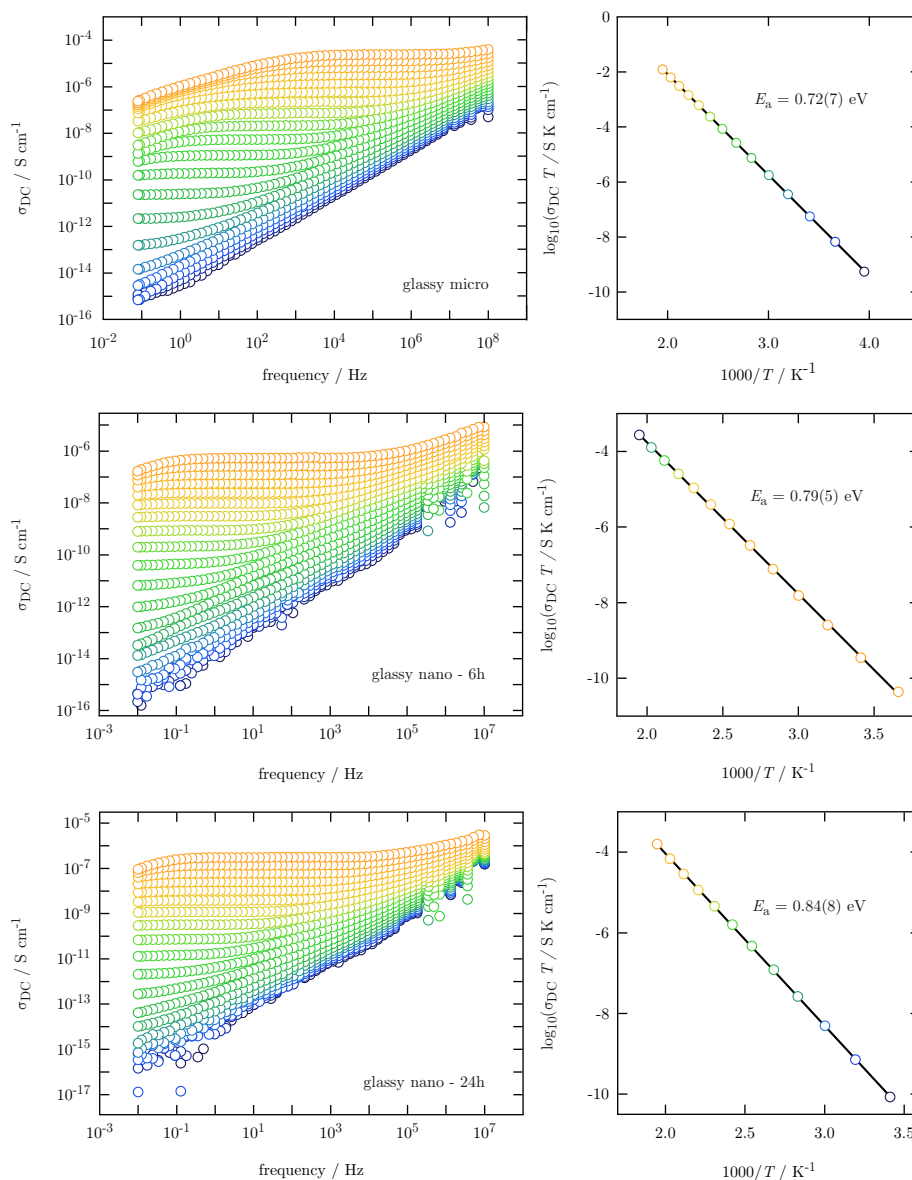


**Figure A.2** – On the left hand side conductivity spectra for all glassy petalite samples (0h, 6h and 24h milling time) and on the right hand side the corresponding Arrhenius plot are presented.

# B

## Experimental

### B.1 Apparatus

#### B.1.1 Solid-state NMR setup

$^{6,7}\text{Li}$  NMR measurements were performed using two different configurations of Bruker Avance III solid-state NMR spectrometers of the wide-bore (WB) type. One device is an Avance III 300 spectrometer equipped with a 7 T magnet corresponding to a  $^6\text{Li}$  resonance frequency of 44 MHz and a  $^7\text{Li}$  resonance frequency of 116 MHz. The other device is an Avance III 500 spectrometer equipped with a 11 T magnet corresponding to a  $^6\text{Li}$  resonance frequency of 74 MHz and a  $^7\text{Li}$  resonance frequency of 194 MHz.

The probe heads that were used for static and magic-angle spinning (MAS) experiments were commercially available solid-state broadband probes by Bruker. A Eurotherm controller in combination with type T thermocouples was used to regulate the temperature.

For static measurements, a broadband teflon probe head with a temperature range of 180 K up to 450 K. was employed. For measurements at temperatures above 450 K, a ceramic probe designed for high-temperature measurements up to 620 K was used.

High-resolution MAS NMR on the Avance III 500 was performed by using 2.5 mm or 4 mm Bruker broadband probe heads, with rotation rates up to 30 kHz and 15 kHz respectively.

For static NMR relaxation experiments, the powders were fire-sealed under vacuum in small DURAN<sup>®</sup> glass tubes typically of 3 - 4 cm length with 5 mm diameter. For MAS NMR experiments, the powders were packed into the corresponding zirconia rotor.

### B.1.2 Impedance spectroscopy setup

Broadband dielectric measurements were done on a Novocontrol Concept 80 impedance system. The setup includes an Alpha-A RF impedance analyzer connected to an active ZS-cell providing a frequency range of starting from  $10^{-4}$  Hz up to 10 MHz. Alternatively, an Agilent 4991E RF impedance analyzer with an RF sample cell can be used extending the frequency range to 3 GHz. A Novocontrol QUATRO cryosystems is responsible for the temperature control allowing measurements to be performed in a range of from 113 K to 670 K. All measurements are performed under inert conditions since the cell is constantly being flushed with dry nitrogen.

For impedance measurements, the powders were pressed to pellets in pressing tools (5, 8 or 10 mm in diameter). 100 nm of gold, serving as electrical contacts, were applied on both sides of the pellet with a Leica EM SCD050 sputter coater.

## B.2 NMR pulse sequences

### Saturation recovery pulse sequence

Spin-lattice relaxation (SLR) rates ( $R_1$ ) in the laboratory frame of reference have been recorded employing the saturation recovery pulse sequence as shown in figure B.1a. The initial train of pulses  $\beta_1 = \pi/2$  is used to destroy the longitudinal magnetization  $M_z$ . The following recovery of the macroscopic longitudinal magnetization  $M_z$  is measured by an additional detection pulse  $\beta_2 = \pi/2$  as a function of the varying delay time  $t_d$ . The amplitude of the resulting free induction decay (FID) is proportional to the magnetization  $M_z$ . This recovery of  $M_z$  can be described by stretched exponentials of the form

$$M_\rho(t_d) = M_{\rho,eq}[1 - \exp(-[t_d/T_1]^\gamma)], \quad (\text{B.1})$$

where  $M_{\rho,eq}$  denotes the equilibrium magnetization and  $\gamma$  the stretching exponent. A recycle delay of  $5 \times T_1$  is employed to ensure that a complete relaxation of the magnetization is achieved. Classical 1D spectra can be obtained through Fourier transformation (FT) of an FID, preferably after full recovery of  $M_z$ .

### Spin-lock pulse sequence

Spin-lattice relaxation rates in the rotating frame of reference ( $R_{1\rho}$ ) have been recorded by a spin-lock pulse sequence illustrated in figure B.1b.[40, 41, 87, 88] An initial  $90^\circ$  pulse  $\beta_1 = \pi/2$  rotates the equilibrium magnetization  $M_{\rho,eq}$  into the  $x$ - $y$  plane where the magnetization is "locked" by the locking pulse  $\beta_2$  for the duration  $t_{lock}$ . After turning off the locking pulse  $\beta_2$ , the magnetization is relaxing towards zero in the field  $B_1$ , this behavior is true for the corresponding FID. The transients are recorded as a function of  $t_{lock}$  and can be parameterized by stretched exponentials.

$$M_\rho(t_{lock}) = M_{\rho,eq}[\exp(-[t_d/T_{1\rho}]^\gamma)]. \quad (\text{B.2})$$

### Solid-echo pulse sequence

Solid-state echoes have been recorded employing the pulse sequence as shown in figure B.1c. An initial pulse  $\beta_1 = \pi/2$  rotates the equilibrium magnetization  $M_{\rho,eq}$  into the  $x$ - $y$  plane and the spins start

to dephase due to transverse relaxation (SSR) during the preparation time  $t_p$ . At the end of  $t_p$ , a refocusing pulse  $\beta_2 = 64^\circ$  is applied resulting in an echo at  $t = 2t_p$ . The echo intensity  $M_{x,y}(t_p)$  can be parameterized with an exponential of the form

$$M_{x,y}(t_p) = M_{x,y}^{eq} [\exp(-[2t_p/T_2]^\gamma)]. \quad (\text{B.3})$$

The magnetization transients are usually described by single exponential functions with a  $\gamma$  of 1. Spectra can be obtained from the echoes by FT starting at the maximum of the echo.

### <sup>6,7</sup>Li NMR SAE pulse sequence

Spin-alignment echoes (SAE) have been recorded employing a Jeener-Broekart pulse sequence as shown in figure B.1d.[54] At fixed preparation time  $t_p$  (between  $10\mu\text{s}$  and  $20\mu\text{s}$ ) the echo amplitudes  $S_2(t_p, t_m)$  are measured as a function of mixing time  $t_m$ . The resulting decay curves can be described by stretched exponentials of the form

$$S_2(t_p, t_m) = A [\exp(-[\text{emph}t_m/\tau_{\text{SAE}}]^\gamma)], \quad (\text{B.4})$$

where  $\tau_{\text{SAE}}$  is the SAE correlation time and  $\gamma$  the stretching exponent. Spin-diffusion and relaxation processes can lead to a second decay step in the curve.[89]

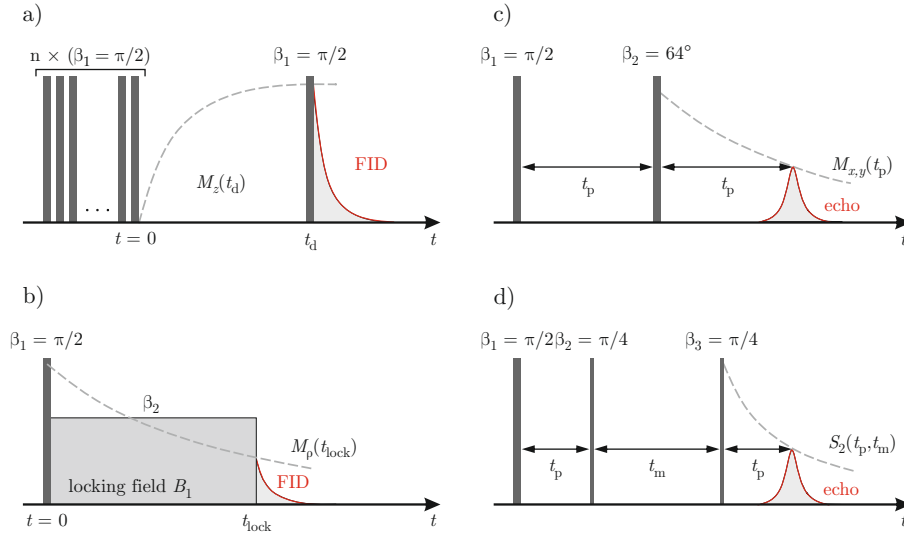


**Figure B.1** – Schematic illustration of NMR pulse sequences used in this work. a) Saturation recovery pulse sequence used for recording SLR rates in the laboratory frame of reference. b) Spin-lock pulse sequence used for recording  $\text{SLR}\rho$  rates in the rotating frame of reference. The second pulse  $\beta_2$  is applied to "lock" the magnetization in the  $x, y$  plane. c) Solid-state echo pulse sequence used for recording solid-echo spectra and  $R_2$ . d) Jeener-Broekart pulse sequence used for recording spin-alignment echoes (SAE).





# Publications

## C.1 Journal articles

### **Synthesis, crystal structure, and stability of cubic $\text{Li}_{7-x}\text{La}_3\text{Zr}_{2-x}\text{O}_{12}$**

Reinhard Wagner, Daniel Rettenwander, Günther J. Redhammer, Gerold Tippelt, Gebhard Sabathi, Maurizio E. Musso, [Bernhard Stanje](#), Martin Wilkening, Emmanuelle Suard and Georg Amthauer. *Inorganic Chemistry*, DOI: 10.1021/acs.inorgchem.6b01825 (2017), 12211 - 12219.

### **$\text{LiBi}_3\text{S}_5$ - A lithium bismuth Sulfide with strong cation disorder**

Suliman Nakhal, Dennis Wiedermann, [Bernhard Stanje](#), Oleksandr Dolotko, Martin Wilkening, Emmanuelle Suard and Martin Lerch. *Journal of Solid State Chemistry*, DOI: 10.1016/j.jssc.2016.03.010 (2016), 60 - 67.

### **High-energy mechanical treatment boosts ion Transport in nanocrystalline $\text{Li}_2\text{B}_4\text{O}_7$**

Dominik Wohlmuth, Viktor Epp, [Bernhard Stanje](#), Anna-Maria Welsch, Harald Behrens and Martin Wilkening. *Journal of the American Ceramic Society*, DOI: 10.1111/jace.14165 (2015), 1687 - 1693.

### **Li ion dynamics along the inner surfaces of layer-structured $2\text{H-Li}_x\text{NbS}_2$**

[Bernhard Stanje](#), Viktor Epp, Suliman Nakhal, Martin Lerch and Martin Wilkening. *ACS Applied Materials and Interfaces*, DOI: 10.1021/am5078655 (2015), 4089 - 4099.

### **"Ionic liquids-in-salt" - a promising electrolyte concept for high-temperature lithium batteries?**

Maciej J. Marczweski, [Bernhard Stanje](#), Ilie Hanzu, Martin Wilkening and Patrik Johansson. *Physical Chemistry Chemical Physics*, DOI: 10.1039/c4cp01133c (2014), 12341 - 12349.

## C.2 Oral presentations

### **Solid electrolytes: extremely fast charge carriers in single crystalline garnet-type $\text{Li}_6\text{La}_3\text{ZrTaO}_{12}$**

Bernhard Stanje, Daniel Rettenwander, Reinhard Uecker, Günther Redhammer and Martin Wilkening — *E-MRS - Fall Meeting 2016*, Warsaw (PL), September 19th-22nd, 2016.

### **Extremely mobile ions in solid electrolytes as seen by NMR**

Bernhard Stanje and Martin Wilkening — *20th International Conference on Solid State Ionics*, Keystone (US), June 14th-19th, 2015.

## C.3 Poster presentations

### **Identifying fast Li ions at the interfaces in composites of ionic liquids (EMIMTFSI) and Li salts (LiTFSI) by long-time $^7\text{Li}$ NMR.**

Bernhard Stanje, Patrick Bottke, Ilie Hanzu, Maciej J. Marczweski, Patrik Johansson and Martin Wilkening — *E-MRS - Spring Meeting 2016*, Lille (FR), May 2nd-6th, 2016.

### **Spatially confined Li diffusion in channel-structured $\text{LiBi}_3\text{S}_5$**

Bernhard Stanje, Suliman Nakhhal, Martin Lerch and Martin Wilkening — *Materials Day*, Graz (AT), September 28th, 2015.

### **Li-Ion dynamics of layer-structured $2\text{H-Li}_x\text{NbS}_2$ studied by $^7\text{Li}$ NMR**

Bernhard Stanje, Viktor Epp, Suliman Nakhhal, Martin Lerch and Martin Wilkening — *15th ECSSC - European Conference on Solid State Chemistry*, Vienna (AT), August 23rd-26th, 2015.

### **Lithium ion dynamics along the inner surface of layer-structured $2\text{H-Li}_x\text{NbS}_2$**

Bernhard Stanje, Suliman Nakhhal, Martin Lerch and Martin Wilkening — *20th International Conference on Solid State Ionics*, Keystone (US), June 14th-19th, 2015.

### **Tracking down fast Li ions in composites of ionic liquids and Li salts by long-time $^7\text{Li}$ NMR spin-lattice relaxation**

Bernhard Stanje, Patrick Bottke, Ilie Hanzu, Maciej J. Marczweski, Patrik Johansson and Martin Wilkening — *DIMAT 2014 - The International Conference on Diffusion in Materials*, Münster (DE), August 17th-22nd, 2014.

### **Li ion diffusion and ionic conduction in nanocrystalline, glassy and nanoglassy aluminosilicate $\text{LiAlSi}_4\text{O}_{10}$**

Bernhard Stanje, Patrick Bottke, Paul Heitjans and Martin Wilkening — *INCOME 2014 - International Conference on Mechanochemistry and Mechanical Alloying*, Krakow (PL), June 22nd-26th, 2014.

# Bibliography

- [1] Chen, N. Y. *Chemical Innovation* **2001**, 3(1), 14–20.
- [2] Sims, R. E. *Mitigation and Adaptation Strategies for Global Change* **2003**, 8(4), 349–370.
- [3] Hall, D. O.; Mynick, H. E.; Williams, R. H. *Nature* **1991**, 353(4), 11–12.
- [4] Dell, R.; Rand, D. *Journal of Power Sources* **2001**, 100(1–2), 2 – 17.
- [5] Chen, J. *Materials* **2013**, 6(1), 156.
- [6] Kim, J. G.; Son, B.; Mukherjee, S.; Schuppert, N.; Bates, A.; Kwon, O.; Choi, M. J.; Chung, H. Y.; Park, S. *Journal of Power Sources* **2015**, 282, 299 – 322.
- [7] Whittingham, M. *Chemical Reviews* **2004**, 104(10), 4271–4301.
- [8] Bottke, P.; Freude, D.; Wilkening, M. *The Journal of Physical Chemistry C* **2013**, 117(16), 8114–8119.
- [9] Wilkening, M.; Heitjans, P. *Phys. Rev. B* **2008**, 77, 024311.
- [10] Bader, B.; Heitjans, P.; Stockmann, H. J.; Ackermann, H.; Buttler, W.; Freilander, P.; Kiese, G.; van der Marel, C.; Schirmer, A. *Journal of Physics: Condensed Matter* **1992**, 4(20), 4779.
- [11] Van der Ven, A.; Ceder, G.; Asta, M.; Tepesch, P. D. *Phys. Rev. B* **2001**, 64, 184307.
- [12] Wilkening, M.; Heitjans, P. *ChemPhysChem* **2012**, 13(1), 53–65.
- [13] Böhmer, R.; Qi, F. *Solid State Nuclear Magnetic Resonance* **2007**, 31(1), 28 – 34.
- [14] Atkins, P.; dePaula, J. *Physical Chemistry: Thermo, Structure, and Change*; W. H. Freeman, 2014.
- [15] Murch, G. E. In *Phase Transformations in Materials*; Wiley-VCH Verlag GmbH, 2005; pages 171–238.

- [16] Mehrer, H. *Diffusion in Solids: Fundamentals, Methods, Materials, Diffusion-Controlled Processes*, Springer Series in Solid-State Sciences; Springer Berlin Heidelberg, 2007.
- [17] Holleman, A.; Wiberg, E.; Wiberg, N. *Lehrbuch der anorganischen Chemie*; de Gruyter, 1995.
- [18] Scholze, H. *Glass: nature, structure, and properties*; Springer-Verlag, 1991.
- [19] Schmalzried, H. *Chemical Kinetics of Solids*; Wiley, 2008.
- [20] Heitjans, P., Kärger, J., Eds. *Diffusion in Condensed Matter*; Springer Nature, 2005.
- [21] Christian, J. W.; Vitek, V. *Reports on Progress in Physics* **1970**, 33(1), 307.
- [22] Cahn, R.; Haasen, P.; Kramer, E. *Materials Science and Technology, Cumulative Index*, Materials Science and Technology; Wiley, 1998.
- [23] Wadhwa, A.; Dhaliwal, E. *A Textbook of Engineering Material and Metallurgy*; University Science Press, 2008.
- [24] Kostorz, G., Ed. *Phase Transformations in Materials*; Wiley-Blackwell, 2001.
- [25] Kittel, C. *Einführung in die Festkörperphysik*; Oldenbourg, 2002.
- [26] Heitjans, P.; Indris, S. *Journal of Physics: Condensed Matter* **2003**, 15(30), R1257.
- [27] The nobel prize in physics 1952. nobelprize.org. **2016**.
- [28] Abragam, A. *The Principles of Nuclear Magnetism*, International series of monographs on physics; Clarendon Press, 1961.
- [29] Keeler, J. *Understanding NMR Spectroscopy*; Wiley, 2011.
- [30] Slichter, C. P. *Principles of Magnetic Resonance (Springer Series in Solid-State Sciences)*; Springer, 2010.
- [31] Kremer, F.; Schönhals, A. *Broadband Dielectric Spectroscopy*; Springer Berlin Heidelberg, 2012.
- [32] Levitt, M. H. *Spin Dynamics: Basics of Nuclear Magnetic Resonance*; Wiley, 2008.
- [33] Mehring, M. *Principles of High Resolution NMR in Solids*; Springer, 1983.
- [34] Duer, M. J. *Introduction to Solid-State NMR Spectroscopy*; Wiley-Blackwell, 2005.
- [35] Kelly, S. W.; Sholl, C. A. *Journal of Physics: Condensed Matter* **1992**, 4(12), 3317–3330.
- [36] Heitjans, P.; Indris, S.; Wilkening, M. *Diffusion Fundamentals* **2005**, 4, 45.1 – 45.20.

- [37] Richards, P. M.; Springer-Verlag Berlin Heidelberg, 1979; pages 141–174; 15.
- [38] Wilkening, M. *Ultralangsame Ionenbewegungen in Festkörpern* Dissertation, Universität Hannover, **2005**.
- [39] Bloembergen, N.; Purcell, E. M.; Pound, R. V. *Phys. Rev.* **1948**, *73*, 679–712.
- [40] Ailion, D.; Slichter, C. P. *Phys. Rev. Lett.* **1964**, *12*, 168–171.
- [41] Slichter, C. P.; Ailion, D. *Phys. Rev.* **1964**, *135*, A1099–A1110.
- [42] Bunde, A.; Dieterich, W.; Maass, P.; Meyer, M. In *Diffusion in Condensed Matter: Methods, Materials, Models*; Heitjans, P., Kärger, J., Eds.; Springer Berlin Heidelberg: Berlin, Heidelberg, 2005; pages 813–856.
- [43] Küchler, W. *Kernspinresonanz-Untersuchungen zur Diffusion von Li in der schichtstrukturierten und der kubischen Interkalationsverbindung  $Li_xTiS_2$*  Dissertation, Universität Hannover, **1992**.
- [44] Heitjans, P.; Schirmer, A.; Indris, S. In *Diffusion in Condensed Matter: Methods, Materials, Models*; Heitjans, P., Kärger, J., Eds.; Springer Berlin Heidelberg: Berlin, Heidelberg, 2005; pages 367–415.
- [45] Richards, P. M. *Solid State Communications* **1978**, *25*(12), 1019 – 1021.
- [46] Küchler, W.; Heitjans, P.; Payer, A.; Schöllhorn, R. *Solid State Ionics* **1994**, *70*, 434 – 438.
- [47] von Smoluchowski, M. *Annalen der Physik* **1906**, *326*(14), 756–780.
- [48] Einstein, A. *Annalen der Physik* **1905**, *322*(8), 549–560.
- [49] Einstein, A. *Annalen der Physik* **1906**, *324*(2), 371–381.
- [50] Qi, M.  *$^2H$ - und  $^7Li$ -NMR-Untersuchungen zur Dynamik an Ionenleitern* Dissertation, Johannes Gutenberg-Universität Mainz, **2003**.
- [51] Ruprecht, B.; Wilkening, M.; Uecker, R.; Heitjans, P. *Phys. Chem. Chem. Phys.* **2012**, *14*, 11974–11980.
- [52] Wilkening, M.; Küchler, W.; Heitjans, P. *Phys. Rev. Lett.* **2006**, *97*, 065901–065905.
- [53] Wilkening, M.; Heitjans, P. *Journal of Physics: Condensed Matter* **2006**, *18*(43), 9849.
- [54] Jeener, J.; Broekaert, P. *Phys. Rev.* **1967**, *157*, 232–240.
- [55] Böhmer, R. *Journal of Magnetic Resonance* **2000**, *147*(1), 78 – 88.

- [56] Böhmer, R.; Jeffrey, K.; Vogel, M. *Progress in Nuclear Magnetic Resonance Spectroscopy* **2007**, *50*(2–3), 87 – 174.
- [57] Barsoukov, E.; Macdonald, J. *Impedance Spectroscopy: Theory, Experiment, and Applications*; Wiley, 2005.
- [58] Einstein, A.; von Smoluchowski, M. *Untersuchungen über die Theorie der Brownschen Bewegung*, Ostwalds Klassiker der exakten Wissenschaften; Deutsch, 1997.
- [59] Nernst, W. *Zeitschrift für Physikalische Chemie* **1888**, *2*(9), 613 – 637.
- [60] Townsend, J. S. *Philosophical Transactions of the Royal Society of London A: Mathematical, Physical and Engineering Sciences* **1900**, *193*, 129–158.
- [61] Einstein, A. *Zeitschrift für Elektrochemie und angewandte physikalische Chemie* **1908**, *14*(17), 235–239.
- [62] Murch, G. *Solid State Ionics* **1982**, *7*(3), 177 – 198.
- [63] Nakhal, S.; Wiedemann, D.; Stanje, B.; Dolotko, O.; Wilkening, M.; Lerch, M. *Journal of Solid State Chemistry* **2016**, *238*, 60 – 67.
- [64] Stanje, B.; Epp, V.; Nakhal, S.; Lerch, M.; Wilkening, M. *ACS Applied Materials & Interfaces* **2015**, *7*(7), 4089–4099.
- [65] Wagner, R.; Rettenwander, D.; Redhammer, G. J.; Tippelt, G.; Sabathi, G.; Musso, M. E.; Stanje, B.; Wilkening, M.; Suard, E.; Amthauer, G. *Inorganic Chemistry* **2016**, *55*(23), 12211–12219.
- [66] Marczewski, M. J.; Stanje, B.; Hanzu, I.; Wilkening, M.; Johansson, P. *Phys. Chem. Chem. Phys.* **2014**, *16*, 12341–12349.
- [67] Kuhn, A.; Narayanan, S.; Spencer, L.; Goward, G.; Thangadurai, V.; Wilkening, M. *Phys. Rev. B* **2011**, *83*, 094302–094313.
- [68] Awaka, J.; Kijima, N.; Hayakawa, H.; Akimoto, J. *Journal of Solid State Chemistry* **2009**, *182*(8), 2046 – 2052.
- [69] Rettenwander, D.; Wagner, R.; Langer, J.; Maier, M. E.; Wilkening, M.; Amthauer, G. *European Journal of Mineralogy* **2016**, *28*(3), 619–629.
- [70] Shin, D. O.; Oh, K.; Kim, K. M.; Park, K.-Y.; Lee, B.; Lee, Y.-G.; Kang, K. *Scientific Reports* **2015**, *5*, 18053.
- [71] Nakano, H.; Dokko, K.; Hara, M.; Isshiki, Y.; Kanamura, K. *Ionics* **2008**, *14*(2), 173–177.

- [72] Thangadurai, V.; Kaack, H.; Weppner, W. J. F. *Journal of the American Ceramic Society* **2003**, *86*(3), 437–440.
- [73] Hyooma, H.; Hayashi, K. *Materials Research Bulletin* **1988**, *23*(10), 1399 – 1407.
- [74] Kuhn, A.; Kunze, M.; Sreeraj, P.; Wiemhöfer, H.-D.; Thangadurai, V.; Wilkening, M.; Heitjans, P. *Solid State Nuclear Magnetic Resonance* **2012**, *42*, 2 – 8.
- [75] Wilkening, M.; Iwaniak, W.; Heine, J.; Epp, V.; Kleinert, A.; Behrens, M.; Nuspl, G.; Bensch, W.; Heitjans, P. *Phys. Chem. Chem. Phys.* **2007**, *9*, 6199–6202.
- [76] Buschmann, H.; Dolle, J.; Berendts, S.; Kuhn, A.; Bottke, P.; Wilkening, M.; Heitjans, P.; Senyshyn, A.; Ehrenberg, H.; Lotnyk, A.; Duppel, V.; Kienle, L.; Janek, J. *Phys. Chem. Chem. Phys.* **2011**, *13*, 19378–19392.
- [77] Epp, V.; Gun, O.; Deiseroth, H.-J.; Wilkening, M. *Phys. Chem. Chem. Phys.* **2013**, *15*, 7123–7132.
- [78] Preishuber-Pflügl, F.; Wilkening, M. *Dalton Trans.* **2016**, *45*, 8675–8687.
- [79] Šepelák, V.; Duvel, A.; Wilkening, M.; Becker, K.-D.; Heitjans, P. *Chem. Soc. Rev.* **2013**, *42*, 7507–7520.
- [80] Heitjans, P.; Masoud, M.; Feldhoff, A.; Wilkening, M. *Faraday Discuss.* **2007**, *134*, 67–82.
- [81] Wilkening, M.; Epp, V.; Feldhoff, A.; Heitjans, P. *The Journal of Physical Chemistry C* **2008**, *112*(25), 9291–9300.
- [82] Qi, F.; Rier, C.; Böhmer, R.; Franke, W.; Heitjans, P. *Phys. Rev. B* **2005**, *72*, 104301–104312.
- [83] Kuhn, A.; Tobschall, E.; Heitjans, P. *Zeitschrift für Physikalische Chemie* **2009**, *223*(10-11), 1359–1377.
- [84] Bottke, P. *NMR-Spektroskopie an nanokristallinem, nanoglasigem und glasigem Eukryptit LiAlSiO<sub>4</sub>* Diplomarbeit, Leibniz Universität Hannover, **2010**.
- [85] Stanje, B.; Bottke, P.; Heitjans, P.; Wilkening, M. **2017**.
- [86] Kuhn, A.; Wilkening, M.; Heitjans, P. *Solid State Ionics* **2009**, *180*(4–5), 302 – 307.
- [87] Wolf, D. *Phys. Rev. B* **1974**, *10*, 2724–2732.
- [88] Martin, M. L. *Organic Magnetic Resonance* **1983**, *21*(12), 770–770.
- [89] Kuhn, A.; Epp, V.; Schmidt, G.; Narayanan, S.; Thangadurai, V.; Wilkening, M. *Journal of Physics: Condensed Matter* **2012**, *24*(3), 035901.

